Frank Ko | Yuqin Wan

Introduction to Nanofiber Materials

CAMBRIDGE

Introduction to Nanofiber Materials

Presenting the latest coverage of the fundamentals and applications of nanofibrous materials and their structures for graduate students and researchers, this book bridges the communication gap between fiber technologists and materials scientists and engineers. Featuring intensive coverage of electroactive, bioactive and structural nanofibers, it provides a comprehensive collection of processing conditions for electrospinning and includes recent advances in nanoparticle-/nanotube-based nanofibers. The book also covers mechanical properties of fibers and fibrous assemblies, as well as characterization methods.

Frank K. Ko is Canada Research Chair Professor in Advanced Fibrous Materials and Director of the Advanced Materials and Process Engineering Laboratory, University of British Columbia.

Yuqin Wan is Research Associate in Advanced Fibrous Materials, Advanced Materials and Process Engineering Laboratory, University of British Columbia, Canada, and Associate Professor in the School of Textiles and Clothing, Jiangnan University, China.

Introduction to Nanofiber Materials

FRANK K. KO

and

YUQIN WAN

University of British Columbia, Vancouver

MRS MATERIALS RESEARCH SOCIETY®
Advancing materials. Improving the quality of life.

CAMBRIDGE
UNIVERSITY PRESS

CAMBRIDGE
UNIVERSITY PRESS

University Printing House, Cambridge CB2 8BS, United Kingdom

Published in the United States of America by Cambridge University Press, New York

Cambridge University Press is part of the University of Cambridge.

It furthers the University's mission by disseminating knowledge in the pursuit of education, learning and research at the highest international levels of excellence.

www.cambridge.org
Information on this title: www.cambridge.org/9780521879835

© Frank K. Ko and Yuqin Wan 2014

This publication is in copyright. Subject to statutory exception and to the provisions of relevant collective licensing agreements, no reproduction of any part may take place without the written permission of Cambridge University Press.

First published 2014

Printed in the United Kingdom by . . .

A catalogue record for this publication is available from the British Library

Library of Congress Cataloguing in Publication data

ISBN 978-0-521-87983-5 Hardback

Cambridge University Press has no responsibility for the persistence or accuracy of URLs for external or third-party internet websites referred to in this publication, and does not guarantee that any content on such websites is, or will remain, accurate or appropriate.

Contents

1 Introduction *page* 1

1.1 How big is a nanometer? 1
1.2 What is nanotechnology? 1
1.3 Historical development of nanotechnology 2
1.4 Classification of nanomaterials 5
1.5 Nanofiber technology 5
1.6 Unique properties of nanofibers 6
1.6.1. Effect of fiber size on surface area 7
1.6.2. Effect of fiber size on bioactivity 7
1.6.3. Effect of fiber size on electroactivity 8
1.6.4. Effect of fiber size on strength 9
References 10

2 Fundamentals of polymers 13

2.1 Polymeric materials 13
2.2 Polymer flow, nonlinearity and heterogeneity 14
2.2.1 Linear kinetics 14
2.2.2 Nonlinear behavior 15
2.2.3 Viscoelastic models 16
2.2.3.1 The basic elements: spring and dashpot 16
2.2.3.2 Maxwell model 17
2.2.3.3 Voigt (Kelvin) model 20
2.2.3.4 Four-element model 21
2.3 Intrinsic structures of polymers 23
2.3.1 Molecular bondings 23
2.3.1.1 Van der Waals forces 24
2.3.1.2 Hydrogen bonding 24
2.3.2 Configuration and conformation 25
2.3.2.1 Configuration 25
2.3.2.2 Conformation 25
2.3.2.3 Other chain structures 26
2.3.3 Order and disorder 27
2.3.3.1 Amorphous and crystal structure 27

2.3.3.2 Orientation 28
2.3.3.3 Measurement of order and disorder 29
2.3.4 Molecular weight and molecular weight distribution 29
2.4 Thermal behavior 32
2.5 Polymer solutions 33
2.5.1 Solubility parameter 33
2.5.2 Solution viscosity 36
2.5.2.1 Intrinsic viscosity 36
2.5.2.2 Intrinsic viscosity and molecular weight 36
2.5.2.3 Measurement of intrinsic viscosity 37
2.6 Fiber, plastic and elastomer 38
2.7 Fiber formation 39
2.7.1 Melt spinning 39
2.7.2 Wet spinning 40
2.7.3 Dry spinning 40
2.7.4 Fiber properties 40
2.7.4.1 Polymer structure and fiber mechanical properties 40
2.7.4.2 Processing and fiber properties 43
References 43

3 Nanofiber technology 45

3.1 Nanofibers forming technology 45
3.1.1 Conjugate spinning (island in the sea) 45
3.1.2 Chemical vapor deposition (CVD) 45
3.1.3 Phase separation (sol–gel process) 46
3.1.4 Drawing 47
3.1.5 Template synthesis 47
3.1.6 Self-assembly 47
3.1.7 Meltblown technology 47
3.1.8 Electrospinning 49
3.2 Electrospinning process 49
3.3 Processing parameters 50
3.3.1 Spinning dope concentration and viscosity 50
3.3.2 Applied voltage 52
3.3.3 Spinning dope temperature 52
3.3.4 Surface tension 52
3.3.5 Electrical conductivity 53
3.3.6 Molecular weight of polymer 53
3.3.7 Spinning distance 54
3.3.8 Spinning angle 55
3.3.9 Orifice diameter 55
3.3.10 Solvent boiling point 55
3.3.11 Humidity 56

3.3.12 Dielectric constant 57
3.3.13 Feeding rate 57
3.4 Melt electrospinning 58
3.5 Applications of nanofibers 59
3.5.1 Reinforcement fibers in composites 59
3.5.2 Protective clothing 59
3.5.3 Filtration 60
3.5.4 Biomedical devices 61
3.5.4.1 Wound dressing 61
3.5.4.2 Medical prostheses 61
3.5.4.3 Tissue scaffolds 61
3.5.4.4 Controlled drug delivery 61
3.5.5 Electrical and optical applications 62
3.5.6 Nanosensors 62
References 62

4 Modeling and simulation 65

4.1 Electrospinning mechanism 65
4.2 Fundamentals of process modeling 65
4.2.1 Newton's law 66
4.2.2 Conservation laws 67
4.3 Taylor cone 67
4.4 Jet profile 68
4.5 Models 69
4.5.1 One-dimensional model 70
4.5.2 Three-dimensional models 72
4.5.2.1 Spivak–Dzenis model 72
4.5.2.2 Rutledge's model 72
4.5.2.3 Wan–Guo–Pan model 73
4.6 Application of models in parametric analysis 74
4.7 Computer simulation 75
References 79

5 Mechanical properties of fibers and fiber assemblies 81

5.1 Structure of hierarchy of textile materials 81
5.2 Size effect on mechanical properties 81
5.3 Theoretical modulus of a fiber 82
5.4 Mechanical properties of nonwovens 84
5.4.1 Geometry of nonwovens 84
5.4.2 Deformation of nonwovens 86
5.5 Mechanical properties of yarns 87
5.5.1 Yarn geometry 88
5.5.2 Mechanical properties of linear fiber assemblies 90

5.5.2.1 Stress analysis 90
5.5.2.2 Strain analysis 92
5.5.3 Mechanical properties of staple yarns 93
5.6 Mechanical properties of woven fabrics 96
5.6.1 Woven fabric geometry 97
References 100

6 Characterization of nanofibers 102

6.1 Structural characterization of nanofibers 102
6.1.1 Optical microscopy (OM) 102
6.1.2 Scanning electron microscopy (SEM) 103
6.1.3 Transmission electron microscopy (TEM) 106
6.1.4 Atomic force microscopy (AFM) 108
6.1.5 Scanning tunneling microscopy (STM) 110
6.1.6 X-ray diffraction 112
6.1.6.1 Wide-angle X-ray diffraction 114
6.1.6.2 Small-angle X-ray scattering 114
6.1.7 Mercury porosimetry 115
6.2 Chemical characterization of nanofibers 116
6.2.1 Fourier transform infra-red spectroscopy (FTIR) 116
6.2.2 Raman spectroscopy (RS) 119
6.2.3 Nuclear magnetic resonance (NMR) 121
6.3 Mechanical characterization of nanofibers 122
6.3.1 Microtensile testing of nanofiber nonwoven fabric 123
6.3.2 Mechanical testing of a single nanofiber 125
6.4 Thermal analysis 128
6.4.1 Thermogravimetric analysis (TGA) 129
6.4.2 Differential scanning calorimetry (DSC) 131
6.5 Characterization of other properties 134
6.5.1 Wettability and contact angle 134
6.5.2 Electrical conductivity 136
6.5.3 Electrochemical properties 137
6.5.3.1 Linear-sweep voltammetry and cyclic voltammetry 137
6.5.3.2 Chronopotentiometry 139
6.5.4 Magnetic properties 140
References 143

7 Bioactive nanofibers 147

7.1 The development of biomaterials 147
7.2 Bioactive nanofibers 148
7.2.1 Nanofibers for tissue engineering 148
7.2.1.1 Extracellular matrices for tissue engineering 148
7.2.1.2 Nanofiber scaffolds for tissue engineering 149

7.2.2 Nanofibers for drug delivery 156
7.2.2.1 Drug delivery systems 156
7.2.2.2 Nanofibers for drug delivery 157
7.2.3 Nanofibers for biosensors 159
7.2.3.1 Biosensors 159
7.2.3.2 Nanofiber biosensors 160
7.3 Assessment of nanofiber bioactivity 161
7.3.1 Assessment of tissue compatibility 163
7.3.2 Assessment of degradation 163
References 163

8 Electroactive nanofibers 167

8.1 Introduction 167
8.2 Conductive nanofibers 167
8.2.1 Conductive polymers and fibers 167
8.2.2 Fundamental principle for superior electrical conductivity 169
8.2.3 Electroactive nanofibers 170
8.3 Magnetic nanofibers 179
8.3.1 Supermagnetism 179
8.3.2 Supermagnetic nanofibers 180
8.4 Photonic nanofibers 182
8.4.1 Polymer photonics 182
8.4.2 Fluorescent nanofibers 184
8.4.3 Photo-catalytic nanofibers 186
References 189

9 Nanocomposite fibers 192

9.1 Carbon nanotubes 192
9.1.1 Structure and properties 192
9.1.1.1 Structure 192
9.1.1.2 Mechanical properties 196
9.1.1.3 Electrical properties 196
9.1.1.4 Thermal properties 197
9.1.2 Dispersion of carbaon nanotubes 197
9.1.2.1 Purification 197
9.1.2.2 Mechanical dispersion 199
9.1.2.3 Chemical dispersion 200
9.1.3 Alignment of carbon nanotubes 205
9.1.3.1 Alignment of carbon nanotubes in solution 205
9.1.3.2 Alignment of carbon nanotubes in matrix 207
9.1.4 Carbon nanotube nanocomposite fibers 209
9.1.4.1 Methods for producing carbon nanotube fibers 210
9.1.4.2 Chemical vapor deposition 210

9.1.4.3 Dry spinning 212
9.1.4.4 Liquid crystal spinning 212
9.1.4.5 Wet spinning 213
9.1.4.6 Traditional spinning 214
9.1.4.7 Electrospinning 214
9.2 Nanoclay 215
9.2.1 Structure and properties 215
9.2.2 Clay nanocomposites 216
9.2.3 Nanoclay nanocomposite fibers 218
9.3 Graphite graphenes 220
9.3.1 Structure and properties 220
9.3.2 Graphene nanocomposites 222
9.3.3 Graphene nanocomposite nanofibers 222
9.4 Carbon nanofibers 223
9.4.1 Vapor-grown carbon nanofibers 223
9.4.2 Electrospun carbon nanofibers 225
9.4.3 Carbon nanofiber composites 226
References 227

10 Future opportunities and challenges of electrospinning 240

10.1 Past, present and future of nanotechnology 240
10.2 Global challenges and nanotechnology 241
10.2.1 Nanofibers in energy 242
10.2.1.1 Electrolytes in fuel cells or batteries 242
10.2.1.2 Supercapacitors 242
10.2.1.3 Dye-sensitized solar cells 243
10.2.1.4 Power transmission lines 243
10.2.2 Nanofibers in filtration 243
10.2.3 Nanofibers in biomedical engineering 244
10.3 Challenges 244
10.3.1 Mechanism analysis 244
10.3.2 Quality control 245
10.3.3 Scale-up manufacturing 245
10.3.4 Structural property improvement 253
10.4 New frontiers 254
References 255

Appendix I Terms and unit conversion 259
Appendix II Abbreviation of polymers 261
Appendix III Classification of fibers 263
Appendix IV Polymers and solvents for electrospinning 264
Index 266

1 Introduction

1.1 How big is a nanometer?

By definition, a nanometer, abbreviated as nm, is a unit for length that measures one billionth of a meter. (1 nm $= 10^{-3}$ μm $= 10^{-6}$ mm $= 10^{-7}$ cm $= 10^{-9}$ m.) Our hair is visible to the naked eye. Using an optical microscope we can measure the diameter of our hair, which is in the range of 20–50 microns(Mm) or 20 000–50 000 nm. Blood cells are not visible to the naked eye, but they can be seen under the microscope, revealing a diameter of about 10 microns or 10 000 nm. The diameter of hydrogen atoms is 0.1 nm. In other words 10 hydrogen atoms can be placed side-by-side in 1 nm. Figure 1.1 provides an excellent illustration of the relative scales in nature. The discovery of nanomaterials ushered us to a new era of materials. We have progressed from the microworld to the nanoworld.

1.2 What is nanotechnology?

According to the National Science Foundation in the United States nanotechnology is defined as [1]:

> Research and technology development at the atomic, molecular or macromolecular levels, in the length scale of approximately 1–100 nanometer range, to provide a fundamental understanding of phenomena and materials at the nanoscale and to create and use structures, devices and systems that have novel properties and functions because of their small and/or intermediate size. The novel and differentiating properties and functions are developed at a critical length scale of matter typically under 100 nm. Nanotechnology research and development includes manipulation under control of the nanoscale structures and their integration into larger material components, systems and architectures. Within these larger scale assemblies, the control and construction of their structures and components remains at the nanometer scale. In some particular cases, the critical length scale for novel properties and phenomena may be under 1 nm (e.g., manipulation of atoms at ~0.1 nm) or be larger than 100 nm. (e.g., nanoparticle(nanoparticle) reinforced polymers have the unique feature at ~ 200–300 nm as a function of the local bridges or bonds between the nano particles and the polymer).

Accordingly nanotechnology is the scientific field that is concerned with the study of the phenomena and functions of matters within the dimensional range of 0.1–100 nm. It is the study of the motion and changes of atoms, molecules, and of other forms of

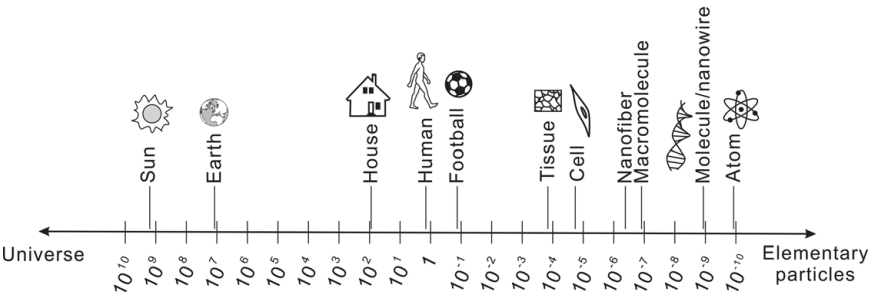

Fig. 1.1 Illustration of relative scale in nature. (The linear distance which each plate represents is indicated on this logarithmic scale in meters.)

matter. Nanotechnology, building upon the foundation of nanoscience, is concerned with the manufacturing of new materials, new devices and the development of research methodology and techniques for new technology.

Nanotechnology can also be referred to as the technology for the formation of nanomaterials and nanodevices, including the formation of nanostructural units according to a specific methodology to form macroscopic treatment (processing) of nanomaterials such as dispersion, forming technology as in the case of the formation of nanofibers and their composites.

Nanotechnology can be organized into three levels. The first level is molecular (atomic) nanotechnology wherein the molecules (atoms) are spatially organized in the nanospace in a repetitive manner. This in turn will create internally ordered nanostructures. Self-assembly and mineralization in biological materials are examples of molecular nanotechnology. The technology for controlling the morphology and uniformity of nanostructures is called the second level of nanotechnology. For example, in colloids and gels we do not concern ourselves with the order of arrangement of the molecule itself at the nanoscale. They form only morphologies of nanostructure of certain regularity. The third level of nanotechnology is concerned with the technology of the formation of nanosacle structures but is unable to control the degree of order of the molecules and atoms in the nanostructures. At the third level of nanotechnology the morphology and uniformity of the nanostructure are also uncontrolled [2].

1.3 Historical development of nanotechnology

Although the use of nanomaterials can arguably be traced back to over 1000 years ago when the smoke from a candle was used in China as ink, the first scientific discussion of nanotechnology is widely attributed to the 1959 Nobel Prize winning physicist Richard Feyman in his well known “There’s Plenty of Room at the Bottom” lecture at the California Institute of Technology (Caltech). In this lecture he boldly challenged his audience in his now famous statement.

People tell me about miniaturization, and how far it has progressed today. They tell me about electric motors that are the size of the nail on your small finger. And there is a device on the market, they tell me, by which you can write the Lord's Prayer on the head of a pin. But that's nothing; that's the most primitive, halting step in the direction I intend to discuss. It is a staggeringly small world that is below. In the year 2000, when they look back at this age, they will wonder why it was not until the year 1960 that anybody began seriously to move in this direction. Why cannot we write the entire 24 volumes of the Encyclopedia Brittanica on the head of a pin?

It is of interest to note that, 40 years after the Feyman lecture, coincidentally in the year 2000, US President Clinton announced the Notational Nanotechnology Initiative (NNI) that kicked-off the global gold rush in nanotechnology. Over a period of 10 years, developed countries have invested over $22.134 billion in nanotechnology research with more than 1/3 ($8.918 billion) of that amount spent in the USA alone [3].

Notwithstanding the foresight of Professor Feyman, the development of nanotechnology as a revolutionary/game-changing technology is the results of three ingredients: (1) the availability of tools to see and manipulate matter at the nanoscale; (2) astute observations and recognition of nanoscale matters and nanoeffects; and (3) sustained financial support from government and industry.

More than a decade after the Feyman lecture, in 1974 Norio Taniguchi, University of Tokyo, coined the word nanotechnology when he made the distinction between engineering of micrometer scale microtechnology and a new submicrometer level which he dubbed 'nanotechnology' [3].

In 1981, IBM's scanning tunneling microscope (STM) was developed at the IBM Zurich Research Laboratory. STM and its offspring, including the atomic force microscope invented in 1986, provided researchers around the world with the basic tools they needed to explore and manipulate materials at the atomic scale [3].

The atomic force microscope was invented in 1985 by ZRL researchers Gerd Binnig and Christoph Gerber, together with Professor Calvin Quate of Stanford University. Their invention earned them the Nobel Prize and expanded the scope of nanotechnology research to nonconducting materials [3].

In 1989, IBM Fellow Don Eigler was the first to controllably manipulate individual atoms on a surface, using STM to spell out 'I-B-M' by positioning 35 xenon atoms and, in the process, perhaps creating the world's smallest logo [3].

Armed with the new tools, several discoveries of fullerenes were made and they have added considerable excitements to the rapidly growing field of nanotechnology. For example, although there are conflicting opinions, Sumio Iijima from Japan is largely credited for the discovery of fullerene-related carbon nanotubes in 1991 [3, 4]. The tubes contained at least two layers, often many more, and ranged in outer diameter from about 3 nm to 30 nm. They were invariably closed at both ends. In 1996, Smalley shared the Nobel Prize in Chemistry with his Rice University colleague Robert Curl and the British chemist Harold Kroto for their discovery of the buckyballs in 1985. A good example of the application of nanoeffects is the nanoshells invented in 1998 by Naomi Halas at Rice University. The nanoshells are a new class of multi-layered nanoscale

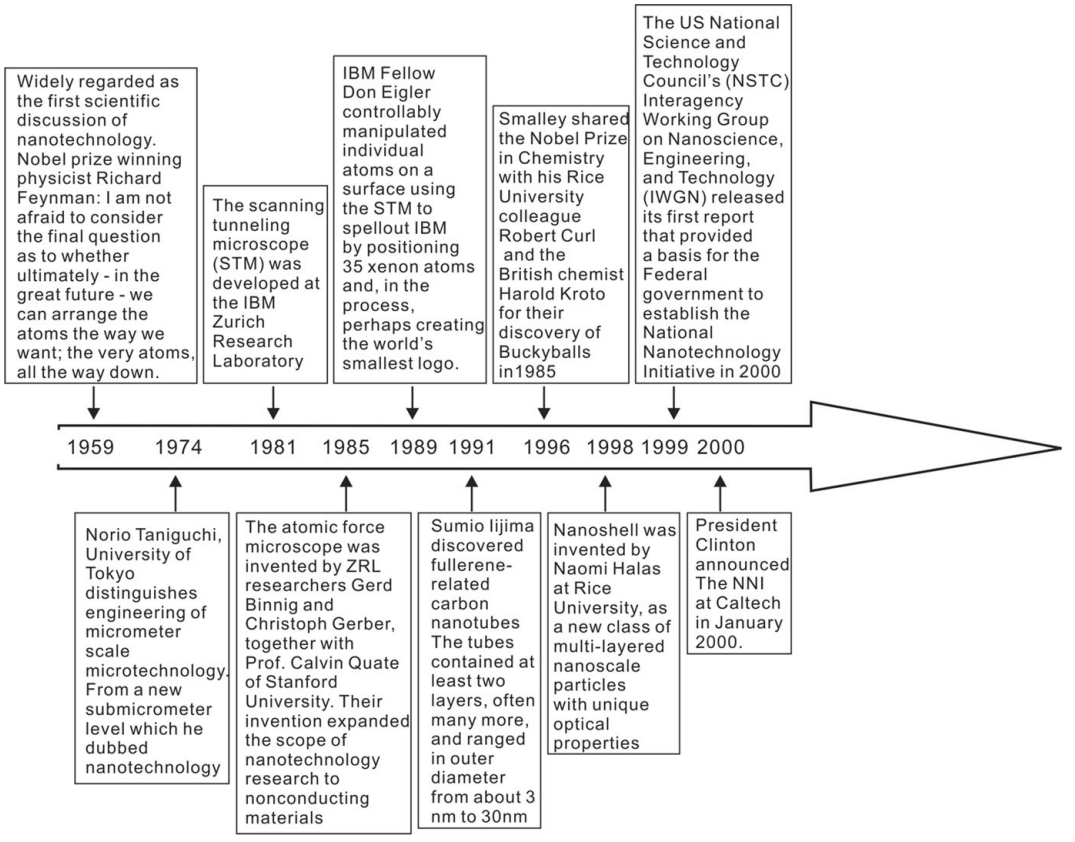

Fig. 1.2 Nanotechnology historical timeline (adapted from Ref. [5] with modifications).

particles with unique optical properties controlled by the thickness and composition of their constituent layers. By varying the relative size of the glass core and the gold shell layer, researchers can 'tune' nanoshells to respond to different wavelengths of light. For biomedical applications, nanoshells can be designed and fabricated to absorb near infrared light. Near-infrared light, a region of the spectrum just beyond the visible range, is optimal for medical imaging and treatment because it passes harmlessly through soft tissue.

With the seed planted by Feyman, the tools invented by researchers in IBM, and the innovative discoveries by scientists from Japan, Rice University and elsewhere in the 1980s and 1990s, created the necessary but insufficient conditions for the coming of the nanotechnology age until the establishment of the National Nanotechnology Initiative thanks largely to dedicated effort of dedicated governmental scientific officers such as Dr. Roco [3]. The 1999 IWGN workshop report prepared by the National Science and Technology Council Committee on Technology Interagency Working Group on Nanoscience, Engineering and Technology (IWGN) forms the basis for the NNI announced by President Clinton in 2000. Figure 1.2 shows the Nanotechnology historical timeline.

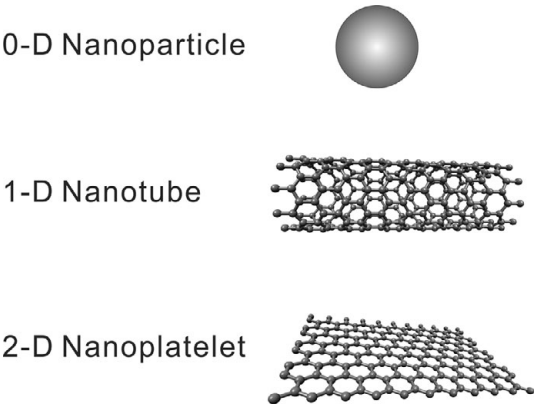

Fig. 1.3 Dimensional classification of nanomaterials.

1.4 Classification of nanomaterials

The materials produced in nanotechnology can be classified according to dimension, chemical composition, materials properties, material applications and manufacturing technology. From the view of dimension, nanomateirals are classified as zero-dimensional (0-D), one-dimensional (1-D) and two-dimensional (2-D) materials, as shown in Fig. 1.3. A 0-D nanomaterial has three directions of nanosymmetry. Quantum dots and nanoparticles are examples of 0-D nanomaterials. 1-D nanomaterials such as nanowires and nanotubes have two directions of nanosymmetry or have dimensions less than 100 nm. Examples of 2-D materials are nanoclays and graphene sheets wherein the through thickness direction is less than 100 nm.

Based on chemical composition we have nanometals, nanoceramics, nanopolymers, nanoglasses and nanoctystals. Regarding material properties we have nanomagnetic materials, nonlinear nanophotonic materials, suerconducting nanomaterials, thermoelectric nanomaterials, semiconducting nanomaterials, etc. One can also classify nanomaterials based on their applications, these include nanoelectronic materials, optoelectronic materials, energy storage nanomaterials, nanosensor materials, nanomedicines, etc.

1.5 Nanofiber technology

Although promising, most nanotechnology research is limited to dozens to a few hundred particles or molecules [6, 7]. In order to realize massive assembly techniques, large-scale devices and commercializable products need to be developed. Another challenge for nanotechnology is the lack of effective and efficient ways for fabrication macroscale structures. To be utilized in this macroworld, nanomaterials need to be converted to micromaterials and macromaterials. Nanofibre technology is a technique involving the synthesis, processing, manufacturing and application of fibers with nanoscale dimension. As a technique of fabrication of continuous 1-D nanomaterials, nanofibre technology is a

promising technique that can massively assemble 1-D and 2-D nanomaterials, realize large-scale production of nanomaterials involved products and prepare continuous 1-D fiberous elements that facilitate the fabrication of microsale and macroscale structures.

Fibers are solid state linear nanomaterials characterized by flexibility and an aspect ratio greater than 1000:1. Nanofibres are defined as fibers with a diameter equal to or less than 100 nm. But in general, all the fibers with a diameter below 1 μm (1000 nm) are recognized as nanofibers. Materials in fiber form are of great practical and fundamental importance. The combination of high specific surface area, flexibility and superior directional strength makes fibers a preferred material form for many applications varying from clothing to reinforcements for aerospace structures. Fibrous materials in the nanometer scale are the fundamental building blocks of living systems. For instance, DNA molecules are double helix strands with a diameter of 1.5 nm, cytoskeleton filaments have a diameter around 30 nm, and even sensory cells such as hair cells and rod cells of the eyes are structures with extra-cellular matrices or a multifunctional structural backbone for tissues and organs formed with nanofibers.

Analogous to nature's design, nanofibers of electronic polymers and their composites can provide fundamental building blocks for the construction of devices and structures that perform unique functions that serve the needs of mankind. Other areas impacted by nanofiber technology include drug delivery systems and scaffolds for tissue engineering, wires, capacitors, transistors and diodes for information technology, systems for energy transport, conversion and storage, such as batteries and fuel cells, and structural composites for aerospace structures.

Considering the potential opportunities provided by nanofibers, there is an increasing interest in nanofiber manufacturing technology. Amongst the technologies, including the template method [8], vapour grown [9], phase separation [10] and electrospinning [9, 11–27], electrospinning has attracted the most recent interest. Using the electrospinning process, Reneker and co-workers [11] demonstrated the ability to fabricate organic nanofibers with diameters as small as 3 nm. These molecular bundles, self-assembled by electrospinning, have only six or seven molecules across the diameter of the fiber! Half of the 40 or so parallel molecules in the fiber are on the surface. Collaborative research in MacDiarmid and Ko's laboratory [12, 15] demonstrated that blends of nonconductive polymers with conductive polyaniline polymers and nanofibers of pure conductive polymers can be electrospun. Additionally, *in situ* methods can be used to deposit films of 25 nm thickness of other conducting polymers, such as polypyrrole or polyaniline, on preformed insulating nanofibers. Carbon nanotubes, nanoplatelets and ceramic nanoparticles can easily be embedded in nanofibers by being dispersed in polymer solutions and consequent electrospinning of the solutions [28].

1.6 Unique properties of nanofibers

By reducing fiber diameters down to the nanoscale, an enormous increase in specific surface area to the level of 1000 m^2/g is possible. The reduction in dimension and increase in surface area greatly affect the chemical, biological reactivity and

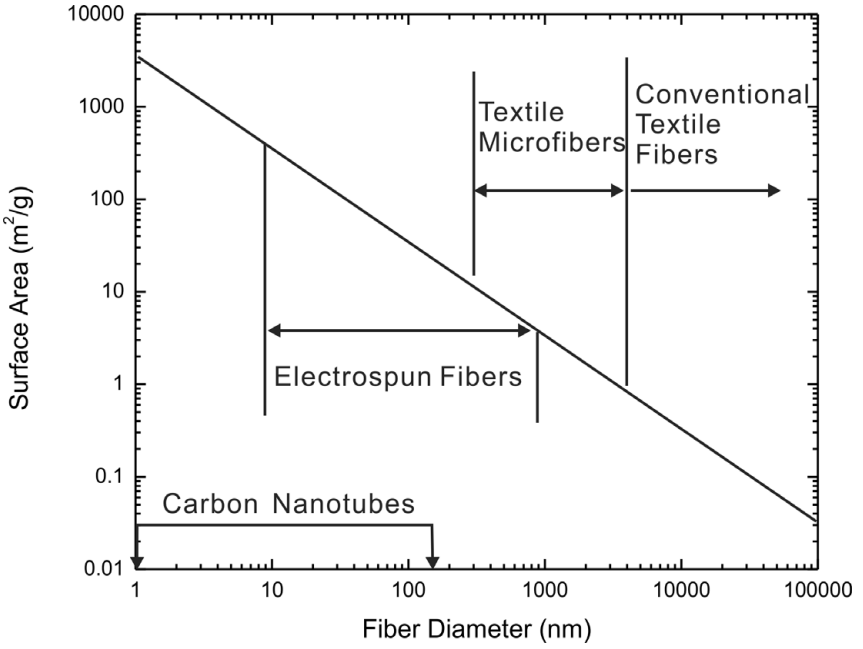

Fig. 1.4 Relation of surface area to fiber diameter [30].

electroactivity of polymeric fibers. By reducing the fiber diameter from 10 μm to 10 nm, a million times increase in flexibility is expected. Recognizing the potential nanoeffect that will be created when fibers are reduced to the nanoscale, there has been an explosive growth in research efforts around the world [29]. Specifically, the role of fiber size has been recognized in significant increase in surface area, bio-reactivity, electronic properties and mechanical properties.

1.6.1 Effect of fiber size on surface area

For fibers having diameters from 5 nm to 500 nm, the surface area per unit mass is around 10 000 to 1 000 000 square meters per kilogram, as shown in Fig. 1.4. In nanofibres that are 3 nm in diameter, and which contain about 40 molecules; about half of the molecules are on the surface. As seen in Fig. 1.4, the high surface area of nanofibers provides a remarkable capacity for the attachment or release of functional groups, absorbed molecules, ions, catalytic moieties and nanometer-scale particles of many kinds. One of most significant characteristics of nanofibers is the enormous availability of surface area per unit mass.

1.6.2 Effect of fiber size on bioactivity

Considering the importance of surfaces for cell adhesion and migration, experiments were carried out in the Ko Laboatory (the Fibrous Materials Laboratory at Drexel University) using osteoblasts isolated from neonatal rat calvarias and grown to

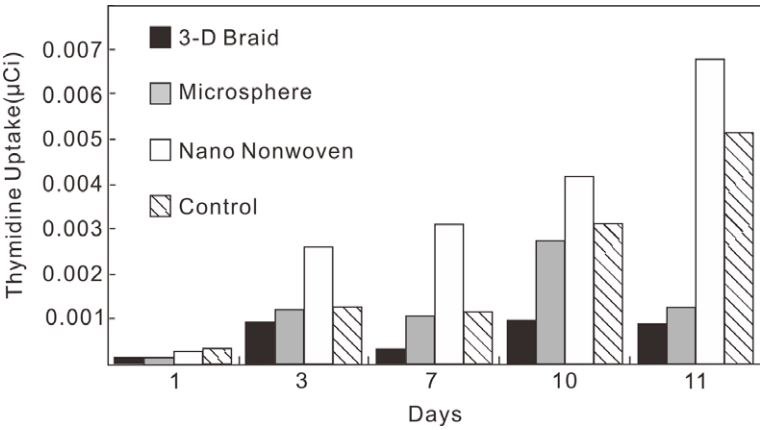

Fig. 1.5 Fibroblast cell proliferation as indicated by the thymidine uptake of cell as a function of time showing that a polylactic–glycolic acid nanofiber scaffold is most favorable for cell growth [30].

confluence in Ham's F-12 medium (GIBCO), supplemented with 12% Sigma foetal bovine on PLAGA sintered spheres, 3-D braided filament bundles and nanofibrils [14]. Four matrices were fabricated for the cell culture experiments. These matrices include (1) 150 300 μm PLAGA sintered spheres, (2) unidirectional bundles of 20 mm filaments, (3) 3-D braided structure consisting of 20 bundles of 20 μm filaments and (4) nonwoven matrices consisting of nanofibrils. The most prolific cell growth was observed for the nanofibrils scaffold as shown in the thymidine–time relationship illustrated in Fig. 1.5. This can be attributed to the greater available surface for cell adhesion as a result of the small fiber diameter which facilitates cell attachment.

1.6.3 Effect of fiber size on electroactivity

The size of the conductive fiber has an important effect on system response time to electronic stimuli and the current carrying capability of the fibre over metal contacts. In a doping–de-doping experiment, Norris *et al.* [15] found that polyaniline/PEO submicron fibrils had a response time an order of magnitude faster than that of bulk polyaniline/PEO. There are three types of contact to a nanopolymeric wire: ohmic, rectifying and tunneling. Each is modified due to nanoeffects. There exist critical diameters for wires below which metal contact produces much higher barrier heights, thus showing much better rectification properties. According to Nabet [31], by reducing the size of a wire we can expect to simultaneously achieve better rectification properties as well as better transport in a nanowire. In a preliminary study [32], as shown in Fig. 1.6, it was demonstrated, using sub-micron PEDT conductive fiber mat, that a significant increase in conductivity was observed as the fiber diameter decreases. This could be attributed to intrinsic fiber conductivity effects or to the geometric surface and packing density effect, or both, as a result of the reduction in fibre diameter.

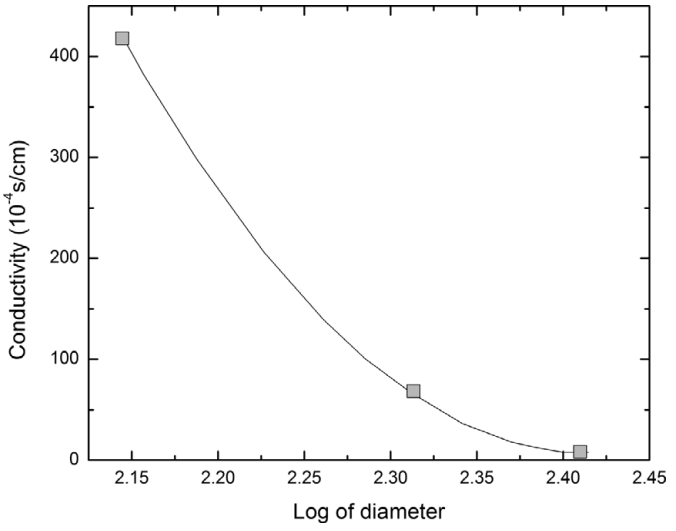

Fig. 1.6 Effect of fiber diameter on electrical conductivity of PEDT nanofibers [30].

1.6.4 Effect of fiber size on strength

Materials in fiber form are unique in that they are stronger than bulk materials. As the fiber diameter decreases, it has been well established in glass fiber science that the strength of the fiber increases exponentially due to the reduction of the probability of including flaws, as shown in Fig. 1.7a. As the diameter of matter gets even smaller, as in the case of nanotubes, the strain energy per atom increases exponentially, contributing to the enormous strength of over 30 GPa for carbon nanotube, as showm in Fig. 1.7b.

Although the effect of fiber diameter on the performance and processibility of fibrous structures has long been recognized, the practical generation of fibers down to the nanometer scale was not realized until the rediscovery and popularization of the electrospinning technology by Professor Darrell Reneker almost a decade ago [16]. The ability to create nanoscale fibers from a broad range of polymeric materials in a relatively simple manner using the electrospinning process coupled with the rapid growth of nanotechnology in the recent years have greatly accelerated the growth of nanofiber technology. Although there are several alternative methods for generating fibers in a nanometer scale, none matches the popularity of the electrospinning technology due largely to the great simplicity of the electrospinning process. In this book we will focus on the electrospinning technology. The relative importance of the various processing parameters in solution electrospinning is discussed. The structure and properties of the fibers produced by the electrospinning process are then examined with particular attention paid to the mechanical and chemical properties. There is a gradual recognition that the deceptively simple process of electrospinning requires a deeper scientific understanding and engineering development in order to capitalize on the benefits promised by the attainment of the nanoscale and to translate the technology from a laboratory curiosity to a robust manufacturing process. To illustrate the method

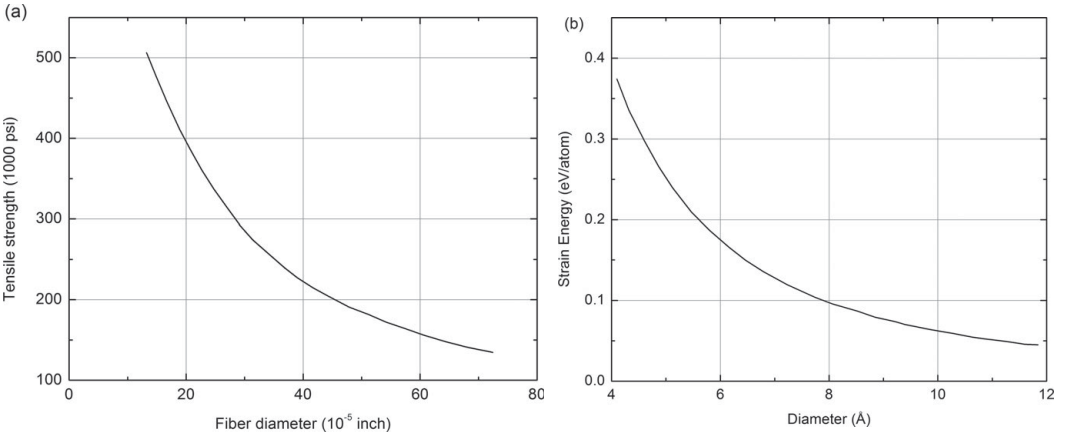

Fig. 1.7 (a) Dependence of glass fiber strength on fiber diameter [33], and (b) strain energy as a function of nanotube diameter (adapted from Ref. [34]).

for connecting properties of materials in the nanoscale to macrostructures, the approach of multi-scale modeling and a concept for the translation of carbon nanotubes to composite fibrous assemblies is presented.

Nanotechnology is anticipated to have a tremendous impact on a broad range of industries including the textile industry as is evident in the stain-resistant clothing and precision filter media. The rapid growth of nanofiber technology in recent years can be attributed to the rediscovery of the 70-year-old electrostatic spinning technology or the electrospinning technology [8]. This technique has been used to produce high-performance filters [9, 10], wearable electronics [11] and for scaffolds in tissue engineering [35] that utilize the high surface area unique to these fibers.

Accordingly, it is the objective of this book to introduce the basic elements of nanofiber technology. Through the electrospinning process, we will examine the parameters that affect the diameter of electrospun fibers. Examples of applications of electrospun fibers will be presented to illustrate the opportunities and challenges of nanofibers.

References

1. Subcommittee, N. *Nanotechnology definition* 2000 February 2000 [cited 2012 April 8]; available from: http://www.nsf.gov/crssprgm/nano/reports/omb_nifty50.jsp.
2. J. T. Bonner, *The Scale of Nature*. New York: Harper and Row, 1969.
3. M. C. Roco, National Nanotechnology Initiative-Past, Present, Future. *Handbook on Nanoscience, Engineering and Technology*, pp. 3.1–3.26, 2007.
4. S. Iijima, "Helical microtubules of graphitic carbon," *Nature*, vol. 354(6348), pp. 56–58, 1991.
5. C. M. Shea, "Future management research directions in nanotechnology: a case study," *Journal of Engineering and Technology Management*, vol. 22(3), pp. 185–200, 2005.

6. M. S. Huda, *et al.*, "Effect of fiber surface-treatments on the properties of laminated biocomposites from poly(lactic acid) (PLA) and kenaf fibers," *Composites Science and Technology*, vol. 68(2), pp. 424–432, 2008.
7. Y. Wang. *Nanomanufacturing technologies: advances and opportunities,* in *IAMOT 2009*. Orlando, Florida, USA, 2009.
8. H. Allcock, and F. Lampe, *Contemporary Polymer Chemistry*. Prentice Hall, 1981.
9. Y. Fan, *et al.*, "The influence of preparation parameters on the mass production of vapor-grown carbon nanofibers," *Carbon*, vol. 38(6), pp. 789–795, 2000.
10. T. Hongu and G. Philips, *New Fibers*. Woodhead Publ. Ltd., Cambridge, 1997.
11. D. H. Reneker, and I. Chun, "Nanometre diameter fibres of polymer, produced by electro-spinning," *Nanotechnology*, vol. 7(3), pp. 216–223, 1996.
12. A. MacDiarmid, *et al.*, "Electrostatically-generated nanofibers of electronic polymers," *Synthetic Metals*, vol. 119(1–3), pp. 27–30, 2001.
13. F. Ko, *et al.*, "Structure and properties of carbon nanotube reinforced nanocomposites," 2002. **DETAILS?**
14. F. Ko, *et al.*, *The Dynamics of Cell–Fiber Architecture Interaction*. Society for Biomaterials, 1998. **DETAILS?**
15. I. D. Norris, *et al.*, "Electrostatic fabrication of ultrafine conducting fibers: polyaniline/polyethylene oxide blends," *Synthetic Metals*, vol. 114(2), pp. 109–114, 2000.
16. J. Doshi and D. Reneker, "Electrospinning process and applications of electrospun fibers," *Journal of Electrostatics*, vol. 35(2), pp. 151–160, 1995.
17. J. Kim and D. Reneker, "Polybenzimidazole nanofiber produced by electrospinning," *Polymer Engineering and Science*, vol. 39(5), pp. 849–854, 1999.
18. A. Formhals, "Process and apparatus for preparing artificial threads," U.S. Patent, 1934.
19. G. Taylor, "Electrically driven jets," *Proceedings of the Royal Society of London. Series A, Mathematical and Physical Sciences (1934–1990)*, vol. 313(1515), pp. 453–475, 1969.
20. C. J. Buchko, *et al.*, "Processing and microstructural characterization of porous biocompatible protein polymer thin films," *Polymer*, vol. 40, pp. 7397–7407, 1999.
21. P. Baumgarten, "Electrostatic spinning of acrylic microfibers," *Journal of Colloid and Interface Science*, vol. 36(1), 1971.
22. L. Larrondo and R. St John Manley, "Electrostatic fiber spinning from polymer melts. I. Experimental observations on fiber formation and properties," *Journal of Polymer Science Polymer Physics Edition*, vol. 19(6), pp. 909–920, 1981.
23. I. Hayati, A. I. Bailey, and T. F. Tadros, "Mechanism of stable jet formation in electrohydrodynamic atomization," *Nature*, vol. 319(6048), pp. 41–43, 1986.
24. I. Hayati, A. Bailey, and T. Tadros, "Investigations into the mechanism of electrohydrodynamic spraying of liquids. II: Mechanism of stable jet formation and electrical forces acting on a liquid cone," *Journal of Colloid and Interface Science*, vol. 117(1), pp. 222–230, 1987.
25. D. Smith, "The electrohydrodynamic atomization of liquids," *IEEE Transactions on Industry Applications*, pp. 527–535, 1986.
26. "*World's best in ultra-fine bicomponent microfibers*," [cited 2009 November 21]; Available from: http://www.hillsinc.net/nanofiber.shtml.
27. J. Deitzel, *et al.*, *"Generation of polymer nanofibers through electrospinning,"* Army Research Lab Aberdeen Proving Ground Md, 1999.
28. M. Roco, R. Williams, and P. Alivisatos, *Nanotechnology research directions: IWGN Workshop report: vision for Nanotechnology R&D in the next decade*, Kluwer Academic Publishers, 2000.

29. F. K. Ko, "Nanofiber technology: bridging the gap between nano and macro world," in *Nanoengineered Nanofibrous Materials*, S. Guceri, Y. G. Gogotsi, and V. Kuznetsov, Ed. Dordrecht: Kluwer Academic Publishers, 2004 p. 544.
30. E. Gallo, A. Anwar, and B. Nabet, "Contact-induced properties of semiconducting nanowires and their local gating," *Nanoengineered Nanofibrous Materials*, pp. 313, 2004.
31. A. El-Aufy, B. Nabet, and F. Ko, Carbon nanotube reinforced (PEDT/PAN) nanocomposite for wearable electronics," *Polymer Preprints*, vol. 44(2), pp. 134–135, 2003.
32. W. H. Otto, "Relationship of tensile strength of glass fibers to diameter," *Journal of the American Ceramic Society*, vol. 38(3), pp. 122–125, 1955.
33. B. Yakobson and P. Avouris, "Mechanical properties of carbon nanotubes," in *Carbon Nanotubes*, M. Dresselhaus, G. Dresselhaus, and P. Avouris, Ed. Berlin Heidelberg: Springer, 2001, pp. 287–327.
34. G. Berry, H. Nakayasu, and T. Fox, "Viscosity of poly (vinyl acetate) and its concentrated solutions," *Journal of Polymer Science Polymer Physics Edition*, vol. 17(11), pp. 1825–1844, 1979.

2 Fundamentals of polymers

In nanotechnology, polymers play a very important role as one of most often employed materials, especially in the fields of nanofibers and nanocomposites. Hundreds of polymers, including natural and synthetic polymers, have been fabricated into nanofibers and nanocomposites in the past 20 years. Thus a fundamental understanding of polymers, especially fiber-making polymers, is essential for people in various fields such as the biological, medical, electrical and material areas that are converging with nanotechnology.

2.1 Polymeric materials

The first polymers to be exploited were natural products such as wood, leather, cotton and grass for fiber, paper, construction, glues and other related materials. Then came the modified natural polymers. Cellulose nitrate was the one that first attained commercial importance for stiff collars and cuffs as celluloid in around 1885. Notably, cellulose nitrate was later used in Thomas Edison's motion picture film. Another early natural polymer material was Chardonnet's artificial silk, made by regenerating and spinning of cellulose nitrate solution, which eventually led to the viscose process that is still in use today. The first synthetic polymer was Bakelite, manufactured from 1910 onward for applications ranging from electrical appliances to phonograph records. Bakelite is a thermoset, that is, it does not flow after the completion of its synthesis. The first generation of synthetic thermoplastics (materials that could flow above their glass transition temperatures) are polyvinyl chloride (PVC), poly(styrene–stat–butadiene), polystyrene (PS), and polyamide 66 (PA66). Other breakthrough polymers include high modulus aromatic polyamides, known as Kevlar™, and a host of high temperature polymers. Table 2.1 lists some of the polymers currently often encountered.

Because of the low price, ease of fabrication, low density, unique and tunable properties such as being insulating, chemical inert, etc., there has been huge growth in the amount and applications of polymer materials during the past 50+ years, and more and more metallic and ceramic objects are being replaced by polymeric ones.

Table 2.1 Commonly encountered polymers

Natural polymers	Proteins	Amino acids	glycine, analine, serine etc
		Fibrous proteins	elastin, collagen, keratn, fibroin etc
		Globular protein	casein, zein, insulin, egg albumin, homoglobin etc
	Carbohydrates	cellulose, starch. chitin, insulin, glycogen	
	Nuclei acids	DNA helix, bases	
	Natural rubbers		
Artificial polymers	Polyamids	Nylon, 66, Nylon 6, Nomex	
	Polyester	Dacron (polyethyleneterephalate), Kodel	
	Polyolefin	Polyethylene, polypropylene	
	Polyvinylchloride		
	Polyvinyldene chloride		
	Polyacrylonitrile	acrylic, modacrylic	
	Polyvinyl alcohol		

2.2 Polymer flow, nonlinearity and heterogeneity

The most unique property of industrial and textile fibers, most plastics and polymers is their combination of strength and toughness. Strength is characteristic of hard and brittle materials, while toughness is characteristic of fluid that tends to flow. Strength and toughness are mutually exclusive properties in most materials except for high polymers. One condition uuder which materials can unify the strength of crystalline materials (which are brittle) with the toughness of liquid-like materials (which are weak) is when the material is heterogeneous, in another words, the constituent molecules can coexist in crystalline and amorphous regions in the same materials. Only large polymer molecules could be present in more-ordered and less-ordered regions at the same time, which makes polymers unique from other types of materials. Furthermore, these large molecules would have to be anisotropic in their mechanical properties and structures; for example, contrasting molecules in nylon with SiO_2 in fused silica.

For many materials, the deformation response to a given external force may be completely elastic and therefore temporary, or completely viscous and hence permanent. Polymers are unique in their responses due to the coexisting of crystalline and amorphous regions in their long chain structures. Polymers exhibit elastic and viscous responses simultaneously under ordinary stress conditions; this is said to be viscoelastic.

2.2.1 Linear kinetics

How a material responds to a load of stress can be described as being between two limiting extremes: elastic or Hookean behavior, and viscous or Newtonian behavior. In an ideally elastic body, Hooke's law applies. Hooke's law states that the deformation or strain of a spring is linearly related to the force or stress applied by a constant specific. Mathematically the stress as a function of the strain is expressed as:

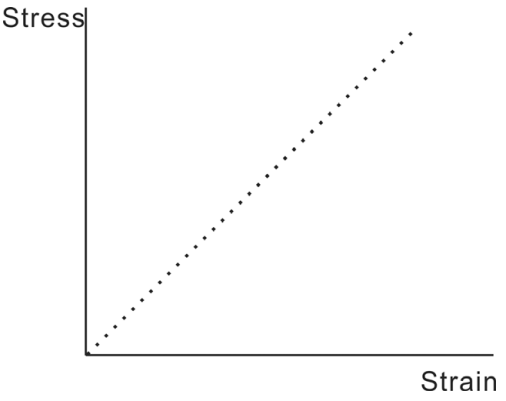

Fig. 2.1 Stress–strain curve of an elastic material.

$$\sigma = E\varepsilon \tag{2.1}$$

$$S = G\gamma, \tag{2.2}$$

where σ is tensile stress, E is elastic tensile modulus and ε the strain. Accordingly S, G and γ are respectively the stress, modulus and strain for shear response. Figure 2.1 shows the stress–strain curve of an elastic material. The elastic constants E and G are related by the following expression:

$$E = 2(1 + \mu)G, \tag{2.3}$$

where μ is the Poisson ratio. For elastic materials μ is about 0.5, i.e. the elastic tensile modulus is three times greater than the shear modulus.

The other limiting extreme is the Newtonian behavior. Most small molecules and ordinary solids are Newtonian or approach it within a fraction of one percent of ordinary shear rate. They flow and obey Newton's law. The material responds to the applied stress by slowly deforming. As the rate of the shear increases, the rate of flow of the material also increases. The Newton's law is described by the following equation:

$$S = \eta\dot{\gamma}. \tag{2.4}$$

Details can be found in Section 2.3.2.

2.2.2 Nonlinear behavior

Since they are viscoelastic, polymers behave in a nonlinear, non-Hookean way. The most elementary manifestations of a polymer's nonlinear viscoelastic behavior are stress relaxation and a phenomenon known as creep, which describes how polymers are strained under constant stress.

If a polymer is is subjected to a fixed strain, the material will exert a retractive (elastic) stress response. As time passes, the stress required to hold the initial strain decays from the initial value to zero. This deformation process is referred to "creep."

Fig. 2.2 Spring element.

This behavior can be explained on a molecular level: when strained, the polymer molecular chain network is entangled, but then seeking to return to its unperturbed state by giving rise to a retractive stress response. After continuous long exposure to the stress, the molecules begin to slide from each other to reestablish an equilibrium status, resulting in decaying stress response.

When the external stress is released, the polymer material will tend to return to its original status. The extent to which the material will recover its original dimensions depends on the magnitude of elastic stress remaining in it. The earlier the strain is relieved, the higher the stress remains and the greater the extent of strain recovery will be.

2.2.3 Viscoelastic models

2.2.3.1 The basic elements: spring and dashpot

Spring (Fig. 2.2) and dashpot (Fig. 2.3) are two basic elements frequently used mathematically to analyze the viscoelastic properties of materials. The inertia effects are often neglected during analysis.

The spring element is analogous to ideal elastic or Hookean behavior. A spring stores energy and responds instantaneously. For a spring,

$$\sigma = E\varepsilon, \tag{2.5}$$

as shown in Fig.2.4, where E can be interpreted as a linear spring constant or Young's modulus.

The dashpot is analogous to pure viscous or Newtonain behavior. Dashpots dissipate energy and characterize the retarded nature of a response. A dashpot will deform continuously at a constant rate when it is subjected to a step of constant stress, as shown in Fig. 2.5a. On the other hand, when a step of constant strain is imposed on the dashpot the stress will be of an infinite value at the instant and then rapidly diminish with time to zero, as shown in Fig. 2.5b [1]:

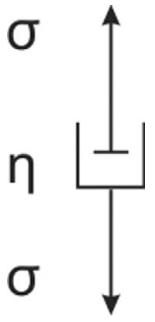

Fig. 2.3 Dashpot element.

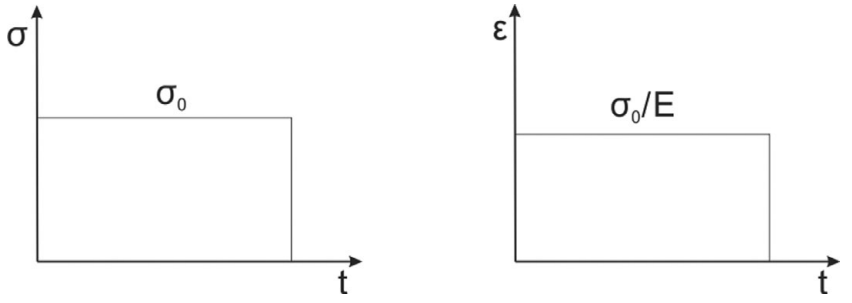

Fig. 2.4 Behavior of a linear spring.

$$\sigma = \eta \frac{d\varepsilon}{dt} = \eta \dot{\varepsilon}, \tag{2.6}$$

where η is the coefficient of viscosity and $\dot{\varepsilon}$ is the to the stress.

2.2.3.2 Maxwell model

A Maxwell model consists of a spring and a dashpot in series, as illustrated in Fig. 2.6. The Maxwell model assumes materials can undergo viscous flow and also respond elastically: both the spring and the dashpot are assumed to be subjected to the same stress but are permitted to respond with independent strains.

Since both elements are connected in series, the total strain will be

$$\varepsilon = \varepsilon_1 + \varepsilon_2 \tag{2.7}$$

or the strain rate will be

$$\dot{\varepsilon} = \dot{\varepsilon}_1 + \dot{\varepsilon}_2 \tag{2.8}$$

and the stress–strain rate relation is illustrated as

$$\dot{\varepsilon} = \frac{\dot{\sigma}}{E} + \frac{\sigma}{\eta}. \tag{2.9}$$

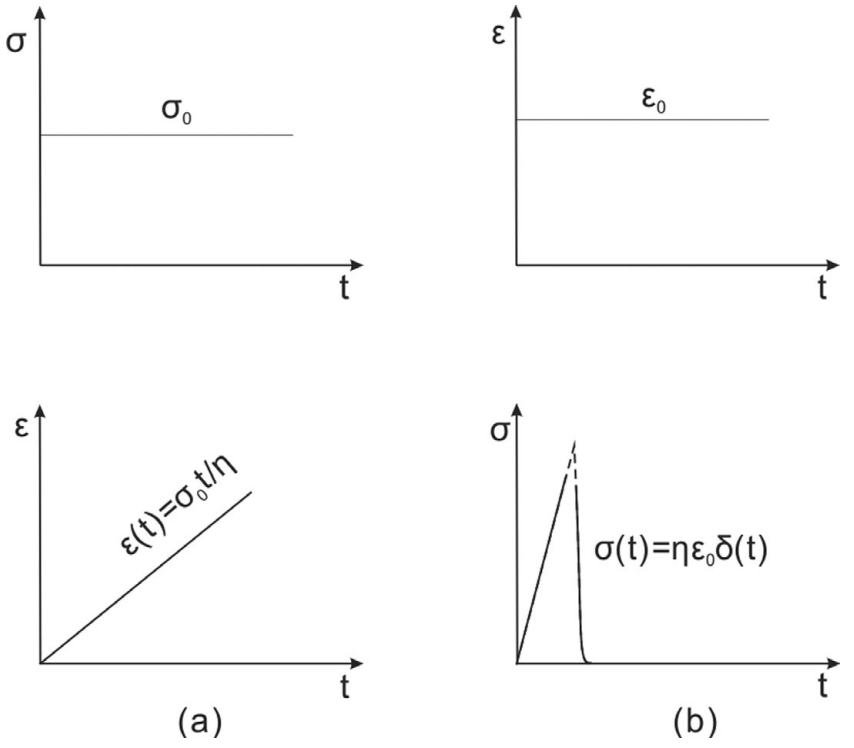

Fig. 2.5 Behavior of a linear viscous dashpot.

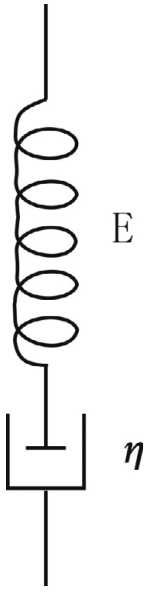

Fig. 2.6 Maxwell model.

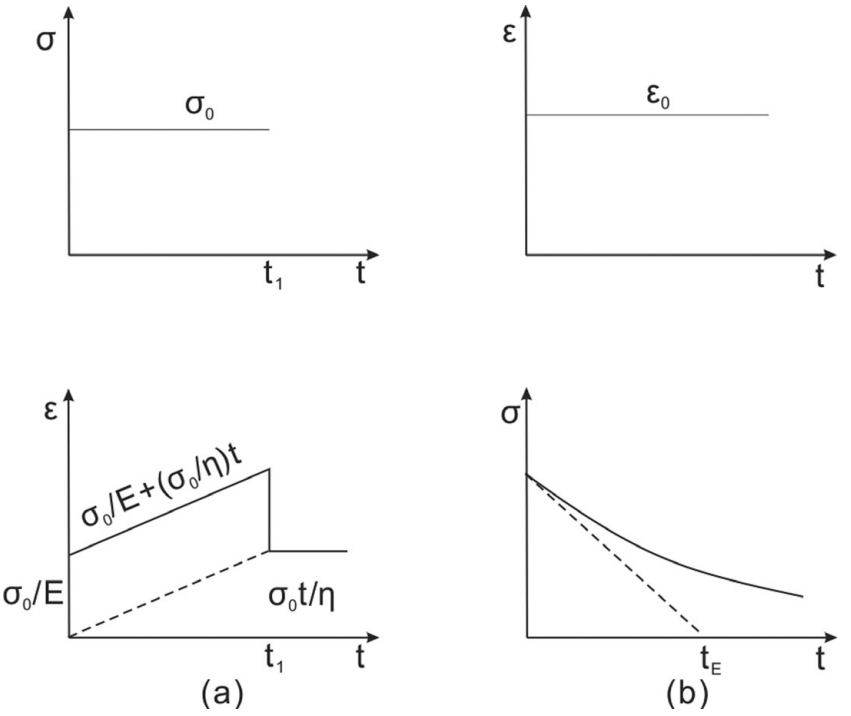

Fig. 2.7 Behavior of Maxwell model: (a) creep and recovery and (b) stress relaxation.

Given the condition that a constant stress $\sigma = \sigma_0$ is applied at $t = 0$, Eq. (2.9) becomes a first-order differential equation of ε. The following strain–time relation is obtained after applying integration together with the initial condition [1]:

$$\varepsilon(t) = \frac{\sigma_0}{E} + \frac{\sigma_0}{\eta} t. \tag{2.10}$$

This equation describes the creep and recovery behavior of the Maxwell model [1]. If the stress is removed from the model, the elastic strain returns to zero instantly, while the viscous strain is withheld. The behavior of the Maxwell model under such condition is as shown in Fig. 2.7a. In other words, the Maxwell model predicts that creep should be constant with time, which is untrue.

If fixed strain, ε_0, is applied to the model with an initial value of stress of σ_0, the stress response will be

$$\sigma(t) = \sigma_0 e^{-Et/\eta} = E\varepsilon_0 e^{-Et/\eta}. \tag{2.11}$$

The rate of stress change is

$$\dot{\sigma} = -(\sigma_0 E/\eta) e^{-Et/\eta}. \tag{2.12}$$

Then the initial rate of change in stress at $t = 0_+$ (where 0_+ refers to the time right after the application of the strain) is $\dot{\sigma} = -(\sigma_0 E/\eta)$, which means the stress will decrease continuously at this initial rate. Therefore the following relaxation equation will be obtained:

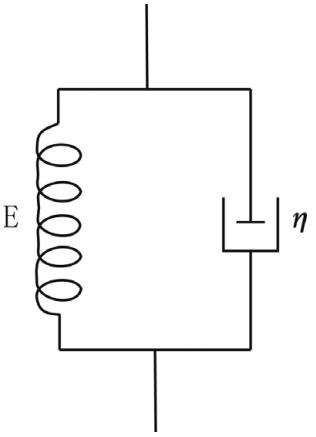

Fig. 2.8 Voigt (Kelvin) model.

$$\dot{\sigma} = -(\sigma_0 E/\eta) + \sigma_0 \tag{2.13}$$

The stress will reach zero at time $t_E = \eta/E$, which is the relaxation time of the Maxwell model, as shown in Fig. 2.7b. The relaxation time characterizes one aspect of the viscoelastic properties of the material. But the stress relaxing to zero is not always the case for real polymers.

2.2.3.3 Voigt (Kelvin) model

A Voigt (Kelvin) model consists of a spring and a dashpot in parallel, as schemed in Fig. 2.8. When a stress is applied, the stress is at first carried entirely by the viscous element which elongates and gradually transfers the load to the elastic element. Finally the elastic element carries the entire stress. This behavior is appropriately called delayed elasticity [1]. It is intuitive to see that both elements are constrained to the same strain but the stresses are additive:

$$\sigma = \sigma_1 + \sigma_2, \tag{2.14}$$

which can be expressed as

$$\dot{\varepsilon} + \frac{E}{\eta}\varepsilon = \frac{\sigma}{\eta}. \tag{2.15}$$

If a constant stress σ_0 is applied to the model at time $t = 0$, the solution to Eq. (2.15) will be

$$\varepsilon = \frac{\sigma_0}{E}(1 - e^{-Et/\eta}). \tag{2.16}$$

This equation implies that the strain increases with a decreasing rate and approaches asymptotically the value of σ_0/E when t tends to infinity, as shown in Fig. 2.9.

The strain rate in creep under a constant stress σ_0 is

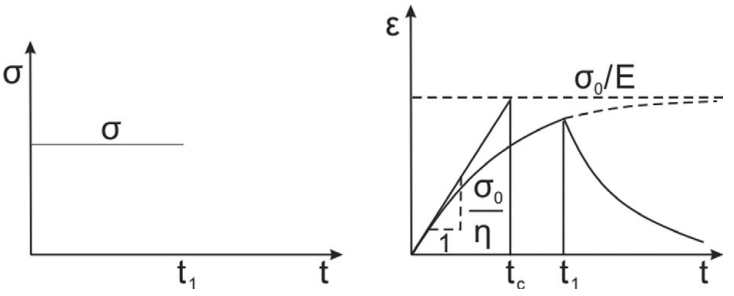

Fig. 2.9 Behavior of Voigt (Kevin) model.

$$\dot{\varepsilon} = \frac{\sigma_0}{\eta} e^{-Et/\eta}. \tag{2.17}$$

Thus, the strain rate at $t = 0_+$ is $\dot{\varepsilon}(0_+) = \sigma_0/\eta$, which approaches asymptotically to zero when t tends to infinity.

If the strain increases at an initial rate of σ_0/η, it will converge the asymptotic value σ_0/E at time $t_c = \eta/E$, known as the retardation time. It is obvious that most of the total strain σ_0/E occurs within the retardation time period since $e^{-Et/\eta}$ approachs the asymptotic value rapidly when $t < t_c$. At $t = t_c$, $\varepsilon = (\sigma_0/E)(1 - 1/e) = 0.63\sigma_0/R$, which means only 37% of the asymptotic strain remains to be accomplished after $t = t_c$ [1].

If the stress is removed at time t_1, the strain following stress removal can be determined by the superposition principle [1].

The strain ε_a resulting from stress σ_0 applied at $t = 0$ is

$$\varepsilon_a = \frac{\sigma_0}{E}(1 - e^{-Et/\eta}). \tag{2.18}$$

The strain ε_b resulting from a stress $(-\sigma_0)$ exterted by the spring at time $t = t_1$ is

$$\varepsilon_a = -\frac{\sigma_0}{E}(1 - e^{-E(t-t_1)/\eta}). \tag{2.19}$$

Then the stain for $t > t_1$ during recovery will be

$$\varepsilon = \varepsilon_a + \varepsilon_b = \frac{\sigma_0}{E} e^{-Et/\eta}(e^{Et_1)/\eta} - 1), \tag{2.20}$$

which indicates the recovery trends toward zero when t approaches to infinity, as illustrated in Fig. 2.9.

The Voigt (Kelvin) model does not show a time-dependent relaxation. Because of the presence of the viscous element, an abrupt change in strain can be accomplished only by an infinite stress. This makes the Voigt model as flawed as the Maxwell model.

2.2.3.4 Four-element model

Since neither the Maxwell nor the Voigt model can accurately describe the behaviors of most viscoelastic materials, the two models are more often used in series, known as the four-element model (schematically shown in Fig. 2.10), to describe the viscoelastic deformation of polymers.

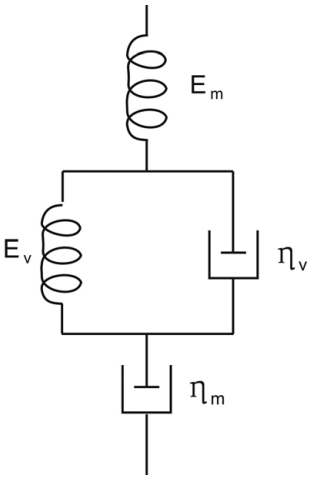

Fig. 2.10 The four-element model.

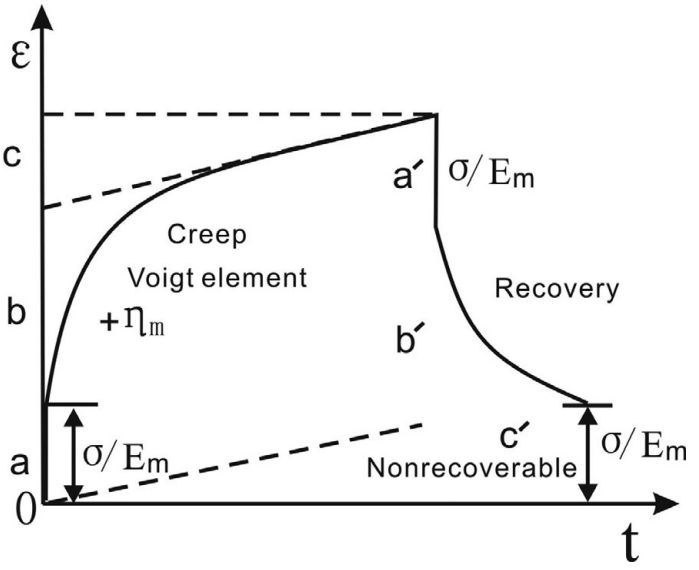

Fig. 2.11 Creep behavior as predicted by the four-element model.

The four-element model is the simplest model that exhibits all the essential features of viscolasticity, as shown in Fig. 2.11. When a stress, σ, is imposed, the model undergoes an elastic deformation, followed by creep. The deformation due to a dashpot in series (η_m) is nonrecoverable. Thus, on removal of the stress, the model undergoes a partial recovery. The strain obtained from each of the components can be simply summed:

$$\varepsilon(t) = \frac{\sigma}{E_m} + \frac{\sigma t}{\eta_m} + \frac{\sigma}{E_v}(1 - e^{-t/\tau}), \tag{2.21}$$

where $\tau = \eta_v/E_v$, which refers to the retardation time.

Table 2.2 General relationships between properties and structures of ploymer [2]

Properties	Crystallinity	Crosslinking	Molecular weight	Molecular weight distribution	Polar backbone units	Backbone stiffening groups
Abrasion resistance	+	+	+	−	+	−
Brittleness	−	M	+	+	+	+
Chemical resistance	+	V	+	−	−	+
Hardness	+	+	+	+	+	+
T_g	+	+	+	−	+	+
Solubility	−	−	−	0	−	−
Tensile strength	+	M	+	−	+	+
Toughness	−	−	+	−	+	−
Yield	+	+	+	+	+	+

+, increase as the factors increase; 0, little or no effect; −, decrease in property; M, property passes through a maximum; V, variable results dependent on particular sample and temperature.

The four-element model provides a crude qualitative representation of the phenomena generally observed with viscoelastic materials: instantaneous elastic strain, retarded elastic strain, viscous flow, instantaneous elastic recovery, retarded elastic recovery and permanent plastic deformation [1]. However, the quantities E and η of the models are not real-life values. More complex arrangements of the elements are often employed, especially when multiple relaxations are involved or accurate representations of engineering data are required.

2.3 Intrinsic structures of polymers

As seen in Section 2.2, the unique properties of polymers originate from their intrinsic structures such as bondings, chain conformations in space, chain configuration, order and disorder structures of polymer molecular chain, molecular weight and molecular weight distribution. The bonds determine how strongly the atoms and molecules are jointed. The configuration and conformation settle the arrangement of molecular chain. The order and disorder structures give the polymer the combination of strength and toughness. The molecular weight and weight distribution measure the viscoelasticity and other physical properties of the polymer. Table 2.2 illustrates how the structures of polymers may affect their properties.

2.3.1 Molecular bondings

The molecular interaction bondings include primary forces (valence bonds) and secondary forces. Atoms in individual polymer molecules are joined to each other by relatively strong covalent bonds, while polymer molecules are attracted to each other by intermolecular forces. The primary forces typically range from 50 to 200 kcal/mole; the

secondary forces range typically from 0.5 to 10 kcal/mole by contrast [3]. Secondary forces can also be found between segments of a long molecular chain.

Primary bonding forces are divided into ionic, metallic and covalent bonding, including coordinate or dative bonding. Ionic bonds form between atoms with largely differing electronegativites and are characterized by a lack of directional bonding. They not typically present for polymer backbones. Similar to ionic bonds, metallic bonds lack bonding direction and are typically absent from polymers. Metallic bonds are generated between atoms having valence electrons that are too small to provide complete outer shells. A covalent bond is a bond in which one or more pairs of electrons are shared by two atoms. Atoms will covalently bond with other atoms in order to gain more stability by sharing their outermost (valence) electrons to form a full electron shell. The bonding lengths of primary bonds are usually about 0.90–2.0 Å. The carbon–carbon bond length falls into the range of about 1.5–1.6 Å [2].

The potential of a polymer to exert strong intermolecular bonding and hence to exhibit high mechanical strength resides fundamentally in the nature of the secondary molecular bonding forces. The energies of secondary bondings are generally one magnitude lower than those of primary bonding forces; however, when associated with large molecules, secondary bonding forces are capable of providing a polymer with strong mechanical properties. The secondary bonding forces most involved in polymers are van der Waals forces and hydrogen forces.

2.3.1.1 Van der Waals forces

Van der Waals forces (or the van der Waals interaction), named after Dutch scientist Johannes Diderik van der Waals, are the sum of the attractive or repulsive forces between molecules. Van der Waals forces are the main type of secondary bonding forces. Van der Waals forces are caused by electromagnetic interactions of nearby particles [3]. A neutral atom or molecule is composed of a positively charged nucleus enclosed by an outer shell of negatively charged electrons. The electrons are mobile, and at any one instant they might find themselves towards one end of the molecule causing deviation in the electron shell density. The deviation generates an infinitesimal magnetic imbalance and turns the molecule as a whole into a small magnet or dipole, and thus electromagnetic interaction is created between this molecule and the nearby ones. In other words, van der Waals forces are the result of intermolecular polarities.

The degree of "polarity" that the temporary dipoles confer on a molecule depends on its surface area [3]: the larger the molecule, the greater the number of temporary dipoles, and thus the higher the intermolecular attractions generated. Molecules with straight chains have a larger surface area, and therefore greater dispersion forces, than branched molecules of the same molecular weight.

2.3.1.2 Hydrogen bonding

Hydrogen bonding occurs when a hydrogen atom is attached to an electronegative atom such as oxygen, nitrogen or fluorine, and involves a hydrogen atom and another electronegative atom. The sole electron of the hydrogen atom is drawn towards the electronegative atom it is attached to, leaving the strongly charged hydrogen nucleus

exposed, which imposes considerable attraction on electrons in another electronegative atom from aother molecule or chemical group and form a protonic bridge, and thus forms the hydrogen bond. A hydrogen bond is not a covalent chemical bond and ranges from 5 to 10 kcal/mole which is substantially stronger than most other types of dipole interaction [3].

2.3.2 Configuration and conformation

The geometric structure of a polymer is described in terms of configuration and conformation. Configuration defines the arrangement of the atoms along a molecular chain, which is permanent unless chemical bonds are broken and the molecule is reformed. Conformation refers to the arrangements of atoms and substituents of a polymer chain brought about by rotation about single bonds.

2.3.2.1 Configuration

The structure of a molecule joined by double bond cannot be changed by physical means (e.g. rotation). The placement of the substituent groups differentiates the polymer molecule into *cis* and *trans* configurations. When substituent groups are on the same side of the double bond, the molecule is in the *cis* configuration, otherwise the *trans* configuration.

In a polymer molecule chain, the structure of repeat units (monomers) is fixed by the chemical bonds between adjacent atoms. The shape or shapes thus created is known as the configuration. The monomers may be joined head-to-head, tail-to-tail or head-to-tail during polymerization, resulting in different chain configurations. The head-to-tail configuration is the thermodynamically and spatially preferred structure, although most addition polymers contain a small percentage of head-to-head placements.

Stereoregularity is a term describing the substituent arrangements in a polymer chain. Three distinct structures have been identified: isotactic, syndiotactic and atactic structures. *Isotactic* describes an arrangement where all substituents are on the same side of the polymer chain, *syndiotactic* depicts a composion of alternating groups and *atactic* refers to a random combination of the groups [4]. Figure 2.12 illustrates the three stereoisomers of polymer chains.

2.3.2.2 Conformation

A single conformation is just a single shape that a chain can adopt. Polymers differing only by rotations about single bonds are said to be two different conformations of that polymer. A planar zigzag conformation (as shown in Fig. 2.13a) can be formed in linear polymers such as polyehthylene, poly(vinyl alcohol) and polyamides since alignment and packing of their crystallines are not disturbed by the presence of bulky side groups. In many instances, the side groups are too bulky to be accommodated in a zigzag conformation. To relieve the steric crowding, the molecules in the main chain rotate and form either a right- or left-handed helix, as shown in Fig. 2.13b. The helical conformation is ofen found in the isotactic and syndotactic α-olefin polymers. A random conformation is a common form that most polymers adopt in amorphous

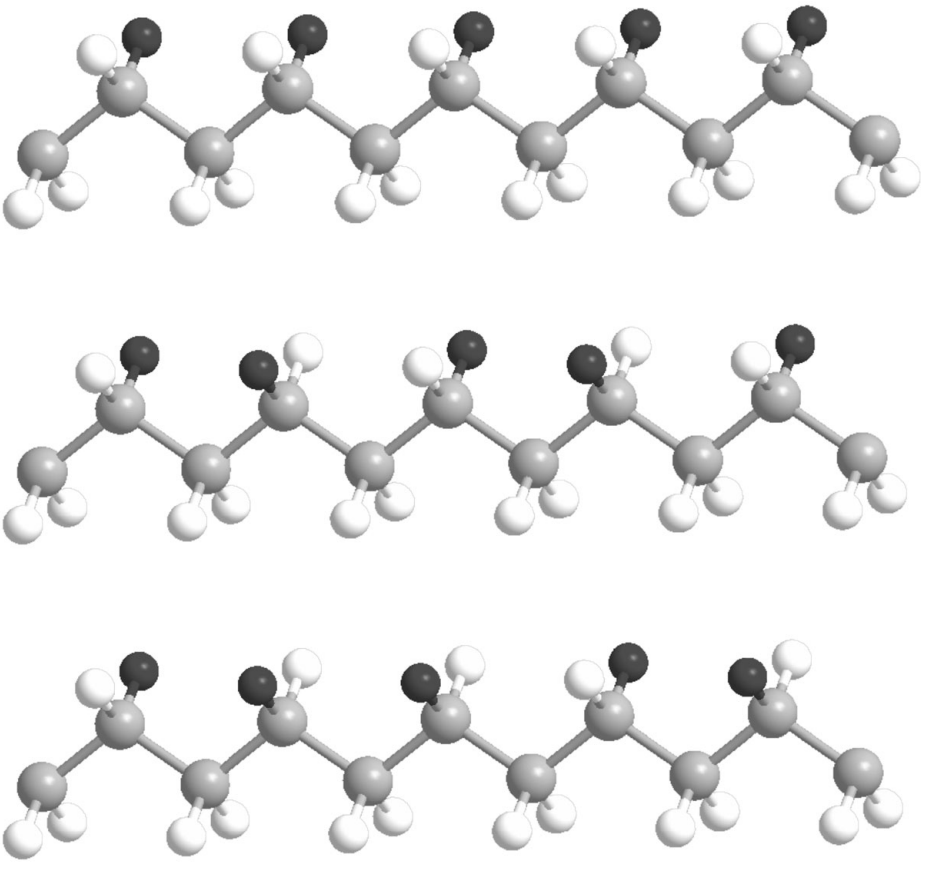

Fig. 2.12 Diagram of three stereoisomers of polymer chain.

systems like solutions, melts or some solids, where rotation about primary valence bonds is relatively free although restricted by bond length, bond angles and steric crowding of side groups.

2.3.2.3 Other chain structures

The geometric arrangement of the bonds is not the only structure that a polymer can alter [5]. A copolymer consists of at least two types of constituent units; therefore copolymers can have different chain structures by changing the arrangement of the units. As shown in Fig. 2.14, copolymers may assume three important types of chain strucutures: random, block and graft structures. An example of a copolymer is Nylon.

Polymer molecules can also form a network structure by cross-links. Cross-links are bonds that link polymer chains together. The bonds can be covalent bonds or ionic bonds. It is notable that polymers with a high enough degree of cross-linking have "memory" [5]. That is, when the polymer is stretched, the chains may straighten out; but once the stress is released they will return to their original position and therefore resume their original shape because the cross-links prevent the individual chains from sliding

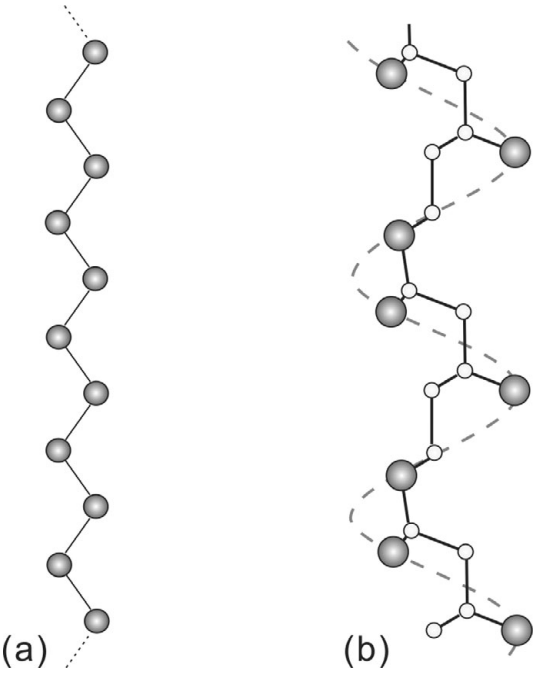

Fig. 2.13 (a) Zigzag conformation of HDPE and (b) helix conformation of isotactic vinyl polymers.

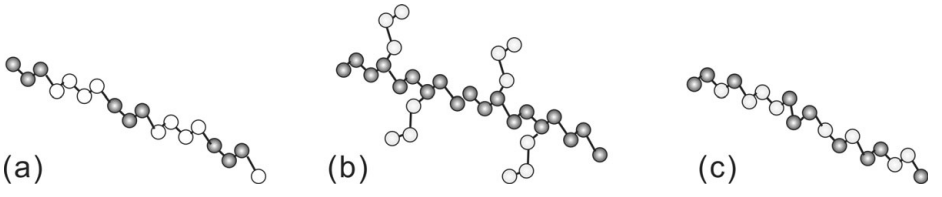

Fig. 2.14 Different structure types of copolymers: (a) block copolymer, (b) graft copolymer and (c) random copolymer [5].

past each other. One example of cross-linking is vulcanization. In vulcanization, a series of cross-links are introduced to an elastomer for improved strength. This technique is commonly used to strengthen rubber.

2.3.3. Order and disorder

2.3.3.1 Amorphous and crystal structure

Polymers in the solid state may be structurally amorphous or crystalline. During solidification, polymer molecules attract to each other and tend to cluster as closely as possible to form a solid with the least possible potential energy. If the chains are folded and packed regularly in a long-range, three-dimensional (3-D) and ordered arrangement, the polymer has a crystalline structure. Otherwise the polymer is in an amorphous state with a

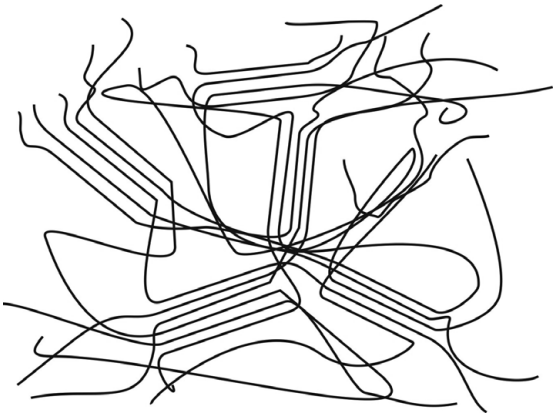

Fig. 2.15 Fringed micelle model (modified from Ref. [7]).

disordered form. Since the polymer chains are too long to always have a perfect arrangement, most polymers have both amorphous and crystalline regions in their solid states.

The arrangement perfection, i.e. the fraction of the total polymer in crystalline regions, is measured as the degree of crystallinity. The crystallinity for polymers may vary from a few percent to about 90% depending on the crystallization conditions [2]. Rapid cooling often decreases the amount of crystallinity since there is not sufficient time to allow the long chains to arrange themselves into a more-ordered structure. Polymers with irregular bulky groups are seldom crystallizable. Ordered polymers are seldom 100% crystalline because of the inability of the long chains to completely disentangle and perfectly align themselves during the time the polymer chain is mobile.

Historically, various folded surfaces, generally imagined as a fringed micelle model, as shown in Fig. 2.15, were important to explain many of the physical properties of polymers, but such fringed micelle models are found not to be consistent with much of the current experimental findings. For instance [6], this model accounts for the X-ray diffraction behavior and the mechanical properties of semicrystalline polymers but fails to explain the optical properties of polymer spherulites and their small-angle X-ray scattering patterns. The actual structures of the amorphous and crystalline regions are complex and still undergoing clarification.

2.3.3.2 Orientation

Orientation measures the alignment of the crystallites in the crystalline and amorphous regions parallel to the material's axis. If a bulk polymer crystallizes in the absence of external forces, there is no preferred orientation of crystallites or molecules in the bulk. If equal numbers of the axes of the chain segments or of the crystallites within this polymer point in every direction in space, the polymer is isotropic. If an external force, such as mechanical drawing, is imposed, the crystallites and molecules will orient in the draw direction.

Orientation dominates the mechanical and physical properties of polymers. Desirable changes in polymer properties such as tensile strength and impact strength may be

Table 2.3 Methods for measuring order and disorder structures [9]

Structural element	Method	Dimensions
Fiber	Optical microscopy	>0.2 μm
Fibrils/lamellae	Electron microscopy	>100 Å
Voids	Small-angle X-ray scattering	1000–10 Å
Crystalline regions	Wide-range X-ray scattering	10–1 Å
Non-crystalline regions	Small-angle X-ray scattering	100–10 Å
	Spectroscopy (IR, NMR, etc.)	Molecular groups
Orientation	X-ray scattering (wide- and small angle, infrared, birefringence, sonic velocity)	Lamellae, crystallites, molecular segments or groups

Table 2.4 Measurement method and their measurement range, perfection and time range

Method	Range	Perfection	Time(sec)
X-ray diffraction	0.7–2 Å 50–100 atoms	1%–2%	1 to 10^7
Electron diffraction	50 atoms	1%	1 to 10^2
Light scattering	50 Å	?	10^{-3} to 10^4
TEM	2 Å	100%	1 to 10^2
SEM	200 Å	?	10^{-3} to 10^4

improved by orientation. However, orientation may also cause undesirable properties including anisotropy properties and dimensional instabilities at elevated temperatures in thermoplastic materials [8]. For instance, synthetic textile fibers shrink on heating above their glass transition temperature due to randomization of the orientated amorphous regions.

2.3.3.3 Measurement of order and disorder

Order and disorder structures in polymers are experimentally measurable. The methods and the according measurable dimensions are listed in Table 2.3. It should be noted that all measurements of order depend not only on the signal to noise ratio, but also requires the polymers have some necessary minimum range of order, some minimum perfection of order, and some minimum time over which the order structure can persist, as shown in Table 2.4. Some of the main measurement methods are to be introduced in Chapter 6.

2.3.4 Molecular weight and molecular weight distribution

The size of a single polymer molecule may be expressed in terms of its molecular weight (MW) or its degree of polymerization (DP). The same bonding forces (*intra*- and *inter*molecular) act in both low- and high-molecular-weight polymers. However, the unique properties and disctinctive behaviors of polymers bear high relevance to their MWs, as shown in Fig. 2.16. Knowledge of the MW and MW distribution along

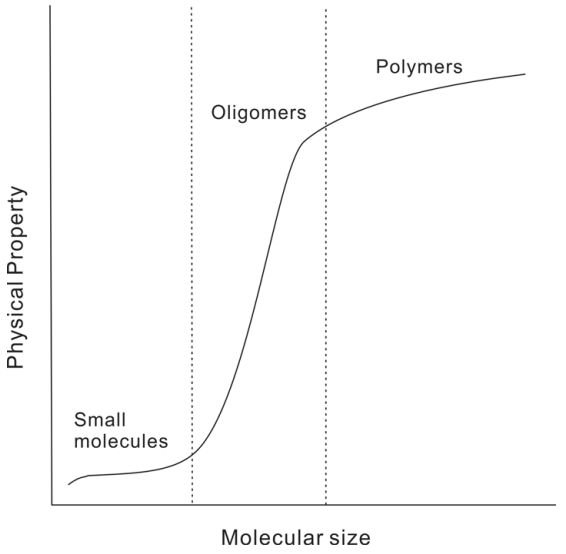

Fig. 2.16 The relationship between physical properties and molecular size.

with a good understanding of the chain conformation, will allow one to be able to predict many of the properties of a polymer. Polymers with small molecules develop hardly any strength. With increasing MW, a polymer will generate a steep rise in performance until a certain level, thereafter the properties change very little with increase of MW [6].

During synthesis, polymer molecules are subjected to a series of random events. Therefore synthetic polymers are not composed of identical molecules, but of a mixture of molecules with molecular weights in a certain range. Molecular weight distribution (MWD) is often used to characterize this property of polymers. Average molecular weight is computed to approximately measure the molecule size of a polymer.

Owing to the heterogeneity of polymer MW, average molecular weight is measured in different ways depending on the way in which the heterogeneity is averaged. The most commonly used ways are weight-average molecular weight, M_w, and number-average molecular weight, M_n. Others are the z-average molecular weight, M_z, and viscosity-average molecular weight, M_v. Below are the formulas showing the relevances between these average molecular weights:

$$\overline{M_n} = \frac{\sum N_i M_i}{\sum N_i} = \frac{1}{\sum (w_i / M_i)} \tag{2.22}$$

$$\overline{M_w} = \frac{\sum W_i M_i}{\sum W_i} = \frac{\sum N_i M_i^2}{\sum N_i} = \sum w_i M_i \tag{2.23}$$

$$\overline{M_z} = \frac{\sum N_i M_i^3}{\sum N_i M_i^2} = \frac{\sum W_i M_i^2}{\sum W_i M_i} \tag{2.24}$$

$$\overline{M_v} = \frac{\sum N_i M_i^{1+a}}{\sum N_i M_i} = \frac{\sum W_i M_i^2}{\sum W_i M_i}, \tag{2.25}$$

where a is a constant between 0.6 and 0.8, M_i is the molecular weight of the ith species, N_i is the number of moles of molecules with molecular weight M_i, W_i denotes the weight of material with molecular weight M_i, and w_i is the weight fraction of molecules of the ith species, which is computed from the following formula

$$W_i = \frac{N_i M_i}{W_t} = \frac{W_i}{W_t}, \tag{2.26}$$

where W_t is the total weight of polymer.

The molecular weight of polymers can be determined by a number of physical and chemical methods including end-group analysis, measurement of colligative properties, light scattering, ultracentrifugation, dilute solution viscosity and gel permeation chromatography (GPC). The number-average weight, M_n, can be obtained from end-group analysis, colligative property measurements and gel permeation chromotography. The weight-average molecular weight, M_w, can be measured from light scattering, ultracentrifugation and gel permeation chromatography. The z-average molecular weight, M_z, comes from GPC, while viscosity-average molecular weight, M_v, comes from the measurement of polymer solution viscosity.

The following relationship holds for a polymer: $\overline{M}_n < \overline{M}_v < \overline{M}_w < \overline{M}_z$. For a random molecular weight distribution, such as produced by many free radical or condensation syntheses, $\overline{M}_n : \overline{M}_w : \overline{M}_z = 1 : 2 : 3$. The ratio $\overline{M}_w/\overline{M}_n$, called the polydispersity index (PDI), are often used to indicate the breadth of the distribution. For many linear systems, $\overline{M}_w/\overline{M}_n$ is about 2. But in highly nonlinear systems, $\overline{M}_w/\overline{M}_n$ may range as high as 20–50. Figure 2.17 illustrates the relationship between $\overline{M}_w$ and $\overline{M}_n$.

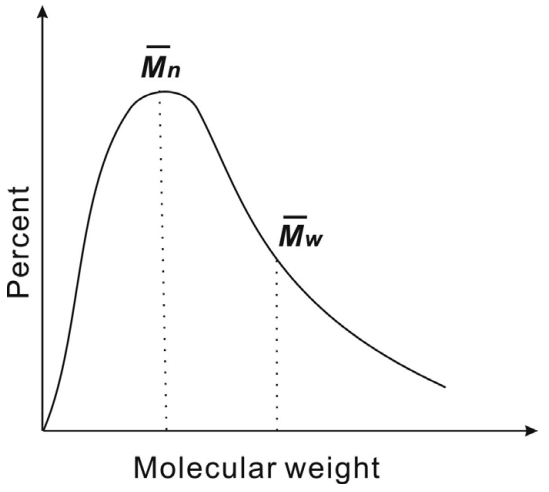

Fig. 2.17 Number-average molecular weight M_n, and weight-average molecular weight, M_w.

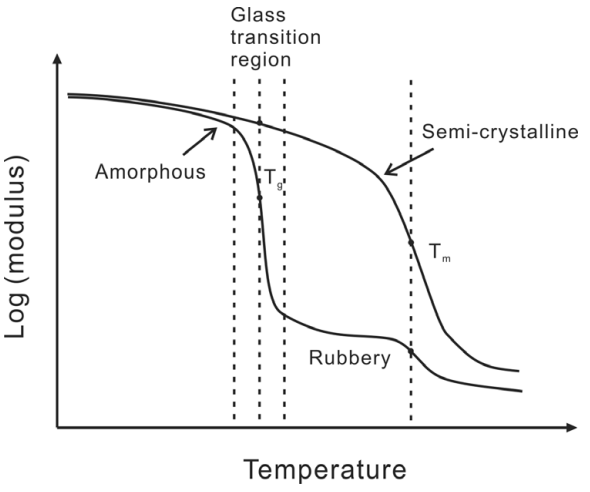

Fig. 2.18 Semi-log plot of polymer modulus (stiffness) versus temperature.

2.4 Thermal behavior

It is well known that matters composed of low-molecular-weight compounds have three states: crystalline, liquid and gaseous. The three states transit upon certain changes of temperature or pressure. By contrast, high-molecular-weight polymers have no gaseous state. At high temperatures, they decompose rather than boil since their "boiling points" are generally higher than their decomposition temperature. Their transition between the solid and liquid forms is rather diffuse and occurs over a temperature range that depends on their polydispersity. Furthermore, they are very viscous on melting and cannot freely flow as in the case of low-molecular-weight materials [6].

Two important temperatures have been identified for polymers. The solid-to-liquid transition temperature range is called the "glass transition temperature," T_g. Glass transition occurs only in an amorphous region. The temperature at which crystalline regions start to melt is referred to as the "melting point," T_m. Note that T_m usually corresponds to the temperature at which the last trace of crystallinity disappears as polymers melt over a range of several degrees. Amorphous polymers undergo glass transition but have no melting point. At low temperatures, amorphous polymers are glassy, hard and brittle. Above T_g, amorphous polymers soften and become rubbery because of the onset of molecular motion. Semi-crystal polymers are elastic and flexible at a temperature above T_g and below T_m. The amorphous regions contribute elasticity and the crystalline regions contribute strength and rigidity. As the temperature increased to T_m, all crystalline structures disappear; the chains are set free and become randomly dispersed. Bulk crystallized polymers only melt. Figure 2.18 shows typical changes in modulus for amorphous and semi-crystalline plastics as the temperature changes. Based on their thermal behavior, polymers are usually classified as thermoplastics or thermosets. Thermoplastics soften and flow under heat and pressure, and harden upon cooling.

Thermosets are incapable of undergoing repeated cycles of softening and hardening. Once the shape of thermosets is set by cross-link, it can't be reformed by remelt.

Thermobehavior of polymers can be characterized by differential scanning calorimetry (DSC) or thermogravimetric analysis (TGA), which will be introduced in detail in Chapter 6.

2.5 Polymer solutions

Dissolution of polymers mainly depends on the nature of the solute and solvent, while the viscosity of the medium, the polymer stucture and polymer molecular weight also have an effect to some extent. Dissolution of polymers is necessarily a slow, two-staged process. First, the solvent molecules diffuse into the polymer producing a swollen gel and, second, the gel slowly breaks down and forms a true solution. For polymers of high molecular weight, this process may take several hours or longer depending on sample size, temperature, and so on. Materials with strong polymer–polymer intermolecular forces due to cross-linking (phenolics), crystallinity (Teflon), or strong hydrogen bonding (native cellulose) will exhibit only a limited degree of swelling in any solvent at ordinary temperatures and will not be truly dissolved without degradation.

2.5.1 Solubility parameter

"Like dissolves like" is one of the simplest and important notions in chemistry. Generally, "like" is appreciated in terms of similar chemical groups or similar polarities [10]. From thermodynamic considerations, the solubility of one component in another is governed by the equation of the free energy of mixing:

$$\Delta G_m = \Delta H_m - T\Delta S_m, \tag{2.27}$$

where ΔG_m, ΔH_m, and ΔS_m are respectively the change in Gibb's free energy, the enthalpy of mixing and the entropy of mixing. T is the absolute temperature.

Dissolution will occur if the free energy of mixing ΔG_m is negative. $T\Delta S_m$ is always positive because there is an increase in the entropy on mixing. Therefore, the sign of ΔG_m is determined by the sign and magnitude of ΔH_m. In an ideal solution, the heat of mixing ΔH_m is zero since the two types of molecules have the same force fields, i.e. $\Delta G_m = -T\Delta S_m$. However, in reality, the intermolecular forces working between similar and dissimilar molecules give rise to a finite heat of mixing. Therefore, positive heats of mixing are the more usual case for relatively nonpolar organic compounds [10]. Hildebrand and Scott proposed the enthalpy of mixing ΔH_m for regular solutions as:

$$\Delta H_m = V_m \phi_1 \phi_2 \left[\left(\frac{\Delta E_1}{V_1} \right)^{1/2} - \left(\frac{\Delta E_2}{V_2} \right)^{1/2} \right]^2, \tag{2.28}$$

where V, V_1, V_2, are the volumes of the solution and components, and the subscripts 1 and 2 denote the solvent and polymer, respectively. ΔE is the molar energy of

Table 2.5 Typical values of δ for various types of solvents [4, 10]

Solvent	δ	Solvent	δ	Solvent	δ
Poorly hydrogen bonded		Moderately hydrogen bonded		Strongly hydrogen bonded	
Difluorodichloromethane	5.1	Diethyl ether	*7.4*	*Dibutyl amine*	8.1
n-Decane	*6.6*	*Diisobutyl ketone*	*7.8*	*2-Ethylhexanol*	*9.5*
n-Pentane	7	*n*-Butyl acetate	8.5	Methyl isobutyl carbinol	10
n-Heptane	7.4	Methyl propionate	8.9	2-Ethylbutanol	10.5
Apco thinner	7.8	Dibutyl phthalate	9.3	*n*-Pentanol	10.9
Solvesso 150	8.5	Dioxane	9.9	*n*-Butanol	11.4
Carbon tetrachloride	*8.6*	*Acetone*	*9.9*	*n-Propanol*	*11.9*
Xylene	*8.8*	*Dimethyl phthalate*	*10.7*	*Ethanol*	*12.7*
Toluene	8.9	2,3-Butylene carbonate	12.1	Methanol	14.5
Benzene	*9.2*	*Propylene carbonate*	*13.3*	*Water*	*23.4*
Tetrahydronaphthalene	9.5	Ethylene carbonate	14.7		
O-Dichlorobenzene	10				
1-Bromonaphthalene	10.6				
Nitroethane	11.1				
Acetonitrile	11.8				
Nitromethane	12.7				

vaporization to a gas at zero pressure, and ϕ_1 and ϕ_2 are volume fractions. The quantity $\Delta E/V$ represents the energy of vaporization per cubic centimeter, referred as the cohesive energy density. According to Eq. (2.28), it is easy to note that "like dissolves like" means $\Delta E_1/V_1$ and $\Delta E_2/V_2$ have nearly the same numerical value.

The sequare root of the cohesive energy density is widely known as the solubility parameter,

$$\delta = (\Delta E/V)^{1/2}. \tag{2.29}$$

Thus, the heat of mixing of two substances depends on the value of $(\delta_1 - \delta_2)^2$. Generally, if $\delta_1 - \delta_2$ is less than 1.7–2.0, the polymer will be expected to be soluble in the solvent. Table 2.5 and Table 2.6 list the typical values of δ for various types of solvents and some polymers respectively. The magnitude of the enthalpy of mixing can be conveniently estimated from these tables.

The solubility parameter of a polymer can be determined by measuring the intrinsic viscosity of the polymer in solvents, if the polymer is soluble in them. During the measurement, several solvents of varying solubility parameter are selected and the intrinsic viscosities of the solutions are plotted against the solubility parameter of the solvents. Since the chain conformation is most expanded in the best solvent, the intrinsic viscosity will be the highest for the best match in solubility parameter.

Values of the solubility parameter may also be calculated by using group molar attraction constants, G, for each group,

$$\delta = \frac{\rho \sum G}{M}, \tag{2.30}$$

Table 2.6 Values of δ for various polymers [4, 10]

Polymers	Δ	
Polyethylene	7.7	8.35
Polypropene	8.3	9.2
Polyisobutene	7.8	8.1
Polyvinylchloride	9.4	10.8
Polyvinylidene chloride	9.9	
Polyvinyl bromide	9.5	
Polyvinylfluoroethylene	6.2	
Polychlorotrifluoroethylene	7.2	7.9
Polyvinyl alcohol	12.6	14.2
Polyvinyl acetate	9.35	11.05
Polyvinyl propionate	8.8	
Polystyrene	8.5	9.3
Polymethyl acrylate	9.7	10.4
Polyethyl acrylate	9.2	9.4
Polypropyl acrylate	9.05	
Polybutyl acrylate	8.8	9.1
Polyisobutyl acrylate	8.7	11.0
Poly-2,2,3,3,4,4,4, heptafluorobutyl acrylate	6.7	
Polymethyl methacrylate	9.1	19.8
Polyethyl methacrylate	8.9	9.15
Polybutyl methacrylate	8.7	9.0
Polyisobutyl methacrylate	8.2	10.5
Poly-*tert*, butyl methacrylate	8.3	
Polyethoxyethyl methacrylate	9.0	9.9
Polybenzyl methacrylate	9.8	10.0
Polyacrylonitrile	12.5	15.4
Polymethacrylonitrile	10.7	
Poly-*a*-cyanomethyl	14.0	14.5
Polybutadiene	0.1	8.6
Polyisoprene	7.9	10.0
Polychloroprene	8.2	9.25
Polyepichlorohydrin	9.4	
Polyethylene terephthalate	9.7	10.7
Polyhexamethylene adipamide	13.6	
Poly(δ-aminocaprylic acid)	12.7	
Polyformaldehyde	10.2	11.0
Polytetramethylene oxide	8.3	8.55
Polyethylene sulfide	9.0	9.4
Polypropylene oxide	7.5	9.9
Polystyrene sulfide	9.3	
Polydimethyl siloxane	7.3	7.6

where ρ represents the density and M is the molecular weight or mer molecular weight for a polymer.

For the value of a solvent mixture, the solubility parameter can be determined by averaging the solubility parameters of the individual solvents by volume.

2.5.2 Solution viscosity

The viscosity of a polymer solution strongly relates to the polymer's physical and engineering properties, such as monomer molecular weight, molecular weight distribution and engineering processibility, etc. A good understanding of the viscosity of a polymer is therefore vital for polymer processing.

2.5.2.1 Intrinsic viscosity

The viscosity of a polymer solution, η, relative to the viscosity of a pure solvent, η_0, is referred to as the relative viscosity, given by

$$\eta_r = \frac{\eta}{\eta_0}. \tag{2.31}$$

The viscosity of the polymer solution is always greater than that of the pure solvent. Therefore the fractional increase in the viscosity resulting from the dissolution of the polymer can be referred as the specific viscosity, η_{sp},

$$\eta_{sp} = \eta_r - 1. \tag{2.32}$$

The polymer coils and the solvent they enclose are assumed as behaving like an Einsteinian sphere uder the action of a shear stress. Polymer chains in dilute solutions are isolated and interact only with each other during brief times of encounter. It is easy to speculate that there is no interaction of polymer coils in an infinite diluted solution. Mathematically this can be achieved by defining intrinsic viscosity, $[\eta]$:

$$[\eta] = \left[\frac{\eta_{sp}}{c}\right]_{c=0}. \tag{2.33}$$

For dilute solutions of which the specific viscosity is just over unity, the logarithm of the relative viscosity can be written as:

$$\ln \eta_r = \ln(\eta_{sp} + 1) \cong \eta_{sp} - \eta_{sp}^2/2 + \cdots. \tag{2.34}$$

Then the intrinsic viscosity is approximately:

$$[\eta] = \left[\frac{\ln \eta_r}{c}\right]_{c=0}. \tag{2.35}$$

2.5.2.2 Intrinsic viscosity and molecular weight

Within a homologous series of linear polymers, the higher the molecular weight the greater the increase in viscosity for a given polymer concentration. This capacity to enhance viscosity or intrinsic viscosity is a reflection of the polymer molecular weight. In the late 1930s and 1940s, Mark, Houwink and Sakurada Mark achieved an empirical relationship between the molecular weight and the intrinsic viscosity:

$$[\eta] = KM^{\alpha}, \tag{2.36}$$

where K and α are constants for a particular polymer–solvent pair at a particular temperature.

This equation has become one of the most important relationships in polymer science and has been widely used. It is possible to calculate the molecular weight from intrinsic viscosity measurements as long as K and α have been established for a particular temperature.

Strictly speaking, this equation covers only a narrow molecular weight range. However, it is relatively easier in practice to use intrinsic viscosity to determine the molecular weights. In order to use it for molecularly heterogeneous polymers, the equation was modified as

$$[\eta] = K\overline{M}_v^{\alpha}, \tag{2.37}$$

where $\overline{M}_v$, is the viscosity average molecular weight.

The quantity K is often give in terms of the universal constant ϕ,

$$K = \phi\left(\frac{\overline{r}_0{}^2}{M}\right)^{3/2}, \tag{2.38}$$

where $\overline{r_0}^2$ represents the mean square end-to-end distance of the unperturbed coil. In terms of the number-average molecular weight, ϕ equals 2.5×10^{21} dl/mol $\cdot$ cm^3.

For theoretical purpose, the Mark–Houwink equation is usually expressed in the form:

$$[\eta] = \phi\left(\frac{\overline{r}_0{}^2}{M}\right)^{3/2} M^{1/2}\alpha^3 = KM^{1/2}\alpha^3. \tag{2.39}$$

By choosing a theta-solvent or θ temperature, the influence of the molecular expansion due to intramolecular interactions can be eliminated. Under these conditions, α equals 1, and the intrinsic viscosity depends only on the molecular weight. Thus Eq. (2.39) is reduced to

$$[\eta] = KM^{1/2}. \tag{2.40}$$

2.5.2.3 Measurement of intrinsic viscosity

Based on the Hagen–Poiseuille law, the viscosity of a liquid or solution can be measured by using a viscometer. Essentially, this involves the measurement of the flow rate of the liquid through a capillary tube which is part of the viscometer. In most experiments, dilute solutions of about 1% polymer are prepared. By measuring the flow time of the solution, t, and that of the pure solvent, t_0, the relative viscosity is determined by

$$\eta_r = \frac{\eta}{\eta_0} = \frac{t}{t_0}. \tag{2.41}$$

The quantity η_r should be about 1.6 for the highest concentration used.

Several concentrations are run and ploted according to Fig. 2.19. The most frequently used instrument is the Ubbelhode viscometer, which equalizes the pressure above and below the capillary.

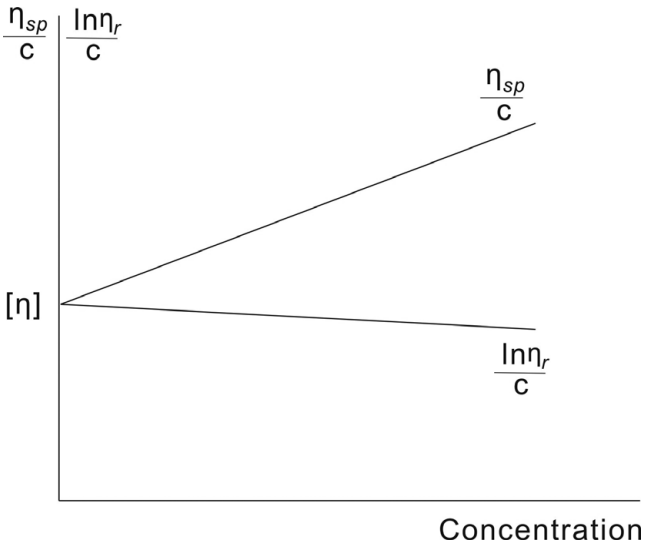

Fig. 2.19 The relationship between concentration and viscosity.

Two practical points must be noted: (1) both lines must extrapolate to the same intercept at zero concentration and (2) the sum of the slopes of the two curves is related through the Huggins equation

$$\frac{\eta_{sp}}{c} = [\eta] + k'[\eta]^2 c \tag{2.42}$$

and the Kraemer equation

$$\frac{\ln \eta_r}{c} = [\eta] + k''[\eta]^2 c. \tag{2.43}$$

Algebraically

$$k' + k'' = 0. \tag{2.44}$$

If either of these requirements is not met, molecular aggregation, ionic effects, or other problems may be indicated. For many polymer–solvent systems, k' is about 0.35 and $k''$is about 0.15, although significant variation is possible.

2.6 Fiber, plastic and elastomer

Fibers are a class of materials that are continuous filaments or are in discrete elongated pieces. In order to form fibers, the polymer must have a relative molecular weight exceeding 12 000 and possess the ability to crystallize. Closely packed, linear and symmetric polymers without side groups are favored for fiber formation. Consequently, fibers are characterized by high modulus, high tensile strength and moderate extensibilities (usually less than 20%) resulting from the strong sencondary molecular attractive forces. Elastomers generally refer to polymers with irregular molecular structure,

weak intermolecular attractive forces and very flexible polymer chains. Therefore elastomers usually have a low initial modulus in tension, but exhibit very high extensibility (up to 1000%). Plastics fall between the two structural extremes represented by fibers and elastomers. However, the boundary between fibers and plastics may sometimes be blurred. Polymers such as polypropylene and polyamides can be used as fibers as well as plastics by adopting proper processing conditions.

2.7 Fiber formation

The process by which fibers are formed from bulk polymer material is termed spinning. The three fundamental techniques for fiber manufacturing are melt spinning, wet spinning and dry spinning.

2.7.1 Melt spinning

Melt spinning is a technique commonly used for polymers that can melt without heavy degradation. This technique is used to fabricate materials that require extremely high cooling rates in order to form a fiber. The cooling rates achievable by melt spinning are on the order of 104–107 °C/s. Nylon, polyester, olefin and saran are the common polymers that produced via this process. Melt spinning is a straightforward process with high spinning speeds and is the least expensive fundamental production technique. Fibers produced from melt spinning do not need solvents and washing, and take the shape of the spinneret hole. Figure 2.20 illustrates the scheme of melt spinning.

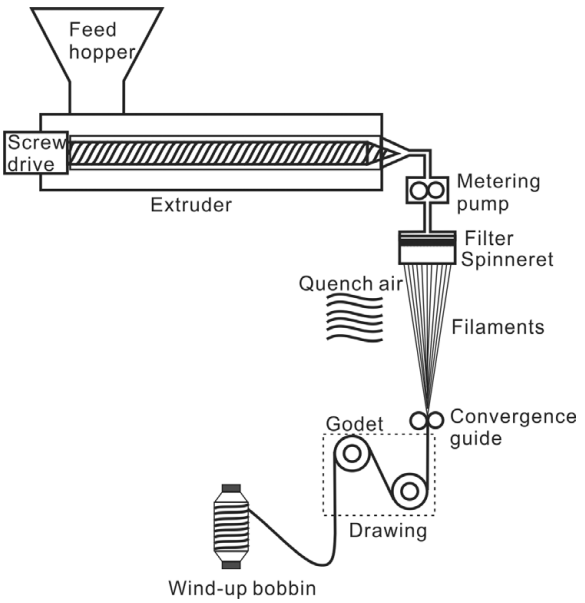

Fig. 2.20 Schematic of melt spinning.

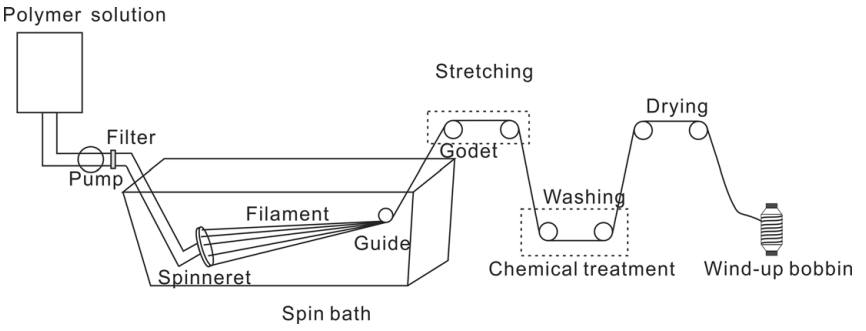

Fig. 2.21 Schematic of wet spinning.

2.7.2 Wet spinning

Wet spinning, as shown in Fig. 2.21, is a fiber-forming technique whereby the polymer solution is spun into a bath where the fiber coagulates and solidifies. It is the oldest and the most complex process for producing fibers. The fibers formed by wet spinning are weak until they are dry. The fibers obtained from wet spinning process require washing and bleaching. Rayon and acrylic are spun via wet spinning.

2.7.3 Dry spinning

Dry spinning is a direct process that spins fibers from a solution into warm air or inert gas, as shown in Fig. 2.22. The fibers solidify as the solvent evaporates. Synthetic polymers such as acetate, orlon acrylic and vinyon can be spun into fibers by using this technique.

2.7.4 Fiber properties

The properties of a fiber rest not only on the polymer it made of, but also on the manufacturing process. The processing determines the range within which a property of the fiber may fall. The physical changes taking place in processing may proceed in various ways. Figure 2.23 illustrates how the polymer structure and processing parameters affect fiber properties.

2.7.4.1 Polymer structure and fiber mechanical properties

As one of the most important properties, fiber modulus has been intensively studied. Sakurada and Kaji indicated that the modulus of a polymer depends primarily on the chain conformation. A method for calculating the modulus by building a relationship between stress and the deformation of crystalline lattice detected by X-ray diffraction has also been established [11]. Table 2.7 collects the values of calculated and experimental moduli of elasticity for polymer crystals of fiber-forming polymers.

Early in 1932, Mark presented the relationship between fiber tensile strength and molecular mass as

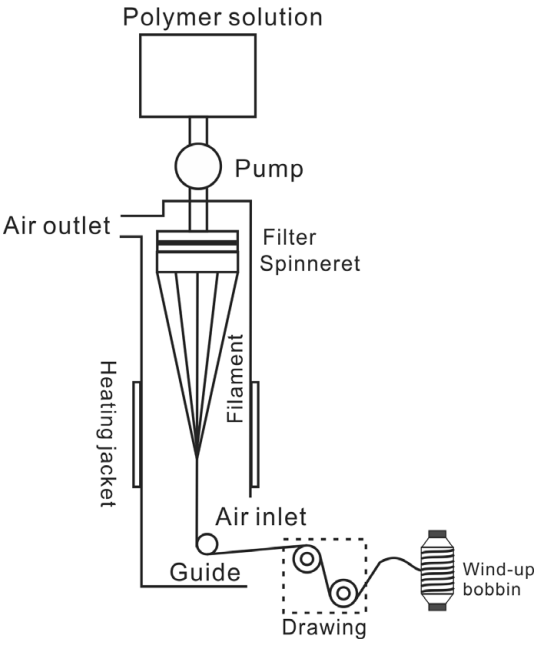

Fig. 2.22 Schematic of dry spinning.

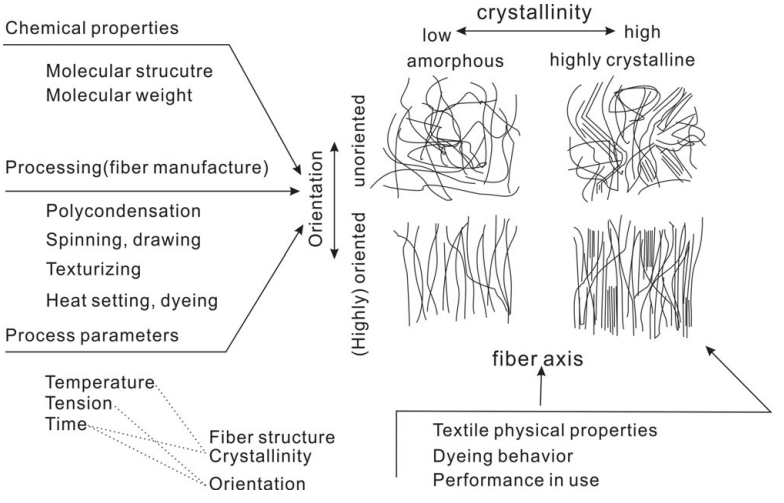

Fig. 2.23 Relationship between fiber properties and polymer structures, and processing [9].

$$\sigma = \sigma_{\infty} - \frac{B}{M_n}, \tag{2.45}$$

where σ is fiber tenacity originally expressed in the weight titer (denier), σ_{∞} is a constant equal to the fiber tenacity at infinite molecular mass, B is a constant depending on the polymer and M_n is number average molecular mass.

Table 2.7 Modulus of elasticity of polymer crystals [11]

Polymer	Modulus of elasticity (GPa)		
	Chain deformation motion	Impulse propagation	X-ray diffraction
Nylon 66	157	210	137
Polyethylene terephthalate (PET)	182	—	74.5
	146	216	137
Polyethylene (PE)	340	194	235
Syn-polyvinyl chloride (PVC)	160–200	124.5	—
Polyvinyl alcohol (PVA)	—	168	245
Polyvinylidene chloride (PVDF)	98	93.5	40.7
Cellulose	180	138	—
	77.5–121	—	—
	57	—	—
Cellulose triacetate	58.9–88.3	82.4	—
Polyacrynitrile (PAN)	147	132.5	—

Regarding brittle materials, the tensile strength is assumed to result from the simultaneous fracture of all the load-bearing bonds in the cross-section where the fracture takes place

$$\sigma = nf, \tag{2.46}$$

where σ is strength, n is number of loading-bearing bonds per unit of cross-section area and f is the strength of an individual bond.

Bueche proposed a formula correlating the maximum strength to polymer density and molecular entanglement:

$$\sigma_\infty = nf = \left(\frac{\rho N}{3M_e}\right)^{2/3} \quad f \text{ at } M = \infty, \tag{2.47}$$

where ρ is the density of polymer, N is Avogadro's number, and M_e is the molecular mass critical in respect to the entanglements.

Turner further applied Flory's end correction factor to Bueche's equation:

$$\sigma_\infty = nf = \left(\frac{\rho N}{3M_e}\right)^{2/3} f\left(1 - \frac{2M_e}{M}\right). \tag{2.48}$$

The modulus of a polymer has also been theoretically calculated from molecule conformation. The example can be found in Chapter 5.

Chain imperfections including chain branching may cause either a decrease of crystallizability, or a change of crystallization rate, which ultimately lower the moduli of polymers and fibers. Cross-linking normally causes difficulties in fiber formation, and subsequently impairs the structure perfection and the mechanical properties of the fiber. However cross-links generated after fiber formation usually play a positive role.

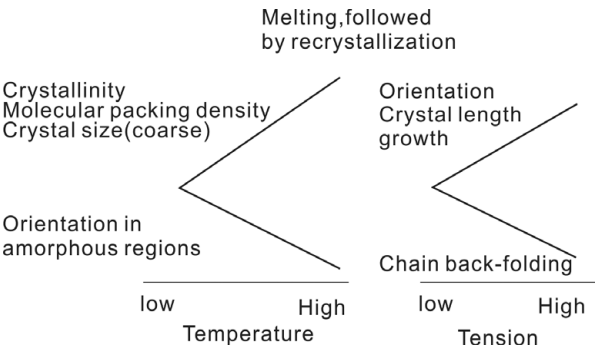

Fig. 2.24 Schematic effect of process conditions on fiber properties [9].

2.7.4.2 Processing and fiber properties

In view of the importance of the process parameters in determining fiber properties, the effects of temperature, tension and time on fiber properties are often evaluated, as shown in Fig. 2.24.

The process temperature influences the shrinkage, birefringence, elongation and tenacity at break, by affecting the crystal structures of polymers. High temperature results in high crystallinity, large crystals and dense molecular packing in the crystal, but coarse structure and disorientation in the amorphous phases [9].

Tension affects the orientation and crystal structures of polymer. Increasing tension leads to increased orientation and length of crystal, and reduction in chain back-folding.

Cold drawing is the principal approach for building up the tensile properties of fibers. The drawability of a fiber is limited to the density of entanglements, the number of tie molecules and the crystalline structure in the undrawn fiber. Low crystalline material is easier to draw. In addition to the importance of the degree of crystallinity, the crystal size determines, to a large extent, how many link molecules will be formed. With increased link molecules, the strength and possible modulus increase. Besides, the smaller the crystallites are, the easier they can be relocated, and the better the distribution of tensile force that can be obtained.

It should be understood that an increase of elongational strength and modulus is accompanied by a decrease of tranverse strength [11]. The more stretches applied on the link molecules, the smaller is the cohesive force between the stretched molecules, and hence a decreased tranverse strength.

References

1. W. Findley, J. Lai, and K. Onaran. *Creep and Relaxation of Nonlinear Viscoelastic Materials: With an Introduction to Linear Viscoelasticity*. Dover Publications, 1989.
2. J. Charles, E. Carraher, *Seymour/Carraher's Polymer Chemistry* (sixth edition). New York: Marcel Dekker, Inc., 2003.

3. J. Burke, "Solubility parameters: theory and application," in *AIC Book and Paper Group Annual*, ed. C. Jensen, vol. 3, 1984.
4. D. J. Williams, *Polymer Science and Engineering*. Englewood Cliffs, New Jersey: Prentice-Hall, Inc., 1971.
5. *Polymer structure*. Polymers and Liquid Crystals [cited 2010 June 25]; Available from: http://plc.cwru.edu/tutorial/enhanced/files/polymers/struct/struct.htm.
6. R. O. Ebewele, *Polymer Science and Technology*. CRC, 2000.
7. W. M. D. Bryant, "Polythene fine structure." *Journal of Polymer Science*, vol. 2(6), pp. 547–564, 1947.
8. D. I. Bower, *An Introduction to Polymer Physics*. Cambridge University Press, 2002.
9. P. M. Latzke, "Testing and influencing the properties of man-made fibers," in *Synthetic Fibers: Machines and Equipment, Manufacture, Properties*, F. Fourné, Ed. Munich: Hanser Gardner Publications, 1999.
10. L. Sperling, *Introduction to Physical Polymer Science*. Wiley-Interscience, 2006.
11. Z. Walczak, *Processes of Fiber Formation*. Amsterdam: Elsevier, 2002.

3 Nanofiber technology

3.1 Nanofiber-forming technology

There are a number of techniques capable of fabricating nanofibers. These techniques include conjugate spinning, chemical vapor deposition, drawing, template synthesis, self-assembly, meltblowing and electrospinning.

3.1.1 Conjugate spinning (island in the sea)

Sea–island-type conjugate spinning involves extruding two polymer components from one spinning die. The fiber islands are arranged in a sea component which is later removed by extraction. Nakata *et al*. reported that continuous PET nanofibers with a diameter of 39 nm could be obtained by sea–island-type conjugate spinning from the flow-drawn fiber with further drawing and removal of the sea component. Figure 3.1 shows a TEM image of PET fiber island and Nylon-6 sea produced by conjugate spinning and flow-drawing [1].

3.1.2 Chemical vapor deposition (CVD)

In a CVD process, a substrate is exposed to one or more volatile precursors, which react and/or decompose on the substrate surface. The desired deposit is synthesized on the substrate surface. The volatile by-products are produced during the process and are removed by gas flow through the reaction chamber. The various forms of material that can be produced via CVD include monocrystalline, polycrystalline, amorphous, and epitaxial. Some examples of such CVD-fabricated materials are silicon, carbon fiber, carbon nanofibers, filaments and carbon nanotubes [2]. Figure 3.2 shows a schematic illustration of a plasma-enhanced CVD setup that can be used for fabricating single-walled carbon nanotubes.

The two most important CVD technologies are low pressure CVD (LPCVD) and plasma enhanced CVD (PECVD). The LPCVD process produces layers with excellent uniformity of thickness and material characteristics at relatively high deposition temperatures (higher than 600 °C) and slow deposition rates. The PECVD process can operate at lower temperatures (down to 300 °C), attributed to the extra energy supplied to the gas molecules by the plasma in the reactor. However, the quality of the films tends to be inferior. A schematic diagram of a typical LPCVD reactor is shown in Fig. 3.2.

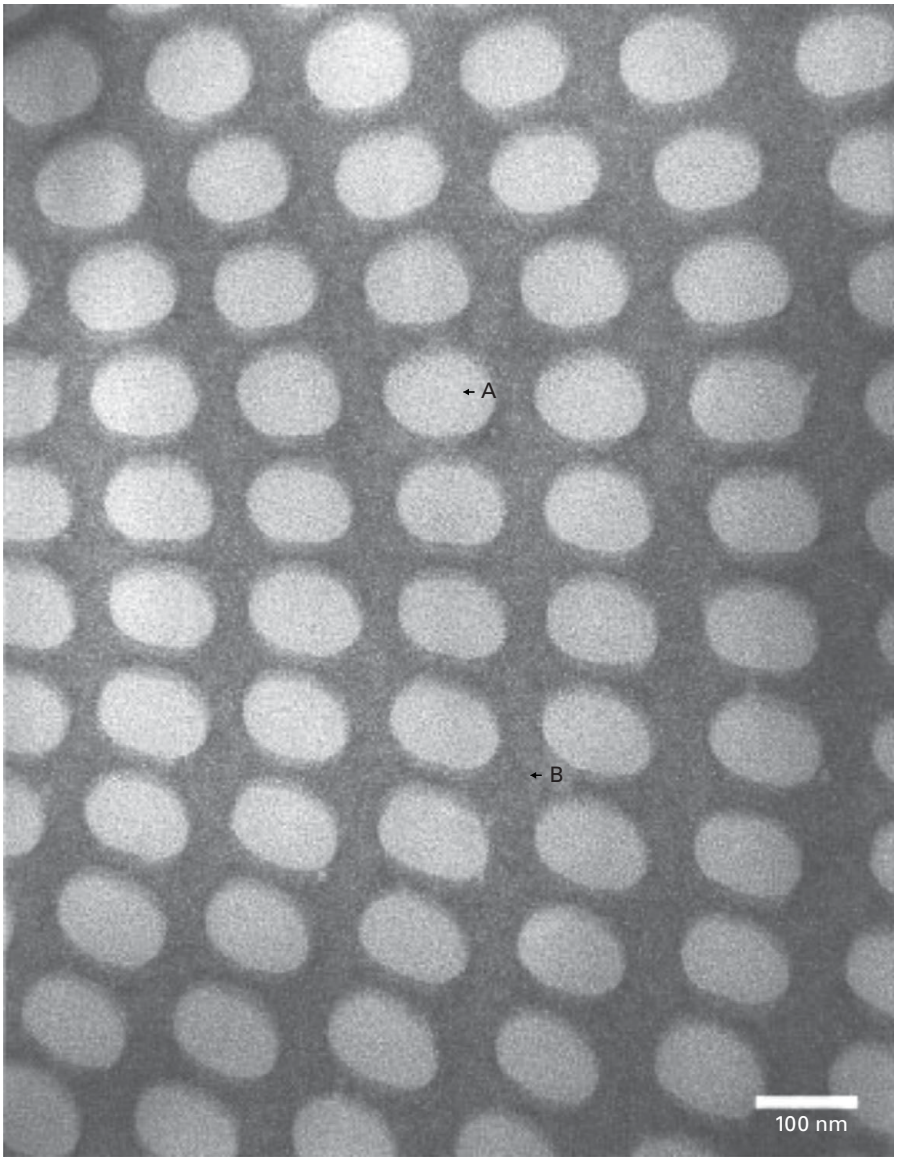

Fig. 3.1 Cross-sectional TEM image of conjugated-spun and flow-drawn fibers [1]: "A" indicates a PET fiber island, and "B" indicates the nylon-6 sea.

3.1.3 Phase separation (sol–gel process)

The phase separation process is a wet-chemical technique. In this process, the sol (or solution) evolves gradually towards the formation of a gel-like network containing both a liquid phase and a solid phase. The process consists of dissolution, gelation, solvent extraction, freezing, and freeze-drying. The basic solid phase, a nanoscale porous foam, is formed as a result. The sol–gel approach is a cheap and low-temperature technique

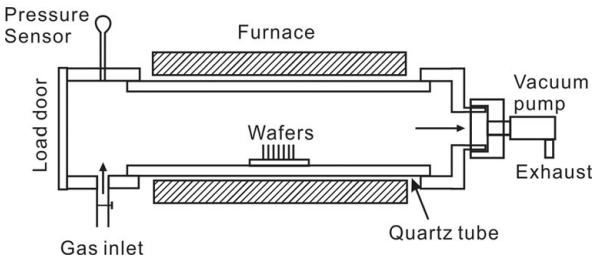

Fig. 3.2 A schematic illustration of a LPCVD setup.

that allows for the fine control of the product's chemical composition. But transforming the solid polymer into the nanoporous form takes a relatively long period of time using the phase-separation process [3].

3.1.4 Drawing

Drawing is a process similar to dry spinning in the synthetic fiber industry, that can make long, continuous single nanofibers. However, only a viscoelastic material that can undergo strong deformations while being cohesive enough to support the stresses developed during pulling can be made into nanofibers through drawing [4].

3.1.5 Template synthesis

The template synthesis method uses a nanoporous membrane as a template to make nanofibers of a solid fibril or a hollow tubule. The materials that can be used to grow tubules and fibrils by template synthesis include electronically conductive polymers, metals, semiconductors and carbon. However, continuous nanofibers cannot be fabricated by this method [5]. Fig. 3.3 shows a schematic diagram of the template preparation for MCo_2O_4 nanotubes use in the application of gas sensors by Zhang *et al*. [6].

3.1.6 Self-assembly

Self-assembly is a process whereby individual, pre-existing components organize themselves into desired patterns and functions. A broad range of peptides and proteins have been shown to produce very stable nanofiber structures. These nanofibers are very well ordered and possess remarkable regularity and, in some cases, helical periodicity. The diameter and the surface structure of the nanofibers can be altered by controlling of the molecular structures [7]. The potential applications of these composite nanofibers include electronics, optics, sensing and biomedical engineering. Figure 3.4 illustrats the self-assembly of various types of peptide materials.

3.1.7 Meltblown technology

Meltblown technology involves the production of fibers in a single step, by extruding a polymer melt through an orifice die and drawing down the extrudate with a jet of hot air

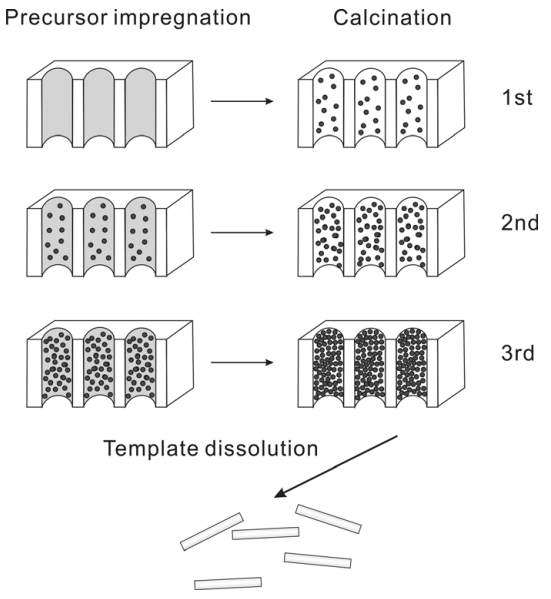

Fig. 3.3 A schematic diagram showing the template preparation for MCo_2O_4 nanotubes [6].

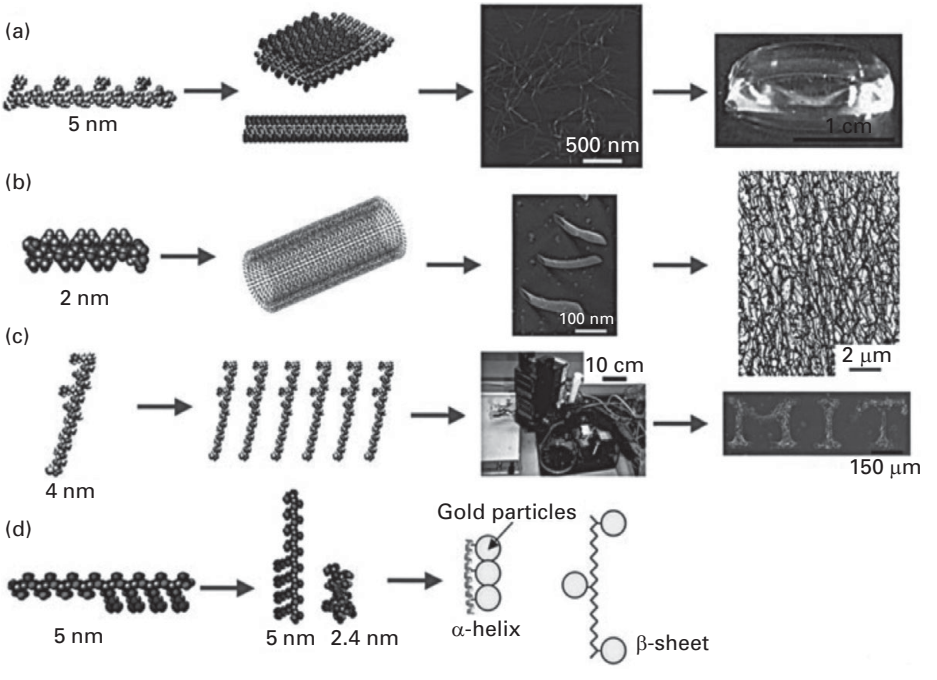

Fig. 3.4 Self-assembly of various peptide materials [7]: (a) the ionic self-complementary peptide, (b) a type of surfactant-like peptide, (c) surface nanocoating peptide and (d) molecular switch peptide.

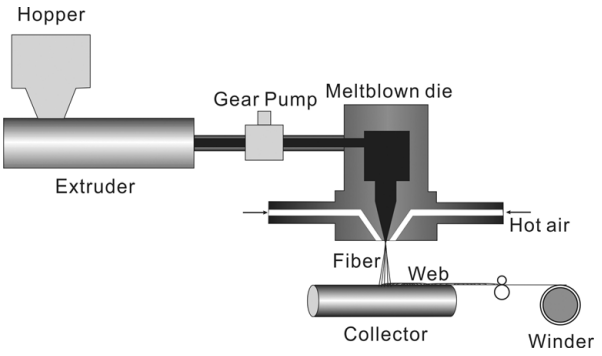

Fig. 3.5 Detailed schematic of meltblowing process.

(typically at the same temperature as the molten polymer). The air exerts the drag force that attenuates the melt extrudate into fibers, which are then collected a few feet away from the die in the form of a nonwoven mat. Figure 3.5 shows a schematic illustration of the melt blowing process.

3.1.8 Electrospinning

Electrospinning is a well-established process for producing ultra-fine fibers, first patented in 1934. The process currently produces micron-scale fibers at a commercially viable level using electrostatic forces to pull fibers from a capillary of polymer solution. According to Deitzel *et al*., the technique can be considered a variation of the electrospray process [8]. The polymer solution consists of a predetermined mixture of polymer suspended in solvent. A drop of polymer solution forms at the tip of the capillary due to gravity and is held in place by surface tension. Formation of the fiber begins when the electrostatic force is greater than the surface tension of the droplet. The fiber is formed as the ejected jet stream is narrowed by whipping itself as a result of an increase in surface charge density due to the evaporation of the solvent. Nanofiber fabrication by electrospinning will be described in detail in the following section.

3.2 Electrospinning process

The electrospinning process involves electrostatic forces in the fiber-formation process. This is different from conventional fiber spinning techniques (melt, dry or wet spinning) that rely on mechanical forces to produce fibers by extruding the polymer melt or solution through a spinneret and subsequently drawing the resulting filaments as they solidify and coagulate. Electrospinning involves the application of an electric field between a capillary tip and a grounded collector via a high-voltage source. A pendant droplet of polymer solution at the capillary tip is transformed to a hemispherical shape and then into a conical shape (known as a Taylor cone) by the electric field. When the intensity of the electric field causes a larger effect than the surface tension of the

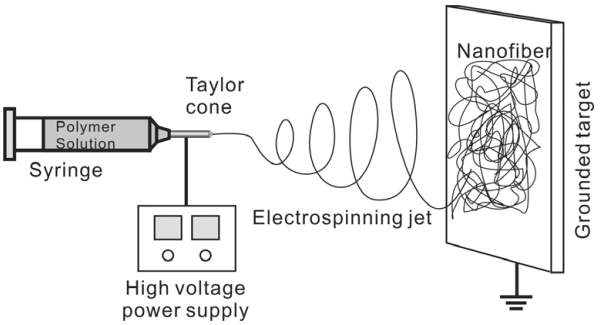

Fig. 3.6 An electrospinning setup.

polymer solution, the solution is ejected towards the grounded metallic collector. If the concentration of the solution is too low, the jet breaks up into droplets. However, when the viscosity is high enough, as indicated by entanglements of the polymer chains, a continuous jet is formed. A series of electrically induced bending instabilities in the air results in stretching and elongation of the jet in a cone-shaped volume. Rapid evaporation of the solvent during the elongation process reduces the fiber diameter. The nonwoven mat collected on the grounded surface contains continuous fibers from the microscale to the nanoscale. Figure 3.6 shows the schematic diagram of an typical electrospinning setup.

3.3 Processing parameters

There are numerous parameters that can affect the transformation of polymer solutions into nanofibers through electrospinning. These parameters include (a) governing variables such as applied voltage at the spinneret, the tip-to-ground distance, the hydrostatic pressure in the capillary tube, (b) ambient conditions such as solution temperature, air flow, and humidity in the electrospinning chamber, and (c) the solution(spinning dope) properties such as viscosity, conductivity, surface tension and elasticity [9]. Spinnability of various polymers has been widely investigated. Fong *et al.* found that electrospinning of PEO solutions (using the cosolvents of water and ethanol) that have viscosities between 1–20 poises and a surface tension in the range of 35–55 dynes/cm was fiber-formable [10]. However, for electrospinning of CA in 2:1 acetone/DMAc, viscosities between 1.2 and 10.2 poises were fiber-formable [11]. These two cases show that the spinnable set of conditions for different polymer solutions is unique. In the following sections, the processing parameters of the electrospinning process are discussed in greater detail.

3.3.1 Spinning dope concentration and viscosity

One of the more significant parameters influencing the fiber diameter is the spinning dope viscosity. A higher viscosity results in a larger fiber diameter [9, 10, 12]. It is to be noted that the spinning dope viscosity is directly proportional to the polymer

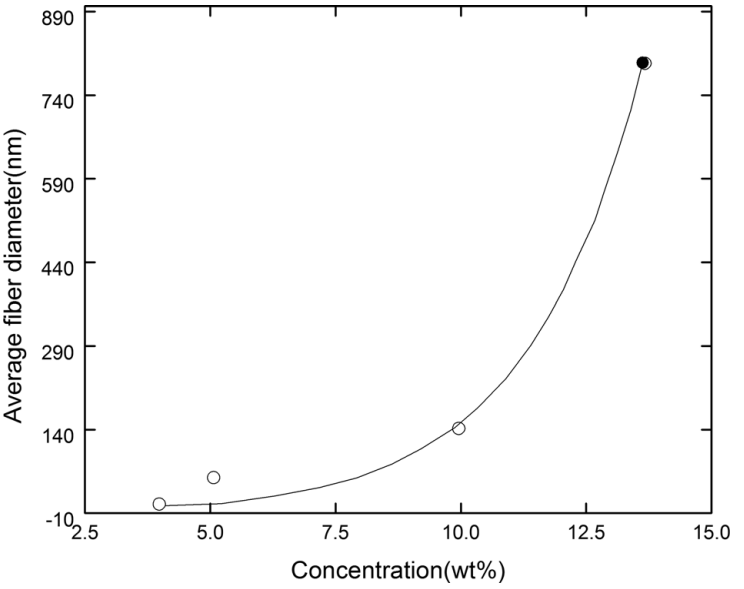

Fig. 3.7 Average fiber diameter of polyurethane fibers is proportional to the cube of the polymer concentration [13].

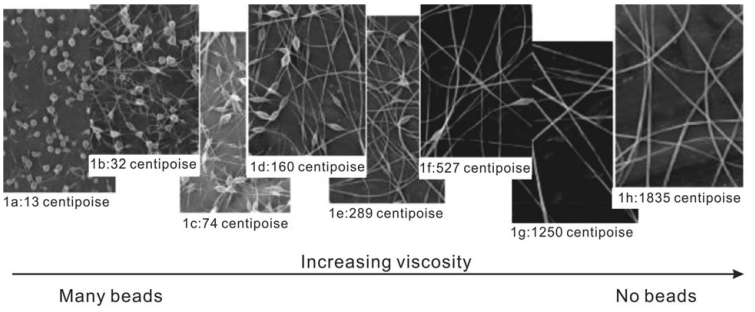

Fig. 3.8 SEM images of electrospun PEO nanofibers from different solutions with different viscosity [10].

concentration. Thus, an increase in polymer concentration will also imply an increase in fiber diameter. Deitzel *et al*. demonstrated that the fiber diameter increased with increasing polymer concentration according to a power law relationship [8]. Demir *et al*. then showed that the fiber diameter was proportional to the cube of the polymer concentration [13]. Figure 3.7 shows that the average diameter of polyurethane fibers is proportional to the cube of the polymer concentration.

Fong *et al*. found that the fiber morphology was influenced by the polymer concentration, thus by the viscosity as well. It was observed that many beads form at low viscosity, resulting in a "beads-on-the-strings" morphology. At high viscosity, beadless fibers were obtained. Figure 3.8 shows the SEM images of electrospun PEO fibers obtained from solutions ranging from low to high viscosity [10].

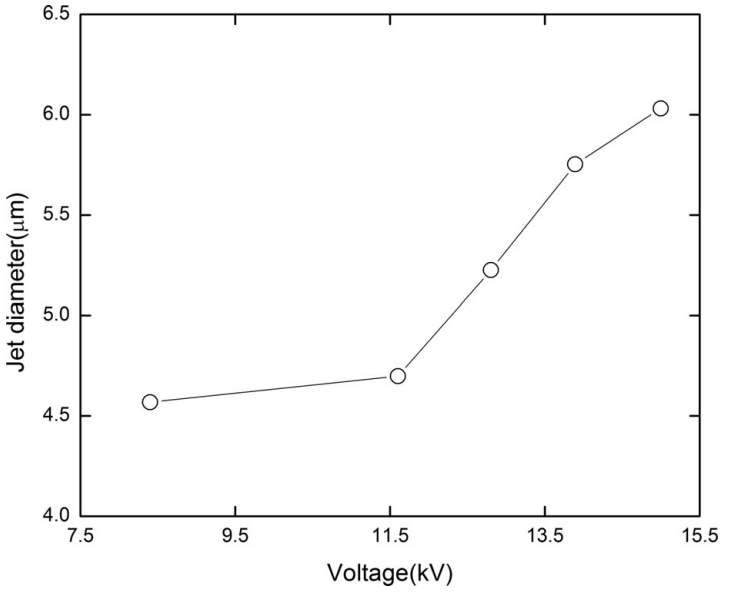

Fig. 3.9 Jet diameter as a function of applied voltage [13].

3.3.2 Applied voltage

Applied voltage is another parameter that affects the fiber diameter. Generally, a higher applied voltage leads to a higher volume of spinning dope ejection, resulting in a larger fiber diameter. Figure 3.9 shows that the jet diameter increases with increasing applied voltage [13].

3.3.3 Spinning dope temperature

Uniformity of the fiber diameter is also a challenge posed by the electrospinning process. Demir *et al*. reported that polyurethane fiber diameters were more uniform when electrospinning was conducted at a high temperature (70 °C) compared to room temperature. The mechanism behind the increased fiber diameter uniformity with increasing spinning dope temperature is not fully understood. It was also noted that the spinnability of the fibers increased with increasing spinning dope temperature. The highest polymer concentration that could be electrospun at room temperature was 12.8 wt% (weight percent), whereas a 21.2 wt% polyurethane polymer solution could be electrospun at a high temperature of 70 °C [13]. Clearly, the spinnability of the polymer solution increases with decreasing viscosity of the solution.

3.3.4 Surface tension

It was observed by Doshi and Reneker that beadless fibers could be obtained by reducing the surface tension of a polymer solution [9]. However, this generalization is

not always true, as shown by Liu and Hsieh in their work producing cellulose fibers by electrospinning of cellulose acetate using dimethylacetamide (DMAc) and acetone as the solvents. Acetone has a surface tension of 23.7 dyne/cm, whereas DMAc has a surface tension of 32.4 dyne/cm. When using either DMAc or acetone alone as the solvent, beads or beaded fibers were obtained. When a cosolvent of DMAc and acetone was used, the surface tension ranging between 23.7 and 32.4 dyne/cm, beadless fibers were observed [11].

3.3.5 Electrical conductivity

The addition of salts into a polymer solution can result in fewer beads and finer fibers. It was explained that a higher charge density on the jet surface was obtained with the addition of the salts, bringing more electrical charge to the jet. An increase in the charge carried by the jet leads to higher elongation forces on the jet under the electric field, resulting in fewer beads and finer fibers. Zong *et al*. reported that, as the salt content in a polymer solution increased, fewer beads and finer fibers were observed [14]. Lee *et al*. also found that using a solvent with a higher electrical conductivity would result in PCL fibers with smaller diameters [15]. Figure 3.10 shows that the PCL diameter decreases as solvent electrical conductivity increases.

3.3.6 Molecular weight of polymer

As molecular weight (MW) is proportional to the polymer chain length, a high MW implies a high degree of polymer chain entanglement. The Berry number, an indication of the degree of polymer chain entanglement, is a product of the intrinsic viscosity and polymer concentration. A high Berry number indicates a high degree of polymer chain entanglement. The Berry number has been found to correlate positively with the fiber morphology and diameter, implying that a higher MW would result in a larger fiber diameter and fewer beads. Koski *et al*. reported that PVA fiber diameter increases with MW and Berry number. At low MW and Berry number (<9), the beaded morphology

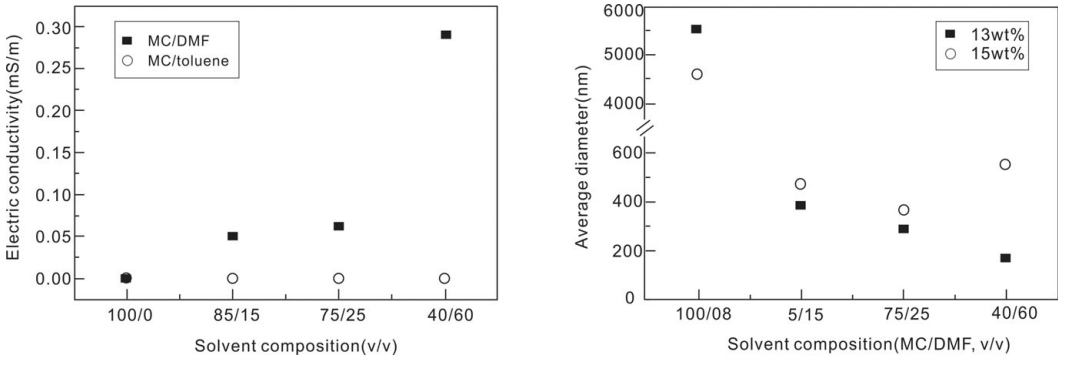

Fig. 3.10 The PCL diameter decreases with increasing electrical conductivity [15].

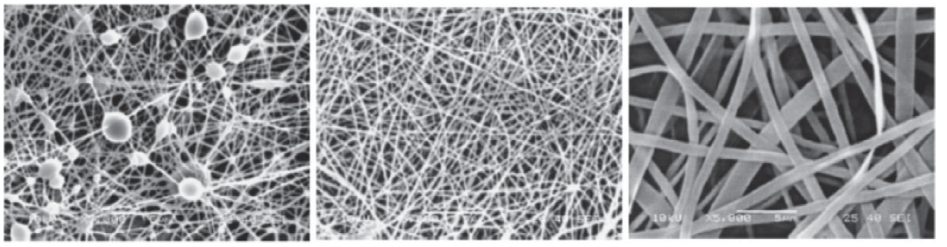

(a) 25wt%, 9000-10000g/mol (b) 25wt%, 13000-23000g/mol (c) 25wt%, 31000-50000g/mol

Fig. 3.11 PVA fiber morphology of 25 wt% polymer concentration with a molecular weight of 9000–50 000 g/mol [16].

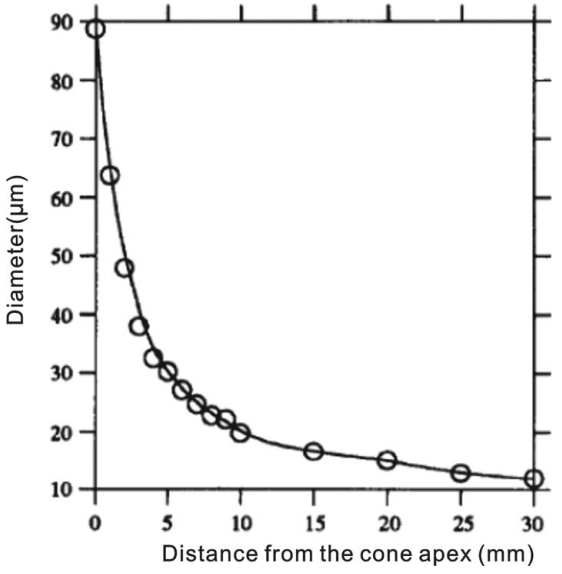

Fig. 3.12 Plot of jet diameter as a function of distance from the apex of the Taylor cone for 4 wt% aqueous PEO solution spun at 10 kV [9].

and circular cross-section are evident, as shown in Fig. 3.11a, b. At high MW and Berry number (>9), flat fibers with large diameters were obtained, as shown in Fig. 3.11c [16].

3.3.7 Spinning distance

The further the distance between the spinneret and the grounded metal screen, the finer the fiber diameter will be, as the fibers have more time and distance to elongate themselves in the instable zone. Doshi and Reneker reported that the jet diameter would decrease with increasing distance from the apex of the Taylor cone, suggesting that the fiber diameter would decrease with increasing distance from the spinneret. Figure 3.12 shows the plot of jet diameter as a function of distance from the apex of the Taylor cone for 4 wt% aqueous PEO solution spun at 10 kV [9].

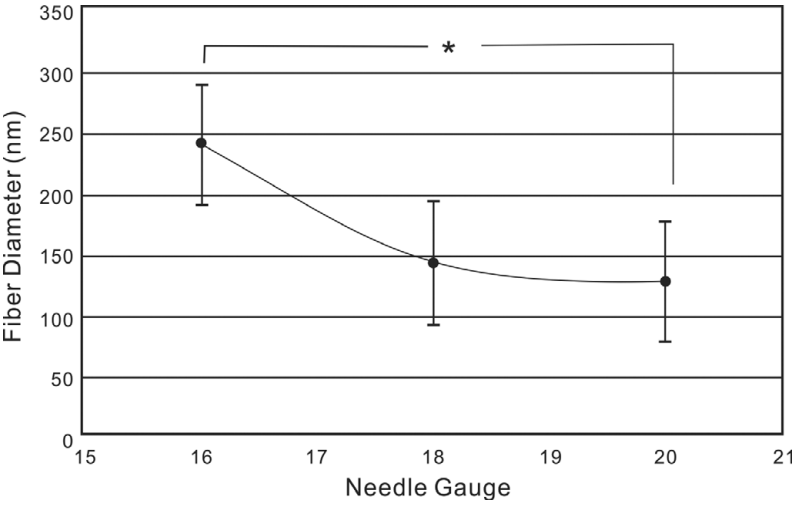

Fig. 3.13 Effect of orifice diameter on the diameter of PLAGA nanofibers with a 16-gauge needle (ID = 1.19 mm), an 18-gauge needle (ID = 0. 84mm), and a 20-gauge needle (ID = 0.58 mm) [18].

3.3.8 Spinning angle

Many spinning angles have been previously studied, with 0°, 45° and 90° being the most common. There is little experimental evidence that spinning angle affects fiber diameter. However, uniformity of the electrospun fibers increased at 45° because the flow rate was often lower and gravity did not allow for formation of as many beads [17].

3.3.9 Orifice diameter

The smaller the orifice diameter, the smaller the fibers tend to be. Dhirendra *et al.* demonstrated that a smaller orifice diameter results in PLAGA nanofibers with smaller diameter [18]. Figure 3.13 shows that the PLAGA fiber diameter decreases with decreasing orifice diameter.

3.3.10 Solvent boiling point

A low boiling point is a desirable characteristic in electrospinning applications because it promotes the evaporation of the solvent under conventional atmospheric conditions. This property promotes the deposition of polymer fibers in an essentially dry state[19]. However, a solvent with an exceedingly low boiling point leads to frequent clogging of the spinneret, due to quick evaporation of the solvent. Wannatong *et al.* reported that polystyrene fiber diameter decreases with increasing solvent boiling point[20]. During its flight to the grounded target, an ejected charged jet is stretched to a much lower diameter. At the same time, the solvent gradually evaporates, causing the viscoelastic properties of the jet to change. As soon as the viscoelastic force exceeds the electrostatic

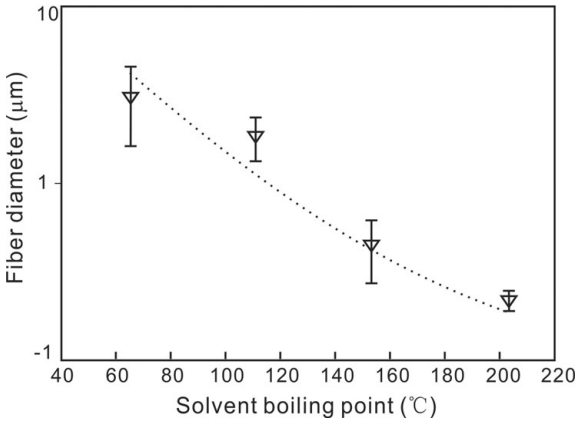

Fig. 3.14 The relationship between polystyrene fiber diameter and solvent boiling point [20].

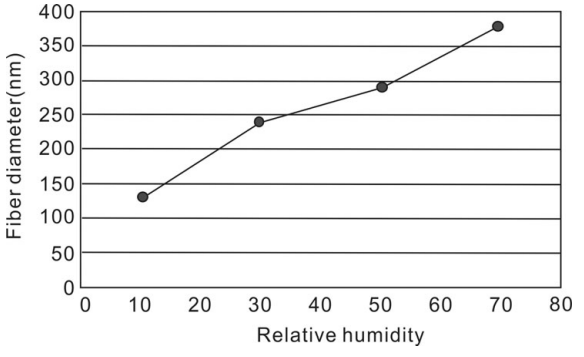

Fig. 3.15 Average polystyrene fiber diameter versus relative humidity (data adapted from Ref. [21]).

force, the jet cannot be stretched much further. Based on this explanation, solutions of PS in both toluene and THF (which have low boiling points of 111 °C and 65–66 °C, respectively) would give fibers with larger diameters than those in m-cresol and DMF (Fig. 3.14).

3.3.11 Humidity

Kim *et al*. found that the average polystyrene fiber diameter increases with increasing relative humidity in the air contained by the electrospinning chamber[21] (Fig. 3.15). The higher relative humidity makes a thicker fiber because the higher electrostatic charge density on the fiber surface is able to split the fibers more.

High humidity affects the evaporation rate of solvent in the jet. Thus when a fiber reaches the receiver, some solvent remains inside. This subsequently evaporates and leaves the fiber a porous structure. Jeun *et al*. reported that the number of pores on the

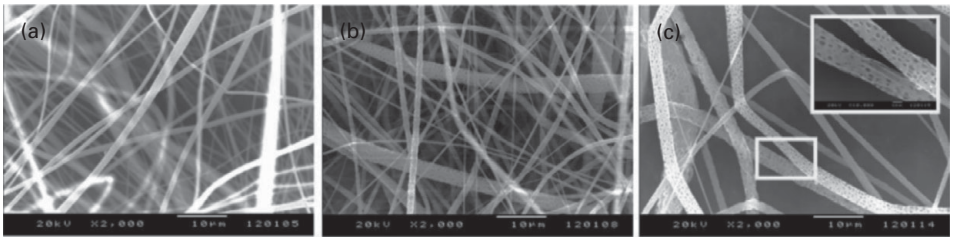

Fig. 3.16 Effect of humidity of the 2.5 wt% PLDLA solution on the fiber morphology (flow rate = 0.005 ml/min, electric voltage = 20 kV) [22]: (a) 30%, (b) 50% and (c) 70%.

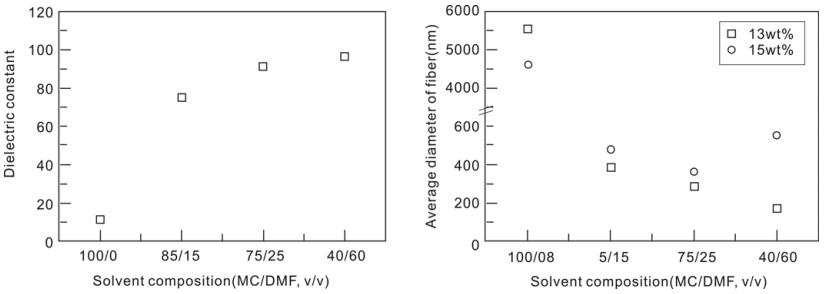

Fig. 3.17 PCL fiber diameter decreases with increasing dielectric constant of the solvent [15].

fiber surface increases with increasing humidity. The influence of relative humidity on the morphology of electrospun poly(L-lactide-co-D, llactide) (PLDLA) fiber is shown in Fig. 3.16. It can be observed that increasing the amount of humidity causes an increase in the number of pores on the surface, the pore diameter and the pore size distribution [22].

3.3.12 Dielectric constant

The dielectric constant is a material property that describes a material's ability to store charge when used as a capacitor dielectric. An increase in the dielectric constant means an increase in the charge storage capacity of the material. Methylene chloride (MC) has a dielectric constant of 9.1, whereas the dielectric constant of dimethyl formamide (DMF) is 36.7. By increasing the composition of DMF in the solvent, the dielectric constant of the solvent increases as a result. The fiber diameter of polycaprolactone (PCL) was found to decrease as the solvent's dielectric constant increases [15], as seen in Fig. 3.17.

3.3.13 Feeding rate

Zong *et al.* reported that a lower solution feeding rate yielded smaller fibers with spindle-like beads. At a higher feeding rate, larger fibers and beads were observed. Since the droplet suspended at the spinneret tip is larger with a higher feeding rate, the

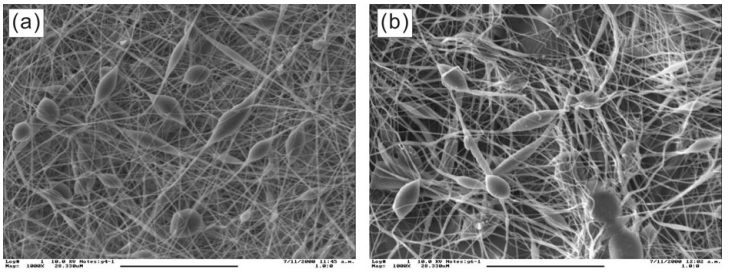

Fig. 3.18 SEM images showing the variation of beaded fibers at different feeding rates[14]: (a) 20 ml/min and (b) 75 ml/min [14].

jet carries the fluid away at a higher velocity. As a result, the electrospun fibers are harder to dry before they reach the grounded target. Consequently, a higher feeding rate results in large beads and junctions in the final membrane morphology [14]. Figure 3.18 shows the SEM images of fibers at a feeding rate of 20 ml/min and 75 ml/min, where (a) shows smaller beads and finer fibers and (b) shows bigger beads and larger fibers.

3.4 Melt electrospinning

The two major types of electrospinning include solution electrospinning and melt electrospinning. Solution electrospinning involves the use of a polymer-and-solvent system in the electrospinning process, whereas the spinning dope of melt electrospinning contains only a polymer melt with no solvent. Solution electrospinning has attracted much more attention than melt electrospinning because of its viability in producing fibers in the nanorange. The decrease in fiber diameter is believed to be caused by the evaporation of the solvent in solution electrospinning, as evidenced by many studies that concluded that fiber diameters increase with decreasing solvent concentrations, thus explaining the difficulty in producing nanofibers by using melt electrospinning [17].

In 2003, Huang *et al*. reported that nearly 100 polymer solutions and only six polymer melts had been successfully electrospun [23]. Dissolution and electrospinning of the polymer solutions were conducted at room temperature under atmospheric conditions. However, electrospinning of polymer melts had to be carried out in a vacuum condition and at a high temperature (200–290 °C) [23]. Given such demanding processing conditions, it is understandable that more nanofibers have been electrospun from polymer solutions than from polymer melts.

Nevertheless, one advantage of melt electrospinning is that cytotoxic solvents are not needed to prepare the spinning dope, and as such the fibers produced by melt electrospinning can be used in biomedical applications such as 3-D tissue scaffolds. In 2006, Dalton *et al*. electrospun polymer melts directly onto fibroblast cells to form layered scaffolds for tissue engineering [24]. The use of melt electrospinning eliminates the possibility of introducing cytotoxic solvents into cell culture during fiber deposition.

3.5 Applications of nanofibers

Owing to their high surface area to volume ratio, nanofibers have the potential to improve significantly current technology and to generate applications in new areas. Potential applications for nanofibers include reinforcement fibers in composites, protective clothing, filtration, biomedical devices, electrical and optical applications, and nanosensors.

3.5.1 Reinforcement fibers in composites

Traditional engineering fibers (such as Kevlar, carbon and glass) have been widely used as reinforcements in composite designs. With reinforcement fibers, the resulting composite materials show superior structural properties including high modulus and strength-to-weight ratios. It has been shown that nanosized materials (carbon nanotubes [25, 26], cellulose nanofibrils [27]) have superior mechanical strength compared to their larger counterparts. Undoubtedly, superior structural properties resulting from the reinforcement with nanofibers can be expected. In 2004, Ko *et al*. demonstrated the feasibility of producing recombinant spider silk fibers by co-electrospinning carbon nanotubes (CNT) with the spider silk protein extracted from the milk produced by Nexia's transgenic goats [28]. The nanoeffects of the CNT were successfully transferred to spider silk fibers, as it was reported that the Young's modulus of the CNT-reinforced spider silk fibers increased by up to 460%. However, this was achieved at the expense of strength and strain to failure. Kim and Reneker investigated the reinforcing effect of electrospun nanofibers of polybenzimidazole (PBI) in both epoxy and rubber matrices [29]. It was found that, with increasing fiber content, the bending Young's modulus and the fracture toughness of the epoxy nanocomposite was only marginally increased, whereas the fracture energy increased significantly. For the rubber nanocomposite, however, the Young's modulus was ten times higher and the tear strength was twice as large as that of the unfilled rubber material. These two studies show that nanofibers have huge potential in many structural applications based on their ability to improve mechanical performances.

3.5.2 Protective clothing

Because of the superior mechanical properties of nanofibers, incorporating them into the design of protective gear such as bullet proof vests and safety helmets holds promise for improving performance and significantly reducing weight. Other protective clothing applications of nanofibers rely on the small pore sizes of nonwoven nanofiber mats and a high surface area. The small pore sizes of nonwoven fiber mats provide a good resistance to penetration by chemical harm agents in aerosol form, and could thus effectively protect users from nuclear, biological and chemical warfare [30, 31]. Because of their great surface area, nanofiber fabrics are capable of neutralizing chemical agents without impeding their air or water vapor permeability [32].

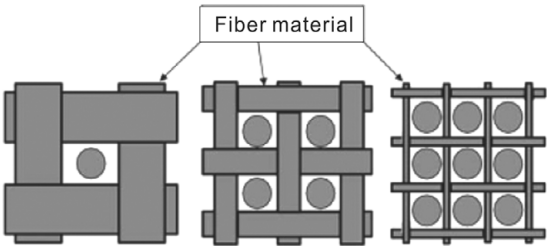

Fig. 3.19 The efficiency of a filter increases with decreasing fiber diameter [23].

Preliminary investigations have indicated that, compared to conventional textiles, electrospun nanofibers present both minimal impedance to moisture vapor diffusion and extreme efficiency in trapping aerosol particles [33].

3.5.3 Filtration

Filtration is widely used in many engineering fields. The future filtration market has been estimated to be up to US $700 billion by 2020 [34]. Filter media are used to produce clean compressed air in industry. These media are required to capture oil droplets as small as 0.3 micron. The advantages of using fiber-based filter media include high filtration efficiency and low air resistance [35]. Filtration efficiency, which is closely related to fiber diameter, is one of the most critical factors for filter performance, as shown in Fig. 3.19. Electrospinning is found to be able to fabricate fiber media for the removal of submicron foreign particles. Since the channels and structural elements of a filter must be comparable in size with the particles or droplets that are to be captured in the filter, one direct way of developing highly efficient and effective filter media is by using nanometer-sized fibers in the filter structure [36]. In general, due to the very high surface-area-to-volume ratio and resulting high surface cohesion, tiny particles of the order of <0.5 mm can be easily trapped in electrospun nanofibrous structured filters and hence the filtration efficiency can be improved. Freudenberg Nonwovens, a major world manufacturer of electrospun products, has been producing electrospun filter media from a continuous web feed for ultra-high efficiency filtration markets for more than 20 years [37, 38]. This is perhaps one of the earliest commercial businesses relevant to electrospinning. Recently, a US patent[39] has disclosed a method for making a dust filter bag, constituting a plurality of layers, including a carrier material layer and a nanofiber nonwoven tissue layer. Polymer nanofibers can also be electrostatically charged to modify the electrostatic attraction of particles without an increase in pressure drop to further improve filtration efficiency. In this regard, the electrospinning process has been shown to integrate the spinning and charging of polymers into nanofibers in one step [35, 40]. In addition to fulfilling the more traditional purpose of filtration, nanofiber membranes fabricated from some specific polymers or coated with some selective agents can also be used, for example, as molecular filters. Such filters can be applicable for the detection and filtration of chemical and biological weapon agents [41].

3.5.4 Biomedical devices

From the perspective of nature, nearly all of the fundamental building blocks of human tissues and organs, including dentin, collagen, bone, cartilage and skin, exist in the form of nanofibers. These biological fibers are characterized by well-organized hierarchical fibrous structures realigning at the nanoscale. As such, bioengineering has become the major area of applications for electrospun nanofibers.

3.5.4.1 Wound dressing

In 2006, Dalton *et al*. electrospun polymer melts directly onto fibroblast cells to form layered scaffolds for tissue engineering [24]. The use of melt electrospinning eliminates any possibility of introducing cytotoxic solvents into the cell culture during fiber deposition. With the aid of an electric field, biodegradable polymer fibers can be electrospun onto the burned location to form a protective fibrous membrane, which would aid wound healing by stimulating skin cell growth into the 3-D scaffolds and eliminate the formation of scar tissue [32, 42]. Nonwoven fibrous membranes (produced via aerosol particle capturing mechanisms) for wound dressing have pore sizes ranging from 500 nm to 1 μm, which are sufficiently small for protecting a wound from bacterial penetration. The high surface area of nanofiber mat is also very efficient for fluid absorption and dermal delivery [43].

3.5.4.2 Medical prostheses

Soft tissue prosthesis applications such as blood vessels using nanofibers fabricated by electrospinning have been proposed. Furthermore, biocompatible polymer nanofibers can also be used as a coating film on an artificial biomedical device such as a hip implant to serve as an interfacial layer between the prosthetic device and the host tissues. The nanofiber coating film is expected to reduce the stiffness mismatch and improve nutrient exchange between the device and host tissues. The use of nanofiber coating films will reduce the chance of device failure after the implantation [44, 45].

3.5.4.3 Tissue scaffolds

Mimicking the structure and biological functions of the extracellular matrix has been one of the challenges in tissue engineering with respect to the design of ideal scaffolds for the treatment of damaged tissues and malfunctioning organs in the human body. Nanofiber scaffolds can serve as a host for cells to seed, migrate and grow. Biocompatible 3-D scaffolds for cell in-growth to achieve tissue repair and replacement are of particular interest in tissue engineering. There is a growing interest in synthetic biopolymer (proteins, starch) and biodegradable polymer (polycaprolactone, poly(lactic acid)) nanofibers, which are capable of forming networks that mimic native tissue structures [46, 47].

3.5.4.4 Controlled drug delivery

Drug delivery with polymer nanofibers is based on the principle that the dissolution rate of a drug increases with increasing surface area of both the drug and the coating. Kenawy and Abdel-Fattah investigated delivery of tetracycline hydrochloride based

on the fibrous delivery matrices of poly(ethylene-co-vinylacetate) and poly(lactic acid), and their blend [48]. As the drug and carrier materials can be mixed together for electrospinning of nanofibers, the likely modes of the drug in the resulting nanostructured products are: (1) the drug as particles attached to the surface of the nanofiber-form carrier, (2) both drug and carrier in nanofiber-form, with the end product being the two kinds of nanofibers interlaced together, (3) a blend of drug and carrier materials integrated into one kind of fiber containing both components, and (4) the carrier material is electrospun into a tubular form in which the drug particles are encapsulated. As drug delivery in the form of nanofibers is still in the early stages of exploration, a real delivery mode, regarding production and efficiency, has yet to be determined.

3.5.5 Electrical and optical applications

The rate of electrochemical reaction is proportional to the surface area of the electrode. Because of the high specific surface area of nanofibers, using nanofibers in electronic devices such as sensors and actuators will potentially reduce the response time to a stimulus. Conductive nanofibers have the potential for many applications, including electrostatic dissipation, corrosion protection, electromagnetic interference shielding and photovoltaic devices[49].

3.5.6 Nanosensors

The high surface-area-to-volume ratio of nanofibers, which improves sensitivity, makes them ideal for sensor applications. Nanofibers from polymers with the piezoelectric effect, such as polyvinylidene fluoride, will render the resulting nanofibrous devices piezoelectric [50]. PLAGA nanofibers have been used as a new sensing interface for fabricating chemical and biochemical sensors [51]. The sensitivities of the nanofiber sensors are reported to be three orders of magnitude higher than those obtained from thin film sensors.

References

1. K. Nakata, *et al*., "Poly (ethylene terephthalate) nanofibers made by sea–island-type conjugated melt spinning and laser-heated flow drawing," *Macromolecular Rapid Communications*, vol. 28(6), pp. 792–799, 2007.
2. M. Terrones, *et al*., "Efficient route to large arrays of CN nanofibers by pyrolysis of ferrocene/melamine mixtures," *Applied Physics Letters*, vol. 75, pp. 3932, 1999.
3. P. Ma, and R. Zhang, "Synthetic nano-scale fibrous extracellular matrix," *Journal of Biomedical Materials Research*, vol. 46(1), pp. 60–72, 1999.
4. T. Ondarcuhu, and C. Joachim, "Drawing a single nanofibre over hundreds of microns," *Europhysics Letters*, vol. 42, p. 215, 1998.
5. L. Feng, *et al*., "Super-hydrophobic surface of aligned polyacrylonitrile nanofibers," *Angewandte Chemie International Edition*, vol. 41(7), pp. 1221–1223, 2002.
6. G. Zhang, B. Guo, and J. Chen, "MCo_2O_4 (M= Ni, Cu, Zn) nanotubes: Template synthesis and application in gas sensors," *Sensors and Actuators B: Chemical*, vol. 114(1), pp. 402–409, 2006.

7. S. Zhang, "Fabrication of novel biomaterials through molecular self-assembly," *Nat. Biotech.*, vol. 21(10), pp. 1171–1178, 2003.
8. J. M. Deitzel, *et al.*, "The effect of processing variables on the morphology of electrospun nanofibers and textiles," *Polymer*, vol. 42(1), pp. 261–272, 2001.
9. J. Doshi, and D. Reneker, "Electrospinning process and applications of electrospun fibers," *Journal of Electrostatics*, vol. 35(2), pp. 151–160, 1995.
10. H. Fong, I. Chun, and D. Reneker, "Beaded nanofibers formed during electrospinning," *Polymer*, vol. 40, pp. 4585–4592, 1999.
11. H. Liu, and Y. Hsieh, "Ultrafine fibrous cellulose membranes from electrospinning of cellulose acetate," *Journal of Polymer Science Part B: Polymer Physics*, vol. 40(18), pp. 2119–2129, 2002.
12. P. Baumgarten, "Electrostatic spinning of acrylic microfibers," *Journal of Colloid and Interface Science*, vol. 36(1), 1971.
13. M. Demir, *et al.*, "Electrospinning of polyurethane fibers," *Polymer*, vol. 43(11), pp. 3303–3309, 2002.
14. X. Zong, *et al.*, "Structure and process relationship of electrospun bioabsorbable nanofiber membranes," *Polymer*, vol. 43(16), pp. 4403–4412, 2002.
15. K. Lee, *et al.*, "Characterization of nano-structured poly (ε-caprolactone) nonwoven mats via electrospinning," *Polymer*, vol. 44(4), pp. 1287–1294, 2003.
16. A. Koski, K. Yim, and S. Shivkumar, "Effect of molecular weight on fibrous PVA produced by electrospinning," *Materials Letters*, vol. 58(3–4), pp. 493–497, 2004.
17. F. Ko, "Nanofiber technology: bridging the gap between nano and macro world," *Nanoengineered Nanofibrous Materials*, p. 1, 2004.
18. D. S. Katti, *et al.*, "Bioresorbable nanofiber-based systems for wound healing and drug delivery: optimization of fabrication parameters," *Journal of Biomedical Materials Research Part B: Applied Biomaterials*, vol. 70B(2), pp. 286–296, 2004.
19. J. Matthews, *et al.*, "Electrospinning of collagen nanofibers," *Biomacromolecules*, vol. 3(2), pp. 232–238, 2002.
20. L. Wannatong, A. Sirivat, and P. Supaphol, "Effects of solvents on electrospun polymeric fibers: preliminary study on polystyrene," *Polymer International*, vol. 53(11), pp. 1851–1859, 2004.
21. G. Kim, *et al.*, "Effect of humidity on the microstructures of electrospun polystyrene nanofibers," *Microscopy and Microanalysis*, vol. 10(S02), pp. 554–555, 2004.
22. J. Jeun, *et al.*, "Electrospinning of Poly (L-lactide-co-D, L-lactide)," *Journal of Industrial and Engineering Chemistry*, vol. 13(4), pp. 592–596, 2007.
23. Z. -M. Huang, *et al.*, "A review on polymer nanofibers by electrospinning and their applications in nanocomposites," *Composites Science and Technology*, vol. 63(15), pp. 2223–2253, 2003.
24. P. Dalton, *et al.*, "Direct in vitro electrospinning with polymer melts," *Biomacromolecules*, vol. 7(3), pp. 686–690, 2006.
25. L. Forro, *et al.*, *Electronic and Mechanical Properties of Carbon Nanotubes, in Science and Application of Nanotubes*, D. Tománek and R. J. Enbody, Ed. Springer–Verlag, 2002, pp. 297–320.
26. M.-F. Yu, *et al.*, "Strength and breaking mechanism of multiwalled carbon nanotubes under tensile load," *Science*, vol. 287(5453), pp. 637–640, 2000.
27. W. Hamad, "On the development and applications of cellulosic nanofibrillar and nanocrystalline materials," *The Canadian Journal of Chemical Engineering*, vol. 84(5), pp. 513–519, 2006.

28. F. Ko, M. Gandhi, and C. Karatzas. Carbon nanotube reinforced spider silk – a model for the next generation of super strong and tough fibers, in *19th American Society for Composites Annual Technical Conference*, 2004, Atlanta, GA.
29. J. Kim and D. Reneker, "Polybenzimidazole nanofiber produced by electrospinning," *Polymer Engineering and Science*, vol. 39(5), pp. 849–854, 1999.
30. P. Gibson, H. Schreuder-Gibson, and D. Riven, "Electrospun fiber mats: transport properties," AIChE 45 (1999). *Full Text via CrossRef| View Record in Scopus| Cited By in Scopus* (146), pp. 190–195.
31. G. Chamberlain and M. Joyce, *Design News*, 20 Aug., 1990.
32. D. Smith, and D. H. Reneker, *PCT/US00/27737*, 2001.
33. P. Gibson, H. Schreuder-Gibson, and D. Rivin, "Transport properties of porous membranes based on electrospun nanofibers," *Colloids and Surfaces A: Physicochemical and Engineering Aspects*, vol. 187–188, pp. 469–481, 2001.
34. A. Suthat, and G. Chase, *Chemical Engineer*, pp. 26–8, 2001.
35. P. Tsai, H. Schreuder-Gibson, and P. Gibson, "Different electrostatic methods for making electret filters," *Journal of Electrostatics*, vol. 54(3–4), pp. 333–341, 2002.
36. K. Graham, *et al*. Polymeric nanofibers in air filtration applications, in *Fifteenth Annual Technical Conference & Expo of the American Filtration & Separations Society*, 2002, Galveston, Texas.
37. J. Halpin, K. Finlayson, and J. Ashton, *Primer on Composite Materials Analysis*. CRC, 1992.
38. H. Schreuder-Gibson, *et al*., "Protective textile materials based on electrospun nanofibers," *Journal of Advanced Materials*, vol. 34(3), pp. 44–55, 2002.
39. D. Emig, A. Klimmek, and E. Raabe, *Dust filter bag containing nano non-woven tissue*, FiberMark Gessner GmbH & Co.: U.S., 2002.
40. S. A. Angadjivand, *et al*., *Method and apparatus for making a nonwoven fibrous electret web from free-fiber and polar liquid*, 3M Innovative Properties Company: U.S., 2002.
41. S. Graham, "Smart'silicon dust could help screen for chemical weapons," *Scientific American*, vol. 3, 2002.
42. D. Martindale, "Scar no more," *Scientific American Magazine*, 2000(7), pp. 34–36.
43. R. A. Coffee, *Dispensing Device and Method for Forming Material*, Electrosols, Ltd.: U.S., 2001.
44. M. M. Hohman, *et al*., "Electrospinning and electrically forced jets. I. Stability theory," *Physics of Fluids*, vol. 13(8), pp. 2201–2220, 2001.
45. C. Buchko, K. Kozloff, and D. Martin, "Surface characterization of porous, biocompatible protein polymer thin films," *Biomaterials*, vol. 22(11), pp. 1289–1300, 2001.
46. A. Fertala, W. Han, and F. Ko, "Mapping critical sites in collagen II for rational design of gene-engineered proteins for cell-supporting materials," *Journal of Biomedical Materials Research Part A*, vol. 57(1), pp. 48–58, 2001.
47. L. Huang, *et al*., "Generation of synthetic elastin-mimetic small diameter fibers and fiber networks," *Macromolecules*, vol. 33(8), pp. 2989–2997, 2000.
48. E.-R. Kenawy and Y. R. Abdel-Fattah, "Antimicrobial properties of modified and electrospun poly(vinyl phenol)," *Macromolecular Bioscience*, vol. 2(6), pp. 261–266, 2002.
49. K. Senecal, *et al*. *Photoelectric Response from Nanofibrous Membranes*, Warrendale, Pa.; Materials Research Society; 2002.
50. A. G. Scopelianos, *Piezoelectric biomedical device*, Ethicon, Inc.: U.S., 1996.
51. S. Kwoun, *et al*. "A novel polymer nanofiber interface for chemical sensor applications," in *2000 IEEE/EIA International Frequency Control Symposium and Exhibilition*, 2000.

4 Modeling and simulation

A key objective in electrospinning is generating fibers of nanoscale diameter consistently and reproducibly. Considerable effort has been devoted to understanding how the parameters affect the spinnability and more specifically the diameter of the fibers resulting from the electrospinning process. Many processing parameters that influence the spinnability and the physical properties of nanofibers have been identified. These parameters include process parameters such as electric field strength, flow rate and spinning distance, spinning dope properties including concentration, viscosity and surface tension, etc., the spinning environment factors like humidity and the spinning setup factors such as the diameter of the orifice and the electrospinning angle. Through observation of the electrospinning process and analyzing these parameters, some governing models have been built and simulations of the motion of jet have been carried out. In this chapter, several main existing models and simulation works will be introduced to help readers build up a brief concept.

4.1 Electrospinning mechanism

For a long period, the mechanism of electrospinning for forming nanoscaled fibers was believed to be a result of a "split" as seen by the naked eye (Fig. 4.1a). The "splitting" is explained by Doshi and Reneker [1, 2] that, as the jet diameter decreases, the surface charge density increases, resulting in high repulsive forces which split the jet into smaller jets splay. When a high-speed camera was used in the investigation of electrospinning jet, unstable bending, also known as "whipping" of jet was observed, and the "bending instability" started being widely accepted as the electrospinning mechanism, as shown in Fig. 4.1b. As described [3, 4], the electrospun jet vigorously bent spirally and stretched inside a conical envelop resulting in a huge stretch ratio and a nanoscale diameter.

4.2 Fundamentals of process modeling

Many approaches have been achieved in analysis, modeling and simulation of electrospinning processes. According to the analyzing objects, theoretical and experimental research mainly focused on three parts: the Taylor cone, the jet and the whole process.

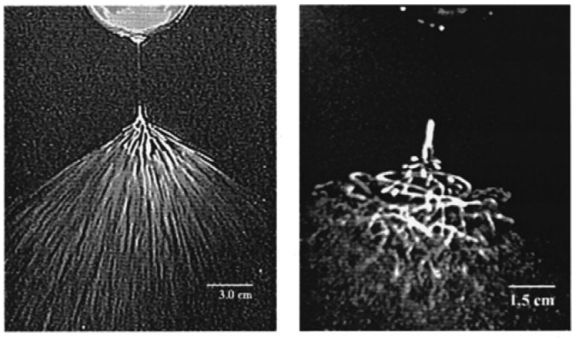

Fig. 4.1 Images of electrospinning jet [3]. (a) Splitting captured at 16.7 camera exposure time; (b) bending instability captured at 1.0 ms camera exposure time.

No matter how simple or complicated the models are, the two major principles employed in the all the analyzing works are very basic and simple: Newton's law for an object's force analysis, and conservation laws for system analysis.

4.2.1 Newton's law

Newton's first law of motion predicts the behavior of objects for which all existing forces are balanced. The first law states that, if the forces acting upon an object are balanced, then the acceleration of that object will be 0 m/s/s. An object will accelerate only if there is a net or unbalanced force acting upon it. The presence of an unbalanced force will accelerate an object – changing its speed, its direction, or both its speed and direction. Newton's second law of motion pertains to the behavior of objects for which all existing forces are not balanced. The second law states that the acceleration of an object is dependent upon two variables – the net force acting upon the object and the mass of the object. As the force acting upon an object is increased, the acceleration of the object is increased. As the mass of an object is increased, the acceleration of the object is decreased.

Newton's second law of motion can be formally stated as follows.

The acceleration of an object as produced by a net force is directly proportional to the magnitude of the net force, in the same direction as the net force, and inversely proportional to the mass of the object.

This statement can be expressed in equation form as follows:

$$a = F/m, \tag{4.1}$$

where a is the acceleration of the object with a mass of m, and F is the net force applied on the object. The above equation is often rearranged to a more familiar form as shown below. The net force is equated to the product of the mass times the acceleration:

$$F = ma. \tag{4.2}$$

As we will see in the following sections, in analyzing the equilibrium status of the Taylor cone, Newton's first law is a very powerful tool. When calculating the jet profiles, Newton's second law is mainly used. And for the whole electrospinning process analysis, Newton's second law also plays a very important role, known as the conservation of linear momentum.

4.2.2 Conservation laws

According to physics, a conservation law is the principle that certain quantities within an isolated system do not change over time. When a substance in an isolated system changes phase, the total amount of mass does not change. When energy is changed from one form to another in an isolated system, there is no change in the total amount of energy. When a transfer of momentum occurs in an isolated system, the total amount of momentum is conserved. The same is true for electric charge in a system: charge lost by one particle is gained by another. Conservation laws make it possible to predict the macroscopic behavior of a system without having to consider the microscopic details of a physical process or chemical reaction.

In modeling the electrospinning processes, conservation of mass, charge, momentum and energy are the four elements to be analyzed.

4.3 Taylor cone

The Taylor cone is one of the main characters of electrospinning process, from which the jets are ejected and formed in fibers. It is believed that through controlling the Taylor cone the electrospun jet profile is controllable and, furthermore, the diameter of electrospun nanofibers is adjustable. Therefore a great deal of theoretical and experimental work has been done on the Taylor cone. Most of the obtained equations were derived from analyzing the equilibrium status of the Taylor cone or, in another words, the force balance analysis of the Taylor cone using Newton's first law. Electric forces and surface tension are the two forces that are considered to be the essential factors.

In the 1960s, Taylor pioneered the theoretical and experimental research into electrically charged jets [5, 6]. He derived the condition for the critical electric potential needed to transform the droplet of liquid into a cone, commonly referred to as the Taylor cone, and for it to exist in equilibrium under the presence of both electric and surface tension forces as

$$V_c^2 = 4\frac{H^2}{L^2}\left(\ln\frac{2L}{R} - \frac{3}{2}\right)(0.117\pi\gamma R), \tag{4.3}$$

where V_c is the critical voltage, H is the distance between the capillary exit and the ground, L is length of the capillary with radius R, and γ is the surface tension of the liquid. In this calculation only inviscid fluids were considered.

A similar equation was found by Hendricks *et al.* [7]:

$$V = 300\sqrt{20\pi\gamma r}, \tag{4.4}$$

where r is the radius of the pendant drop. Above this potential, the drop becomes fluid dynamically unstable.

In 1995, Doshi and Reneker [1] investigated the electrospinning process, and calculated the electric field strength at the apex of the cone, as shown below:

$$E = \sqrt{\frac{4\gamma}{\varepsilon_0 R}}. \tag{4.5}$$

Hayati investigated the velocity profile inside the liquid cone at the base of an electrically driven jet both numerically and experimentally [8, 9] and calculated the electric stress on the surface of the cone as

$$\tau_t = \varepsilon_0 E_n E_t, \tag{4.6}$$

where ε_0 is the permittivity of free space, and E_n and E_t are respectively the normal and tangential electric field subjected to the jet surface.

4.4 Jet profile

Since the most important product parameter in electrospinning is the diameter of nanofibers, there has been considerable interest in understanding the jet profile of electrically charged jets. Investigation of the behavior of thin liquid jets in electric fields can be traced back to the work of Rayleigh [10, 11] in 1882, later studies of Zeleny [12], and today's studies of electrospun jet. Studies of electrically charged jets are mainly based on Newton's second law by considering how the forces such as the solution viscosity, flow rate and electronic force accelerate a jet as it flows downward.

Baumgarten was the first to systematically investigate the electrospinning process [13]. Using microflash photographs, he observed that "fiber loops shot out radially from the jet" for the first time. After a series of studies of the effects of solution viscosity, flow rate, voltage and gap, Baumgarten calculated the radius of the jet as

$$r \propto \sqrt{4\varepsilon V m/\rho}, \tag{4.7}$$

where r is the radius of the jet, m/ρ is the flow rate and V is the voltage.

By assuming all electric energy is transformed into kinetic energy and neglecting the effect of viscosity, the acceleration of the jet was obtained [13] as

$$a = \frac{F}{m} - \frac{4\varepsilon V^2}{\rho y^2 r}, \tag{4.8}$$

where y is the axial distance from the center of the hemisphere. The boundary conditions for this equation are $v = 0$ and $y = r$ at $t = 0$.

Fridrikh *et al*. [14] obtained the terminal jet radius r_t as follows:

$$r_t = \left(\gamma\bar{\varepsilon}\frac{Q^2}{I^2}\frac{2}{\pi(2\ln\chi - 3)}\right)^{1/3}, \tag{4.9}$$

where γ is the surface tension, ε is the dielectric permittivity, Q is the flow rate, I is the electric current, and $\chi \sim R/h$ is the dimensionless wavelength of the instability responsible for the normal displacements.

By introducing the dimensionless jet radius $\widetilde{R} = R/R_0$ and axial coordinate $\widetilde{z} = z/z_0$, where $z_0 = \rho Q^3/2\pi^2 R_0^4 E_0 I$, and the characteristic jet radius, R_0, is taken as equal to the radius of the capillary orifice, Spivak and Dzenis [15] came up with a dimensionless equation for the jet radius:

$$\frac{d}{d\widetilde{z}}\left\{\widetilde{R}^{-4} + W_e\widetilde{R}^{-1} - \gamma\widetilde{R}^2 - \frac{1}{R_e}\left(\frac{1}{2}\frac{d}{d\widetilde{z}}\left(\widetilde{R}^{-2}\right)\right)^m\right\} = 1. \tag{4.10}$$

The dimensionless parameters in this equation are defined as follows. The Weber number, $W_e = \left(2\pi^2 R_0^3\sigma_s\right)/\left(\rho Q^2\right)$, describes the ratio of the surface tension forces to the inertia forces. The parameter $\gamma = \left(\pi^2 I^2 R_0^6\right)/4\varepsilon_0\rho Q^4$ describes the ratio of the electric forces to the inertia forces. The effective Reynolds number for the fluid is characterized by the power-law relationship, known as the Oswald–deWaele law, $\hat{\tau}^c = \mu\left[tr\left(\bar{\dot{\gamma}}^2\right)\right]^{m-1/2}\bar{\dot{\gamma}}$, where μ is a constant, $\bar{\dot{\gamma}}$ is state of strain tensor, m is flow index. $R_e = \left(Q^2\rho\right)/\left(2\pi^2 R_0^4\varpi\right)\left[\left(4\pi E_0 I R^2\right)/\left(Q^2\rho\right)\right]^{-m}$ describes the ratio of the inertia forces to the viscous forces.

Rutledge *et al*. [16] found that the jet behavior near the nozzle is sensitive to operating conditions, jet geometry and fluid properties. However, far from the nozzle, the scaling for the radius of the jet r is determined mainly by operating conditions:

$$r = \frac{\lceil\rho Q^3\rceil^{1/4}}{\lfloor 2\pi^2 I E_\infty\rfloor}z^{-1/4}. \tag{4.11}$$

4.5 Models

The foundational axioms of fluid dynamics are the conservation laws. In electrospinning, the pendant droplet of the polymer solution at the capillary tip is deformed into a Taylor cone under the influence of an electrostatic field. When the voltage overcomes the surface tension, a fine charged jet is ejected and moves towards the receiver. Thus, apart from the three common conservation relationships: the mass conservation, the energy conservation and the momentum conservation, there is another very important conservation relation in electrospinning: the charge conservation due to the applied electric field. The influence factors involved in electrospinning are very complicated, and include hydrostatic pressure, flow rate, electric field strength, viscosity and conductivity of polymer solutions, and even temperature gradient effects. For a thorough understanding of the electrospinning process, enormous efforts have been involved in

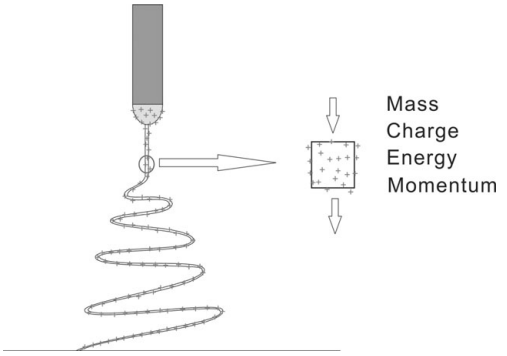

Fig. 4.2 Conservations in electrospinning process.

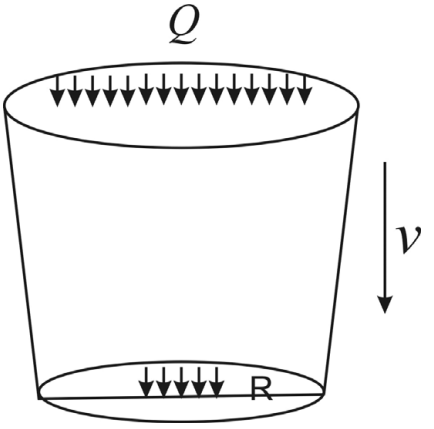

Fig. 4.3 Mass conservation.

modeling this process and building models. Figure 4.2 shows the conservations occuring in the electrospinning process.

4.5.1 One-dimensional model

For a simple and quick analysis, the one-dimensional (1-D) steady governing model for electrospinning jet can be written as follows [4, 17–23].

Assuming the jet is steady, as shown in Fig. 4.3, according to the law of conservation of mass, the mass (flow rate Q) flows in the jet channel will equals the mass flows out. Denote the instantaneous flow velocity by v and the radius of jet by R. Then, we write the conservation equation of mass as

$$\pi R^2 \rho v = Q. \tag{4.12}$$

For the conservation of charges, the equation is usually in the form of current I. The current flowing through the jet channel at a given time is considered composed of two part: the current generated by the motion of surface charges, and the current generated by the motion of body charges. (Fig. 4.4)

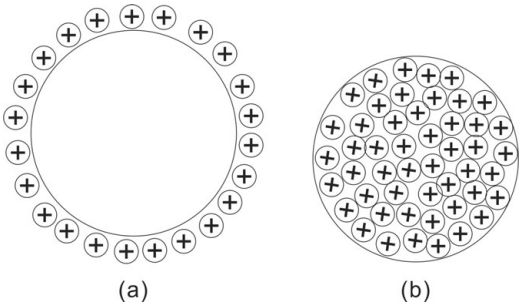

Fig. 4.4 Charges distributed on the surface of the jet (a) and in the body of jet (b).

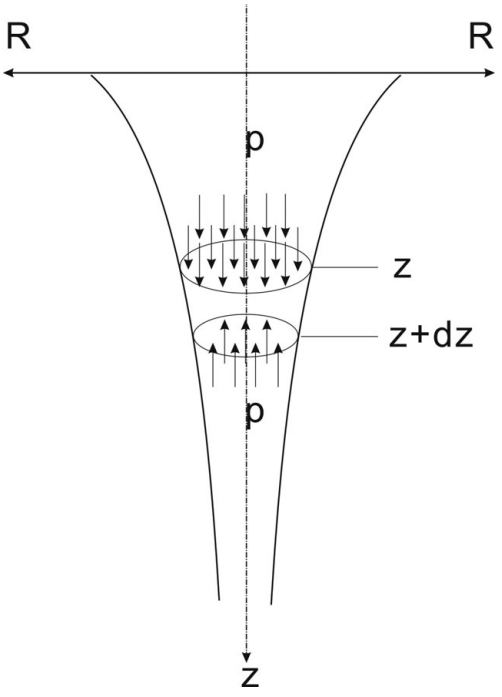

Fig. 4.5 Hydrostatic pressure on fluid segment.

$$\pi R^2 KE + 2\pi Rv\sigma = 1, \tag{4.13}$$

where E is the intensity of applied electric field and σ is the density of surface charge.

In linear momentum analysis, the internal pressure p, the electric force, the viscous force τ and the body force g are considered, as shown in Fig. 4.5.

The conversion of linear momentum is written as

$$\rho \frac{d}{dz}\left(\frac{v^2}{2}\right) = -\frac{dp}{dz} + \frac{2\sigma E}{r} + \frac{d\tau}{dz} + \rho g. \tag{4.14}$$

4.5.2 Three-dimensional models

According to the same rules, 3-D models for the electrospinning process have also been established respectively by Spivak and Dzenis, Rutledge's group and Wan *et al*.

4.5.2.1 Spivak–Dzenis model

In this model, the conservation of mass and charge are simply written as below [15, 24]:

(1) conservation of mass

$$\nabla \cdot v = 0, \tag{4.15}$$

(2) conservation of electric charge

$$\nabla \cdot J = 0. \tag{4.16}$$

Regarding linear momentum analysis, only viscous and electric forces are considered:

$$\rho(v \cdot \nabla)v = \nabla T^m + \nabla T^e. \tag{4.17}$$

The right-hand side of the linear momentum balance equation is the sum of viscous and electric forces. Rheologic behavior of polymer fluids is described by the power-law constitutive equation, known as the Oswald–deWaele model:

$$T^m = \mu\left(II_{\dot{\gamma}}\right)^{\frac{m-1}{2}}\dot{\gamma} - pI, \tag{4.18}$$

where μ is viscosity, $II_{\dot{\gamma}}$ is the second invariant of the rate of strain tensor $\dot{\gamma}$, m is the flow index, p is hydrostatic pressure, and I is the unit tensor. Viscous Newtonian fluids are described by $m = 1$, pseudoplastic (shear thinning) fluids are described by $0 < m < 1$, and dilatant (shear thickening) fluids are described by $m > 1$.

The electric stress tensor T^e is the Maxwell tensor:

$$T^e = \varepsilon\left(\vec{E} \otimes \vec{E} - \frac{\vec{E} \cdot \vec{E}}{2}\right). \tag{4.19}$$

4.5.2.2 Rutledge's model

Assuming that the jet is a long, slender object and substituting leading order terms of a perturbative expansion in the aspect ratio, Rutledge's group [22, 25] derived another set of equations for electrospinning process:

(1) conservation of mass:

$$\partial_t\left(\pi h^2\right) + \partial_z\left(\pi h^2 v\right) = 0, \tag{4.20}$$

(2) conservation of charge:

$$\partial_t(2\pi h\sigma) + \partial_z\left(2\pi h\sigma v + \pi h^2 KE\right) = 0, \tag{4.21}$$

(3) momentum balance, or the Navier–Strokes equation :

$$\partial_t v + \partial_z\left(\frac{v^2}{2}\right) = -\frac{1}{\rho}\partial_z p + g + \frac{2\sigma E}{\rho h} + \frac{3v}{h^2}\partial_z\left(h^2\partial_z v\right). \tag{4.22}$$

By introducing non-dimensional parameters, they obtained non-dimensionalized equations for the above equations:

$$\partial_t\left(h^2\right) + \left(h^2 v\right)' = 0, \tag{4.23}$$

$$\partial_t(\sigma h) + \left(\sigma h v + \frac{k^*}{2} h^2 E\right)' = 0, \tag{4.24}$$

$$\partial_t v + v v' = -\left(\frac{1}{h} - h'' - \frac{E^2}{8\pi} - 2\pi\sigma^2\right)' + \frac{2\sigma E}{\sqrt{\beta} h} + g^* + \frac{\partial v^{*2}}{h^2}\left(h^2 v'\right)', \tag{4.25}$$

where h is the radius of the jet at axial coordinate z, v is the axial velocity of the jet and is constant across the jet cross-section to leading order, σ is the surface charge density and E is the electric field in the axial direction. The prime ($'$) denotes differentiation with respect to z.

The non-dimensional equations are made by choosing a length scale r_0, related to the diameter of the capillary; a time scale $t_0 = \sqrt{\rho r_0^3/\gamma}$, where γ is the surface tension and ρ is the density of the fluid; an electric field strength $E_0 = \sqrt{\gamma/(\varepsilon - \overline{\varepsilon}) r_0}$, where $\varepsilon/\overline{\varepsilon}$ is the permittivity of the fluid(air); and a surface charge density $\sqrt{\gamma\overline{\varepsilon}/r_0}$. The dimensionless asymptotic field is $\Omega_0 = E_\infty/E_0$. The material properties of the fluid are characterized by four dimensionless parameters: $\beta = \varepsilon/\overline{\varepsilon} - 1$; the dimensionless viscosity $v^* = \sqrt{v^2/\rho\gamma r_0}$; the dimensionless gravity $g^* = g\rho r_0^2/\gamma$; and the dimensionless conductivity $K^* = K\sqrt{\rho r_0^3/\beta\gamma}$.

4.5.2.3 Wan–Guo–Pan model

Upon the application of a very high electric field, molecular polarization induced by the electric field is likely. And, accordingly, the current and momentum of jet will be different (Fig. 4.6). Thus a more integral model was established [21]:

$$\frac{\partial q_e}{\partial t} + \nabla \cdot J = 0, \tag{4.26}$$

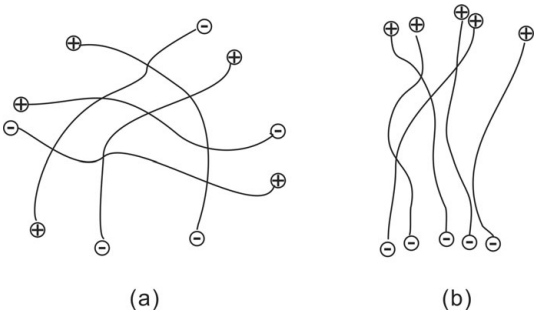

Fig. 4.6 Electric field induced molecular polarization: (a) unoriented molecular chains and (b) polarized oriented molecular chains.

$$\rho \frac{Dv}{Dt} = \nabla \cdot t + \rho f + q_e E + (\nabla E) \cdot P, \tag{4.27}$$

$$\rho c_p \frac{DT}{Dt} = Q_h + \nabla \cdot q + JE + E \cdot \frac{DP}{Dt}, \tag{4.28}$$

where $\partial q_e/\partial t$, $(\nabla E)\cdot P$ and $E \cdot DP/Dt$ are respectively the current, force and energy generated by the polarized molecular chains.

This set of conservation laws can constitute a closed system when it is supplemented by appropriate constitutive equations for the field variables such as polarization. The most general theory of constitutive equations determining the polarization, electric conduction current, heat flux and Cauchy stress tensor has been developed by Eringen and Maugin:

$$P = \varepsilon_p E, \tag{4.29}$$

$$J = KE + \sigma v + \sigma_T \nabla T, \tag{4.30}$$

$$q = \kappa \nabla T + \kappa_E, \tag{4.31}$$

$$t = -\widetilde{p}\underline{\underline{I}} + \eta\left[\nabla v + (\nabla v)^t\right], \tag{4.32}$$

where ε_p, K, μ_m, σ, σ_T, κ, κ_E and η are coefficients that relate to the material properties and depend only on temperature in the case of an incompressible fluid.

4.6 Application of models in parametric analysis

By simplifying and analyzing models, the relationships between process parameters are predictable, as well as the relationship between jet diameters and process parameters. The most systematic work on parameter relationship analysis and parameter prediction has been done by He and Wan based on the one-dimensional model [23, 26–28].

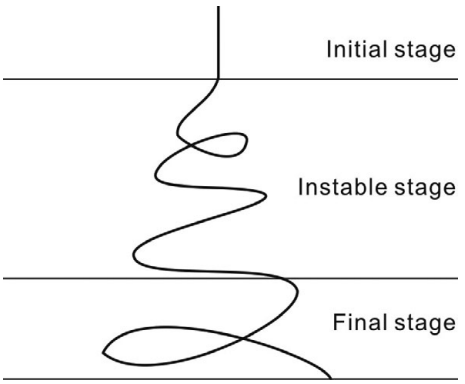

Fig. 4.7 Three stages of electrospun jet.

As shown in Fig. 4.7, the jet was divided into three stages: the initial, unstable and final stages. Each stage was investigated by analyzing the 1-D model.

At the initial stage of the electrospinning, the jet is stable and straight, and the electrical force is dominant over all the other forces on the jet. So Eq. (4.14) may be rewritten as:

$$\frac{d}{dz}\left(\frac{v^2}{2}\right) = \frac{2\sigma E}{\rho r}. \tag{4.33}$$

From Eqs. (4.1), (4.11) and (4.36), the scaling law for the jet diameter was obtained as

$$r \propto z^{-1/2}. \tag{4.34}$$

During the unstable stage, the electric force and viscous force reach a balance, thus

$$\frac{2\sigma E}{\rho r} + \frac{d\tau}{dz} \approx 0. \tag{4.35}$$

Assume the gradient of pressure is constant, then

$$\frac{d}{dz}\left(\frac{v^2}{2}\right) = \text{constant}. \tag{4.36}$$

we can rewrite it as

$$\frac{d}{dz}\left(r^{-4}\right) \propto r^0, \tag{4.37}$$

which shows the scaling law for jet diameter in the unstable stage is

$$r \propto z^{-1/4}. \tag{4.38}$$

If the distance approaches infinity, the acceleration in the axial direction vanishes, thus

$$\frac{d}{dz}\left(\frac{v^2}{2}\right) \to 0, \tag{4.39}$$

which leads to the scaling law for the jet diameter in the final stage:

$$r \propto z^0. \tag{4.40}$$

The scaling laws satisfy the data obtained by Shin *et al*. [22] very well (Fig. 4.8).

4.7 Computer simulation

Modeling the jet by a system of connected viscoelastic dumbbells and analyzing the momentum balance of these dumbbells, Reneker and Yarin studied the jet motion through computer simulation [29].

In this model [29], they took electrical forces and surface tension effects into consideration, but neglected the Earth's gravity and aerodynamic forces. The segment

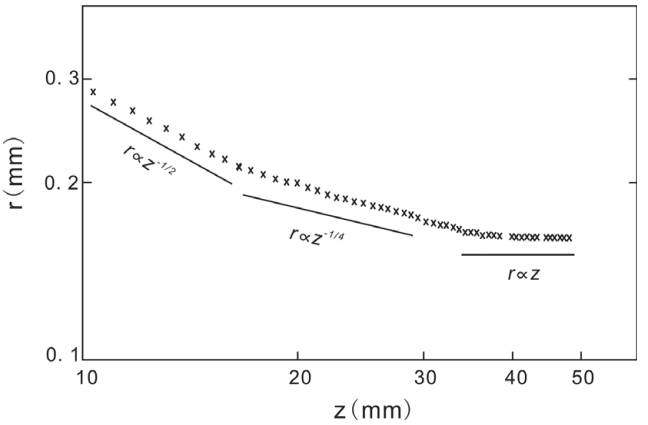

Fig. 4.8 Relationship between the jet radius and the axial distance (data adapted from Ref. [22]).

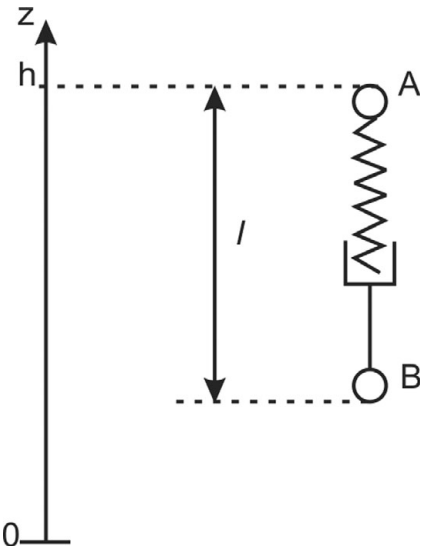

Fig. 4.9 Viscoelatic dumbbell representing a segment of the rectilinear part of the jet [29].

of the jet was modeled as a viscoelastic dumbbell, as shown in Fig. 4.9. The dumbbell comprises two beads, A and B, each possessing a charge e and mass m. The position of bead A is fixed and bead B is acting by Coulomb repulsive forces from bead A, $-e^2/l^2$ and the force due to the external field $-eV_0/h$. The dumbbell, AB, models a viscoelastic Maxwellian liquid jet. Therefore the stress, σ, pulling B back to A is given by

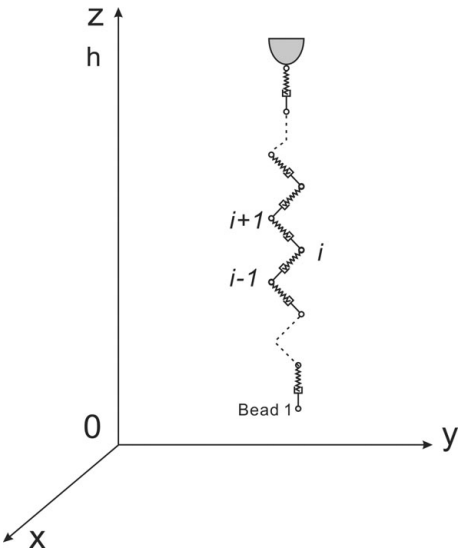

Fig. 4.10 Elctrospun jet modeled by a system of beads connected by viscoelastic elements [29].

$$\frac{d\sigma}{dt} = G\frac{dl}{ldt} - \frac{G}{\mu}\sigma, \tag{4.41}$$

where t is time, G and μ are the elastic modulus and viscosity, respectively, and l is the filament length.

The momentum balance for bead B is

$$m\frac{dv}{dt} = -\frac{e^2}{l^2} - \frac{eV_0}{h} + \pi r^2, \tag{4.42}$$

where r is the cross-sectional radius of the filament, and v is the velocity of bead B that satisfies the kinematics equation

$$\frac{dl}{dt} - v. \tag{4.43}$$

The electrospun jets was then modeled by a system of beads possessing charge e and mass m connected by viscoelastic elements [29], as shown in Fig. 4.10, which generalizes the models of Fig. 4.9 and Fig. 4.11.

The parameters corresponding to the element connecting bead i with bead $(i+1)$ are denoted by subscript u (up), those for the element connecting bead i with $(i-1)$ by subscript d (down). The rates of strain of the elements are given by $(dl_{ui}/dt)/l_{ui}$ and $(dl_{di}/dt)/l_{di}$. The viscoelastic forces acting along the elements are similar to Eq. (4.41):

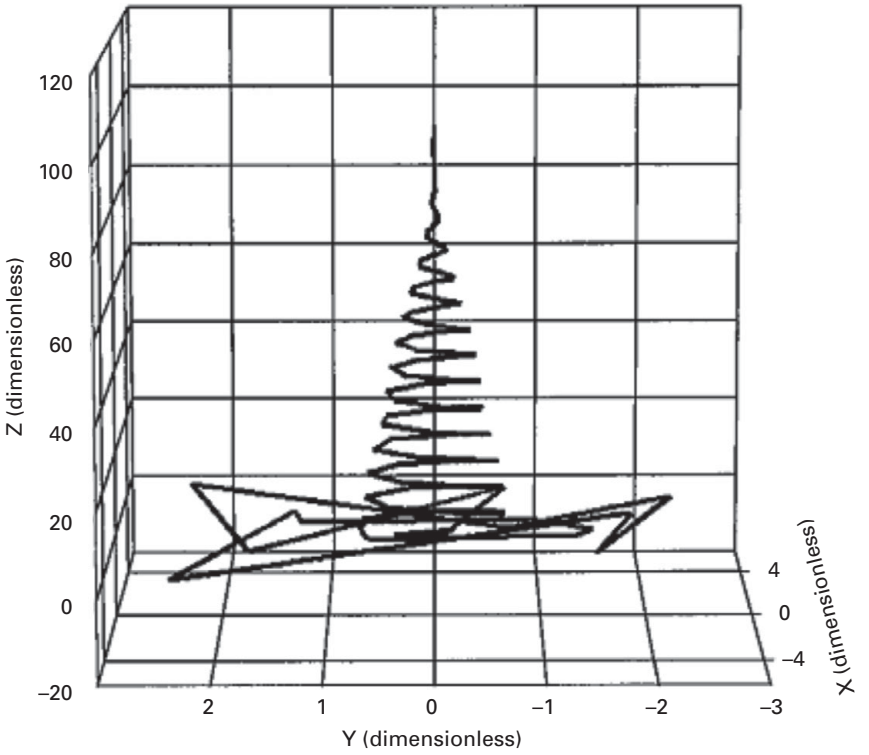

Fig. 4.11 Temporal growth of the bending instability along the straight segment of a charged jet subject to a small perturbation that is initially periodic in space [3].

$$\frac{d\sigma_{ui}}{dt} = G\frac{1}{l_{ui}}\frac{dl_{ui}}{dt} - \frac{G}{\mu}\sigma_{ui}, \tag{4.44a}$$

$$\frac{d\sigma_{di}}{dt} = G\frac{1}{l_{di}}\frac{G}{\mu}\sigma_{di}. \tag{4.44b}$$

According to Newton's second law, the equation governing the radius vector of the position of the ith bead $r_i = ix_i + jy_i + kz_i$ in the following form:

$$m\frac{d^2r_i}{dt^2} = \sum_{\substack{j=1,N \\ J\neq 1}} \frac{e^2}{R_{ij}^3}\left(r_i - r_j\right) - e\frac{V_0}{h}k + \frac{\pi r_{ui}^2\sigma_{ui}}{l_{ui}}\left(r_{i+1} - r_i\right)$$
$$-\frac{¶r_{di}^2\sigma_{di}}{l_{di}}\left(r_i - r_{i-1}\right) - \frac{a\pi(r^2)_{rv}k_i}{\left(x_i^2 + y_i^2\right)^{1/2}}. \tag{4.45}$$

For the first bead, $i=1$, and N, the total number of beads, is also 1. As more beads are added, N becomes larger and the first bead $i = 1$ remains at the bottom end of the growing jet. For this bead, all the parameters with subscript d should be set equal to zero since there are no beads below $i = 1$.

To consider the temporal instability of an established jet, the calculation began from a long rectilinear filament $0 \leq z \leq h$ containing a fixed number of beads [29]. The filament was perturbed by moving it laterally, at $t = 0$, everywhere along its axis by the functions [29]

$$\begin{aligned} x &= 10^{-3} L \cos\left(\frac{2\pi}{\lambda} z\right) \frac{h - z}{h} \\ y &= 10^{-3} L \sin\left(\frac{2\pi}{\lambda} z\right) \frac{h - z}{h}, \end{aligned} \tag{4.46}$$

where λ is the wavelength of the perturbation. Then the temporal evolution of the path was calculated.

In all cases, the system of Eqs. (4.44) and (4.45) was solved numerically, assuming the stresses σ_{ui} and σ_{di} and the radial velocity dr_i/dt were zero at $t = 0$. The calculation shows that small perturbations increased dramatically as the Earnshaw-like instability grew. As the calculation progresses, the beads move further and further apart. The graph becomes quite irregular when the separation between the beads is larger than the radius of the spiral path because the beads are connected by straight lines in this model [29]. The simulation results in reasonable agreement with the experimental evidence and shows that viscoelastic forces along the jet and the surface tension tend to stabilize the charged jet (Fig. 4.11).

References

1. J. Doshi, and D. Reneker, "Electrospinning process and applications of electrospun fibers," *Journal of Electrostatics*, vol. 35(2), pp. 151–160, 1995.
2. X. Fang, and D. Reneker, "DNA fibers by electrospinning," *Journal of macromolecular science. Physics*, vol. 36(2), pp. 169–173, 1997.
3. D. H. Reneker, *et al*., "Bending instability of electrically charged liquid jets of polymer solutions in electrospinning," *Journal of Applied Physics*, vol. 87, p. 4531, 2000.
4. J. J. Feng, "The stretching of an electrified non-Newtonian jet: a model for electrospinning," *Physics of Fluids*, vol. 14, p. 3912, 2002.
5. G. Taylor, "Disintegration of water drops in an electric field," *Proceedings of the Royal Society of London. Series A. Mathematical and Physical Sciences*, vol. 280(1382), pp. 383–397, 1964.
6. G. Taylor, "Electrically driven jets," *Proceedings of the Royal Society of London. Series A. Mathematical and Physical Sciences*, vol. 313(1515), pp. 453–475, 1969.
7. C. Hendricks, *et al*., "Photomicrography of electrically sprayed heavy particles," *AIAA J*, vol. 2(4), pp. 733–737, 1964.
8. I. Hayati, A. I. Bailey, and T. F. Tadros, "Investigation into the mechanisms of electrohydrodynamic spraying of liquids," *Journal of Colloid and Interface Science*, vol. 117(1), p. 205, 1987.
9. I. Hayati, A. I. Bailey, and T. F. Tadros, "Mechanism of stable jet formation in electrohydrodynamic atomization," *Nature*, vol. 319(6048), pp. 41–43, 1986.
10. Lord Rayleigh, *Philosophical Magazne and Journal*, vol. 44, p. 184, 1882.
11. Lord Rayleigh, *Further Observations Upon Liquid Jets*, 1882.

12. J. Zeleny, "Instability of electrified liquid surfaces," *Physical Review*, vol. 10 (Copyright (C) 2010 The American Physical Society), p. 1, 1917.
13. P. Baumgarten, "Electrostatic spinning of acrylic microfibers," *Journal of Colloid and Interface Science*, vol. 36(1), 1971.
14. S. V. Fridrikh, *et al*., "Controlling the fiber diameter during electrospinning," *Physical Review Letters*, vol. 90 (Copyright (C) 2010 The American Physical Society), p. 144 502, 2003.
15. A. F. Spivak, and Y. A. Dzenis, "Asymptotic decay of radius of a weakly conductive viscous jet in an external electric field," *Applied Physics Letters*, vol. 73(21), pp. 3067–3069, 1998.
16. G. Rutledge, *et al*., "Electrostatic spinning and properties of ultrafine fibers," *National Textile Center Research Briefs-Materials Competency*, 2003.
17. A. M. Gañán-Calvo, "On the theory of electrohydrodynamically driven capillary jets," *Journal of Fluid Mechanics*, vol. 335, pp. 165–188, 1997.
18. A. M. Gañán-Calvo, "Generation of steady liquid microthreads and micron-sized monodisperse sprays in gas streams," *Physical Review Letters*, vol. 80 (Copyright (C) 2010 The American Physical Society), p. 285, 1998.
19. A. M. Gañán-Calvo, Cone-jet analytical extension of Taylor's electrostatic solution and the asymptotic universal scaling laws in electrospraying, *Physical Review Letters*, vol. 79 (Copyright (C) 2010 The American Physical Society), p. 217, 1997.
20. J. J. Feng, "Stretching of a straight electrically charged viscoelastic jet," *Journal of Non-Newtonian Fluid Mechanics*, vol. 116(1), pp. 55–70, 2003.
21. Y. Q. Wan, Q. Guo, and N. Pan, "Thermo-electro-hydrodynamic model for electrospinning process," *International Journal of Nonlinear Sciences and Numerical Simulation*, vol. 5(1), pp. 5–8, 2004.
22. Y. M. Shin, *et al*., "Experimental characterization of electrospinning: the electrically forced jet and instabilities," *Polymer*, vol. 42(25), pp. 09955–09967, 2001.
23. J. H. He, Y. Q. Wan, and J. Y. Yu, "Allometric scaling and instability in electrospinning," *International Journal of Nonlinear Sciences and Numerical Simulation*, vol. 5, pp. 243–252, 2004.
24. A. F. Spivak, Y. A. Dzenis, and D. H. Reneker, "A model of steady state jet in the electrospinning process," *Mechanics Research Communications*, vol. 27(1), pp. 37–42, 2000.
25. M. M. Hohman, *et al*., "Electrospinning and electrically forced jets. I. Stability theory," *Physics of Fluids*, vol. 13(8), pp. 2201–2220, 2001.
26. J. H. He, and Y. Q. Wan, "Allometric scaling for voltage and current in electrospinning," *Polymer*, vol. 45(19), pp. 6731–6734, 2004.
27. J. H. He, Y. Q. Wan, and J. Y. Yu, "Application of vibration technology to polymer electrospinning," *International Journal of Nonlinear Sciences and Numerical Simulation*, vol. 5, pp. 253–262, 2004.
28. J. H. He, Y. Q. Wan, and J. Y. Yu, "Scaling law in electrospinning: relationship between electric current and solution flow rate," *Polymer*, vol. 46(8), pp. 2799–2801, 2005.
29. D. H. Reneker, *et al*., "Bending instability of electrically charged liquid jets of polymer solutions in electrospinning," *Journal of Applied Physics*, vol. 87(9), pp. 4531–4547, 2000.

5 Mechanical properties of fibers and fiber assemblies

Polymer, metallic and ceramic materials in fibrous form are of fundamental importance in materials engineering. Fibrous materials are the basic building blocks for the backbone of most natural and man-made engineering structures, ranging from the skeletal structure of animals to advanced fiber-reinforced composites.

To fulfill themselves as textile materials, fibers and fiber assemblies possess some unique properties. They are combinations of strength and toughness, they are flexible, soft, porous (permeable to air, vapor and light, etc.), lightweight and mostly textured. As an essential requirement to fiber and fiber assemblies, mechanical properties are undoubtedly the most important properties that need to be characterized and investigated. In this chapter, we will look at the mechanical properties of fiber assemblies from single fiber to fiber fabrics.

5.1 Structure of hierarchy of textile materials

Traditionally fibers are defined as soft materials with a length-to-diameter ratio above 10^3 and a diameter ranging from several to 100 microns. The emergence of nanofibers broadens the span of fibers to the nanoscale world.

For engineering applications, fibers are usually employed in different forms such as yarns/ropes, woven textiles and nowoven textiles. The structure hierarchy of textile materials is shown in Fig. 5.1.

5.2 Size effect on mechanical properties

Similar to the Hall–Petch relationship, fiber diameter plays a very important role in nanofiber strength and surface energy [2], as shown in Fig. 5.2:

$$\tau = \tau_0 + \frac{\kappa_\tau}{d^\alpha}, \text{when } d < 100\,\text{nm}, \tag{5.1}$$

$$E = E_0 + \frac{\kappa_E}{d^\beta}, \tag{5.2}$$

where κ_τ and κ_E are the fitting parameters (material constants), τ_0 and E_0 are the strength and surface energy of the bulk material, respectively; d is the fiber diameter and $0 < d < 100$ nm; and $\alpha > 0$ and $\beta > 0$ are scaling exponents.

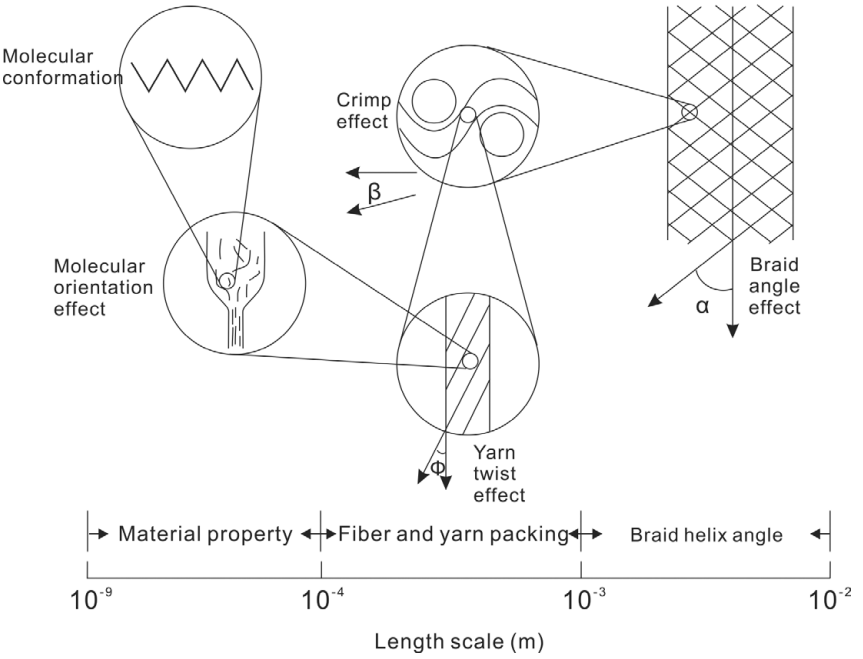

Fig. 5.1 Structure hierarchy of textile materials [1].

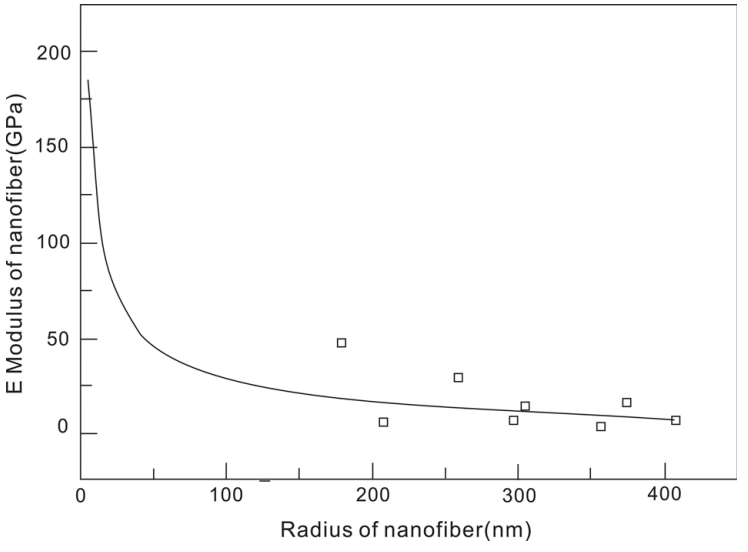

Fig. 5.2 The relation between the radius and modulus of nanofiber [2].

5.3 Theoretical modulus of a fiber

Assuming that the total deformation is due to intramolecular dilation, the calculation of the tensile modulus along the *c*-axis of the crystal will reduce to the calculation of the effective force constant of a single molecule along its axis. The required information for

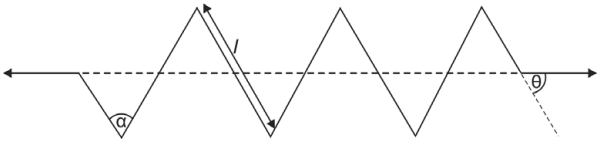

Fig. 5.3 Model for the calculation of the tensile modulus of a polymer chain (modified from Ref. [3]).

this calculation comprises of the unit cell dimensions, bond lengths and angles and the force constants for bond-length and bond-angle deformation.

Take polyethylene, for example, according to the procedure of Trealore [3]. Let the bond lengths be l and the angle between successive bonds α, as shown in Fig. 5.3. Forces F are applied at the two ends of n segments along the axis of the molecules. Let the bonds make an angle θ with the direction of F. If the total length of the molecule is $L = nl \cos \theta$, where n is the number of carbon atoms, then the total deformation ΔL under a force F is

$$\Delta L = n(\cos \theta \Delta L - l \sin \Delta\theta). \tag{5.3}$$

The deformation of each bond, ΔL, is produced by the force $F \cos \theta$ and is given by

$$\Delta l = \frac{F}{k_l} \cos \theta, \tag{5.4}$$

where k_l is the force constant governing the separation of two carbon atoms. The deformation $\Delta\theta = -\Delta\alpha/2$, is produced by a torque of $\frac{1}{2} Fl \sin \theta$ acting around each of the bond angles and is given by

$$\Delta\theta = -\frac{1}{4} \frac{Fl}{k_\alpha} \sin \theta, \tag{5.5}$$

where k_α is the valence-angle deformation constant. The tensile modulus is defined

$$E = \frac{F/A}{\Delta L/L}. \tag{5.6}$$

From Eqs. (5.3),(5.4) and (5.5),

$$\frac{\Delta L}{F} = n\left[\frac{\cos^2 \theta}{k_l} + \frac{l^2 \sin^2 \theta}{4k_\alpha}\right]. \tag{5.7}$$

The equation is simplified if the valence-angle force constant k_α is replaced by another force constant k_p. When the valence angle opens by $\Delta\alpha$, one of the carbon atoms moves a distance $l\Delta\alpha$ with respect to the other. The energy involved in the distortion, $\Delta\omega$, may be written in terms of $l\Delta\alpha$,

$$\Delta w = \frac{1}{2} k_\alpha (\Delta\alpha)^2 = \frac{1}{2} k_p (l\Delta\alpha)^2. \tag{5.8}$$

Substituting k_p in Eq. (5.7),

$$\frac{\Delta L}{F} = n\left[\frac{\cos^2\theta}{k_l} + \frac{\sin^2\theta}{4k_p}\right]. \tag{5.9}$$

Therefore, the modulus is given by

$$E = \frac{l\cos\theta}{A}\left[\frac{\cos^2\theta}{k_l} + \frac{\sin^2\theta}{4k_p}\right]^{-1}. \tag{5.10}$$

The cross-sectional area of each chain $A = 18.25$ Å^2. The C–C bond length $l = 1.53$Å and valence angle $\alpha = 112°$. For values of $k_l = 4.36 \times 10^2$ N/m and $k_p = 0.35 \times 10^2$ N/m, we have $E = 182$ GPa.

Using force constants determined from low-frequency Raman shifts of normal hydrocarbons, Shimanouchi, Asahina and Enomoto obtain the theoretical value, $E = 340$ GPa.

5.4 Mechanical properties of nonwovens

Nonwoven is a word that described a fibrous structure fabricated directly from fiber to fabric. The fibers are held together mechanically or chemically in a nonwoven, resulting in a mechanically stable, self-supporting, flexible, web-like structure. According to the bonding method, nonwovens can be classified as chemically bonded, mechanically bonded, spun bonded and stitch bonded. Meltblown nonwovens are a type of spun-bonded nonwoven. They are produced by extruding melted polymer materials through a spin net or die to form long thin fibers which are stretched and cooled by passing hot air as they fall from the die.The fibers fall onto a conveyor belt and bond into a web that is collected into rolls and subsequently converted to finished products. From a process point of view, electrospinning is a similar technique to meltblown, and from the standpoint of structure, electrospun nanofiber webs are the same as spun-bonded nonwovens. Therefore understanding of the analytical methods of mechanical properties of nonwovens will be a great help for analysis of the mechanical properties of electrospun nanofiber products.

5.4.1 Geometry of nonwovens

The geometry of nonwovens can be analyzed by investigating a unit circle (a circle of unit diameter).

Let $N(\theta)$ be the number of continuous fibers through the entire thickness of the fabric that lie within $\pm(\Delta\theta/2)$ of any prescribed angle θ per unit width perpendicular to the direction of the fibers. The sum total of $N(\theta)$ over all angles is:

$$N_f = \sum N(\theta), \tag{5.11}$$

where N_f is the total number of fibers in a unit circle drawn on the fabric, as shown in Fig. 5.4a. With a dimension of length^{-1}, N_f is obtained by redistributing all the fibers in

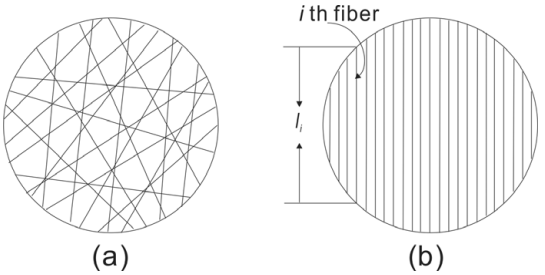

Fig. 5.4 (a) N_f fibers through the thickness of the fabric in a unit circle. (b) The N_f fibers being redistributed in the circle to be parallel to each other in a two-dimensional (2-D) plane.

the unit circle such that they lie parallel to their real direction in the fabric plane, shown in Fig. 5.4b. Every fiber maintains its original length in the circle. The number of these fibers per unit width perpendicular to the fibers equals exactly N_f in a statistical sense. These fibers can be taken spaced a distance $1/N_f$ apart. If the ith fiber of the set of N_f fibers has a length l_i, then area A_i allocated to the ith fiber is approximately

$$A_i \cong l_i \left[\frac{1}{N_f}\right]. \tag{5.12}$$

The summation of A_i over all the N fibers gives approximately the total area A_u of the unit circle, i.e.

$$A_u = \sum_{i=1}^{N_f} A_i \cong \frac{1}{N_f} \sum_{i=1}^{N_f} l_i. \tag{5.13}$$

From this, N_f is found to be

$$N_f \cong \frac{\sum_{i=1}^{N_f} l_i}{A_f}. \tag{5.14}$$

Since $\sum_{i=1}^{N_f} l_i$ represents the total length of the fibers in A_u, N_f, in fact, represents the total fiber length per unit area.

The fiber-orientation distribution function $\phi(\theta)$, i.e. the fraction of total fibers that lie in the direction of θ, is defined as [4]:

$$\phi(\theta) = \frac{N(\theta)}{\Delta\theta N_f}. \tag{5.15}$$

As $\Delta\theta$ approaches zero, $\phi(\theta)$ becomes:

$$\phi(\theta) = \frac{1}{N_f} \frac{dN}{d\theta}. \tag{5.16}$$

It is, therefore, concluded that

$$\frac{dN}{d\theta} = N_f \phi(\theta). \tag{5.17}$$

N_f can also be expressed as

$$N_f = \frac{W\frac{\pi}{4}b^2}{\lambda L_f}, \tag{5.18}$$

where W is fabric weight, b is cell width, λ is fiber diameter and

$$\lambda = \frac{\pi}{4}b. \tag{5.19}$$

The fiber distribution function will be

$$\frac{N}{N_f}(\theta) = \sum\nolimits_{i=1}^{N} A_i \cos^i(\theta). \tag{5.20}$$

5.4.2 Deformation of nonwovens

In the case that the nonwoven is under uniaxial loading, the stress and strain can be analyzed based on the assumption that there is no lateral contraction during the deformation.

Assuming the fibers have discrete orientation, as shown in Fig. 5.5, the axial strain, fiber starin and elementral tranverse strain will, respectively, be:
axial strain

$$\varepsilon_F = \frac{\delta y_i}{y_i}, \tag{5.21}$$

fiber strain

$$\varepsilon_f = \frac{\delta_{ij}}{l_i}, \tag{5.22}$$

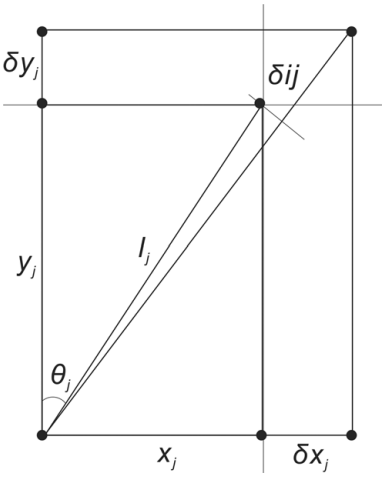

Fig. 5.5 Strain of fiber.

elemental transverse strain

$$\varepsilon_T = \frac{\delta x_i}{x_i} = 0, \tag{5.23}$$

and the strain along the fiber axis [5] is

$$\varepsilon_f = \varepsilon_F \cos^2\theta. \tag{5.24}$$

Then the corresponding stress on the nonwovern along the fiber axis will be [5]

$$\sigma_F = \int_{-\pi/2}^{\pi/2} E_f \varepsilon_f \cos^2(\theta)\, d\theta = \int_{-\pi/2}^{\pi/2} E_f \varepsilon_F \cos^4(\theta)\phi(\theta)\, d\theta. \tag{5.25}$$

The subscripts, f and F, respectively, denote fiber and fabric.

For uniform fiber orientation distribution, we have

$$\phi(\theta) = \frac{1}{\pi}. \tag{5.26}$$

Substitute Eq. (5.26) into Eq. (5.25) to obtain

$$\sigma_F = \frac{3}{8} E_f \varepsilon_F, \tag{5.27}$$

which implies

$$\frac{E_F}{E_f} = \frac{3}{8}. \tag{5.28}$$

According to Eq. (5.20), the total fabric load will be

$$F = \frac{3}{8} N_f A_f E_f \varepsilon_f. \tag{5.29}$$

5.5 Mechanical properties of yarns

A yarn is a linear fibrous assembly consisting of textile fiber of discrete length (staple yarn or spun yarn) or continuous filaments (continuous filment yarn). Yarns are the building blocks for the formation of knitted, woven or braided textile structures. Accordingly, the conversion of nanofibers into yarn will create a pathway to the formation of higher-order two-dimensional (2-D) and three-dimensional (3-D) textile structures. Yarns can be produced by various yarn formation systems including spun yarn, twisted filament yarn and textured yarns [6]. The fiber material properties and the resulting yarn geometry (twist, denier, etc.) determine the performance properties of a yarn and, consequently, dictate the processing methods and applications for which a yarn is suited. As shown in Fig. 5.6, the mechanical properties of the various types of yarns differ, which can be attributed to the variation in yarn structural features.

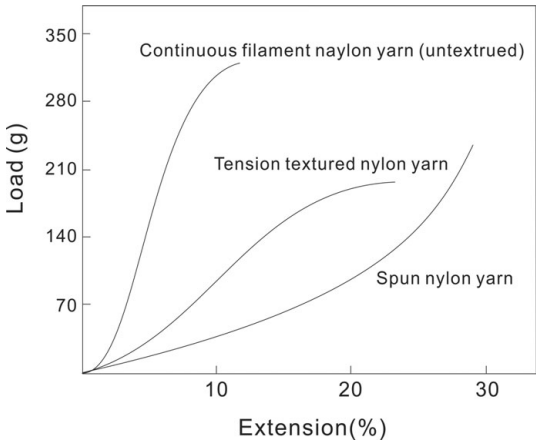

Fig. 5.6 Stress–strain curves of some synthetic filament yarns [7].

5.5.1 Yarn geometry

The geometric parameters that describe a linear fiber assembly include the shape of the bundle cross-section, the number of fibers in the cross-section, the bundle twist level, the degree of fiber migration in the radial direction and the fraction of interfiber packing. Usually, the fiber bundles are assumed to be circular in cross-section but, in reality, the fibers or filaments can be packed in various shapes. Most engineering fibers, such as glass and carbon, have a circular or near-circular cross-section with a constant diameter. In the case of yarns produced from electrospun fibers or from carbon nanofiber and nanotubes, the fiber packing geometry in the yarn is more complex due to the ultrafine nature of the fibers and the high level of cohesion between fibers due to friction and secondary force effect. In a nanofiber yarn, the constituent fiber itself is often an assembly of fibrils. Keeping this in mind, as a first approximation, we assume classical yarn mechnics applied in the analysis of yarns consisting of nanofibers.

The geometry of interfiber packing in fiber bundles has been studied by a number of researchers. Three basic idealized forms of circular fiber packing were identified: open packing, in which the fibers are arranged in concentric layers (Fig. 5.7a); square packing, in which the fibers are enclosed by a square (Fig. 5.7b); and close packing, in which the fibers are arranged in a hexagonal pattern, as in the case of carbon nanotube fibers (Fig. 5.7c).

In open-packed bundles the fiber volume fraction, defined as fiber-to-bundle area ratio, has been computed as a function of the number of fibers. If the outer ring is completely filled and the fibers are circular, the fiber volume fraction will be [9]

$$V_{f\ open} = 1 - \frac{3N_r(N_r - 1) + 1}{\left(2N_f - 1\right)^2}, \tag{5.30}$$

where N_r is the number of rings and its relationship to the number of fibers N_f is given by

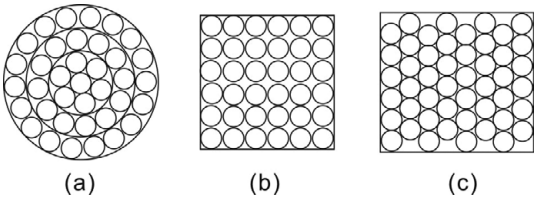

Fig. 5.7 Idealized fiber packings: (a) open packing; (b) square packing; (c) close packing [8].

$$N_r = \frac{1}{2} + \left[\frac{1}{4} + \frac{1}{3}\left(2N_f - 1\right)\right]^{1/2}. \tag{5.31}$$

For large numbers of fibers the fiber volume fraction approaches 0.75.

In squared-packed bundles, the fibers are arranged in a square. For any number of circular fibers, if the outer layer is completely filled, the fiber volume fraction can be shown to equal the area ratio of a circle to an enclosing square [8]:

$$V_{fsquare} = \frac{\pi}{4} = 0.785. \tag{5.32}$$

Similar to square packing, the fiber volume fraction of a close-packed bundle is equal to the area ratio of a circle to an enclosing hexagon [8]:

$$V_{fsquare} = \frac{\pi}{2\sqrt{3}} = 0.907. \tag{5.33}$$

The level of bundle fiber volume fraction predicted by the above models applies equally to other shapes if the number of fibers is sufficiently large.

Twists are inserted into fiber bundles (yarns) to maintain the integrity of the yarn structure, improve the tensile strength of spun yarn and resist lateral stresses in continuous filament yarns. Staple yarns usually require more twist than filament yarns. For twisted fiber bundles, the fibers are no longer aligned along the bundle axis. Instead, the fibers are oriented in a helical configuration within the bundle, as shown in Fig. 5.8. The assumptions underlying this geometric model are characterized by the following postulates: (1) the yarn is circular in cross-section and is uniform in the yarn structure; (2) the axis of the circular cylinders coincides with the yarn axis; and (3) the fibers fall into a rotationally symmetrical array in the cross-sectional view (all yarns the fibers in each layer assume the same distance from central axis of the yarn).

Define *twist* (T, tpi or tpm) the number of twist within a unit length, then we have:

$$h = \frac{1}{T}, \tag{5.34}$$

$$l^2 = h^2 + (2\pi r)^2, \tag{5.35}$$

$$L^2 = h^2 + (2\pi R)^2, \tag{5.36}$$

$$\tan\phi = \frac{2\pi r}{h} = 2\pi r T, \tag{5.37}$$

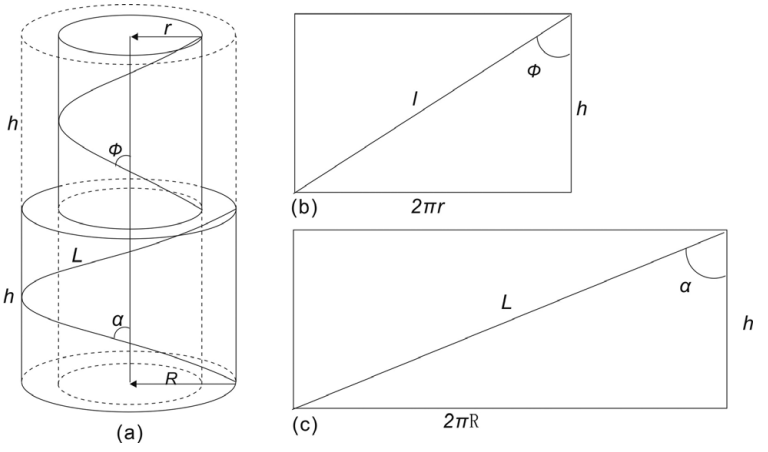

Fig. 5.8 (a) Idealized yarn geometry; (b) "opened out" diagram of cylinder at radius r; and (c) "opened out" at yarn surface [10].

$$\tan\alpha = \frac{2\pi R}{h} = 2\pi RT. \tag{5.38}$$

According to Hearle *et al*. [10], yarn diameter is related to the number of filaments (n) in the yarn and the packing fraction of the fibers (κ) in the following relationship:

$$D = \left(\frac{\kappa}{nd^2}\right)^{1/2}, \tag{5.39}$$

where D is the diameter of the yarn, and d is the diameter of the fiber.

The fiber volume fraction of a yarn is actually equal to its fiber packing fraction, i.e. $V_f = \kappa$. Combining Eqs. (5.38) and (5.39), we have [8]

$$V_f = n\left(d + \frac{\tan\alpha}{\pi dT}\right)^{-2}. \tag{5.40}$$

Clearly, for a given twist level inserted into the fiber bundle, as fiber orientation angle increases, yarn diameter increases whereas the fiber volume fraction decreases, as can be seen in Fig. 5.9, which is useful in determining the twist level of fiber bundles. For example, to obtain a fiber volume fraction (or fiber packing fraction) 0.8 and a fiber orientation angle l0°, a twist level of 3 tpi should be used for the 12k, 7 μm fiber diameter carbon yarns [8, 11].

5.5.2 Mechanical properties of linear fiber assemblies

5.5.2.1 Stress analysis

The application of an external tensile load, P, along the axis of a yarn results in forces being applied to the various fibers. In general, the only stresses that can possibly act on the cross-section of a fiber are illustrated in Fig. 5.10. They are: (1) a tensile force, p_r, in the direction along the fiber axis and normal to the fiber

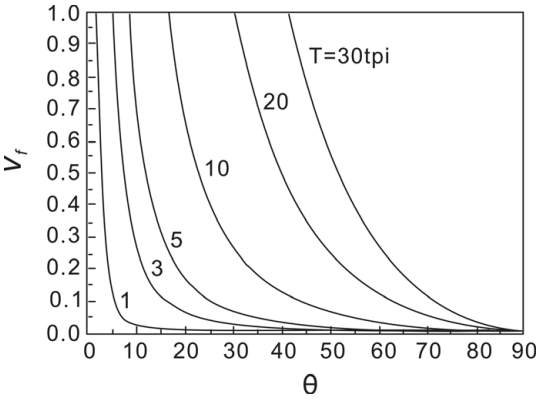

Fig. 5.9 Relationship of fiber volume fraction to fiber orientation at various twist levels [8].

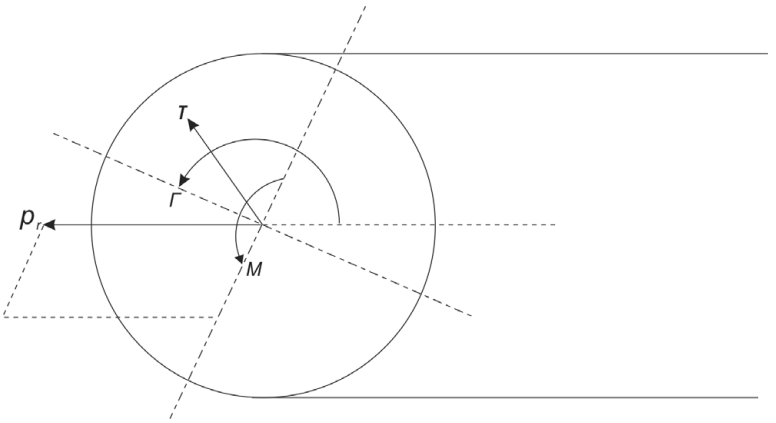

Fig. 5.10 General stresses in fibers.

cross-section; (2) a shear force, τ, acting tangential to the fiber cross section; (3) a bending moment, M; and (4) a torsional moment, Γ [12].

Assuming the fibers are perfectly flexible and incapable of resisting any axial compressive forces, in addition to the extremely large ratio of fiber length to fiber diameter, the stresses M, τ, and Γ vanish and the only force acting is a direct tension, p_r. Then the contribution of p_r to the total load P acting on the yarn in tension is $p_r \cos \phi_r$ per fiber, therefore [12]

$$P = \sum_{n=1}^{N_f} p_r \cos \phi_r. \tag{5.41}$$

In reality each filament in the yarn would assume a different orientation. To simplify the analysis, the continuum approach is used by assuming the yarn consists of rotationally symmetric rings of fibers and the fibers in the yarn are consolidated into an equivalent solid continuous medium rather than a group of discretely individual fibers. Thus the yarn is treated with the use of differential elements of area as opposed to individual fibers. Then the force dp_r is written as

$$dp_r = \sigma_r dN_f A_f, \tag{5.42}$$

where σ_r is stress intensity at the radial position, dN_f is the number of fibers in an element of area A, and A_f is the cross-sectional area of fiber.

So, dA is written as

$$dA = 2\pi r dr \tag{5.43}$$

and dN_f can be written as

$$dN_f = \left[\frac{N_f}{\pi R^2}\right] 2\pi r dr \cos\phi_r. \tag{5.44}$$

Substitute Eq. (5.44) into Eq. (5.42),

$$dp_r = \sigma_r \left[\frac{N_f A_f}{\pi R^2}\right] 2\pi r \cos\phi_r dr. \tag{5.45}$$

Since the packing factor of the yarn is $V_f = N_f A_f / \pi R^2$,

$$dp_y = \sigma_r V_f 2\pi r \cos\phi_r dr. \tag{5.46}$$

Tension in the yarn direction $dp_y = dp_r \cos\phi_r$ will be

$$dp_y = 2\pi V_f \sigma_r r \cos^2\phi_r dr. \tag{5.47}$$

And the total load on the yarn is therefore

$$p_y = 2\pi V_f \int_0^R \sigma_r r \cos^2\phi_r dr. \tag{5.48}$$

From the identity $\cos^2\phi = 1/(1 + \tan^2\phi)$ and Eq. (5.37), it is apparent that

$$\cos^2\phi_r = \frac{1}{1 + 4\pi^2 r^2 T^2}. \tag{5.49}$$

Thus

$$p_y = 2\pi V_f \int_0^R \frac{\sigma_r r}{1 + 4\pi^2 r^2 T^2} dr. \tag{5.50}$$

5.5.2.2 Strain analysis

Considering the change in fiber angle is very small, i.e. $\phi \approx \phi'$, as shown in Fig. 5.11, then [5]

$$l = \frac{L}{\cos\phi} \tag{5.51}$$

and

$$\Delta l = \Delta L \cos\phi. \tag{5.52}$$

Since $\varepsilon_y = \Delta L / l$,

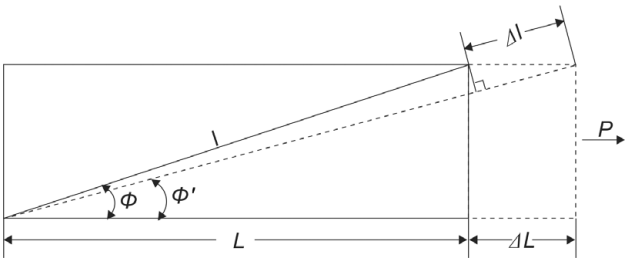

Fig. 5.11 Deformation in twisted yarns.

$$\varepsilon_f = \frac{\Delta l}{l} = \frac{\Delta L \cos\phi}{L/\cos\phi} = \varepsilon_y \cos^2\phi, \tag{5.53}$$

substitute into Eq. (5.49) to give

$$\varepsilon_f = \frac{\varepsilon_y}{1 + 4\pi^2 R^2 T^2}. \tag{5.54}$$

Assume fibers and yarns are Hookean material, then

$$\sigma_f = E_f \varepsilon_f, \tag{5.55}$$

which can be written as

$$\sigma_f = E_f \varepsilon_y \cos^2\phi. \tag{5.56}$$

Substitute Eq. (5.56) into Eq. (5.48),

$$\begin{aligned} p_y &= 2\pi V_f \int_0^R E_f \varepsilon_f \cos^4\phi dr \\ &= \left(\pi V_f R^2\right) E_f \varepsilon_f \cos^2\phi. \end{aligned} \tag{5.57}$$

It can be also shown that

$$E_y = E_f \cos^2\phi. \tag{5.58}$$

5.5.3 Mechanical properties of staple yarns

In many nanofiber structures such as carbon nanotubes and carbon nanofibers, the fibers are not continuous. The discrete fibers in the assembly are held together by secondary forces and or frictional cohesions. Using classical staple yarn mechanics one may think that cohesive forces between the fibers/fibrils would include secondary forces between fibers.

Taking a single fiber in the yarn as our object of analysis, and assuming the compressive stress applied to the this fiber is uniform due to twist effect, and the frictions between fibers obey Amontons' laws, the distribution of tensile stress on the fiber is as shown in Fig. 5.12.

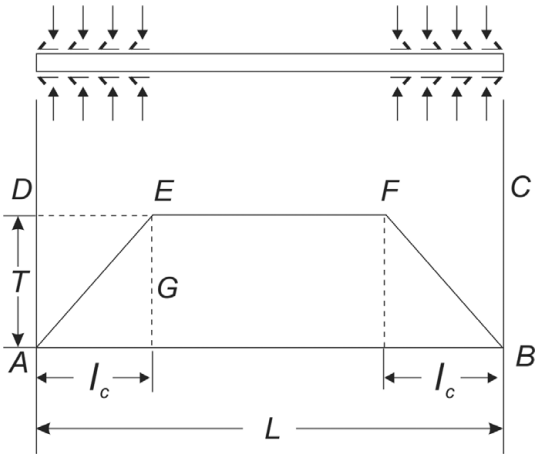

Fig. 5.12 Distribution of tensile stress on the fiber.

We define the slippage factor, S, as the fractional reduction in fiber contribution to the longitudinal tension T, then express S in terms of energy, and we then have

$$S = \frac{ABCD - AED - BFC}{ABCD} = 1 - \frac{AGED}{ABCD}. \tag{5.59}$$

Here

$$\begin{aligned} ABCD &= L \cdot T \\ AGED &= l_c \cdot T, \end{aligned} \tag{5.60}$$

where L is the fiber length, and l_c is the slippage length, which is defined as the critical length of the fiber on which the total surface friction equals the breaking strength of this fiber.

Therefore

$$S = 1 - \frac{l_c}{L}. \tag{5.61}$$

At E and F, the force resisting slippage should be equal to the constant fiber tension resulting from the strain in the structure. That is

$$F = T = 2\pi r l_c G, \tag{5.62}$$

where F is force-resisting slippage, r is fiber radius, and G is the force per unit surface area resisting slippage.

Since

$$T = \pi r^2 \sigma_f \tag{5.63}$$

we have

$$l_c = \frac{r\sigma_f}{2G}. \tag{5.64}$$

The slippage depends on the frictional resistance, thus

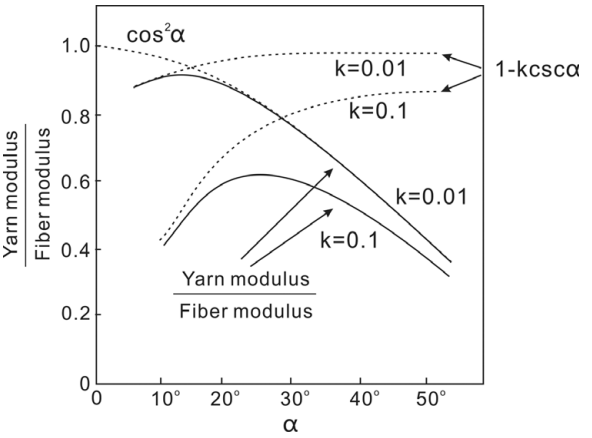

Fig. 5.13 Numerical plot of equations derived in Ref. [10].

$$G = \mu N, \tag{5.65}$$

where N is the normal stress acting on the fiber surface.

The slippage factor can be rewritten as

$$S = 1 - \frac{r\sigma_f}{2L\mu N}. \tag{5.66}$$

Considering the slippage of fibers in yarn, Hearle *et al*. [10] obtained the following relationships:

$$\begin{aligned} \frac{\sigma_y}{\sigma_f} &= A\cos^2\phi(1 - k\,\mathrm{cosec}\,\phi) \\ &= A\cos^2\alpha(1 - k\,\mathrm{cosec}\,\alpha) \end{aligned} \tag{5.67}$$

and

$$\frac{E_y}{E_f} = \cos^4\alpha(1 - k\,\mathrm{cosec}\,\alpha), \tag{5.68}$$

where $k = \left(\sqrt{2}/3L_f\right)(rQ/\mu)^{1/2}$, Q is the migration factor, and μ is the fiber coefficient of friction which increases as slippage increases and decreases when slippage decreases. Q is an experimentally determined factor.

Figure 5.13 shows a numerical plot with $k = 0.01$ and 0.1. The separate effects of obliquity ($\cos^2\alpha$) and slip ($1 - k\,\mathrm{cosec}\,\alpha$) are clearly indicated.

Using a different approach, Platt *et al*. obtained:

$$P_y = N_f A_f \sigma_f \left(1 - \frac{r}{2\mu GL}\right), \tag{5.69}$$

where r is the fiber radius, μ is the fiber friction, G is shear resistance and L is the fiber length.

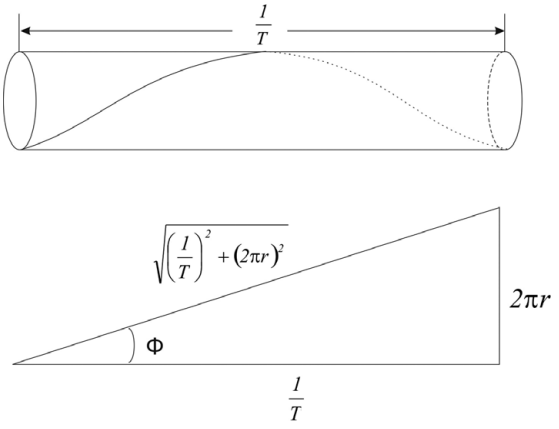

Fig. 5.14 Geometry of the twist effect.

This relation involves the concept of critical length. The fiber must be long enough to be locked into the structure, otherwise deformation could occur only due to slippage.

As shown in Fig. 5.14, for a staple fiber, the twist angle is related to its twist and radius:

$$\cos^2\phi = \left(\frac{\frac{1}{T}}{\sqrt{\left(\frac{1}{T}\right)^2 + (2\pi r)^2}}\right)^2 = \frac{1}{1 + 4\pi^2 r^2 T^2}. \tag{5.70}$$

According to Eq. (5.58), the translational efficiency for spun yarns can be estimated by the following relationship:

$$\frac{\sigma_y}{\sigma_f} = \cos^2\theta\left(\frac{TM}{5}\right), \tag{5.71}$$

where *TM* is the twist multiplier.

Figure 5.15 shows the translation efficiency of a continuous filament and staple yarn.

5.6 Mechanical properties of woven fabrics

The performance characteristics of a fabric are functions of the fiber materials' properties, the yarn geometry and the geometry of the fabric. The finishing (chemical and mechanical modification) that the fabric receives is equally important for the appearance and the functional properties of a fabric. Before one can make effective use of the combination of materials, geometry and finishing technique to design a fabric that has the desirable properties (engineering of a fabric), we need to be acquainted with the materials, the geometry and the finishing techniques. In this section, the geometry and mechanical properties of fabrics is introduced.

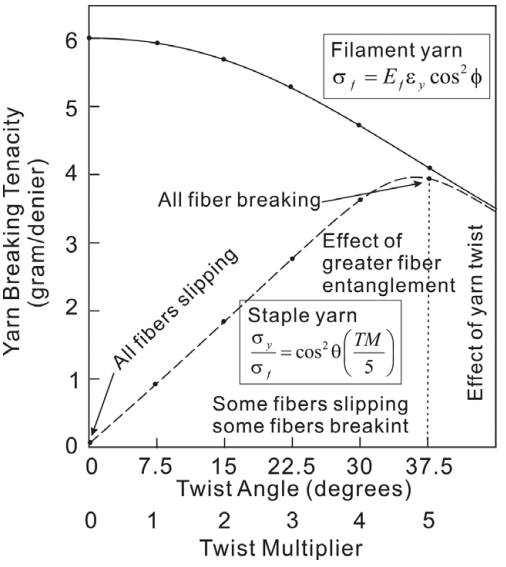

Fig. 5.15 Effect of twist on the breaking tenacity of filament yarn and staple yarn.

5.6.1 Woven fabric geometry

Figure 5.16 gives the unit cell geometry for plain biaxial weave, as proposed by Dow and Ramnath [13]. In their analysis, Dow and Ramnath assumed circular yarn cross-section, the same yarn diameter and pitch length for both fill and warp yarns. The expression of the fiber volume fraction was derived as

$$V_f = \left(\frac{\pi}{4}\right)\kappa \frac{2\frac{l}{d} + 4\theta}{\left(\frac{L}{d}\right)^2 \left(\frac{T}{d}\right)}, \tag{5.72}$$

where κ is the fiber packing fraction, d is the yarn diameter, L is the pitch length, T is the fabric thickness and l is the dimension, as shown in Fig. 5.16. The yarn inclination angle to the fabric plane, θ, is given by

$$\theta = \tan^{-1} \frac{2}{\sqrt{(L/d)^2 - 3}} - \tan^{-1}(d/L). \tag{5.73}$$

The fabric thickness is very close to two yarn diameter, i.e.

$$T \approx 2d \tag{5.74}$$

and approximately

$$\frac{l}{d} = \frac{1}{\tan\theta}. \tag{5.75}$$

Equation (5.72) is then simplified to

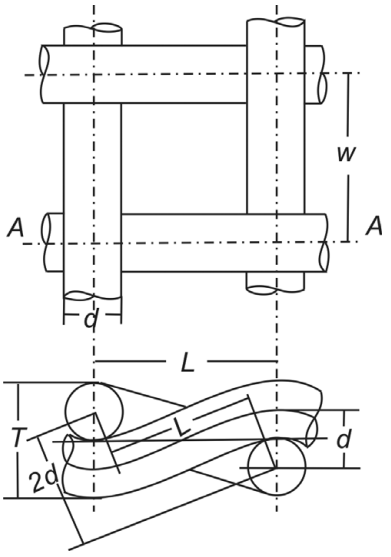

Fig. 5.16 Unit cell geometry of plain weave proposed by Dow and Ramnath [13].

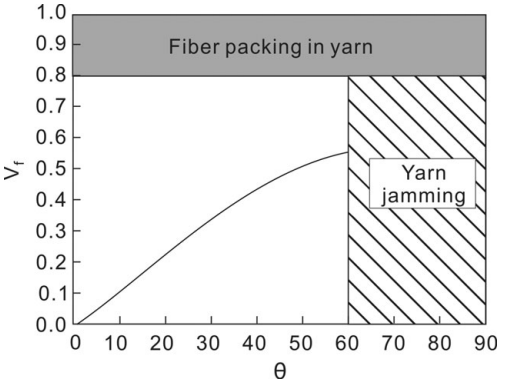

Fig. 5.17 Relationship of fiber volume fraction to fiber orientation for plain weave [8].

$$V_f = \left(\frac{\pi}{4}\right)\kappa \frac{\dfrac{1}{\tan\theta} + 2\theta}{\left(\dfrac{L}{d}\right)^2}. \tag{5.76}$$

Figure 5.17 plots the fiber volume fraction against the yarn inclination angle. It can be seen that as the inclination angle increases, the pitch length becomes longer, which results in a lower fiber volume fraction. The woven fabric has the tightest structure at the inclination angle of 60° (when $L/d = 3$ in Eq. (5.73). In this calculation, the fiber packing fraction κ is assumed to be 0.8. The above analysis is given only for the simplest of woven structures. Different weave patterns, non-circular yarn cross-sectional shape, different yarn dimensions and pitch lengths for fill and warp yarns can be analyzed [8].

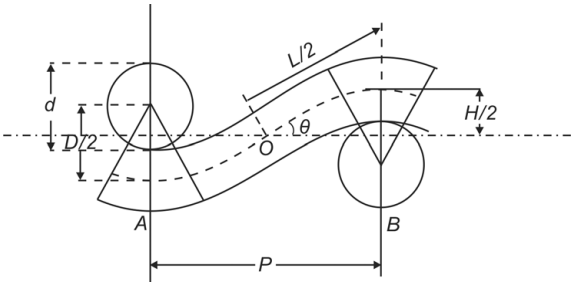

Fig. 5.18 Unit cell geometry of plain weave proposed by Peirce [14, 15].

While the Dow–Ramnath model provides a modern analsyis of woven fabrics from the composite structure point of view, one should recognize the original contribution of Peirce [14, 15] and Haas and Dietzius [16] who pioneered the quantitative analysis of textile fabric structures. Figure 5.18 shows Peirce's model of unit cell of plain weave. According to Peirce, the main parameters relates to unit cell geometry are: crimp, C, which determines the amount of elongation; diameter, D, which determines the relationship between the paths of two sets of yarns; texture, P; and thickness, H, the distance between center of fabric and the center of yarn. These parameters can be expressed as follows.

(1) Crimp (C):

$$C_1 = \frac{L_1 - P_2}{P_2} = \frac{L_1}{P_2} - 1, \tag{5.77}$$

$$C_2 = \frac{L_2}{P_1} - 1. \tag{5.78}$$

(2) Diameter (D):

$$D = H + H_2 = d_1 + d_2. \tag{5.79}$$

(3) Texture (P)

$$\begin{aligned} P_1 &= (L_2 - D\theta_2)\cos\theta_2 + D\sin\theta_2, \\ P_2 &= (L_1 - D\theta_1)\cos\theta_1 + D\sin\theta_1. \end{aligned} \tag{5.80}$$

(4) Thickness (H):

$$\begin{aligned} H_1 &= (L_1 - D\theta_1)\sin\theta_2 + D(1 - \cos\theta_1), \\ H_2 &= (L_2 - D\theta_2)\sin\theta_2 + D(1 - \cos\theta_2). \end{aligned} \tag{5.81}$$

Here, θ is the yarn inclination angle, L is the modular length, and the subscripts 1 and 2 are, respectively, warp and filling.

There are seven equations and 11 unknowns included in these relationships. In order to solve the seven simultaneous nonlinear algebraic equations, at least four parameters need to be determined. The solutions can be obtained by graphical methods (graphical means [14, 17, 18] or nomograph [19]) or by a computer method. The computational flow is shown in Fig. 5.19.

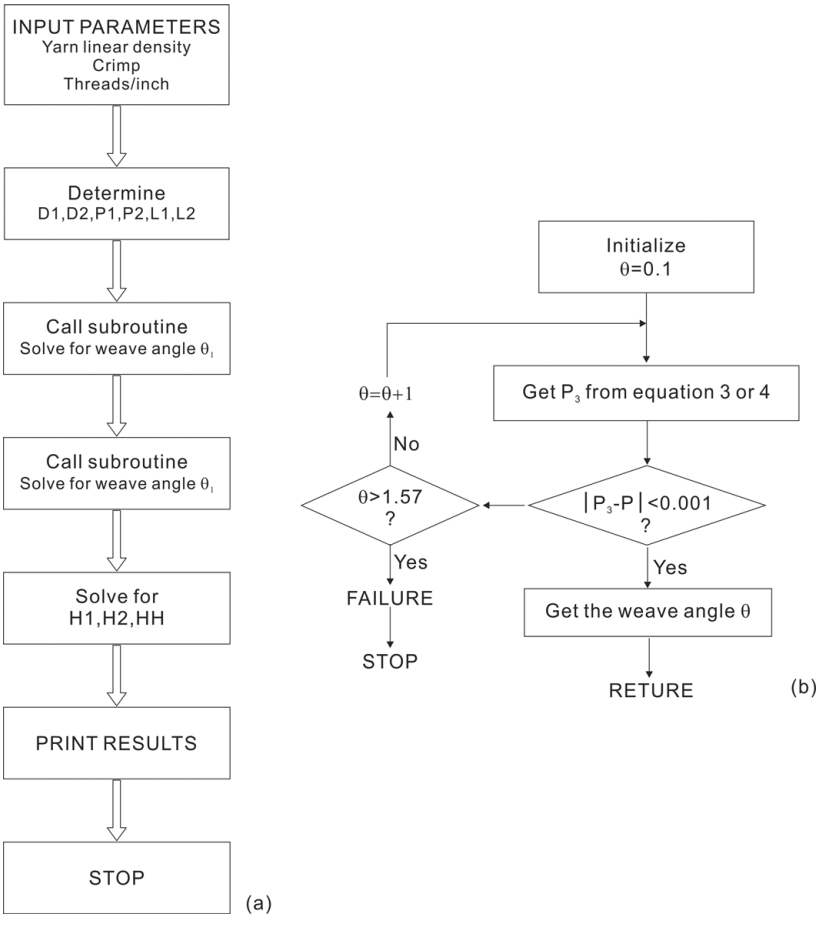

Fig. 5.19 (a) Computational flow for Peirce's equations. (b) Subroutine computational flow.

References

1. F. Ko, and M. Gandhi, "Producing nanofiber structures by electrospinning for tissue engineering," in *Nanofibers and Nanotechnology in Textiles*, P. J. Brown and Kathryn Stevens, Ed. Woodhead Publishing, in association with The Textile Institute, 2007: p. 22.
2. J. H. He, Y. Q. Wan, and L. Xu, "Nano-effects, quantum-like properties in electrospun nanofibers," *Chaos, Solitons and Fractals*, vol. 33(1), pp. 26–37, 2007.
3. L. Treloar, "Calculations of elastic moduli of polymer crystals: I. Polyethylene and nylon 66," *Polymer*, vol. 1, pp. 95–103, 1960.
4. W. D. Freeston, and M. M. Platt, "Mechanics of elastic performance of textile materials: Part XVI: bending rigidity of nonwoven fabrics," *Textile Research Journal*, vol. 35(1), pp. 48–57, 1965.
5. D. W. R. Petterson, "Mechanics of nonwoven fabrics," *Industrial & Engineering Chemistry*, vol. 51(8), pp. 902–903, 1959.

6. B. C. Goswami, J. G. Martindale, and F. Scardino, *Textile Yarns; Technology, Structure, and Applications*. John Wiley and Sons, 1977.
7. Piller, B., *Bulked Yarns: Production, Processing and Applications*. Czechoslovakia: SNTL-Publishers of Technical Literature, in coedition with the Textile Trade Press, 1973.
8. Ko, F. and G. Du, *Textile Preforming Handbook of Composites*, 1998, p. 397.
9. G. -W. Du, T. -W. Chou, and P. Popper, "Analysis of three-dimensional textile preforms for multidirectional reinforcement of composites," *Journal of Materials Science*, vol. 26(13), pp. 3438–3448, 1991.
10. J. Hearle, P. Grosberg, and S. Backer, *Structural Mechanics of Fibers, Yarns, and Fabrics*. New York: Wiley-Interscience, 1969.
11. F. Ko, and G. Du, Processing of textile preforms, in *Advanced Composites Manufacturing*, T. G. Gutowski, Ed. New York. John Wiley & Sons, Inc., 1997.
12. M. M. Platt, "Mechanics of elastic performance of textile materials: III. Some aspects of stress analysis of textile structures – continuous-filament yarns," *Textile Research Journal*, vol. 20(1), pp. 1–15, 1950.
13. N. Dow, and V. Ramnath, *Analysis of woven fabrics for reinforced composite materials (NASA CR-178275)*. National Aeronautics and Space Administration, Hampton (VA 23681–0001), Washington, DC, 1987.
14. F. Peirce, "Geometrical principles applicable to the design of functional fabrics," *Textile Research Journal*, vol. 17(3), p. 123, 1947.
15. F. Peirce, "The geometry of cloth structure," *Journal of the Textile Institute Transactions*, vol. 28(3), pp. 45–96, 1937.
16. R. Haas, and A. Dietzius, *The stretching of the fabric and the deformation of the envelope in nonrigid balloons*. National Advisory Committee for Aeronautics, 1918.
17. L. Love, "Graphical relationships in cloth geometry for plain, twill, and sateen weaves," *Textile Research Journal*, vol. 24(12), p. 1073, 1954.
18. E. V. Paintert, "Mechanics of elastic performance of textile materials: Part VIII: Graphical analysis of fabric geometry," *Textile Research Journal*, vol. 22(3), pp. 153–169, 1952.
19. D. P. Adams, E. R. Schwarz, and S. Backer, "The relationship between the structural geometry of a textile fabric and its physical properties: Part VI: Nomographic solution of the geometric relationships in cloth geometry," *Textile Research Journal*, vol. 26(9), pp. 653–665, 1956.

6 Characterization of nanofibers

Knowing the basic properties of nanofibers (such as morphology, molecular structure and mechanical properties) is crucial for the scientific understanding of nanofibers and for the effective design and use of nanofibrous materials. In order to evaluate and develop the manufacturing process, the composition, structure and physical properties must be characterized to decide whether the produced fibers are suitable for their particular application. Evaluation of the various production parameters in processes such as electrospinning is a critical step towards production of nanofibers commercially. Many common techniques used to characterize conventional engineering materials, as well as some not so common techniques, have been employed in the characterization of nanofibers. Table 6.1 shows the scales of fibers and the corresponding characterizations techniques. To provide an overall understanding, some of the general characterization techniques for structural, chemical, mechanical, thermal and other properties will be introduced in this chapter.

6.1 Structural characterization of nanofibers

The morphological characterization techniques briefly discussed herein are: optical microscopy (OM), scanning electron microscopy (SEM), transmission electron microscopy (TEM), atomic force microscopy (AFM) and scanning tunneling microscopy (STM). These methods characterize the morphology and determine fiber diameter, pore size and porosity, all of which are necessary to evaluate the various production parameters. The techniques for the characterization of order/disorder of molecular structures using X-ray diffraction (XRD) are also covered in this section. Furthermore, mercury porosimetry, a special technique for porosity measurement, is introduced.

6.1.1 Optical microscopy (OM)

An optical microscope, otherwise known as a "light microscope," is a type of microscope that is operated by using visible light and a system of objective lenses to achieve image magnification of small samples. Optical microscopes are the oldest and simplest of microscopes. The resolution of an optical microscope is given by:

Table 6.1 Scale of fibers and according characterization techniques

Fiber		SWCNT MWCNT NF Whisker Fiber Wire
Process		CVD Electrospinning Spinning Drawing Extrusion
Scale		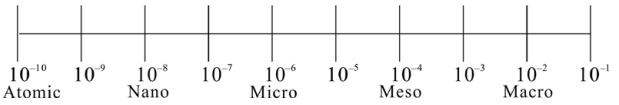
		10^{-10} 10^{-9} 10^{-8} 10^{-7} 10^{-6} 10^{-5} 10^{-4} 10^{-3} 10^{-2} 10^{-1}
		Atomic Nano Micro Meso Macro
Testbeds	Composition	EELS AES XPS EDX Raman FTIR XRD
		Elemental composition Chemical bonds Crystal structure
	Structure	TEM STM AFM SEM Light microscopy
	Phisical	AFM Nanoindentation MEMS Test devices Conventional
	properties	Mechanical, electrical, magnetic, optical

$$R = 0.61\frac{\lambda}{n \cdot \sin\ \alpha} = 0.61\frac{\lambda}{NA}, \tag{6.1}$$

where R is the resolution of the image, λ is the wavelength of white light, n is the refractive index, α is the refracted angle and NA is the numerical aperture. The best possible resolution that can be resolved by an optical microscope is 200 nm. [1]. Figure 6.1 shows an optical microscope.

Generally speaking, geometric properties of nanofibers such as fiber diameter, diameter distribution, fiber orientation and fiber morphology can be characterized with a fairly high degree of accuracy by using an optical microscope. Figure 6.2 shows an optical micrograph of cellulose acetate nanofibers at 100× magnification. The red scale bar has a length of 1 micron.

6.1.2 Scanning electron microscopy (SEM)

Scanning electron microscopy (SEM) is capable of producing high-resolution images of a sample surface. Compared to OM, SEM provides a better understanding of the microstructure of a sample due to higher resolution, greater depth of field, and its sensitivity to surface morphology. In a scanning electron microscope, electrons from a tungsten or lanthanum hexaboride (LaB_6) cathode are thermionically emitted and accelerated towards an anode. Alternatively, the electrons can be emitted via field emission (FE), hence FE-SEM. The main two reasons for using tungsten as the cathode in SEM are that it confers the highest melting point and lowest vapor pressure of all metals. The electron beam typically has an energy ranging from several hundred eV to 100 keV. The beam is focused by one or two condenser lenses into a beam with a very fine focal point, with diameter ranging from 0.4 nm to 5 nm. When the primary electron beam interacts with the sample, electrons lose energy by repeated scattering and absorption within a pear-shaped volume of the sample. This pear-shaped volume is known as the interaction volume, which extends from less than 100 nm to around 5 μm

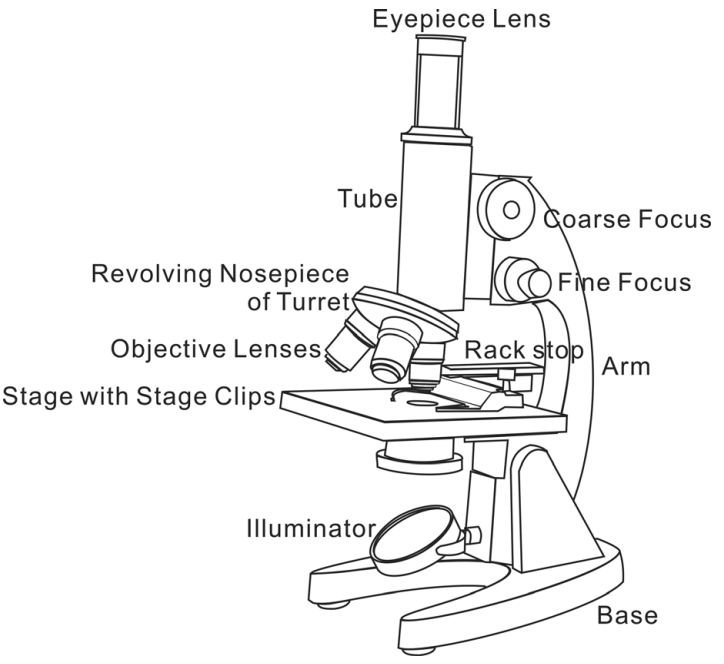

Fig. 6.1 An optical microscope.

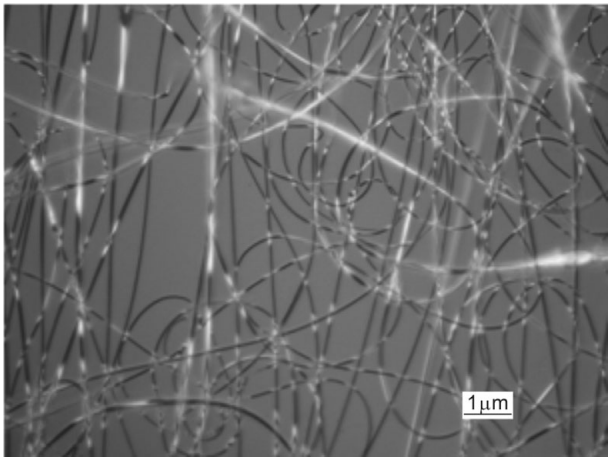

Fig. 6.2 An optical micrograph of cellulose acetate nanofibers at 100× magnification.

into the surface. The size of the interaction volume depends on the electron energy (accelerating voltage), the atomic number of the sample and the sample's density. The energy exchange between the electron beam and the sample results in electron emission and electromagnetic radiation. The electrons are detected and an image is produced. A larger interaction volume causes backscattered electrons to emit from a larger area of the specimen. The backscattered electrons interact with the specimen on

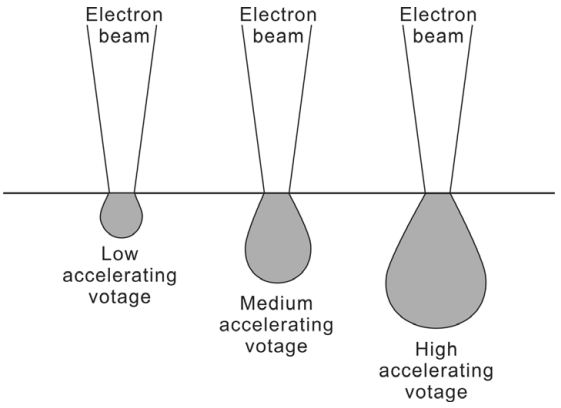

Fig. 6.3 Interaction volume of the sample with increasing accelerating voltage [3].

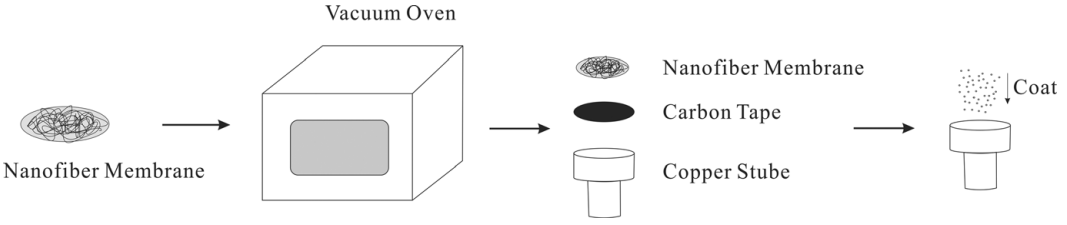

Fig. 6.4 Nanofiber sample preparation for SEM.

their way out, producing secondary electrons which are further away from the original spot size. Consequently, the resolution of the image obtained using a higher voltage is reduced. Figure 6.3 shows the interaction volume of the sample at different accelerating voltages [2].

An SEM sample must be conductive to prevent charging and it must be vacuum compatible. Thus a nanofiber sample must be dried and coated with gold before it can be observed with SEM. Figure 6.4 illustrates the general procedure.

In recent years, SEM has become one of the most widely used techniques and has been reported in the literature for measuring fiber diameter and the study of general fiber morphological characteristics [4–6]. Owing to the capability of measuring nanometer dimensions, SEM has also been combined with AFM cantilevers as a nanomanipulator, which can be worked as the load sensor to measure the mechanical properties of nanofibers or just manipulate nanofibers [7]. Yu *et al*. reported that the tensile properties of individual multi-walled carbon nanotubes were successfully measured using AFM cantilever tips under SEM [8]. They designed a nanomanipulator so that the carbon nanotubes could be manipulated in three dimensions inside the microscope, by attaching the tips of the AFM [9]. Samuel *et al*. reported mechanical testing of pyrolyzed polymer nanofibers with the aid of SEM [10]. They utilized a micro-device with a leaf-spring load cell, which was actuated externally with a piezo-motor. The average length of a sample was 10 μm, and the maximum engineering strain on the sample was 15%. Because of the

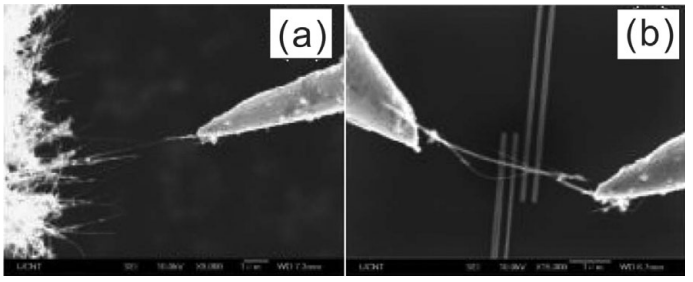

Fig. 6.5 Fabricating carbon nanotube transistors on pre-patterned electrodes on a Si substrate [7]. (a) Adhesion of a bundle at the end of tip. (b) Positioning the MWCNT on electrodes and pressing the MWCNT by the counter CNT bundle.

small sample length, SEM was used for high magnification imaging to measure displacements. Lim *et al.* [7] installed two nanomanipulators inside a field-emission scanning electron microscope (FE-SEM) for manipulation of nanostructured materials. The nanomanipulators can travel about 20 mm with a minimum increment of 1 nm, providing various manipulation freedoms such as moving, bending, cutting and biasing. With these nanomanipulators, they conducted *in situ* characterization of the electrical breakdown of multi-walled carbon nanotubes (MWCNTs). Figure 6.5 illustrates the SEM images of an MWCNT mounted between two AFM cantilevers for mechanical testing.

6.1.3 Transmission electron microscopy (TEM)

Transmission electron microscopy (TEM) is an imaging technique whereby a beam of electrons is transmitted through a specimen and forms an image that is magnified and directed to appear on either a fluorescent screen or a layer of photographic film, or to be detected by a sensor such as a CCD camera. The theoretical resolution of TEM is 0.02 nm. However, due to spherical aberration, the practical resolution is approximately 0.2 nm [11].

In TEM, a crystalline material interacts with the electron beam mostly by diffraction rather than absorption. The intensity of the transmitted beam is affected by the volume and density of the material through which it passes. The intensity of the diffraction depends on the orientation of the planes of atoms in a crystal relative to the electron beam. At certain angles the electron beam is diffracted strongly from the axis of the incoming beam, while at other angles the beam is largely transmitted. Modern microscopes are often equipped with specimen holders that allow the user to tilt the specimen to a range of angles in order to obtain specific diffraction conditions, and apertures placed below the specimen allow the user to select for electrons that are diffracted in a particular direction.

A high-contrast image can therefore be formed by blocking electrons deflected away from the optical axis of the microscope by adjusting the aperture to allow only unscattered electrons through. This produces a variation in electron intensity that reveals information about the crystal structure, and can be viewed on a fluorescent screen, recorded on photographic film or captured electronically.

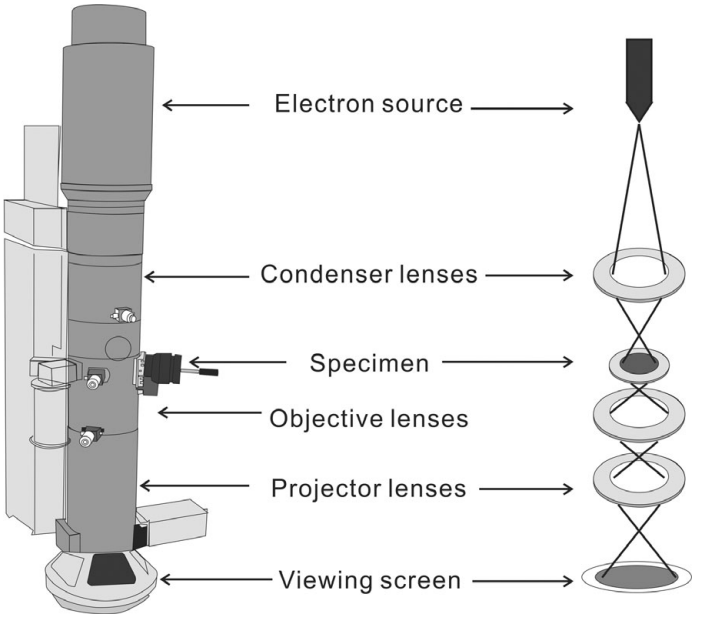

Fig. 6.6 Components of a TEM instrument.

This technique (known as bright field or light field) is particularly sensitive to extended crystal lattice defects (such as dislocations) in an otherwise ordered crystal. As the local distortion of the crystal around the defect changes, the angle of the crystal plane and intensity of scattering will vary around the defect. As the image is formed by the distortion of the crystal planes around the defect, the contrast in these images does not normally coincide exactly with the defect, but is slightly to one side.

It is also possible to produce an image from electrons deflected by a particular crystal plane. By either moving the aperture to the position of the deflected electrons, or by tilting the electron beam so that the deflected electrons pass through the centred aperture, an image can be formed consisting of only deflected electrons, known as a dark field image. Figure 6.6 shows the basic components of a TEM instrument.

In the most powerful diffraction contrast TEM instruments, crystal structure can be investigated by high-resolution transmission electron microscopy (HRTEM), also known as phase contrast imaging, as the images are formed due to phase differences of electron waves scattered through a thin specimen [12].

Like SEM, TEM can be used to characterize geometric properties of nanofibers such as fiber diameter, diameter distribution, fiber orientation and fiber morphology (e.g. cross-section shape and surface roughness). The use of TEM does not require the sample to be in a dry state, as in the SEM. Hence, nanofibers electrospun from a polymer solution can be directly observed under TEM [13].

TEM can also be used to study the fiber alignment in composite nanofibers. McCullen *et al*. [14] utilized TEM to examine the presence and alignment of MWCNT in PEO nanofibers. Figure 6.7a shows that MWCNT were embedded and aligned in PEO

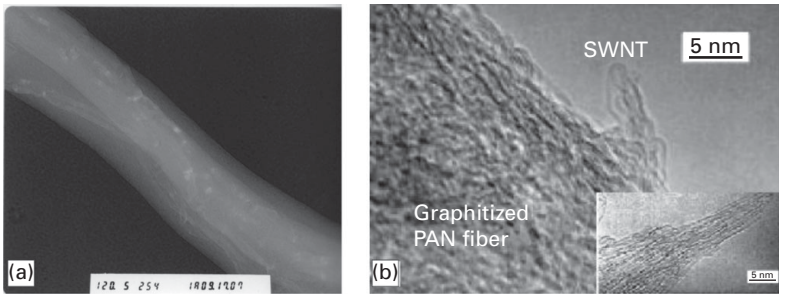

Fig. 6.7 (a) TEM image of a core–shell structured PAN nanofibers with MWCNTs embedded in both core and shell and (b) TEM image of SWCNT stick out of PAN nanofibers [15].

nanofibers. As shown in Fig. 6.7b, aligned SWCNT embedded in PAN nanofibers were also investigated with TEM [15].

When preparing a nanofiber sample for AFM, a carbon-coated metal mesh for AFM is usually positioned between the tip of the syringe and the receiver when electrospinning. As the nanofibers move towards the receiver, some fibers will stick to the mesh, and therefore a mesh with nanofibers attached is obtained for AFM observation. Figure 6.8 shows a metal mesh for AFM.

Nanomanipulators can be installed in an atomic force microscope as well as in a scanning electron microscope. Kuzumaki *et al*. [16] selectively performed deformation, cutting off and bonding of individual CNT using a dual-nanomanipulation system installed in a high-resolution transmission electron microscope. These processes were directly observed *in situ* at a lattice resolution of 0.1 nm.

6.1.4 Atomic force microscopy (AFM)

The atomic force microscope (also known as a scanning force microscope) is a very high-resolution scanning probe microscope. The atomic force microscope was invented by Binnig, Quate and Gerber in 1986, and is one of the foremost tools for imaging, measuring and manipulating matter at the nanoscale [17]. The theoretical resolution of a TEM is at a fraction of a nanometer, which is more than 1000 times better than the optical diffraction limit.

An AFM instrument is composed of a microscale cantilever with a pointed tip at its end that is used to scan the specimen surface. Typically, the cantilever is made of silicon or silicon nitride, with a tip radius of curvature on the nanoscale. When the tip is brought sufficiently close to a sample surface, the cantilever deflects due to forces between the tip and the sample, as governed by Hooke's law. Depending on the situation, forces that are measured in AFM include the mechanical contact force, van der Waals forces, capillary forces, chemical bonding, electrostatic forces, magnetic forces, Casimir forces and solvation forces [18]. In addition to force, other quantities may be simultaneously measured through the use of specialized probes. Typically, the deflection is measured by using a laser spot reflected from the top of the cantilever into

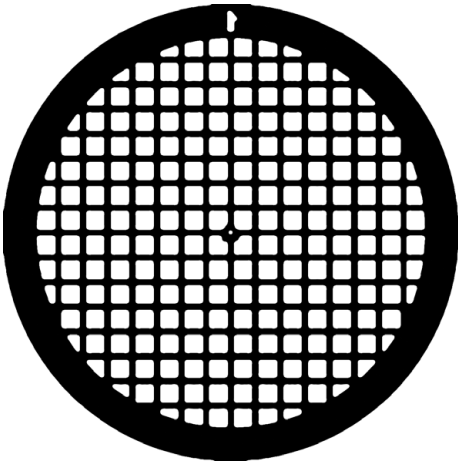

Fig. 6.8 A metal mesh for TEM.

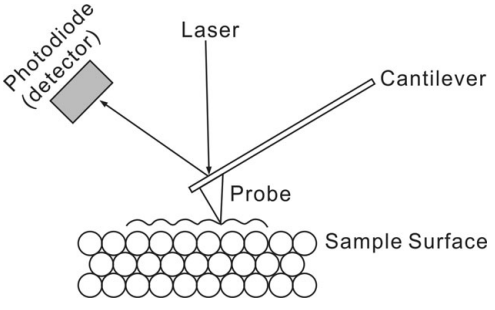

Fig. 6.9 Schematic diagram of AFM.

an array of photodiodes. Other methods used include optical interferometry, capacitive sensing or piezoresistive AFM cantilevers. These cantilevers are fabricated with piezoresistive elements that act as a strain gage. Using a Wheatstone bridge, strain in the AFM cantilever due to deflection can be measured, but this method is not as sensitive as laser deflection or interferometry.

If the AFM instrument tip were scanned at a constant height, there would be a risk that the tip would collide with the surface, causing damage. Hence, in most cases a feedback mechanism is employed to adjust the tip-to-sample distance, in order to maintain a constant force between the tip and the sample. Traditionally, the sample is mounted on a piezoelectric tube, which can move the sample in the z direction for maintaining a constant force, and the x and y directions for scanning the sample. Alternatively a "tripod" configuration of three piezo crystals may be employed, with each responsible for scanning in the x, y and z directions. This eliminates some of the distortion effects seen with a tube scanner. The resulting map of the area $s = f(x, y)$ represents the topography of the sample. Figure 6.9 illustrates the schematic diagram of AFM.

Similar to SEM and TEM, AFM can be used to characterize geometric properties of nanofibers such as fiber diameter, diameter distribution, fiber orientation and fiber

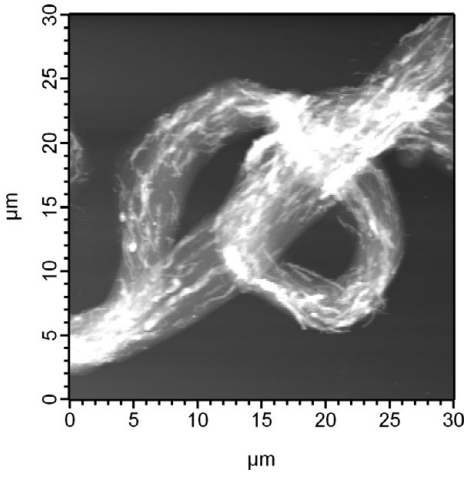

Fig. 6.10 AFM image of MWCNT-reinforced electrospun cellulose fibers.

morphology (e.g. cross-section shape and surface roughness) [13]. However, an accurate measurement of the nanofiber diameter with AFM requires a rather precise procedure. The fibers appear larger than their actual diameters because of the AFM instrument tip geometry [19]. For a precise measurement, fibers crossing to each other on the surface are generally chosen. The upper horizontal tangent of the lower fiber is taken as a reference, and the vertical distance above this reference is considered to be the exact diameter of the upper nanofibers [20]. Figure 6.10 shows an AFM image of an MWCNT reinforced electrospun cellulose fibers. Single MWCNTs coated on the surface of the fibers are distinguishable. The diamension of MWCNTs can be measured with AFM as well.

6.1.5 Scanning tunneling microscopy (STM)

Scanning tunneling microscopy (STM) is a powerful technique for viewing surfaces at the atomic level. Its development in 1981 won its inventors, Gerd Binnig and Heinrich Rohrer (at IBM Zürich), the Nobel Prize in Physics in 1986 [21]. The technique of STM probes the density of states of a material by using tunneling current. For STM, good resolution is considered to be 0.1 nm lateral resolution and 0.01 nm depth resolution [22]. The STM can be used not only in ultra-high vacuum but also in air and various other liquid or gas ambients, and at temperatures ranging from near zero to several hundred kelvin [23].

The STM instrument is based on the concept of quantum tunneling. When a conducting tip is brought very near to a metallic or semiconducting surface, a bias between the two can allow electrons to tunnel through the vacuum between them. For low voltages, this tunneling current is a function of the local density of states (LDOS) at the Fermi level, E_f, of the sample [23]. Variations in current as the probe passes over the surface are translated into an image. However, STM can be a challenging technique, as it requires extremely clean surfaces and sharp tips.

The components of an STM instrument include a scanning tip, piezoelectric controlled height, an *x*,*y* scanner, coarse sample-to-tip control, a vibration isolation system and a computer [24]. The resolution of an image is limited by the radius of curvature of the scanning tip of the microscope. Additionally, image artifacts can occur if the tip has two tips at the end, rather than a single atom; this leads to "double-tip imaging," a situation in which both tips contribute to the tunneling [22]. Therefore it has been essential to develop processes for consistently obtaining sharp, usable tips. The tip is often made of tungsten or platinum–iridium, although gold is also used. Tungsten tips are usually made by electrochemical etching, and platinum–iridium tips are made by mechanical shearing [22]. Owing to the extreme sensitivity of tunnel current to height, proper vibration isolation is imperative for obtaining usable results. In the first scanning tunneling microscope, by Binnig and Rohrer, magnetic levitation was used to keep the instrument free of vibrations; now spring systems are often used, and additional mechanisms for reducing eddy currents are implemented [23]. The maintenance of tip position with respect to the sample, scanning the sample in raster fashion and acquring the data are all computer controlled [25]. The computer is also used for enhancing the image with the help of image processing as well as performing quantitative morphological measurements.

To use an STM instrument, the tip is first brought into close proximity of the sample by some coarse sample-to-tip control. The values for common sample-to-tip distance, *W*, range from about 4 Å to 7 Å, which is the equilibrium position between attractive (3 Å $< W <$ 10 Å) and repulsive ($W <$ 3Å) interactions [23]. Once tunneling is established, piezoelectric transducers are implemented to move the tip in three directions. As the tip is rastered across the sample in the *x*–*y* plane, the density of states, and therefore the tunnel current, changes. This change in current with respect to position can itself be measured, or the height, *z*, of the tip corresponding to a constant current can be measured. These two modes are called the constant height mode and the constant current mode, respectively [23]. In the constant current mode, feedback electronics adjust the height by applying a voltage to the piezoelectric height control mechanism [25]. This leads to a height variation, and thus the image comes from the tip topography across the sample and gives a constant charge density surface; this means contrast on the image is due to variations in charge density [24]. In the constant height mode, the voltage and height are both held constant while the current changes to keep the voltage from changing; this leads to an image made of current changes over the surface, which can be related to charge density. The benefit to using a constant height mode is that it is faster, as piezoelectric movements require more time to register the change in constant current mode than the voltage response in constant height mode [24]. In addition to scanning across the sample, information on the electronic structure of the sample can be obtained by sweeping voltage and measuring current at a specific location [22]. This type of measurement is called scanning tunneling spectroscopy (STS).

The technique of STM has primarily been used to provide direct 3-D imaging of the surface topography of nanomaterials such as organically modified SWCNT [26, 27]. Specifically, the first STM study of fluorinated SWCNT revealed a banded

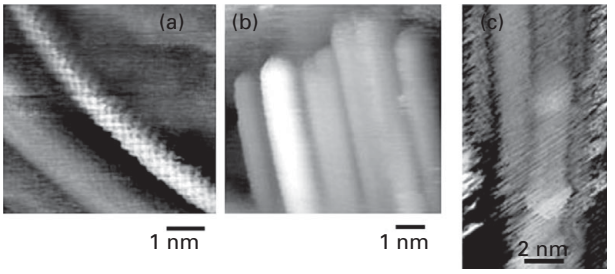

Fig. 6.11 Constant current STM images (Vbias, 200–1000 mV, It, 0.2–1 nA, T, 298 K, under UHV), of purified p-SWCNT showing the carbon lattice on the sidewall (a), the terminals (b), and some irregular structures (c) which are attributed to amorphous carbon or catalyst particles adhered to the carbon surface [29].

structure which indicates the regions of fluorination.[28] Figure 6.11 shows the STM images of p-SWCNT.

Although current literature surrounding the characterization of nanofibers by using STM is sparse, STM is a powerful technique for studying the surface modification and topography of functionalized nanofibers, which can eventually assist in the understanding of interfacial reaction of the nanofibers. Moreover it has been demonstrated that STM is capable of moving and arranging atoms as designed, which shows the potential of utilizing STM to move nanofibers and design nanostructures in the very near future. Figure 6.12 shows UBC written with STM provided by Yan's group in UBC.

6.1.6 X-ray diffraction

X-ray diffraction (XRD) is a very important technique that has long been used to address all issues related to the crystal structure of solids, including lattice constants and geometry, identification of unknown materials, orientation of single crystals, preferred orientation of polycrystals, defects and stresses, etc.

In XRD, a collimated beam of X-rays, with a wavelength typically ranging from 0.7 Å to 2 Å, is incident on a specimen and is diffracted by the crystalline phases in the specimen according to Bragg's law:

$$\lambda = 2d \sin \theta, \tag{6.2}$$

where d is the spacing between atomic planes in the crystalline phase and λ, is the X-ray wavelength. The intensity of the diffracted X-rays is measured as a function of the diffraction angle 2θ and the speciment's orientation. Strong diffraction from a set of planes results when the angles of incidence and diffraction, θ, are equal, and the path difference AOB between the two beams is equal to an integral number of wavelengths, $n\lambda$, Figure 6.13 illustrates the principle of XRD. The X-ray diffraction pattern is used to identify the specimen's crystalline phases and to measure its structural properties.

The crystallite size, D, can be estimated from the peak width with Scherrer's formula [30]:

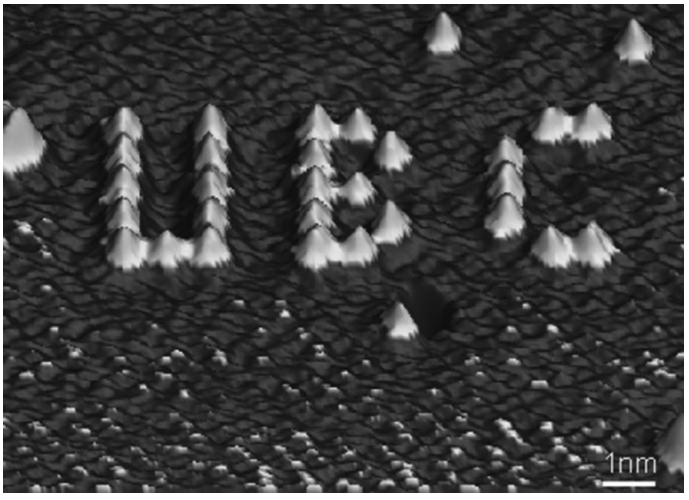

Fig. 6.12 UBC written with STM (copyright authorized by Dr. Yan Pennec).

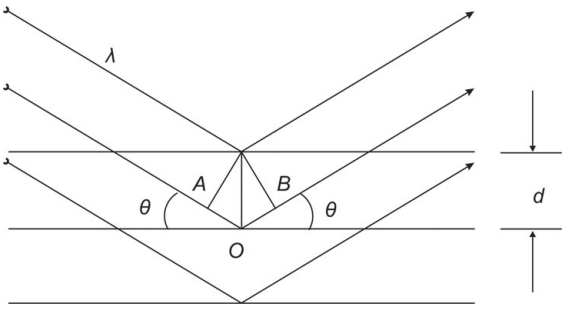

Fig. 6.13 The principle of XRD.

$$D = \frac{K\lambda}{B\cos\theta_B}, \tag{6.3}$$

where λ is the X-ray wavelength, B is the full width of height maximum (FWHM) of a diffraction peak, θ_B is the diffraction angle, and K is Scherrer's constant, of the order of unity for usual crystal. However, one should be alerted to the fact that nanoparticles often form twinned structures; therefore, Scherrer's formula may produce results different from the true particle sizes. In addition, X-ray diffraction provides only the collective information of the particle sizes and usually requires a sizable amount of powder. It should be noted that since the estimation would work only for very small particles, this technique is very useful in characterizing nanoparticles. Similarly, the film thickness of epitaxial and highly textured thin films can also be estimated with XRD [31].

The technique of XRD is nondestructive and does not require elaborate sample preparation, which partly explains the wide usage of the method in characterization of materials, including nanofibers [32, 33].

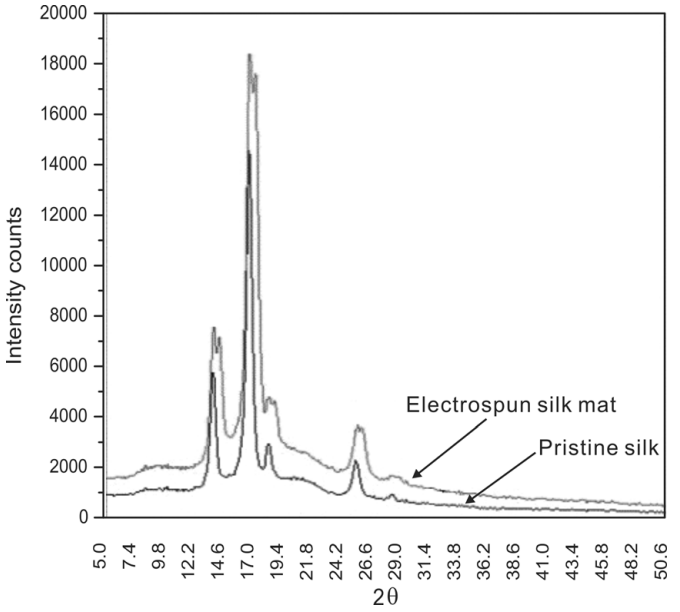

Fig. 6.14 WAXD of pristine and electrospun silk fibers [34].

6.1.6.1 Wide-angle X-ray diffraction

Wide-angle X-ray scattering (WAXS) or wide-angle X-ray diffraction (WAXD) is an X-ray diffraction technique that is often used to determine the crystalline structure of polymers. This technique specifically refers to the analysis of Bragg peaks scattered to wide angles, which implies that they are caused by sub-nanometer sized structures. The diffraction pattern generated allows the determination of the chemical composition or phase composition of the film, the texture of the fiber (preferred alignment of crystallites), the crystallite size and presence of fiber stress.

Figure 6.14 shows the WAXD patterns of pristine and electrospun fibers. The similarities between the patterns of the two systems strongly suggest structural similarity between the pristine and electrospun fibers. The crystallinity of the fibers was determined through this pattern [34].

6.1.6.2 Small-angle X-ray scattering

Small-angle X-ray scattering (SAXS) is another powerful technique for characterizing nanostructured materials. Strong diffraction peaks result from constructive interference of X-rays scattered from ordered arrays of atoms and molecules. A lot of information can be obtained from the angular distribution of scattered intensity at low angles. The elastic scattering of X-rays (wavelength 0.1. . . 0.2 nm) by a sample that has inhomogeneities at the nanometer level, is recorded at very low angles, typically, 0.1°–10°. The technique of SAXS is capable of delivering structural information of macromolecules between 5 nm and 25 nm, of repeat distances in partially ordered systems of up to 150 nm [35]; USAXS (ultra-small-angle X-ray scattering) can resolve even larger dimensions.

We can use SAXS for the determination of the microscale or nanoscale structure of particle systems in terms of such parameters as averaged particle sizes, shapes, distribution and surface-to-volume ratio. The materials can be solid or liquid and they can contain solid, liquid or gaseous domains (so-called particles) of the same or another material in any combination. Not only particles, but also the structure of ordered systems likes lamellae, and fractal-like materials can be studied. The method is accurate, nondestructive and usually requires only a minimum of sample preparation.

Small-angle X-ray scattering has also been widely used in characterization of nanofibers for superstructure investigations [36, 37]. Figure 6.15 shows a SAXS pattern recorded from a bundle of electrospun PA66 nanofibers. The image does not reveal any lamellar superstructure (a structure on a scale larger than the unit cell with a repeating long period). The elliptical shape of the diffuse small-angle scattering indicates elongated nanostructures, possibly nanofibrils or voids between them. Melt-drawn PA66 fibers exhibit a long period of 100 Å. Therefore, it is believed that the extremely rapid structural formation and the high draw ratio have no significant effect on crystallite structure formation within the nanofibers during the electrospinning process [37].

6.1.7 Mercury porosimetry

Nanofiber membranes have potential applications in many areas including filtration, cell culture matrix and as battery separators, etc. For such applications, pore structures are very important characteristics.

A variety of techniques can be used to investigate the continuous porosity of porous materials. The most direct way is image analysis of TEM or SEM micrographs. But this technique has a drawback relating to the fact that it provides only a 2-D projection of a 3-D structure. Mercury porosimetry is a well-established technique for the characterization of porous materials. It is widely accepted as a standard measure of total pore volume and pore size distribution in the macropore and mesopore ranges.

Mercury intrusion measurements are extremely simple in principle, although a number of experimental complications need to be considered. In the usual procedure, a small specimen is first dried to empty the pores of any existing fluid. It is then weighed, transferred to a chamber, which is then evacuated, and mercury is introduced to surround the specimen. Since mercury does not wet the sample spontaneously, it does not intrude into empty pores unless pressure is applied. Pressure in progressive increments is then applied to the mercury, and the intrusion of mercury at each step is monitored. The set of pressure steps and corresponding volumes intruded provides the basic data for pore size distribution calculations, as shown in Fig. 6.16 [38]. The analysis of the distribution of the specific surface area and of the specific pore volume in relation with the pore size from mercury porosimetry data is classically based on Washburn's equation [39]:

$$d = \frac{-4\gamma \cos\theta}{P}, \tag{6.4}$$

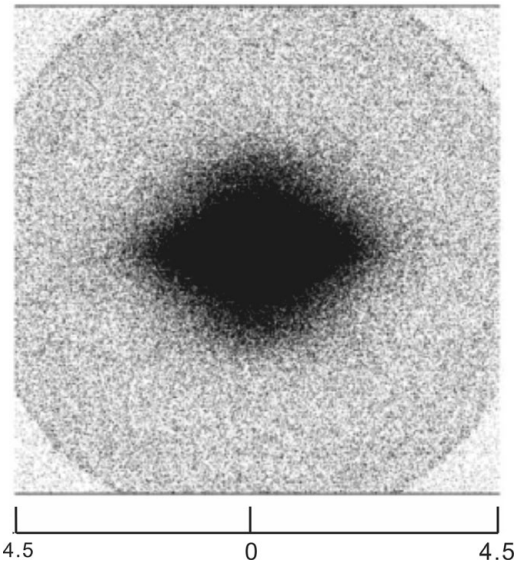

Fig. 6.15 SAXS pattern recorded from a bundle of electrospun PA66 nanofibers [37].

where d is the diameter of the cylinder being intruded, γ is the surface tension of mercury, θ is the contact angle of mercury on the solid, and P is the applied pressure.

Figure 6.17 shows a representative plot of pore diameter distribution of electrospun PLGA fibers. The data were obtained from mercury porosimetry measurements. From this figure, pore diameter distribution, total pore volume, total pore area, and porosity of the structure were calculated.

6.2 Chemical characterization of nanofibers

6.2.1 Fourier transform infra-red spectroscopy (FTIR)

Fourier transform infra-red spectroscopy is a measurement technique whereby spectra are collected based on measurements of the temporal coherence of a radiative source, using time-domain measurements of the infra-red radiation. A Fourier transform infra-red (FTIR) spectrometer is a Michelson interferometer with a movable mirror. By scanning the movable mirror over some distance, an interference pattern is produced that encodes the spectrum of the source, which turns out to be its Fourier transform. In its most basic form, a Fourier transform spectrometer consists of two mirrors located at a right angle to each other and oriented perpendicularly, with a beam-splitter placed at the vertex of the right angle and oriented at a 45° angle relative to the two mirrors. Radiation incident on the beam-splitter from one of the two "ports" is then divided into two parts, each of which propagates down one of the two arms, and is reflected off one of the mirrors. The two beams are then recombined and transmitted out of the other port. When the position of one mirror is continuously varied along the axis of the

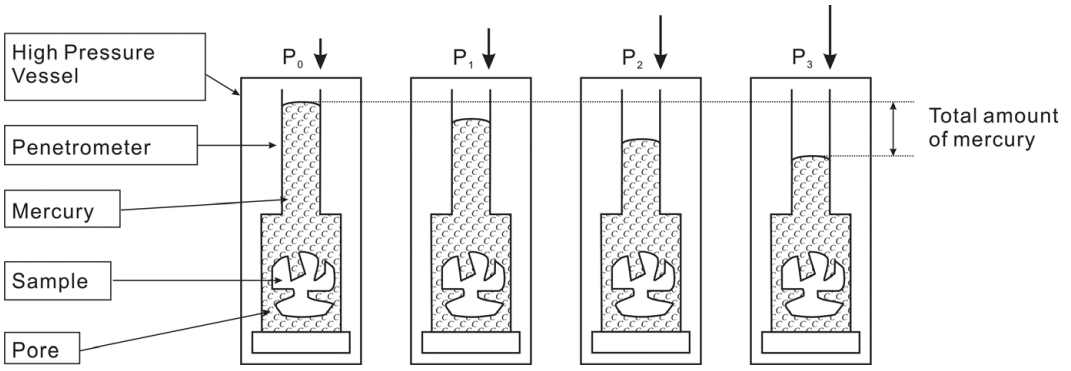

Fig. 6.16 Principle of mercury porosimetry.

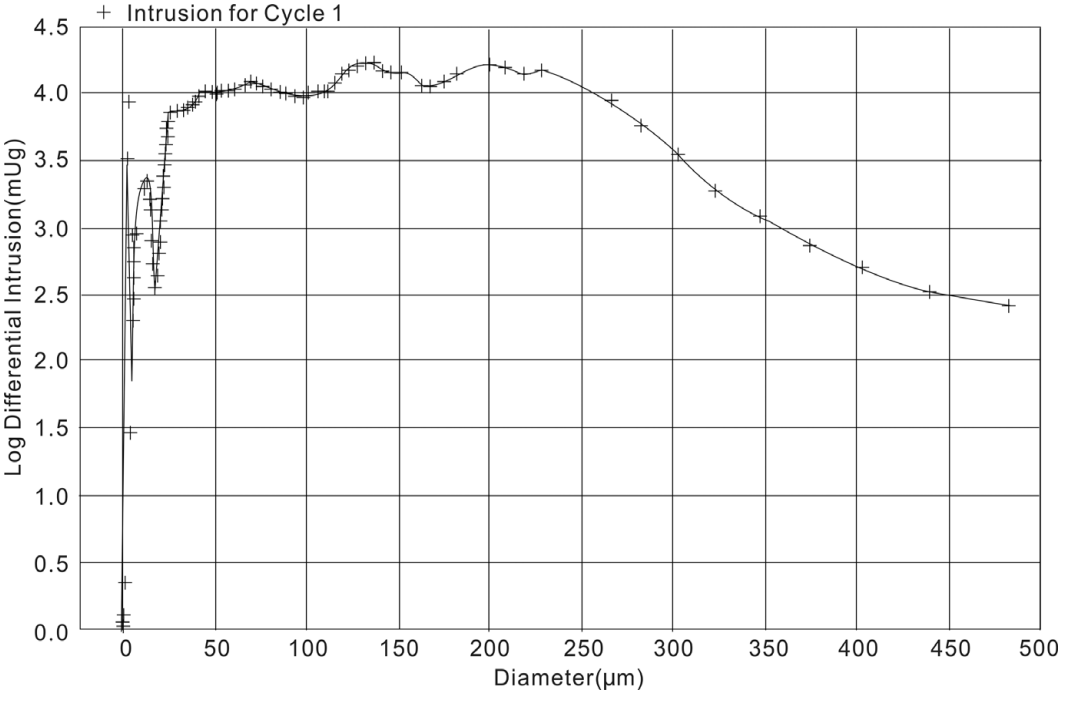

Fig. 6.17 Representative plot of pore diameter distribution. Each log differential intrusion value indicates the relative quantity of pores of a specific diameter [40].

corresponding arm, an interference pattern is swept out as the two phase-shifted beams interfere with each other. Figure 6.18 illustrates a Michelson (or Fourier transform) interferometer that forms the basic setup of an FTIR spectrometer.

The energy released by an infra-red photon is small but it is sufficient to excite vibrations and rotations and other collective motions of the molecules in the sample. A net change in molecular dipole due to vibration and rotation is required for absorption of the infra-red radiation. The electric field interacts with the molecular dipole and absorption of infra-red radiation occurs at discrete frequencies. When there

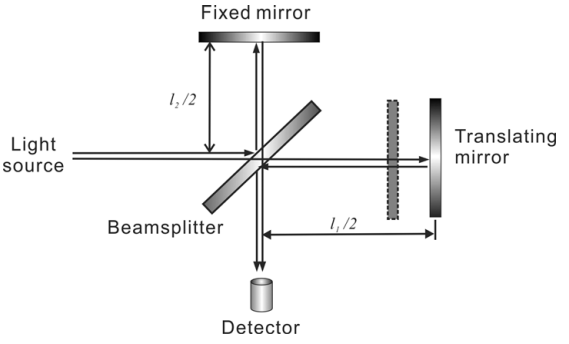

Fig. 6.18 A Michelson interferometer.

is no net change in the dipole moment, there is no infra-red absorption. Quantum mechanical solution of a harmonic oscillator, which is governed by$E = \left(v + \frac{1}{2}\right)\frac{h}{2\pi}\sqrt{\frac{k}{\mu}}$, yields discrete energy levels, where v is the vibrational quantum number (integer ≥ 0). The absorption of infra-red radiation involves transition between adjacent energy levels ($\Delta v = \pm 1$). Wavenumbers (cm^{-1}, which are proporational to energy or frequency), are usually used in FTIR. The governing equation for the change in the energy due to infra-red absorption is $\Delta E = \frac{h}{2\pi}\sqrt{\frac{k}{\mu}} = hv$. Like any other absorption spectroscopy, the infra-red absoption spectroscopy relies upon Beer's law, where $A(\lambda) = -\log T(\lambda) = -\log\frac{P(\lambda)}{P_0(\lambda)} = \varepsilon(\lambda)bc$.

To measure the absorbance, P (intensity of light after passing through sample) and P_0 (intensity of incident light) have to be determined. The absorption frequency is related to the type of bond, whereas the absorption intensity is related to the concentration of species in the sample. The FTIR spectrum has a group frequency region and a fingerprint region. The fingerprint region is sensitive to differences in molecular structure, which is useful for identification of molecular structural changes. The group frequency region is weakly dependent on the environment, which is useful as the absorbance band for a particular functional group.

There are two operation modes for an FTIR spectrometer: (1) transmission and (2) reflection. Typically FTIR is performed in the transmission mode using the KBr pellet method. Alternatively, FTIR can also be done in the reflection mode, where the specular reflection can be obtained from reflective samples with thin organic coating.

In the reflection mode, P_0 is more difficult to quantify. As such, the R_0 of an uncoated surface is measured, followed by the measurement of R of the surface of the sample of interest. Absorbance of the infra-red radiation is governed by $A \approx \frac{\Delta R}{R} = \frac{R_0 - R}{R_0} = 1 - \frac{R}{R_0} = 1 - 10^{-A}$ [41].

The limitations of FTIR include: (1) strong IR radiation absorption by H_2O and CO_2; (2)a good blank sample is needed because P_0 determination is important; and (3)thick samples cause too much scattering and thus very little light is transmistted.

The technique of FTIR has been widely used to study the changes of the conformational structures that occur to a polymer during the electrospinning process. Ayutsede

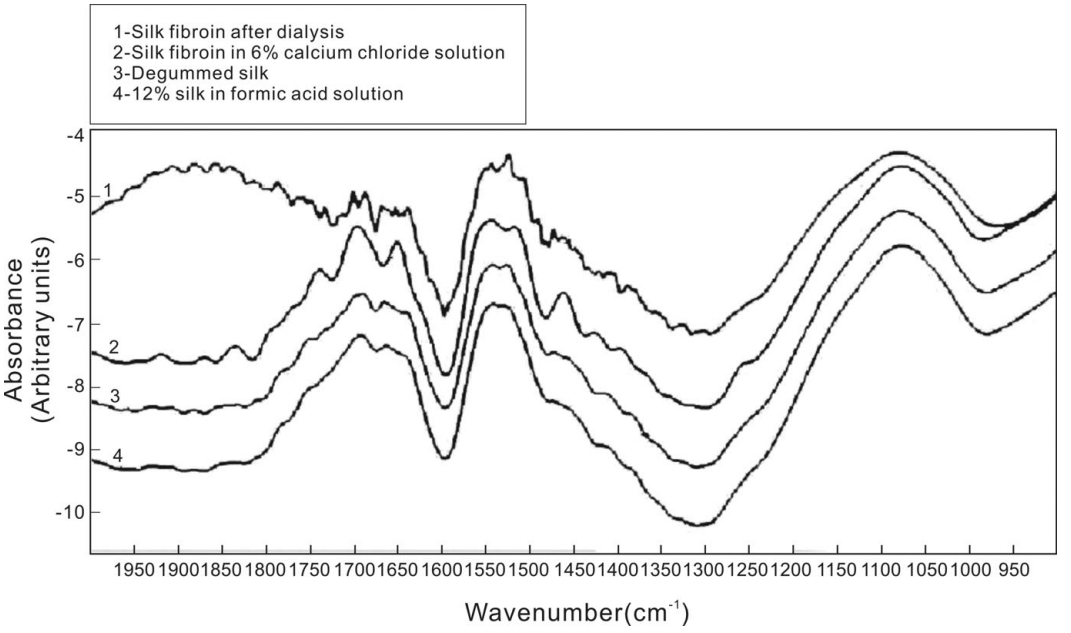

Fig. 6.19 The FTIR spectra of (1) dialyzed silk fibroin in water, (2) 6% silk fibroin in calcium chloride solution, (3) degummed silk fiber and (4) 12% silk fibroin in formic acid [34].

et al. used FTIR to compare the structural and concentration changes between pre-spun fibroin solutions and post-spun fibers of *Bombyx mori* silk [34]. Figure 6.19 illustrates the FTIR spectra of the silk fibroin in four different forms.

6.2.2 Raman spectroscopy (RS)

Raman spectroscopy is a spectroscopic technique used in condensed matter physics and chemistry to study vibrational, rotational, and other low-frequency modes in a system [42]. It depends on inelastic scattering, or Raman scattering, of monochromatic light, usually from a laser in the visible, near infra-red, or near ultra-violet range. The laser light interacts with phonons or other excitations in the system, resulting in the energy of the laser photons being shifted up or down. The shift in energy gives information about the phonon modes in the system. Infra-red spectroscopy yields similar, but complementary information.

Typically, a sample is illuminated with a laser beam (Ar^+ ion, 488 nm) from irradiation of CCl_4. The emitted radiation includes Rayleigh scattering, Stokes scattering and anti-Stokes scattering. Light from the illuminated spot is collected with a lens and sent through a monochromator. Wavelengths close to the laser line, due to elastic Rayleigh scattering, are filtered out while the rest of the collected light is dispersed onto a detector.

Spontaneous Raman scattering is typically very weak, and as a result the main difficulty of Raman spectroscopy is separating the weak inelastically scattered light

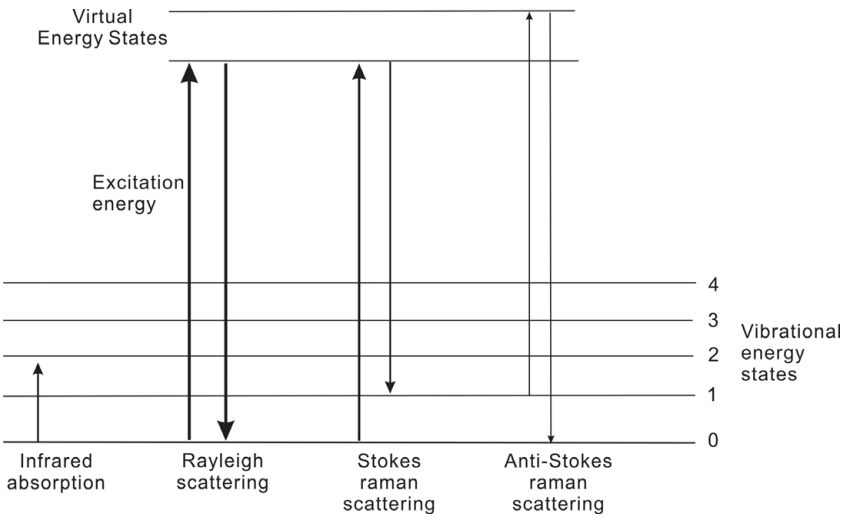

Fig. 6.20 Energy level diagram showing the states involved in the Raman signal. The line thickness is roughly proportional to the signal strength from the different transitions.

from the intense Rayleigh scattered laser light. Raman spectrometers typically use holographic diffraction gratings and multiple dispersion stages to achieve a high degree of laser rejection. In the past, photomultiplier tubes were the detectors of choice for dispersive Raman setups, resulting in long acquisition times. However, the recent use of CCD detectors has made dispersive Raman spectral acquisition much more rapid.

The Raman effect occurs when light impinges upon a molecule and interacts with the electron cloud of the bonds of that molecule. The incident photon excites one of the electrons into a virtual state. For the spontaneous Raman effect, the molecule will be excited from the ground state to a virtual energy state, and will relax into a vibrational excited state, which generates Stokes Raman scattering. If the molecule was already in an elevated vibrational energy state, the Raman scattering is then called anti-Stokes Raman scattering.

A molecular polarizability change or a certain amount of deformation of the electron cloud with respect to the vibrational coordinate is required for the molecule to exhibit the Raman effect. The amount of the polarizability change will determine the intensity, whereas the Raman shift is equal to the vibrational level that is involved. Figure 6.20 illustrates an energy level diagram showing the states involved in the Raman signal.

Raman spectroscopy is commonly used for chemical structure investigation since chemical bonds in molecules have specific vibrational information that therefore provides fingerprints by which the molecule can be identified. The fingerprint regions of organic molecules is in the range 500–2000 cm^{-1} [43]. Like FTIR, Raman spectroscopy is capable of following the changes in conformational structure and chemical bondings of a sample.

The Raman effect is based on polarizability of the bond, which is a measure of deformability of bond. To have Raman scattering, a momentary distortion of electrons

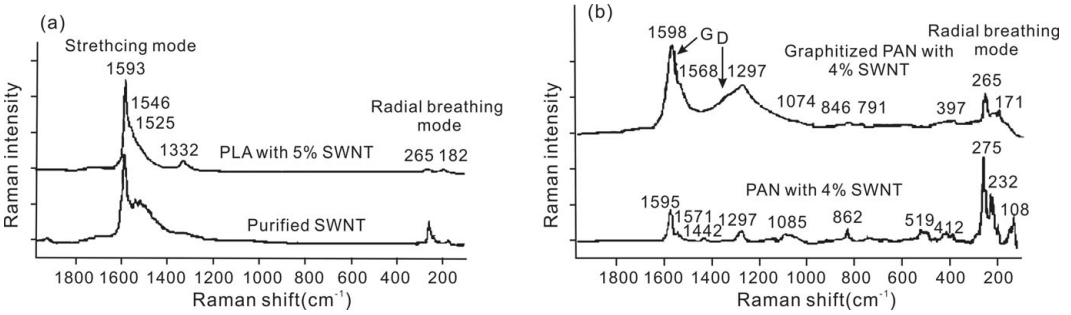

Fig. 6.21 Raman spectra of composite nanofibrils [15]. (a) Raman spectra of original purified SWCNTs and PLA with 5 wt% SWCNT, obtained using 514.5 nm excitation wavelength, and (b) Raman spectra of PAN with 4 wt% SWCNT before and after graphitization, using 780 nm excitation wavelength. The spectra of composite nanofibrils with SWCNT show all the typical peaks of SWCNT.

in a bond (polarization) is required to create a termporarily induced dipole moment. The Raman effect, therefore, needs to be a function of the distance between the two nuclei.

Because water is not a strong Raman scatterer, samples with water in them can be analyzed using Raman spectroscopy. However, samples with a source of fluorescence can swamp much smaller Raman signals, which is a major problem for Raman spectroscopy.

Raman spectroscopy has been commonly used for comparing the structural and concentration changes between pre-spun fibroin solutions and the post-spun fibers [44]. The two modes that are used in Raman spectroscopy are the radial breathing mode (RBM) and the tangential (stretching) mode. Ko *et al*. [15] used Raman spectroscopy to confirm the inclusion of SWCNTs in PAN and PLA nanofibers, see Fig. 6.21.

RBM peaks can be used to estimate the diameter of SWCNT by following this equation [45, 46]:

$$\omega_R = 224 \ \text{cm}^{-1}/d. \tag{6.5}$$

6.2.3 Nuclear magnetic resonance (NMR)

Nuclear magnetic resonance (NMR) is a physical phenomenon based upon the quantum mechanical magnetic properties of an atomic nucleus. NMR spectroscopy is one of the principal techniques used to obtain physical, chemical, electronic and structural information about molecules due to the chemical shift and Zeeman effect on the resonant frequencies of the nuclei. It is a powerful technique that can provide detailed information on the topology, dynamics and 3-D structure of molecules in solution and the solid state. In NMR, a spin interacts with a magnetic or an electric field. Spatial proximity and/or a chemical bond between two atoms can give rise to interactions between nuclei. In general, these interactions are orientation dependent. In media with no or little mobility (e.g. crystals powders, large membrane vesicles,

molecular aggregates), anisotropic interactions have a substantial influence on the behavior of a system of nuclear spins. In contrast, in a classical solution-state NMR experiment, Brownian motion leads to an averaging of anisotropic interactions. In such cases, these interactions can be neglected on the timescale of the NMR experiment. Consider nuclei which have a spin of one-half, like ^{1}H, ^{13}C or ^{19}F. The nucleus has two possible spin states: $m = ½$ or $m = -½$ (also referred to as up and down or α and β, respectively). The energies of these states are degenerate – that is to say, they are the same. Hence the populations of the two states (i.e. number of atoms in the two states) will be exactly equal at thermal equilibrium. If a nucleus is placed in a magnetic field, however, the interaction between the nuclear magnetic moment and the external magnetic field mean the two states no longer have the same energy. The energy of a magnetic moment μ when in a magnetic field B_0 (the zero subscript is used to distinguish this magnetic field from any other applied field) is given by the negative scalar product of the vectors:

$$E = -B_0\mu = -\mu_z B_0 = -m\hbar\gamma B_0. \tag{6.6}$$

As a result, the different nuclear spin states have different energies in a non-zero magnetic field. In hand-waving terms, we can talk about the two spin states of a spin ½ as being aligned either with or against the magnetic field. If γ is positive (true for most isotopes) then $m = ½$ is the lower energy state. The energy difference between the two states is

$$\Delta E = \hbar\gamma B_0. \tag{6.7}$$

Resonant absorption will occur when electromagnetic radiation of the correct frequency to match this energy difference is applied. The energy of a photon is $E = h\nu$, where ν is its frequency. Hence absorption will occur when

$$\nu = \frac{\Delta E}{h} = \frac{\gamma B_0}{2\pi}. \tag{6.8}$$

These frequencies typically correspond to the radiofrequency range of the electromagnetic spectrum. It is this resonant absorption that is detected in NMR [47].

For characterization of electrospun nanofibers, NMR allows the determination of the various coordinate sites and local environment of specific nuclei. Ohgo *et al.* used ^{13}C solid state NMR to identify the structures of the as-spun and chemically treated *Bombyx mori* silk fibers [48] Figure 6.22 illustrates the ^{13}C CP/MAS NMR spectra of nonwoven *B. mori* silk fibers prepared (a) as-spun and (b) after methanol treatment.

6.3 Mechanical characterization of nanofibers

Mechanical properties of materials describe their characteristic responses to applied loads and displacements. Mechanical tests serve all aspects of the science and technology of materials and their utilization. Depending on how the loads are applied, materials have different deformation modes: tensile, compression, bending, shear and

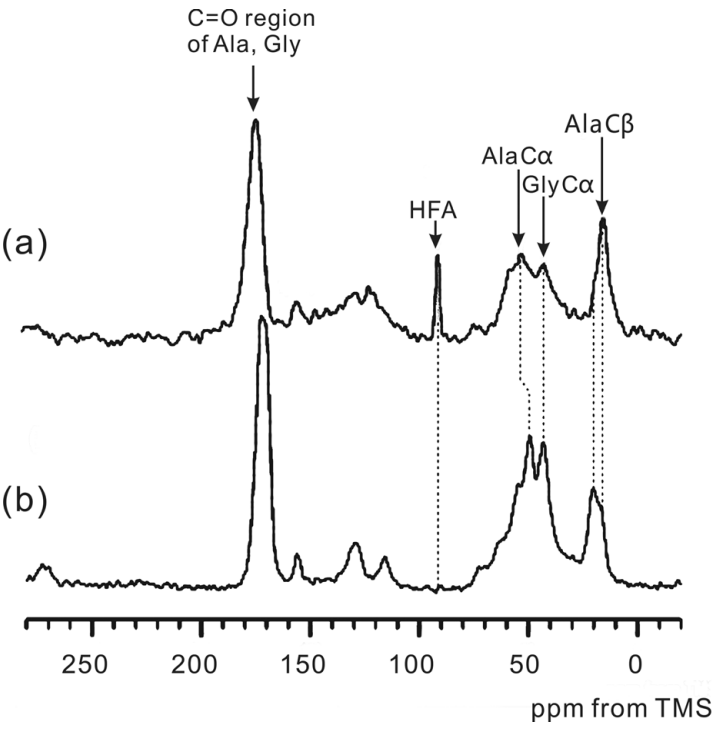

Fig. 6.22 ^{13}C CP/MAS NMR spectra of nonwoven *Bombyx mori* silk fibers prepared (a)as-spun and (b) after methanol treatment [48].

torsion. Since fibers and fiber assemblies are 1-D structures and therefore the main form of applied loads is stretching, we will discuss only tensile testing of nanofibers herein.

6.3.1 Microtensile testing of nanofiber nonwoven fabric

Considering an axial tensile test for a fiber of cross-section area A, in which a force F is applied and the fiber ungoes an elongation Δl comparing the orginal testing length of l. For comparing the mechanical behavior, the nominal stress σ ($= F/A$, SI unit is Pa $=$ N/m^2) is usually used for object force measurement. In the case of fibers, specific stress σ_{sp} is often introduced by dividing the force by the fiber linear density (ρ_l), the accepted practical unit is *N*/tex or *N*/denier. The conversion for the specific stress unit to engineering stress unit can be obtained by simply multiplying specific stress by fiber density:

$$\sigma(\text{GPa}) = \sigma_{\text{sp}}(N/\text{tex}) \times \text{density}(\text{g}/\text{cm}^3). \tag{6.9}$$

Two types of curves are used: the load–elongation(F–Δl) curve and the stress–strain (σ–ε, where ε=$\Delta l/l$) curve. Useful parameters obtained from stress–strain curves are initial modulus E, strength (the stress at failure σ_f), strain at failure and toughness ε_f.

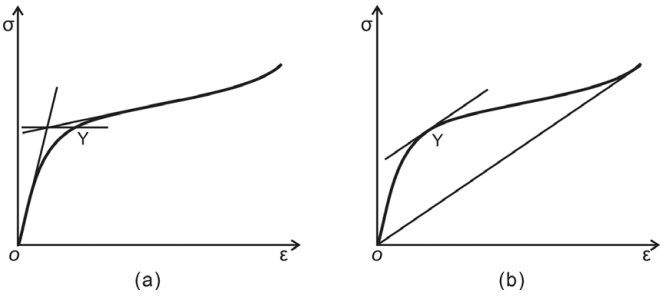

Fig. 6.23 Yield point of the stress–strain curve.

The yield point (Y) is defined as the point on the stress–strain curve at which the material begins to deform plastically. The strength at the yield point is called the yield strength. Before the yield point the material deforms elastically and the initial modulus can be calculated from Hooke's law:

$$E = \frac{d\sigma}{d\varepsilon}. \tag{6.10}$$

Elastic deformation is recoverable. The deformation above the yield point, known as plastic deformation, is not recoverable, and the material will not return to its initial shape. Fibers and fiber assemblies usually do not have an obvious yied point. In order to locate a precise position, Meredith [49] [2] suggested defining the yield point as the point at which the tangent to the curve is parallel to the line joining the origin to the breaking point, as in Fig. 6.23a. Coplan [50] defined the yield point as occurring at the stress given by intersection point of the tangent at the origin with the tangent having the least slope, as shown in Fig. 6.23b. Alternatively, when there are considerable linear regions both above and below the yield region, the point of intersection of the tangents may be taken as the yield point.

Toughness can be determined by measuring the area underneath the stress–strain curve. It is defined as the energy of mechanical deformation per unit volume prior to the fracture of material. Toughness describes the ability to absorb mechanical or kinetic energy up to failure. Its mathematical description is:

$$K = \frac{\text{Energy}}{\text{Volume}} = \int_0^{\varepsilon_f} \sigma d\varepsilon. \tag{6.11}$$

In the case of nonwoven nanofibrous structures the specific stress can be determined by first obtaining the membrane stress (force/specimen width) and then obtain the membrane stress by areal density as shown below. Please note the units to be used in order to obtain the linear density unit. For example, in order to express specific stress in N/tex:

$$\sigma_{sp}(N/\text{tex}) = \frac{\text{force(N)}}{\text{width(mm)}} \times \frac{1}{\text{areal density}(\text{g/m}^2)}. \tag{6.12}$$

For microtensile testing of nanofiber nonwoven fabric, the KES-G1 microtensile tester is one of the more commonly used microtensile testing devices, as shown in Fig. 6.24.

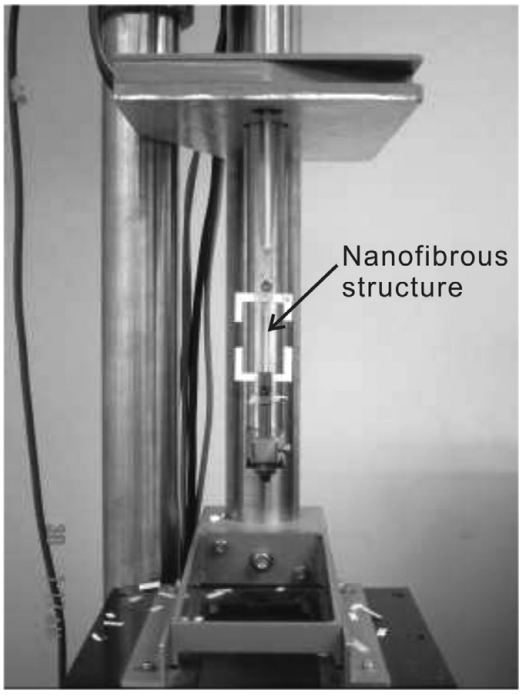

Fig. 6.24 A KES-G1 microtensile tester.

The outputs of KES-G1 are voltage and time, which correspond to force (stress) and displacement (strain), respectively. The ultimate tensile strength and its corresponding strain can be obtained through the microtensile tester. Figure 6.25 shows the stress–strain curves of nonwoven silk fibers reported by Ohgo *et al*. [48].

6.3.2 Mechanical testing of a single nanofiber

The AFM cantilever can also be used to characterize mechanical properties such as the strength and stiffness of nanofibers. By clamping the nanofiber between an AFM tip and a tungsten wire, a tensile test can be conducted on the fiber [51]. Figure 6.26 shows an SEM image of a carbonized nanofiber clamped between an AFM tip and a tungsten wire. Figure 6.27 shows a stress–strain curve of a PAN single nanofiber.

Pushing an AFM tip into nanofibers to apply a transverse compression load on the fiber can be a method for evaluation of the elastic modulus of a single nanofiber based on the approach of Kracke and Damaschke [15]. This method utilizes the following relationship:

$$dF/d(\Delta z) = \left(2/\pi^{1/2}\right) E^* A^{1/2}, \tag{6.13}$$

where F is the normal force, d is the tube diameter, Δz is the indentation depth, A is the contact area and E^* is the effective Young's modulus of the contact as defined by

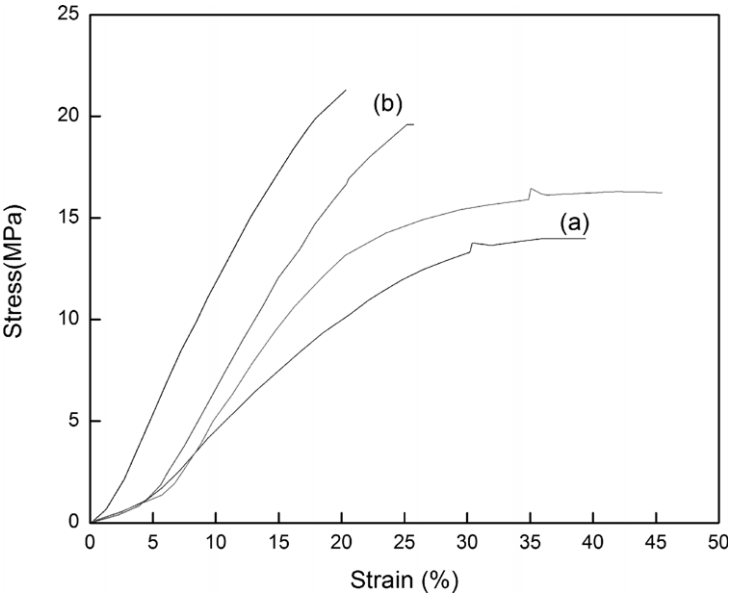

Fig. 6.25 Stress–strain curves of nonwoven silk fibers after methanol treatment: (a) *B. mori* silk and (b) *S. c. ricini* silk. The stress–strain experiments were performed twice for each fiber [48].

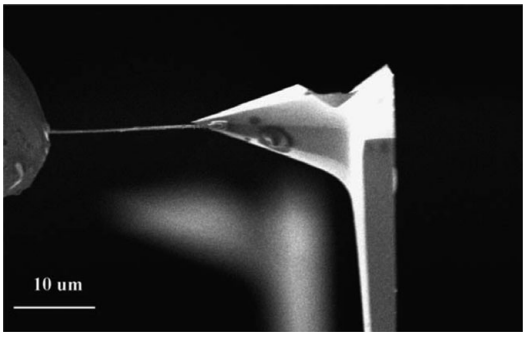

Fig. 6.26 An SEM image of a carbonized nanofiber clamped between an AFM tip and a tungsten wire. A smaller AFM cantilever on the same AFM chip is present in the background [51].

$$1/E^* = \left(1 - v_1^2\right)/E_1 + \left(1 - v_2^2\right)/E_2. \tag{6.14}$$

Here E_1, E_2, v_1 and v_2 are the elastic moduli and the Poisson's ratios of the sample and the tip respectively.

Figure 6.28 shows the load indentation curves from a set of stabilized experiments measured with CNT/PAN and neat PAN fibers placed on a mica substrate.

The AFM technique can also be used to characterize the roughness of fibers. The roughness value is the arithmetic average of the deviations of height from the central horizontal plane given in terms of millivolts of measured current. [20].

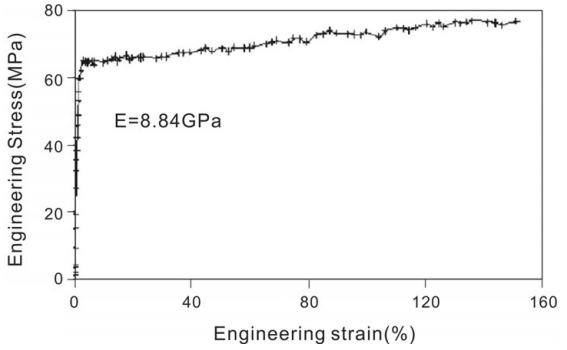

Fig. 6.27 Engineering strain–stress curve of an electrospun PAN nanofiber [52].

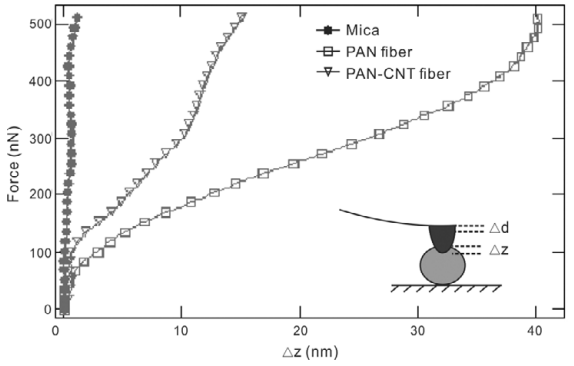

Fig. 6.28 Load indentation curves from a set of experiments [15].

As is well known, AFM is not specially designed for the mechanical testing of nanofibers. Therefore there is strong demand for a nanotensile tester specialized for the testing of nanoscaled fibrous materials. Several companies have realized that this strong demand implies a promising market in both academic and industrial areas, and have invented some nanotensile instruments such as the Agilent T150 universal testing machine (UTM) (MTS Nano Bionix 858) and the Hysitron nanoTensile 5000. These instruments offer superior means of nanomechanical characterization and enable researchers to understand dynamic properties of compliant fibers via the largest dynamic range in the industry.

Here we take the T150 UTM as an example. The T150 system from Agilent Technologies, as pictured in Fig. 6.29a, is a universal testing machine. It employs a nanomechanical actuating transducer (NMAT) head to produce tensile force (load on sample) using electromagnetic actuation combined with a precise capacitive gauge, delivering outstanding sensitivity over a large range of strain. Figure 6.29b shows a schematic of the NMAT. During tensile elongation, the T150 UTM holds the NMAT head stationary and moves the crosshead, providing a very stable system that ensures the lowest noise floor. The force applied is determined by the current applied to the NMAT's voice coil, which pulls the test specimen downward. The displacement is then

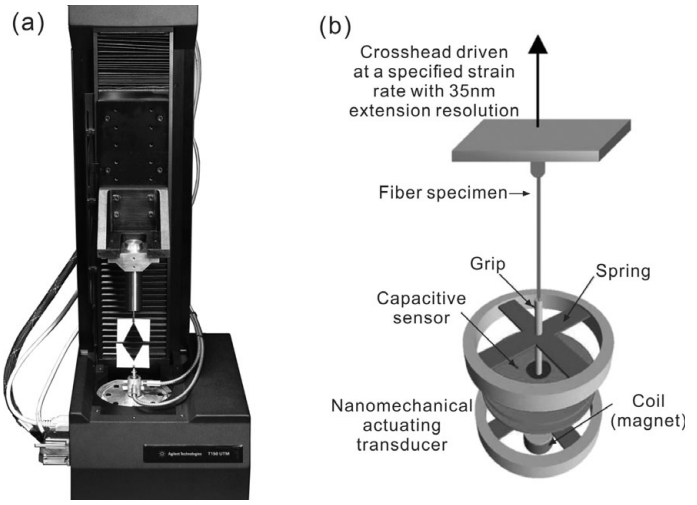

Fig. 6.29 (a) The Agilent T150 universal testing machine (UTM); (b) nanomechanical actuating transducer (NMAT) head of the Agilent T150 UTM.

measured by the NMAT's capacitive gauge. The NMAT provides a maximum linear displacement of ± 1 mm with resolution of <0.1 nm and a maximum load of 500 mN with resolution of 50 nN. The T150 is equipped with a micropositioner stage, which is a helpful sample guide that ensures the sample is orthogonal and aids in the positioning of the upper grip. It is capable of testing in three-point bend, four-point bend, compression and tension. In addition, an indentation kit including an inversion footer is available, allowing the system to be used as an indenter. The whole system is usually placed on an antivibration table for vibration isolation and enclosed to minimize the air flow influence during testing.

Tan *et al*. [53] performed tensile tests on single electrospun PCL microfibers using the MTS Nano Bionix 858, the predecessor of the Agilent T150 UTM. Aligned electrospun fibers were collected and prepared for tensile tests. The PCL microfibers exhibited the characteristic low strength and low modulus but high extensibility nature of PCL at room temperature. The mechanical properties were found dependent on fiber diameter, as shown in Fig. 6.30. The fibers with smaller diameter had higher strength but lower ductility due to the higher "draw ratio" applied to the fiber during electrospinning. Ko's group drew the same conclusion in their investigation of tensile stress-strain response of small-diameter electrospun PCL fibers using the Agilent T150 UTM [54].

6.4 Thermal analysis

Thermal properties are important for material engineering. For thermal analysis, several methods are commonly used: differential thermal analysis (DTA, temperature difference), differential scanning calorimetry (DSC, heat difference), thermogravimetric analysis (TGA, mass), thermomechanical analysis (TMA, dimension), dilatometry

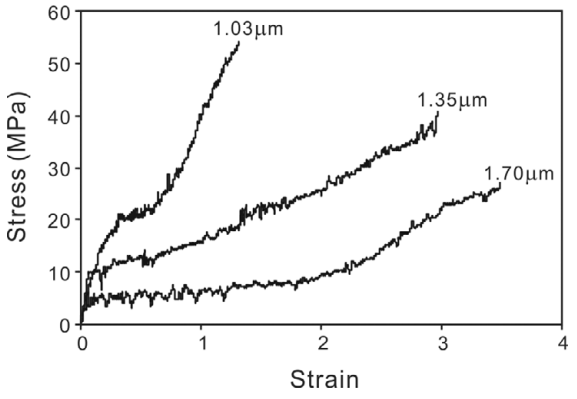

Fig. 6.30 Plot of stress against strain for electrospun PCL microfibers at various fiber diameters [53].

(DIL, volume), dynamic mechanical analysis (DMA, mechanical stiffness and damping), dielectric thermal analysis (DEA, dielectric permittivity and loss factor), evolved gas analysis (EGA, gaseous decomposition products) and thermo-optical analysis(TOA, optical properties). Among those methods, TGA and DAS are the two most-used, and they will be introduced in this section.

6.4.1 Thermogravimetric analysis (TGA)

The technique of TGA measures changes in sample mass with temperature by using a thermobalance, which is sometimes referred to as a thermogravimetric analyzer. One should note that mass is a measure of the amount of matter in a sample, whereas weight refers to the effect of the gravitational force on a mass, and thus varies from one geographical location to another. A thermobalance is a combination of a suitable electronic microbalance with a furnace, a temperature programmer and computer for control, that allows the sample to be simultaneously weighed and heated or cooled in a controlled manner, and the mass, time, and temperature data to be captured. The balance should be in a suitably enclosed system so that the nature and pressure of the atmosphere surrounding the sample can be controlled. Figure 6.31 shows a schematic thermobalance.

Results from TGA experiments can be presented in a variety of graphical ways. Mass or mass percent is usually plotted as the ordinate (y-axis) and temperature or time as the abscissa (x-axis). Mass percent has the advantage that results from different experiments can be compared on normalized sets of axes. When time is used as the abscissa, a second curve of temperature versus time needs to be plotted to indicate the temperature programme used [55].

Actual TGA curves obtained may be classified into various types, as shown in Fig. 6.32. Possible interpretations of the curves can be found in Ref [55].

Knowledge of the thermal stability range of materials provides information on problems such as the hazards of storing explosives, the shelf-life of materials and the

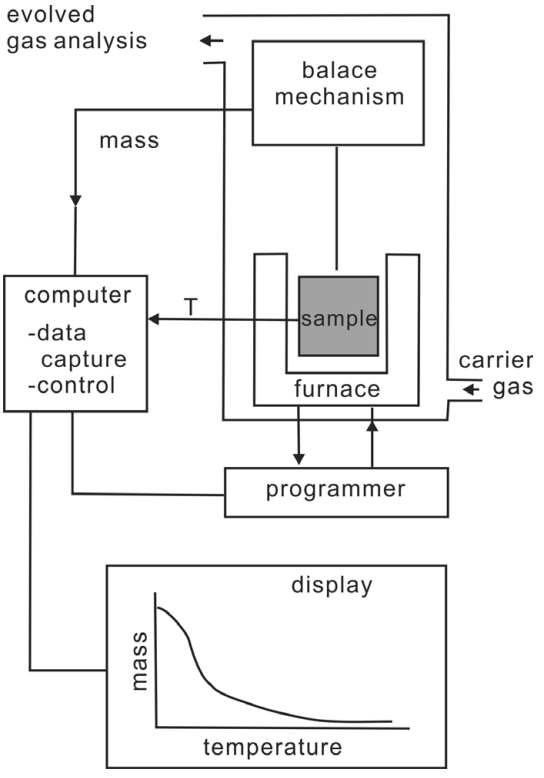

Fig. 6.31 A schematic thermobalance [55].

conditions for drying them. By using an atmosphere of air or oxygen, the conditions under which oxidation and degradation of polymers become catastrophic can be determined. The TG curves for more complex materials, composite polymers, are not always immediately interpretable in terms of the exact reactions occurring. Such curves can, however, be used for "fingerprint" purposes.

As observed in Fig. 6.33, pure PVA fibers exhibited two weighted-loss steps. The weight loss around 350 °C and 450 °C was considered to reflect the decomposition of side chain (T-ds) and main chain (T-dm) of PVA, respectively. However, for PVA/silica fibers, three degradation steps could be observed. The first step was between 50 °C and 300 °C, the second step was between 300 °C and 400 °C, and the third step was above 400 °C. The first weight loss process, which was associated with the loss of absorbed moisture and/or with the evaporation of trapped solvent (H_2O or C_2H_5OH from TEOS), was independent of the composition for all samples. The second weight loss process corresponded to the degradation of PVA by dehydration on the polymer side chain, whose decomposition temperature was around 350 °C. In the third weight loss process, the polymer residues were further degraded at approximately 450 °C, corresponding to the decomposition of main chain of PVA (T-dm). As seen in Fig. 6.33, the degradation temperature was ambiguous with the increase of the silica. These suggested that some bonding between the polymer and silica formed [56].

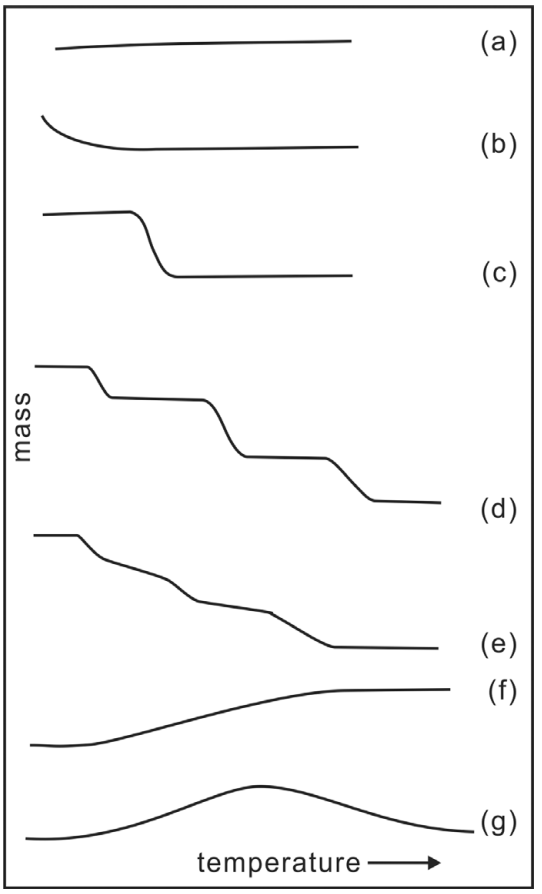

Fig. 6.32 Main types of TG curves [55].

6.4.2 Differential scanning calorimetry (DSC)

Differential scanning calorimetry is a thermoanalytical technique in which the difference in the amount of heat required to increase the temperature of a sample and reference is measured as a function of temperature. Both the sample and reference are maintained at nearly the same temperature throughout the controlled-temperature programme. Any difference in the independent supplies of power to the sample and the reference is then recorded against the programmed (reference) temperature. Generally, the temperature program for a DSC analysis is designed such that the sample holder temperature increases linearly as a function of time. The reference sample should have a well-defined heat capacity over the range of temperatures to be scanned. The apparatus is shown schematically in Fig. 6.34, and a schematic DSC curve demonstrating the appearance of several common features shows in Fig. 6.35.

Thermal events in the sample thus appear as deviations from the DSC baseline, in either an endothermic or exothermic direction, depending upon whether more or

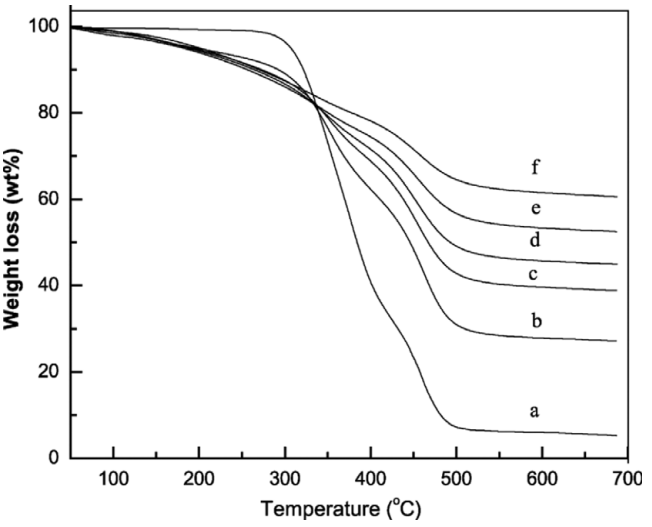

Fig. 6.33 TG curves of various PVA/silica fibers with different silica content: (a) 0 wt% (pure PVA), (b) 22 wt%, (c) 34 wt%, (d) 40 wt%, (e) 49 wt%, (f) 59 wt% [56].

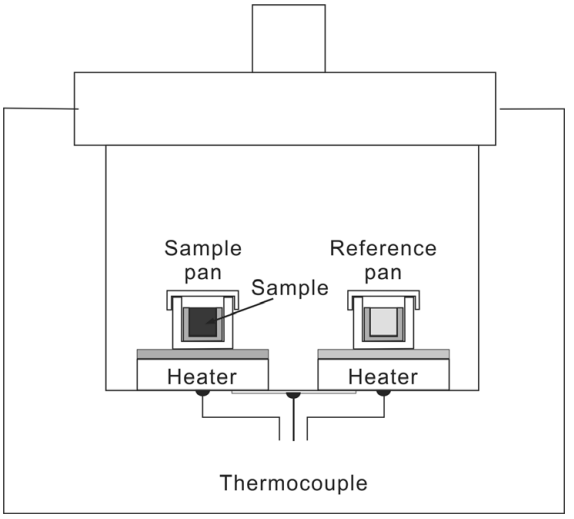

Fig. 6.34 Schematic DSC.

less energy has to be supplied to the sample relative to the reference material. In DSC, endothermic responses are usually represented as being positive, i.e. above the baseline, corresponding to an increased transfer of heat to the sample compared to the reference [55]. By observing the difference in heat flow between the sample and reference, differential scanning calorimeters are able to measure the amount of heat absorbed or released during a physical transformation such as phase transitions. DSC may also be used to observe more subtle phase changes, such as glass transitions.

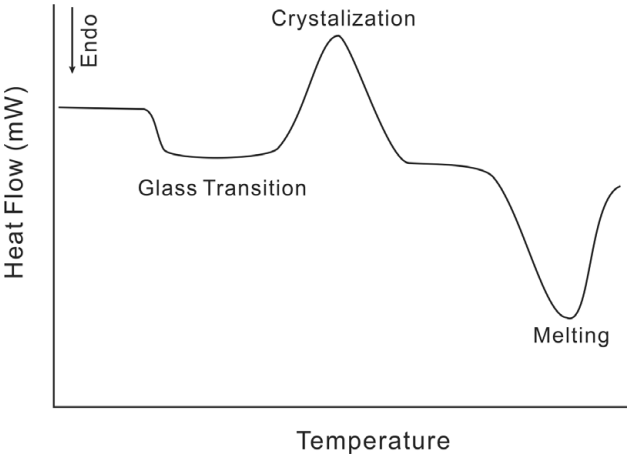

Fig. 6.35 Schematic DSC curve.

The result of a DSC experiment is a curve of heat flux versus temperature or versus time. This curve can be used to calculate enthalpies of transitions. This is done by integrating the peak corresponding to a given transition as expressed by [57]

$$\Delta H = KA, \tag{6.15}$$

where ΔH is the enthalpy of transition, K is the calorimetric constant and A is the area under the curve. The calorimetric constant will vary from instrument to instrument, and can be determined by analyzing a well-characterized sample with known enthalpies of transition

The technique of DSC is used widely for examining polymers to check their composition. Melting points and glass transition temperatures for most polymers are available from standard compilations, and the method can show up possible polymer degradation by the lowering of the expected melting point, T_m, for example. The percentage crystallinity of a polymer can also be found by using DSC since the heat of fusion can be calculated from the area under an absorption peak from the DSC graph. Impurities in polymers can be determined by examining thermograms for anomalous peaks, and plasticizers can be detected at their characteristic boiling points.

Figure 6.36 shows the DSC thermograms of semi-crystalline PLLA resin and electrospun PLLA membranes dried under vacuum at room temperature, and of a quenched sample, which was prepared by first melting PLLA at 220 °C and then rapidly quenching with ice water. It was found that the as-received PLLA exhibits a crystallinity of 35.5%, whereas the electrospun PLLA membrane exhibits barely any crystallinity. The electrospun membrane shows a large crystallization peak at 103 °C, but the quenched samples does not show any apparent crystallization peak under the temperature scan with the same heating rate (20 °C/min), which suggested that cold crystallization of the electrospun membranes during heating is enhanced, probably due to the chain orientation. The decrease in glass transition temperature can be attributed to the very large surface-to-volume ratio of the electrospun membranes having air as the

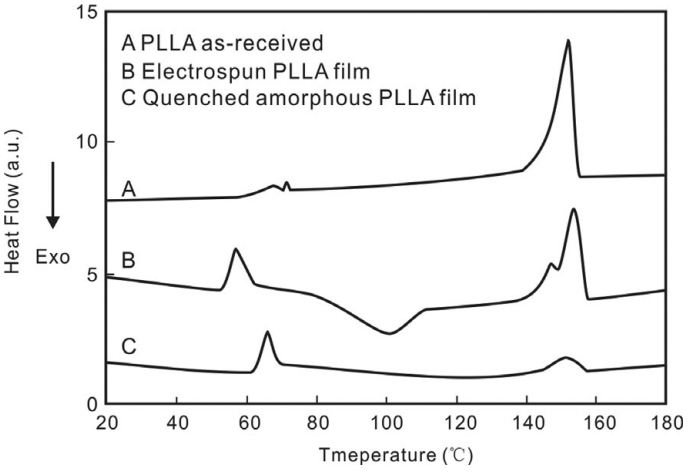

Fig. 6.36 DSC thermograms of as-received PLLA (line A); electrospun PLLA dried at room temperature (line B) and quenched PLLA in ice water (line C) [36].

plasticizer. The extent of crystallinity in electrospun PLLA membrane is very low, indicating that the majority of the chains are in the non-crystalline state. This was explained by the rapid solidification process of stretched chains under a high elongation rate during the later stages of electrospinning hindering the development of crystallinity, as the chains do not have time to form crystalline registration [36].

6.5 Characterization of other properties

6.5.1 Wettability and contact angle

Wettability is a very important property of nanofiber products when the applications relate to fluids in such fields as filtration and bioengineering with regards to the requirements set by converting and end use.

Consider a drop of water resting on a horizontal membrane, the drop of water will adopt a position between completely spreading out on the surface or a round drop resting lightly on the surface. Between these two extremes, the general shape of the drop will exhibit a measurable contact angle. The force exerted by the air–water interfacial tension acts at a tangent to the surface of the drop with its horizontal component, pulling the circumference of the drop toward its center. The water–solid interfacial tension pulls the circumference of the water drop area of contact with the solid toward the center. At the equilibrium these two forces are balanced by the air–solid interfacial tension acting to pull the circumference of the drop's area of contact away from its center [58].

Figure 6.37 shows the schematic of the wetting of solid surfaces. The surface is water-wet (hydrophilic) when the contact angle is less than 90° and the pressure difference across the interface is positive; it is neutral-wet at contact angles close to 90°; and the surface is hydrophobic for angles greater than 90°. The contact angle and interfacial tensions of a sessile drop are related according to Young's equation:

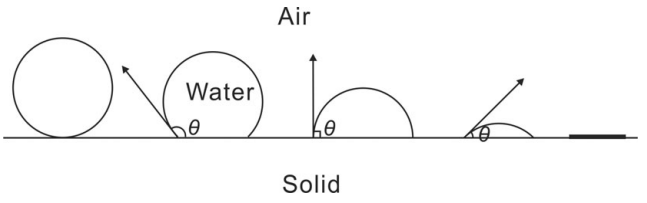

Fig. 6.37 Schematic of wettability.

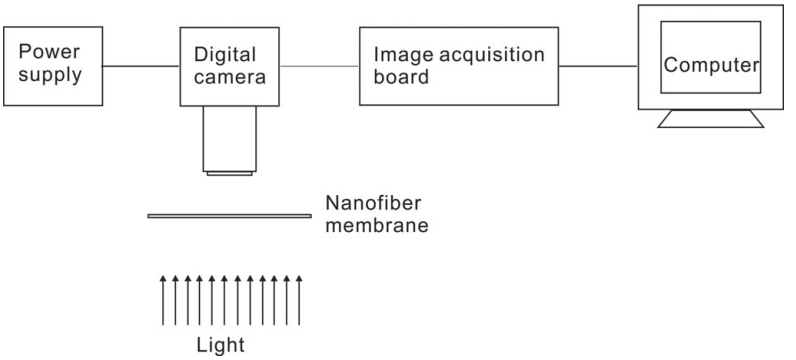

Fig. 6.38 Schematic of a pc-based wettability system.

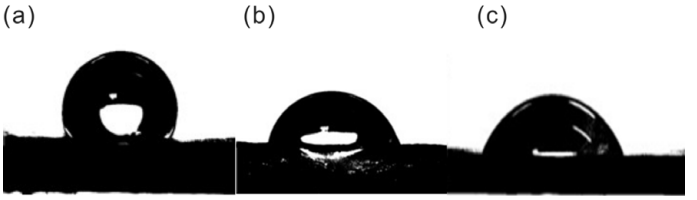

Fig. 6.39 Wettability of (a) an electrospun PLA nanofiber, (b) a 1 wt% chitosan coated electrospun PLA nanofiber and (c) an 8 wt% chitosan coated electrospun PLA nanofiber

$$\gamma_s = \gamma_{sl} + \gamma_l \cos\theta. \tag{6.16}$$

The wettability of a nanofiber product can be tested by measuring the contact angle. The TRI Wettability System is a pc-based wettability characterization system. Figure 6.38 shows the schematic of a pc-based system. It provides a visualization system suitable for the characterization of wettability and absorbency of porous fibers/fiber bundles/yarns; has the ability to obtain dynamics of complete droplet shape for slow and fast absorption processes; and from the source data and absorption process modeling, structural and transport parameters of nanofibrous system can be extracted. Distilled water and/or different fluid droplets can be utilized for the measurement. Figure 6.39 shows the images captured with a pc-based wettability characterization system. The contact angle of an electrospun PLA nanofiber decreased from 119.05° to 60.84° as the weight ratio of coated chitosan increased from 0% to 8%.

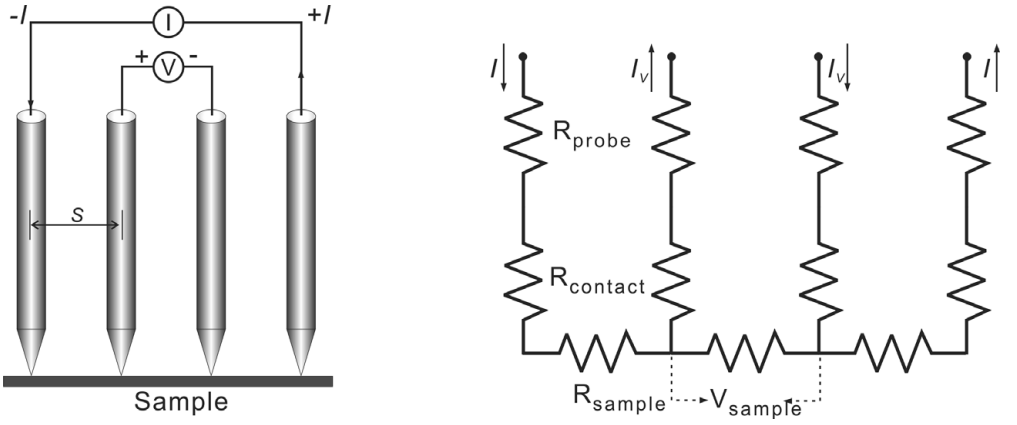

Fig. 6.40 Schematic of 4-point probe configuration.

6.5.2 Electrical conductivity

For general purpose resistance measurements and current–voltage (I–V) curve generation, 2-point electrical measurements are normally used. However, when the resistance being measured is relatively low, or the resistance of the probes or the contacts is relatively high, a 4-point probe will yield more accurate results.

The purpose of the 4-point probe is to measure the resistivity of any semiconductor material. It can measure either bulk or thin film specimen. A typical 4-point probe setup consists of four equally spaced tungsten metal tips with finite radius. Each tip is supported by springs on the other end to minimize sample damage during probing. The four metal tips are part of an auto-mechanical stage that travels up and down during measurements. A high-impedance current source is used to supply current through the outer two probes; a voltmeter measures the voltage across the inner two probes to determine the sample resistivity, as shown in Fig. 6.40. Typical probe spacing s is around 1 mm.

For a very thin film (thickness $t << s$), assume that the metal tip is infinitesimal, samples are semi-infinite in lateral dimension and a ring protrusion of current emanaties from the outer probe tips. The differential resistance is:

$$\Delta R = \rho\left(\frac{dx}{A}\right), \tag{6.17}$$

where ρ is the resistivity and A is the area of the ring, which is expressed as $A = 2\pi xt$.

The integration between the inner probe tips will be:

$$R = \int_{x_1}^{x_2} \rho \frac{dx}{2\pi xt} = \int_{s}^{2s} \frac{\rho}{2\pi t}\frac{dx}{x} = \frac{\rho}{2\pi t}\ln 2. \tag{6.18}$$

Consequently, for $R=V/2I$, the resistivity for a thin sheet is:

$$\rho = \frac{\pi t}{\ln 2}\left(\frac{V}{I}\right). \tag{6.19}$$

This expression is independent of the probe spacing s. In general, the sheet resistivity can be expressed as:

$$R_s = \rho/t = k(V/I), \tag{6.20}$$

where k is a geometric factor that will be different for different samples.

As a simple and useful tool, the 4-point probe system has been widely used to measure the electrical conductivity (resistivity) of nanofiber membranes [59, 60].

6.5.3 Electrochemical properties

6.5.3.1 Linear-sweep voltammetry and cyclic voltammetry

The terms voltammetry covers a range of techniques involving the application of a linearly varying potential between a working electrode and a reference electrode in an electrochemical cell with electrolyte in between. The current through the cell is monitored continuously. A graph is traced on a recorder of current against potential, this is known as a voltammogram [61].

The most straightforward technique is linear-sweep voltammetry (LSV). In linear-sweep voltammetry (LSV) the current at a working electrode is measured while the potential between the working electrode and the reference electrode is swept linearly in time. The voltage is scanned from a lower limit to an upper limit, and the current response is plotted as a function of voltage. The characteristics of the linear-sweep voltammogram recorded depend on a number of factors including the rate of the electron transfer reaction (s), the chemical reactivity of the electroactive species and the voltage scan rate.

Choi *et al*. [62] used linear-sweep voltammetry to determine the electrochemical stability of electrospun poly(vinylidene fluoride) nanofibrous membrane. The measurement was done with a three-electrode electrochemical cell consisting of a nickel working electrode, a lithium reference, and a counterelectrode. The measurement was made at room temperature, the potential was scaned between 2.0 V and 5.0 V and the scan rate was 1 mV/s. The oxidation peak of the PVDF nanofibrous electrolyte was observed at about 4.5 V, which is 0.6 V higher than the value of 3.9 V for free liquid electrolyte, as shown in Fig. 6.41.

Compared with LSV, cyclic voltammetry (CV) takes the experiment a step further. In a cyclic voltammetry experiment, the working electrode potential is ramped linearly versus time, as in LSV, and when it reaches a set potential, the working electrode's potential ramp is inverted. This inversion can be repeated multiple times during a single experiment. The current at the working electrode is plotted against the applied voltage to give the cyclic voltammogram trace. The utility of cyclic voltammetry is highly dependent on the analyte being studied. The analyte has to be redox active, and is highly desired for it to be able to display a reversible wave. When an analyte is reduced or oxidized on a forward scan and is then reoxidized or rereduced in a predictable way on the return scan, a reversible wave will be obtained.

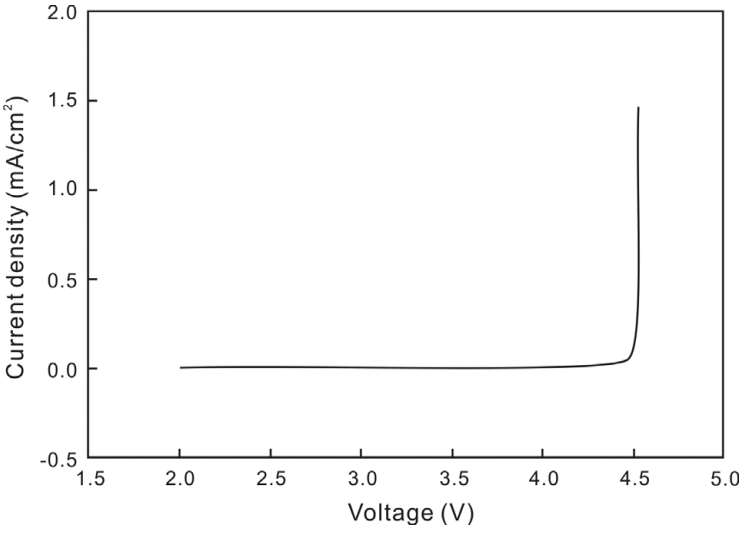

Fig. 6.41 Linear-sweep voltammogram of PVDF nanofibrous polymer electrolyte [62].

For a reversible electrochemical reaction the CV recorded has certain well-defined characteristics.

(I) The voltage separation between the current peaks is

$$\Delta E = E_{pa} - E_{pc} = \frac{59}{n}\text{mV}, \tag{6.21}$$

where, E_{pa} and E_{pc} are, respectively, the oxidation and reduction peak potentials.

(II) The positions of peak voltage do not alter as a function of the voltage scan rate.

(III) The ratio of the peak currents is equal to one

$$\frac{i_{pa}}{i_{pc}} = 1, \tag{6.22}$$

where i_{pa} and i_{pc} are, respectively, the oxidation and reduction peak currents.

(IV) The peak currents are proportional to the square root of the scan rate

$$\begin{aligned} i_{pa} &\propto \sqrt{V} \\ i_{pc} &\propto \sqrt{V}, \end{aligned} \tag{6.23}$$

where V is the scan rate.

Because of the interest in developing supercapacitors from electrospun nanofiber electrolytes, CV has been actively employed in the characterization of electrochemical properties of nanofibers [63–66] Lee *et al*. [67] used CV to evaluate the electrochemical performance of electrospun carbon nanofiber (CNF) and polypyrrole (Ppy) coated electrospun CNF with GC/Ppy; the CV curves are as shown in Fig. 6.42. The CV curves show that the addition of Ppy improves the electrode capacitance dramatically.

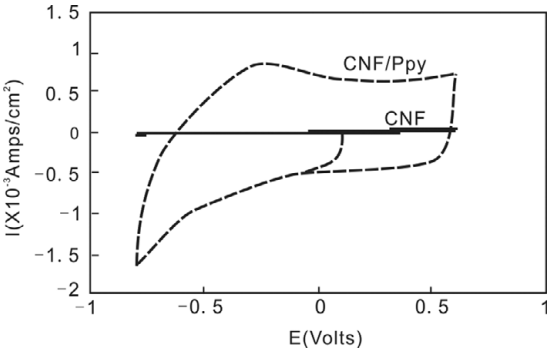

Fig. 6.42 CV curves of CNF and CNF/Ppy [67].

6.5.3.2 Chronopotentiometry

Chronopotentiometry (CP) involves the study of voltage transients at an electrode upon which a constant current is imposed [68]. It is also known as galvanostatic voltammetry. In this technique, a constant current is applied to an electrode, and its voltage response indicates the changes in electrode processes occurring at its interface. Considering the electron transfer reaction $O + e^- = R$, for example. Before the current step, the concentration of O at the electrode surface is the same as in the bulk solution. The initial potential is the rest potential or the open circuit potential (E_{oc}). Once the (reducing) current step has been applied, O is reduced to R at the electrode surface in order to support the applied current, and the concentration of O at the electrode surface therefore decreases. This sets up a concentration gradient for O between the bulk solution and the electrode surface, and molecules of O diffuse down this concentration gradient to the electrode surface. The potential is close to the redox potential for $O + e^- = R$, and its precise value depends upon the Nernst equation:

$$E = E^0 + \frac{0.059}{n} \log \frac{C_O^s}{C_R^s}, \tag{6.24}$$

where $C_O^s$and C_R^s are the surface concentrations of O and R, respectively. These concentrations vary with time, so the potential also varies with time, which is reflected in the finite slope of the potential vs. time plot at this stage. Once the concentration of O at the electrode surface is zero, the applied current can no longer be supported by this electron transfer reaction, so the potential changes to the redox potential of another electron transfer reaction. If no other analyte has been added to the solution, the second electron transfer reaction will involved reduction of the electrolyte; that is, there is a large change in the potential.

Chronopotentiometry is a common tool in the study of electrochemical storage and energy conversion devices (e.g. fuel cells, batteries and super capacitors). Lee *et al*. [67] conducted a series of CP measurements on electrospun CNF and Ppy coated CNF electrodes at different current densities. The result is as shown in Fig. 6.43. They also used the CP results to calculate the specific capacitance of Ppy. The equation used is: specific capacitance (F/g) = I /m / (dV/dt), where I is the current applied (A), m is the

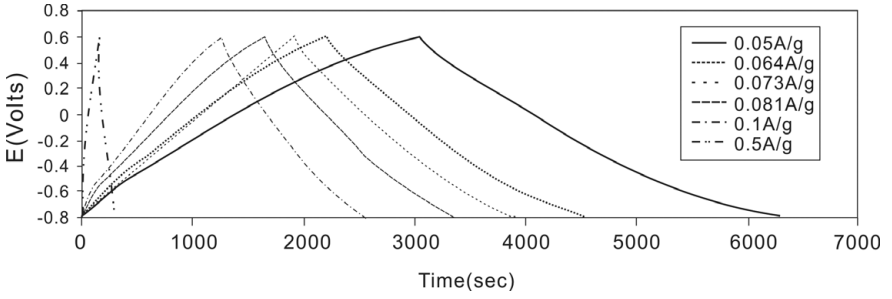

Fig. 6.43 CP results of CNF/Ppy [67].

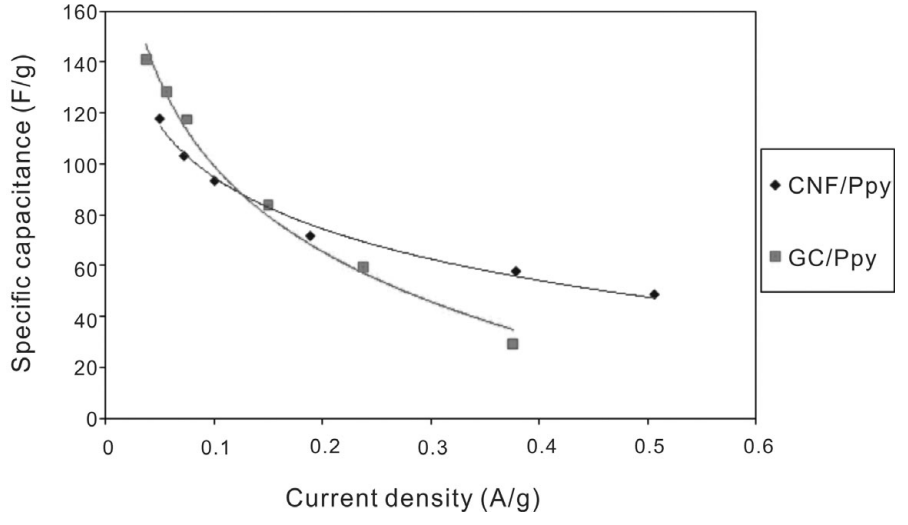

Fig. 6.44 Specific capacitance calculated from CP data vs current density [67].

mass of Ppy (g), and dV/dt is the slope (V/s) of the curves. The calculated specific capacitance as a function of current density from both electrodes is summarized in Fig. 6.44. At the same discharge rate of 0.05 A/g, the specific capacitance is 117 F/g for CNF/Ppy and 132 F/g for GC/Ppy. These capacitances are relatively high compared to previous studies incorporating Ppy with single (or multi)-walled carbon nanotubes in aqueous electrolyte. The result also demonstrated that Ppy is able to retain its intrinsic capacitance in the fibrous form.

6.5.4 Magnetic properties

Apply an external magnetic field, H, to a material, the material will respond to the magnetic field by generating a flux, i.e. the materials will be magnetized. The relation between the magenitc field and the flux density, known as induction, B, is described as:

$$B = \mu H = \mu_0 H + M, \tag{6.25}$$

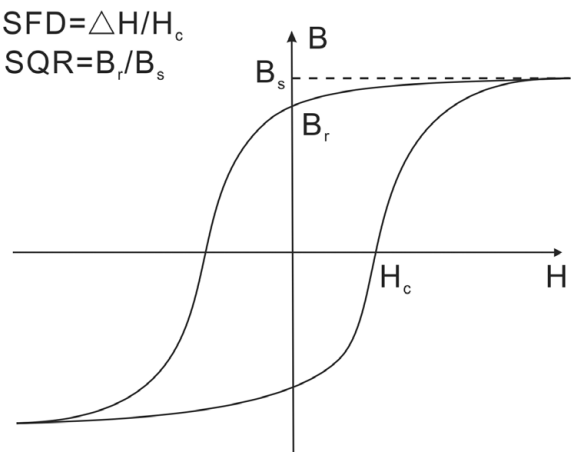

Fig. 6.45 A typical hysteresis loop of a ferromagnetic material.

where μ_0 is the permeability of free space, μ is the absolute permeability and M is the magnetization. And the magnetic susceptibility, χ, is defined to describe the relation between magnetization and magnetic field

$$M = \chi H, \tag{6.26}$$

which gives

$$\mu = \mu_0(1 + \chi). \tag{6.27}$$

In most materials the permeability is very close to unity and typically differs from unity by a few parts per 10^5. Materials that have $\mu < 1$ are diamagnetic, and paramagnetic materials have $\mu > 1$. For ferromagnetic materials, the value of μ can be very large.

Vibrating sample magnetometer (VSM) systems are usually used to measure the magnetic properties of materials as a function of magnetic field, temperature and time. This technique involves vibrating the sample at low frequencies (e.g. 80 Hz) in the gradient region of a copper detection coil and using a lock-in amplifier to detect the response. These instruments are capable of achieving sensitivities down to about 10^{-9} Am^2 for a second average. Powders, solids, liquids, single crystals and thin films are all readily accommodated in a VSM. The sensitivity, accuracy, speed and ease of use of VSMs have made them the most widely used instrument for magnetic characterization of materials. Generally a hysteresis loop is measured to give the relationship between the magnetization and the applied magnetic field H. The parameters extracted from the hysteresis loop are used to characterize the magnetic properties of materials, including the saturation magnetization M_s, the resonance M_r, the coercivity H_c, the squareness ratio SQR, μ, defined by the slope of the curve, and the switching field distribution SFD. Figure 6.45 shows a typical hysteresis loop of a ferromagnetic material. The squareness ratio is essentially a measure of how square the hysteresis loop is. The formal definition of the coercivity H_c is the field required to reduce the magnetization to zero after saturation. H_c is a very complicated parameter for magnetic films and is related to the reversal

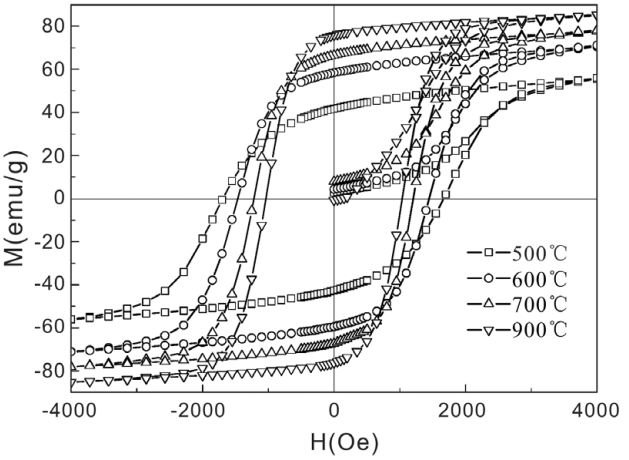

Fig. 6.46 Magnetic properties of the electrospun $CoFe_2O_4$ nanoribbons and nanofibers at low temperature (2 K) [69].

mechanism and the magnetic microstructure, i.e. shape and dimensions of the crystallites, nature of the boundaries, and also the surface and initial layer properties, etc.

Wang *et al*. [69] measured the magnetic properties of $CoFe_2O_4$ nanofibers calcinated at different temperatures. The hysteresis loop is as shown in Fig. 6.46. As the figure suggests, saturation magnetizations of these fibers decrease with decreasing calcination temperature due to the decrease of $CoFe_2O_4$ nanoparticles which determines the magnetic properties of the fibers. The SQR (M_r/M_s) for nanofibers also increased with the increase of temperature. The M_r/M_s for nanofibers calcinated at 600℃ is equal to the theoretical value, and the values for nanofibers calcinated at 700℃ and 900℃ are 0.86 and 0.89, respectively, which are higher than the theoretical value. This indicates that such 1-D nanostuctures consist of randomly oriented equiaxial particles with cubic magnetic anisotropy.

With a SQUID (superconducting quantum interference device) magnetometer–susceptometer (SQUID-MS), both accuracy and sensitivity can be achieved during measurements of magnetism and magnetic properties of materials. A SQUID-MS combines several superconducting components, including a SQUID, superconducting magnet, detection coils, flux transformer and superconducting shields. For a measurement, a sample, typically less than a few millimeters in size, is attached to a sample rod and scanned through the center of a first- or second-order superconducting gradiometer, which forms a closed flux transformer that is coupled to a SQUID. The signal from the SQUID is then recorded as a function of sample position. The shape and magnitude of the response curve can then be analyzed for a corresponding magnetic moment. SQUID-MS systems typically offer the ability to measure in applied fields of up to 7 T over a temperature range from above room temperature down to below 2 K [70].

Bayat et al[71, 72] measured the magnetic properties of electrospun Fe_3O_4/carbon composite nanofibers using a SQUID-MS (Quantum Design, CA, USA). The magnetic moment (emu) as a function of applied magnetic field (Oe) at room temperature (300 K)

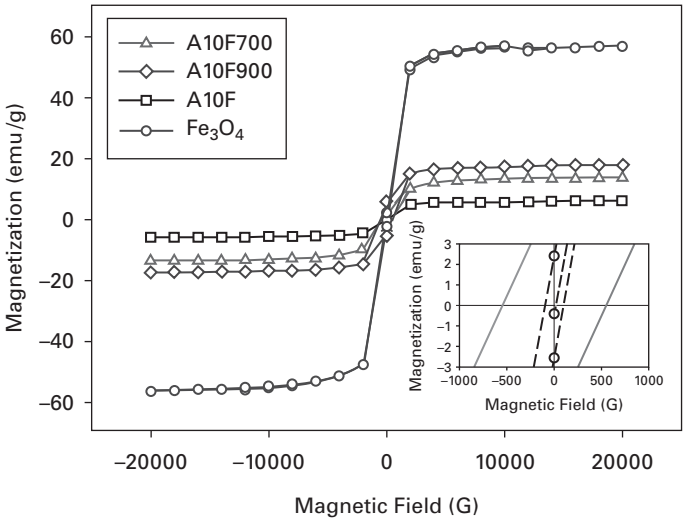

Fig. 6.47 Magnetic hysteresis loop of Fe_3O_4 nanoparticles and electrospun Fe_3O_4/carbon composite nanofibers [71].

is shown as Fig. 6.47. The M_s of pristine electropun PAN nanofibers with 10 wt% Fe_3O_4 increased from 5.2 emu/g to 12 emu/g and 16 emu/g after carbonization at 700 °C and 900 °C, respectively. At the same time, the H_c value increased from 105 Oe for pristine sample to 500 Oe and 600 Oe, respectively. The inset shown in Fig. 6.47 exhibits the hysteresis in pristine electrospun sample in comparison to Fe_3O_4 nanoparticles. This results proved that the electrospinning method was capable of translating magnetic behavior of Fe_3O_4 nanoparticles into the nanofibrous structure due to relatively uniform distribution of Fe_3O_4 nanoparticles in the matrix.

References

1. J. Cowhig, *The World Under the Microscope. The World of Nature*. London: Orbis Books, 1974.
2. G. Danilatos, "Foundations of environmental scanning electron microscopy," *Advances in Electronics and Electron Physics*, vol. 71, pp. 109–250, 1988.
3. Scanning Electron Microscope (SEM)-Machine Variables. [cited 2010 May 11]; Available from: http://131.229.88.77/microscopy/semvar.html#introduction.
4. F. Ko, and M. Gandhi, Producing nanofiber structures by electrospinning for tissue engineering, in *Nanofibers and Nanotechnology in Textiles*, P. J. Brown, and Kathryn Stevens Ed. Woodhead Publishing, in association with The Textile Institute, 2007, p. 22.
5. D. H. Reneker, and I. Chun, "Nanometre diameter fibres of polymer, produced by electrospinning," *Nanotechnology*, vol. 7(3), pp. 216–223, 1996.
6. F. K. Ko, *et al*. "Structure and properties of carbon nanotube reinforced nanocomposites," in *Proceedings of the 43rd Structures, Structural Dynamics and Materials Conference*, vol. 3, pp. 1779–1787, Derver, Co, April 2002.

7. S. C. Lim, *et al*., "Nanomanipulator-assisted fabrication and characterization of carbon nanotubes inside scanning electron microscope," *Micron*, vol. 36(5), pp. 471–476, 2005.
8. M. Yu, *et al*., "Strength and breaking mechanism of multiwalled carbon nanotubes under tensile load," *Science*, vol. 287(5453), p. 637, 2000.
9. M. Yu, *et al*., "Three-dimensional manipulation of carbon nanotubes under a scanning electron microscope," *Nanotechnology*, vol. 10, pp. 244–252, 1999.
10. B. Samuel, *et al*., "Mechanical testing of pyrolysed poly-furfuryl alcohol nanofibres," *Nanotechnology*, vol. 18(11), pp. 115 704–115 704, 2007.
11. R. Wang, *OM, SEM, TEM, AFM*. MTRL592B Lecture Notes, 2007.
12. M. O'Keefe, and Y. Shao-Horn, "Sub-ångstrom atomic-resolution imaging from heavy atoms to light atoms," *Microscopy and Microanalysis*, vol. 10(01), pp. 86–95, 2004.
13. S. Megelski, *et al*., "Micro- and nanostructured surface morphology on electrospun polymer fibers," *Macromolecules*, vol. 35(22), pp. 8456–8466, 2002.
14. S. McCullen, *et al*., "Morphological, electrical, and mechanical characterization of electrospun nanofiber mats containing multiwalled carbon nanotubes," *Macromolecules*, vol. 40(4), pp. 997–1003, 2007.
15. F. Ko, *et al*., "Electrospinning of continuous carbon nanotube-filled nanofiber yarns," *Advanced Materials*, vol. 15(14), pp. 1161–1165, 2003.
16. T. Kuzumaki, *et al*., "Selective processing of individual carbon nanotubes using dual-nanomanipulator installed in transmission electron microscope," *Applied Physics Letters*, vol. 79(27), pp. 4580–4582, 2001.
17. A. Humphris, M. Miles, and J. Hobbs, "A mechanical microscope: High-speed atomic force microscopy," *Applied Physics Letters*, vol. 86, p. 034106, 2005.
18. D. Sarid, *Scanning Force Microscopy*. Oxford University Press, 1994.
19. R. Jaeger, H. Schonherr, and G. Vancso, "Chain packing in electro-spun poly (ethylene oxide) visualized by atomic force microscopy," *Macromolecules*, vol. 29(23), pp. 7634–7636, 1996.
20. M. Demir, *et al*., "Electrospinning of polyurethane fibers," *Polymer*, vol. 43(11), pp. 3303–3309, 2002.
21. G. Binnig, and H. Rohrer, "Scanning tunneling microscopy," *IBM Journal of Research and Development*, vol. 30(4), p. 355, 1986.
22. C. Bai, *Scanning Tunneling Microscopy and its Application*, 2nd edition Springer, 1999.
23. C. Chen, *Introduction to Scanning Tunneling Microscopy*. USA: Oxford University Press, 1993.
24. Bonnell, D., "Basic principles of scanning probe microscopy," in *Scanning Probe Microscopy & Spectroscopy: Theory, Techniques, and Applications*, ed. D. Bonnell and B. Huey, Ed. New York: Wiley-VCH, Inc., 2001, pp. 7–42.
25. K. Oura, *et al*., *Surface Science: an Introduction (Advanced Texts in Physics)*. 2003. **DETAILS**?
26. P. Kim, *et al*., "STM study of single-walled carbon nanotubes," *Carbon*, vol. 38(11–12), pp. 1741–1744, 2000.
27. H. Ago, *et al*., "STM study of molecular adsorption on single-wall carbon nanotube surface," *Chemical Physics Letters*, vol. 383(5–6), pp. 469–474, 2004.
28. K. F. Kelly, *et al*., "Insight into the mechanism of sidewall functionalization of single-walled nanotubes: an STM study," *Chemical Physics Letters*, vol. 313(3–4), pp. 445–450, 1999.
29. D. Bonifazi, *et al*., "Microscopic and spectroscopic characterization of paintbrush-like single-walled carbon nanotubes," *Nano Letters*, vol. 6(7), pp. 1408–1414, 2006.

30. L. S. Birks, and H. Friedman, "Particle size determination from X-ray line broadening," *Journal of Applied Physics*, 17, 1946.
31. A. Segmüller, and M. Murakami, *Characterization of Thin Films by X-ray Diffraction. Thin Films from Free Atoms and Particles*. New York: Academic Press, pp. 325–351, 1985.
32. D. Li, Y. Wang, and Y. Xia, "Electrospinning of polymeric and ceramic nanofibers as uniaxially aligned arrays," *Nano Letters*, vol. 3(8), pp. 1167–1171, 2003.
33. H. Fong, *et al*., "Generation of electrospun fibers of nylon 6 and nylon 6-montmorillonite nanocomposite," *Polymer*, vol. 43(3), pp. 775–780, 2002.
34. J. Ayutsede, *et al*., "Regeneration of *Bombyx mori* silk by electrospinning. Part 3: characterization of electrospun nonwoven mat," *Polymer*, vol. 46(5), pp. 1625–1634, 2005.
35. O. Glatter, and O. Kratky, *Small Angle X-ray Scattering*. London: Academic Press, 1982.
36. X. Zong, *et al*., "Structure and process relationship of electrospun bioabsorbable nanofiber membranes," *Polymer*, vol. 43(16), pp. 4403–4412, 2002.
37. E. Zussman, *et al*., "Tensile deformation of electrospun nylon-6, 6 nanofibers," *Journal of Polymer Science–B–Polymer Physics Edition*, vol. 44(10), pp. 1482–1489, 2006.
38. S. Diamond, "Mercury porosimetry: an inappropriate method for the measurement of pore size distributions in cement-based materials," *Cement and Concrete Research*, vol. 30(10), pp. 1517–1525, 2000.
39. E. W. Washburn, "Note on a method of determining the distribution of pore sizes in a porous material," *Proceedings of the National Academy of Sciences of the United States of America*, vol. 17(4), pp. 115–116, 1921.
40. W. -J. Li, *et al*., "Electrospun nanofibrous structure: a novel scaffold for tissue engineering," *Journal of Biomedical Materials Research*, vol. 60(4), pp. 613–621, 2002.
41. D. Bizzotto, *MTRL592B Lecture: Micro-Raman and micro-FTIR for surface analysis*, 2007.
42. D. Gardiner, and H. Bowley, *Practical Raman Spectroscopy*. Springer Verlag, 1989.
43. P. Matousek, *et al*., "Numerical simulations of subsurface probing in diffusely scattering media using spatially offset Raman spectroscopy," *Applied spectroscopy*, vol. 59(12), pp. 1485–1492, 2005.
44. J. Stephens, *et al*., ""Real time" Raman studies of electrospun fibers," *Applied Spectroscopy*, vol. 55(10), pp. 1287–1290, 2001.
45. A. Rao, *et al*., "Effect of van der Waals interactions on the Raman modes in single walled carbon nanotubes," *Physical Review Letters*, vol. 86(17), pp. 3895–3898, 2001.
46. W. Weber, and R. Merlin, *Raman Scattering in Materials Science*. Berlin: Springer, 2000.
47. J. Akitt, and B. Mann, *NMR and Chemistry: an Introduction to Modern NMR Spectroscopy*. CRC, 2000.
48. K. Ohgo, *et al*., "Preparation of non-woven nanofibers of *Bombyx mori* silk, *Samia cynthia ricini* silk and recombinant hybrid silk with electrospinning method," *Polymer*, vol. 44(3), pp. 841–846, 2003.
49. R. Meredith, "The tensile behaviour of raw cotton and other textile fibres," *Journal of Textile Instruments*, vol. 36, p. 107, 1945.
50. M. J. Coplan, in *W.A.D.C. Technical Report*, US Air Force, pp. 53–21.
51. E. Zussman, *et al*., "Mechanical and structural characterization of electrospun PAN-derived carbon nanofibers," *Carbon*, vol. 43(10), pp. 2175–2185, 2005.
52. M. Naraghi, *et al*., "Novel method for mechanical characterization of polymeric nanofibers," *Review of Scientific Instruments*, vol. 78, p. 085108, 2007.
53. E. P. S. Tan, S. Y. Ng, and C. T. Lim, "Tensile testing of a single ultrafine polymeric fiber," *Biomaterials*, vol. 26(13), pp. 1453–1456, 2005.

54. S. Chan, *et al*., *Tensile Stress-Strain Response of Small-diameter Electrospun Fibers*, 2012, Agilent Technologies application note.
55. M. Brown, *Introduction to Thermal Analysis: Techniques and Applications*. Netherlands: Springer, 2001.
56. C. Shao, *et al*., "Fiber mats of poly(vinyl alcohol)/silica composite via electrospinning," *Materials Letters*, vol. 57(9–10), pp. 1579–1584, 2003.
57. M. J. O'Neill, "The analysis of a temperature-controlled scanning calorimeter," *Analytical Chemistry*, vol. 36(7), pp. 1238–1245, 1964.
58. E. C. Donaldson, and W. Alam, *Wettability*. Gulf Publishing Company, 2008.
59. H. S. Kim, *et al*., "Carbon nanotube-adsorbed electrospun nanofibrous membranes of nylon 6," *Macromolecular Rapid Communications*, vol. 27(2), pp. 146–151, 2006.
60. P. K. Kahol, and N. J. Pinto, "An EPR investigation of electrospun polyaniline-polyethylene oxide blends," *Synthetic Metals*, vol. 140(2–3), pp. 269–272, 2004.
61. B. R. Eggins, *Chemical Sensors and Biosensors*, England: John Wiley & Sons Ltd., 2002.
62. S. W. Choi, *et al*., "An electrospun poly(vinylidene fluoride) nanofibrous membrane and its battery applications," *Advanced Materials*, vol. 15(23), pp. 2027–2032, 2003.
63. C. Kim, and K. Yang, "Electrochemical properties of carbon nanofiber web as an electrode for supercapacitor prepared by electrospinning," *Applied Physics Letters*, vol. 83, p. 1216, 2003.
64. C. Kim, *et al*., "Supercapacitor performances of activated carbon fiber webs prepared by electrospinning of PMDA-ODA poly(amic acid) solutions," *Electrochimica Acta*, vol. 50(2–3), pp. 883–887, 2004.
65. M. Abidian, D. Kim, and D. Martin, "Conducting-polymer nanotubes for controlled drug release," *Advanced Materials*, vol. 18(4), pp. 405–409, 2006.
66. J. Huang, *et al*., "Electrospun palladium nanoparticle-loaded carbon nanofibers and their electrocatalytic activities towards hydrogen peroxide and NADH," *Advanced functional materials*, vol. 18(3), pp. 441–448, 2008.
67. N. Lee, *et al*., *Polypyrrole Coated Carbon Nanofibers for Supercapacitor Electrodes*, in *SAMPE*2010: Seattle.
68. D. Linden, and T. B. Reddy, eds. *Handbook of Batteries (3rd Edition)*. McGraw-Hill, 2002.
69. Z. Wang, *et al*., "Preparation of one-dimensional $CoFe_2O_4$ nanostructures and their magnetic properties," *The Journal of Physical Chemistry C*, vol. 112(39), pp. 15 171–15 175, 2008.
70. J. Clarke, and A. Braginski, *The SQUID Handbook: Applications of SQUIDs and SQUID Systems*. Vch Verlagsgesellschaft Mbh, 2004.
71. M. Bayat, H. Yang, and F. Ko, *Electrical and Magnetic Properties of Fe_3O_4/Carbon Composite Nanofibres*, in *SAMPE*2010: Seattle.
72. M. Bayat, H. Yang, and F. Ko, "Electromagnetic properties of electrospun Fe_3O_4/carbon composite nanofibers," *Polymer*, vol. 52(7), pp. 1645–1653, 2011.

7 Bioactive nanofibers

7.1 The development of biomaterials

A biomaterial has been defined by Hench and Erthridge as a synthetic material used to replace a part or a function of the body in a safe, reliable, economic and physiologically acceptable manner. The Celmson University Advisory Board for Biomaterials has formally defined a biomaterial to be "a systemically and pharmacologically inert substance designed for implantation within or in a medical device, intended to interact with biological systems." Biomaterials have been widely used in many areas, including replacement of damaged parts (artificial hip), assisting in healing (sutures), improving biological functions (pacemaker, contact lens), correcting abnormalities (spinal rods), cosmetics (augmentation mammoplasty), aiding diagnoses (probes) and aiding treating (catheters). A material is considered biocompatible if it causes no irritation, allergic or toxic responses when used in a biological system [1] Table 7.1 provides some examples of biomaterials used in the body.

Biotechnology and nanotechnology are the two of twenty-first century's most promising technologies. Convergence of these two technologies is expected to create innovations and play a vital role in various biomedical applications. The symposium in 2000 entitled "Nanoscience and Technology: Shaping Biomedical Research" held by the National Institutes of Health Bioengineering Consortium (BECON) addressed eight areas of nanoscience and nanotechnology, which include synthesis and use of nanostructures, applications of nanotechnology to therapy, biomimetic and biologic nanostructures, electronic–biology interface, devices for early detection of disease, tools for the study of single molecules, nanotechnology and tissue engineering [2].

In a living system, the characteristics of a biological tissue are based on a hierarchical classification system of the levels of its structure – the nanoscale fundamental building blocks, and the fibrous form of the fundamental building blocks. The convergence of biomaterial science and nanotechnology elicits specific interactions with cell integrins and thereby direct cell proliferation, differentiation and extracellular matrix production and organization [3]. Reducing the fiber diameter can proportionally increase the ratio of the exposed polymer chains together with its functional groups. Polymer nanofibers can provide a proper route to emulate or duplicate biosystems – a biomimetic approach. On the other hand, cells attach and organize well around fibers with diameters smaller than themselves. Many researchers [4–9] have shown evidence that, apart from surface chemistry, the nanoscale surface features and topography also have important effects on

Table 7.1 Materials for use in the body

Materials	Advantages	Disadvantages	Examples
Polymers (nylon, silicone rubber, polyester, polytetrafuoroethylene, etc.)	Resilient, easy to fabricate	Deforms with time, may degrade	Sutures, blood vessels, hip socket, ear, nose, other soft tissues,
Metals (Ti and its alloys, Co–Cr alloys, stainless steels, Au, Ag, Pt, etc.)	Strong, tough, ductile	May corrode, dense, difficult to make	Joint replacements, bone plates and screws, dental root implants, pacer and suture wires
Ceramics (aluminum oxide, calcium phosphates including hydroxyapatite, carbon)	Very biocompatible, inert, strong in compression	Brittle, not resilient, difficult to make	Dental; femoral head of hip replacement, coating of dental and orthopedic implants
Composites (carbon–carbon, wire or fiber reinforced bone cement)	Strong, tailor-made	Difficult to make	Joint implants, heart valves

regulating cell behavior in terms of cell adhesion, activation, proliferation, alignment and orientation. Recently, electrospinning has been widely studied as an enabling technology to develop bioactive nanofibers for various biomedical applications including tissue engineering, drug delivery and biosensors, as shown in Fig. 7.1.

7.2 Bioactive nanofibers

7.2.1 Nanofibers for tissue engineering

7.2.1.1 Extracellular matrices for tissue engineering

Over 20 years ago, tissue engineering had already been recognized by the US National Science Foundation as an emerging area of national importance [10]. Tissue engineering is a promising approach to treat the loss or malfunction of a tissue or organ without the limitations of current therapies. Tissue engineering typically uses exogenous 3-D extracellular matrices (ECMs) to engineer new natural tissues from isolated cells. This approach is based on the following observations [11]. (1) Every tissue undergoes remodeling. (2) Isolated cells tend to reform the appropriate tissue structure under appropriate conditions. (3) Although isolated cells have the capacity to form the appropriate tissue structure, they do so only to a limited degree when placed as a suspension into tissue. Such cells begin without any intrinsic organization and have no template to guide restructuring. (4) Tissue cannot be implanted in large volumes; cells will not survive if they are located more than a few hundred micrometers from the nearest capillary. Thus, the ECMs are designed so that the scaffold guides cell organization and growth and allows diffusion of nutrients to the transplanted cells. Figure 7.2 shows how the ECMs work as tissue engineering scaffolds.

Synthetic ECMs provide an adhesion substrate for transplanted cells and serve as a delivery medium into specific sites in the body. Highly porous matrices with a large surface-area-to-volume ratio are desirable in order to allow delivery of a high density of

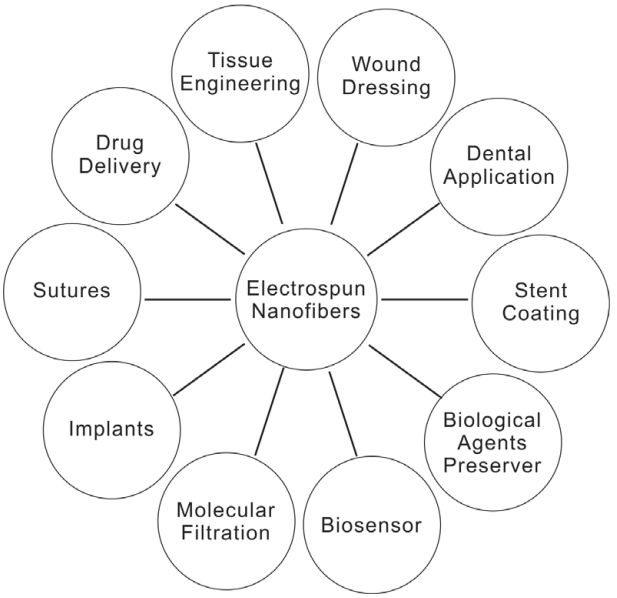

Fig. 7.1 Biomedical applications of polymer nanofibers.

cells and maintain a potential space for tissue development. The ECMS shoud be able to promote the ingrowth of blood vessels to facilitate metabolic transport to and from surrounding native tissue since vascularization of engineered tissues is critical, as cells more than approximately 200 μm from a blood supply are either metabolically inactive or necrotic, owing to the limitation of nutrient diffusion (e.g. oxygen). It is possible to control the vascularization of engineered tissue by controlling the fiber diameter, porosity and pore size of the synthetic ECM and by incorporating angiogenic factors [2].

7.2.1.2 Nanofiber scaffolds for tissue engineering

The goal in developing new tissue engineering technology is to obtain a biocompatible 3-D platform that can act as a temporary host for tissue cells as they attach, proliferate and differentiate into the specific tissue that needs to be repaired. Nonwoven nanofiber mats are widely known for their porous, interconnected, 3-D structures and relatively large specific surface areas, rendering nanofibers an ideal form of materials to mimic the natural ECM required for tissue engineering [13]. Figure 7.3 outlines the various aspects of a tissue engineering nanofibers scaffold system. The nanofiber scaffold can bind cells and act as the platform for their activity, which is very similar to the extracellular matrices in native tissue providing cell anchorage through ligands and influencing cell activity. On top of that, the scaffold can also protect the bioactive molecules. Additionally, the large number of biocompatible polymers ready for nanofiber fabrication is a driving force behind this combination of nanotechnology and biomedical technology.

Nanofibers are unique in that they mimic the extracellular biological matrices (ECM) of tissues and organs. Studies of cell–nanofiber interactions have shown that cells adhere and proliferate well when cultured on polymer nanofibers [15–17]. Khil *et al.* [18]

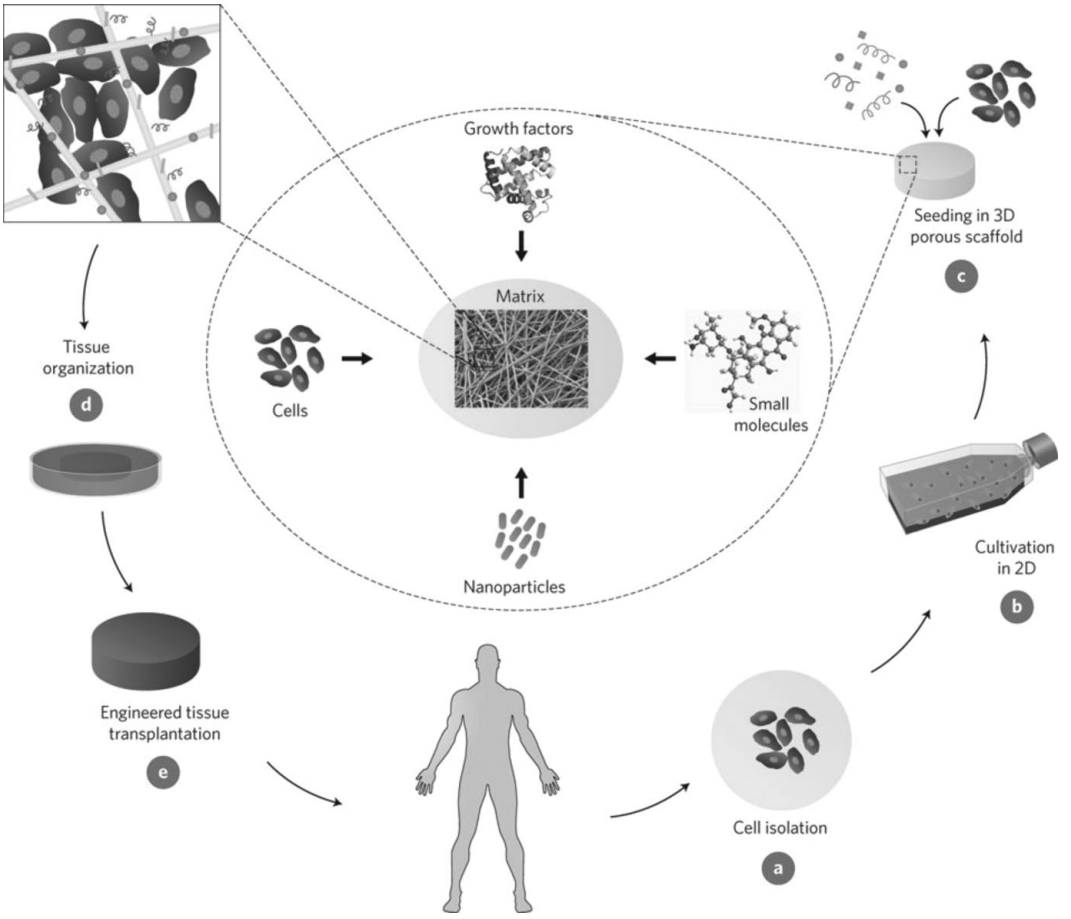

Fig. 7.2 A tissue engineering concept involves seeding cells within porous biomaterial scaffolds [12]. (a) Cells are isolated from the patient and may be cultivated (b) *in vitro* on 2-D surfaces for efficient expansion. (c) Next, the cells are seeded in porous scaffolds together with growth factors, small molecules, and micro- and/or nanoparticles. The scaffolds serve as a mechanical support and a shape-determining material, and their porous nature provides high mass transfer and waste removal. (d) The cell constructs are further cultivated in bioreactors to provide optimal conditions for organization into a functioning tissue. (e) Once a functioning tissue has been successfully engineered, the construct is transplanted on the defect to restore function.

fabricated electrospun PCL porous filaments with fiber diameters ranging from 0.5 μm to 12 μm for 3-D scaffold matrices. Their study indicated that the porous matrices were beneficial to cell proliferation and these woven fabrics, which consisted of porous filaments obtained via electrospinning, also provided an environment that supported tissue proliferation and might be suitable for tissue engineering scaffolds. Figure 7.4 illustrates the difference in the growth kinetics for cells in control and PCL woven matrix. Venugopal *et al.*'s study on polycaprolactone-blended collagen nanofibrous membrane showed the same results for proliferation of fibroblast [19]. They compared the proliferation result of human dermal fibroblast on PCL, PCL-blended collagen, and

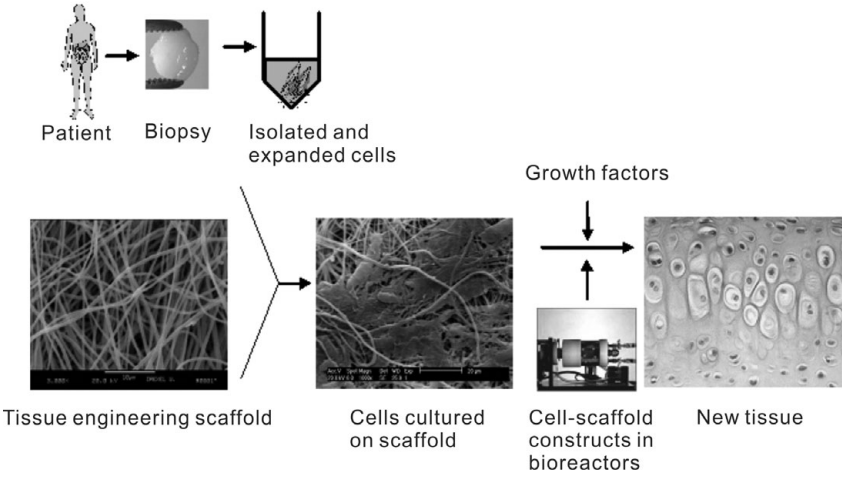

Fig. 7.3 Different aspects of a tissue engineering scaffold system [14].

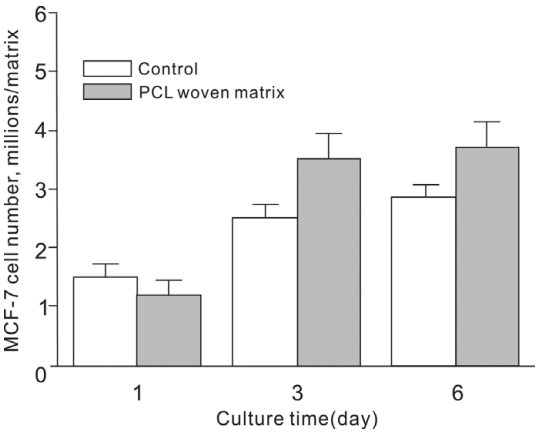

Fig. 7.4 Comparison of the growth kinetics for cells in control and PCL woven matrix [18].

collagen nanofiber scaffolds, at different time lengths, which once again proved the advantage of nanofibrous scaffolds for tissue engineering, as shown in Fig. 7.5.

A number of biopolymers and biodegradable polymers have been electrospun as nonwoven membranes used as scaffolds for tissue engineering in recent years. Examples of materials that have shown potential as skin tissue scaffold include collagen, silk, chitosan and alginate. The images in Fig. 7.6 show examples of electrospun chitosan and alginate fabricated by Leung [20]. The resultant nanofibers were cross-linked with calcium nitrate to enhance structural integrity in aqueous environments. A small amount of poly(L-lysine) was added into the cross-linking bath to enhance cell adhesion, entrapping the protein in the cross-linked alginate matrix. Fibroblast cells were cultured on alginate nanofiber scaffolds with and without poly(L-lysine). With the poly(L-lysine), a

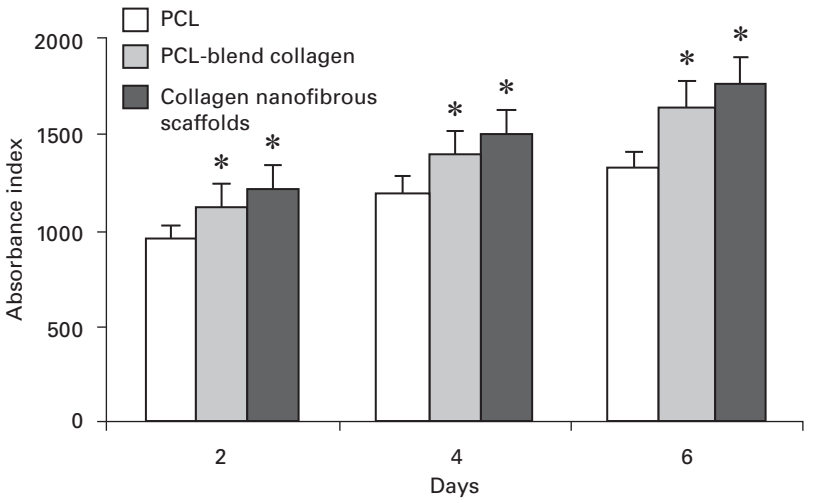

Fig. 7.5 Proliferation of human dermal fibroblast on PCL, PCL-blended collagen, and collagen nanofiber scaffolds ($n = 6$) [19].

significant increase in cell attachment compared to the alginate nanofiber scaffold without the protein was observed. Moreover, fibroblast cells remained viable after 21 days. Figure 7.7 shows fibroblast cells on the alginate nanofiber scaffold with poly(L-lysine).

Also, nanofibers can be engineered to provide bioactive agents, growth factors, drugs, therapeutics and genes to stimulate tissue regeneration and further enhancing the performance [21, 22]. As well as encouraging tissue cells to attach and proliferate, it is also possible to mimic the layered structure of human skin through pre-seeding keratinocytes or fibroblasts onto the scaffolds. Keratin is the major protein found in keratinocytes, which constitute 95% of the cells in the epidermis. Both Yuan *et al.* and Li *et al.* have electrospun PLA nanofibers with keratin derived from wool [23, 24]. Yuan *et al.* reported superior viability and proliferation of NIH-3T3 fibroblast cells on PLA–keratin nanofibers compared to plain PLA nanofibers, whereas Li *et al.* seeded MC3T3 osteoblast cells and reported an increased number of cells observed on the PLA–keratin scaffold than the plain nanofiber control.

In bone regeneration, the incorporation of hydroxyapatite has been widely studied due to its ability to interact with bone cells and resemblance to the apatite found in human bones. Jose *et al.* [25] fabricated PLGA-hydroxyapatite nanofibers, and reported that porosity of the scaffold depends on fiber alignment and the incorporation of hydroxyapatite. Nie *et al.* [26] also demonstrated the use of PLGA–hydroxyapatite nanofibers, but containing bone morphogenetic protein-2 (BMP-2) plasmid encapsulated in chitosan. BMP-2 is known to be able to induce bone healing, whereas hydroxyapatite can enhance attachment to bone cells. Furthermore, the presence of hydroxyapatite enhanced the release of the BMP-2 due to its hydrophilicity in a hydrophobic matrix. The authors also implanted the PLGA scaffolds into mice and reported that the PLGA-hydroxyapatite composite nanofiber with BMP-2 in chitosan can enhance the healing of bone segmental defects. Furthermore, transfection efficiency of the BMP-2 was able to be maintained at

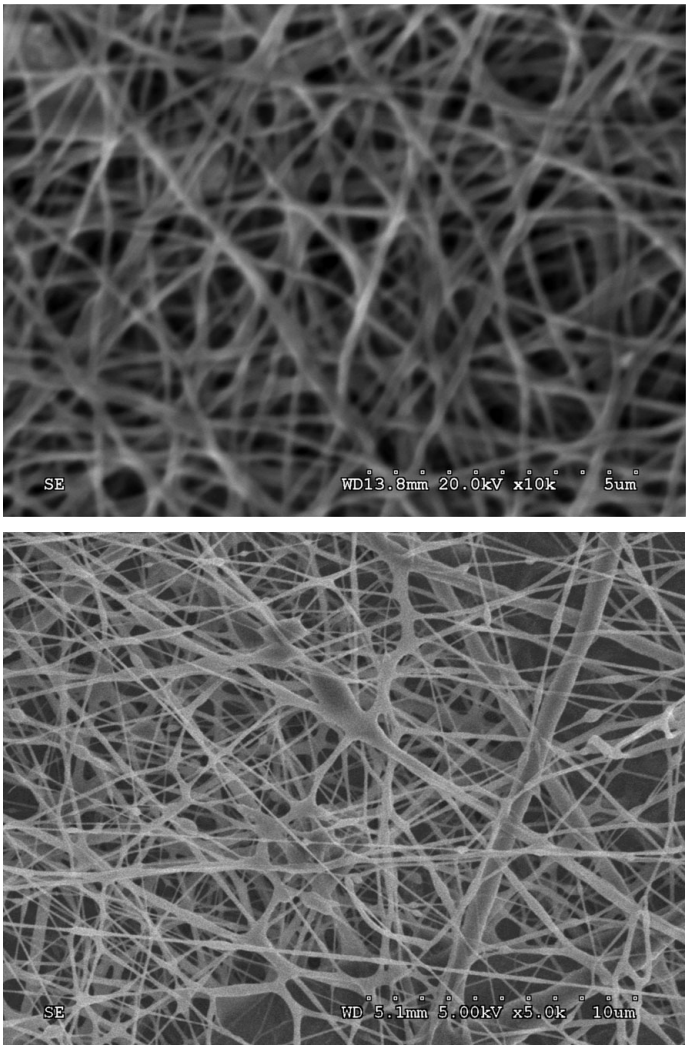

Fig. 7.6 Electrospun nanofibers of alginate (left) and chitosan (right) [20].

a high level. Besides the PLGA-hydroxyapatite composite nanofiber with BMP-2, Price *et al*. [27] has examined the use of carbon nanofibers as a possible scaffold for osteoblast attachment. They reported that osteoblast cell adhesion on the carbon nanofiber increases with decreasing carbon fiber size and increasing fiber surface energy, and that adhesion of competing cells such as fibroblasts can be reduced through adjustment of the fiber size and surface energy. The osteoblast adhesion is found to be higher than for the metals used in existing implants [27].

Hepatocytes are liver cells, and a scaffold for growing then will be helpful for liver regeneration. This may become a promising alternative to liver transplantation, which is plagued by problems such as donor shortage and hepatic failure [28]. Chu *et al*. [29]

Fig. 7.7 Fibroblast cell on alginate nanofibres with poly(L-lysine).

have developed a chitosan nanofiber scaffold for hepatocyte culturing. Compared to a chitosan cast-film, hepatocyte adhesion on the nanofiber scaffold was superior, and cells remained viable. To assess the cell activity, they compared hepatocyte functions through the synthesis of proteins such as albumin, glycogen and urea, and reported that the nanofiber scaffold outperformed the cast-film control in this respect. Chua *et al*. [30] has also reported a hepatocyte nanofibrous scaffold composed of PCLEEP containing galactose ligand, which can aid cell attachment, spheroid formation and functional maintenance of hepatocytes.

For neural tissue engineering, Xie *et al*. [31] studied the effect of embryonic stem cell differentiation on randomly and uniaxially oriented PCL nanofibers and demonstrated that neurite outgrowth is higher for the aligned nanofiber scaffold, since the stem cells tend to elongate parallel to the fibers. The same observation is also made by Yang *et al*.; this group reported that neurite outgrowth is higher on aligned PLA fibers [32].

Xu *et al*. [33] demonstrated that human coronary artery smooth muscle cells can be cultured on electrospun nanofibrous scaffolds of the copolymer poly-L-lactic acid/poly-ε-caprolactone (or PLLA/PCL). The study showed reasonable cell proliferation and normal morphology. The orientation of the nanofiber can lead to guided proliferation of muscle cells along the aligned nanofibers in a directional manner characterized by the orientation of the cytoskeletal protein α-actin, as shown in Fig. 7.8.

Vaz *et al*. demonstrated that the electrospun PLA/PCL bi-layered tube presents appropriate characteristics to be considered as a candidate scaffold for blood vessel tissue engineering [34] Figure 7.9 shows the SEM micrographs of electrospun PLA/PCL constructs after culture with 3T3 mouse fibroblasts at different time lengths.

The morphology of nanofibers can be tailored to deliver the mechanical properties necessary to support cell growth, proliferation, differentiation and motility. Nanofiber scaffolds are most commonly applied as a nonwoven fabric, but individual fibers can be

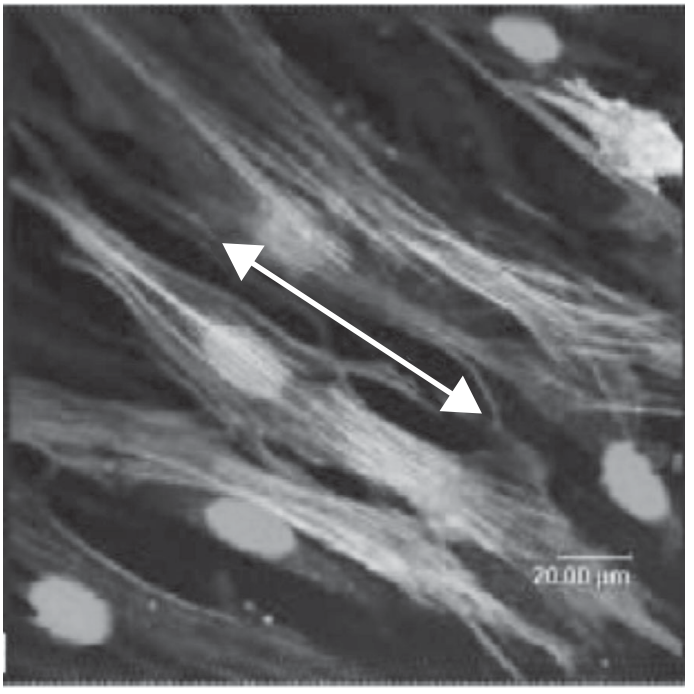

Fig. 7.8 Confocal laser scanning micrographs of immunostained α-actin filaments in SMCs after 1 day of culture on aligned nanofibrous scaffold [33].

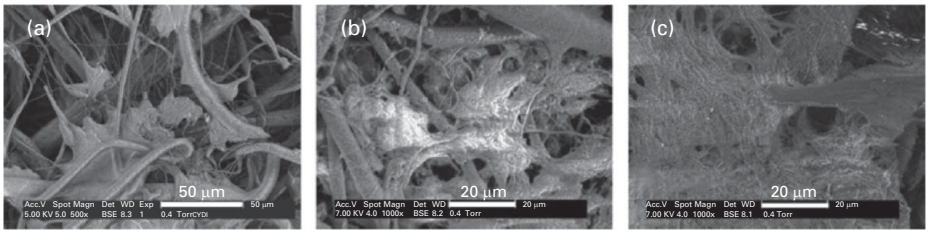

Fig. 7.9 SEM micrographs of electrospun PLA/PCL constructs after culture with 3T3 mouse fibroblasts for: (a) 1 week; (b) 2 weeks; and (c) 4 weeks [34].

highly aligned depending on the specific application. Furthermore, nanofibers can also be woven or braided into various structures suitable for biomedical applications [35]. Different woven or braided structures that can be useful for surgical implants are shown in Fig. 7.10, and are also detailed by Ko [36]. It can be observed that textile technology, such as weaving and braiding, can be used to fabricate hierarchical fibrous structures with nanofibers being at the smallest level, which can be a closer structural mimic of the hierarchical fibrous structures in biological tissues. Such hierarchical structures can result in a range of size scales and porosities which may be advantageous in certain surgical applications and in obtaining desired mechanical properties. Examples of yarns and fabrics suitable for various surgical applications have also been outlined [37].

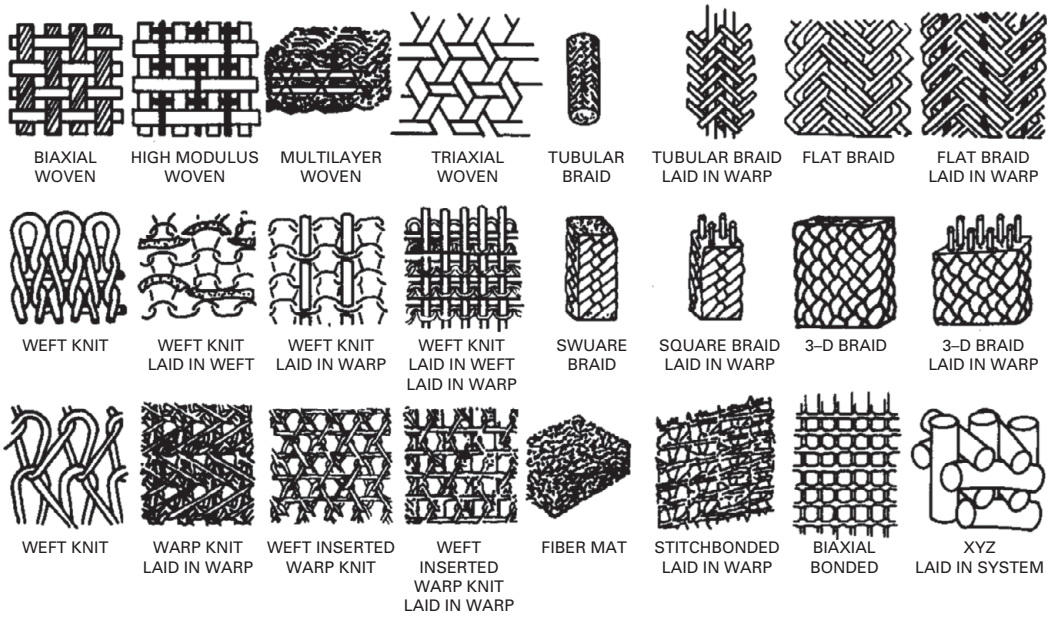

Fig. 7.10 Woven and braided structures for surgical implants [14]

7.2.2 Nanofibers for drug delivery

7.2.2.1 Drug delivery systems

The prevalent methods for drug administration, namely oral and intravenous routes, are not always the most efficient routes for a particular treatment. These conventional free drug therapy methods have many disadvantages such as the low bioavailability of the drug at the target site, toxic side effects of the drug on healthy tissues, and degradation of the drug in the body before reaching the desired site of action. Drug delivery systems are designed to ensure the drug distribution in a manner such that its major fraction interacts exclusively with the target tissue at the cellular and subcellular level in addition to providing the desired kinetics for a specific duration [38]. Therefore, problems associated with the administration of free drugs can be overcome or ameliorated.

The rate of release from a drug carrier is controlled by the properties of the carrier material, the properties of the drug used and the type of drug carrier system. The release rate can also be controlled by using external stimulants like pH, ionic strength, temperature, magnetism and ultrasound, depending on the type of delivery vehicle used [38]. The mechanism of drug release can be either (a) diffusion of the drug from the encapsulating carrier, (b) biodegradation of the carrier, (c) swelling of the carrier followed by diffusion of the drug, or (d) a combination of the aforementioned mechanisms. Through proper drug delievery system design, drugs can be selectively delivered to the target site in requisite doses without affecting healthy tissues and organs.

7.2.2.2 Nanofibers for drug delivery

Drug delivery with polymer nanofibers is based on the principle that the dissolution rate of a drug particulate increases with increased surface area of both the drug and the corresponding carrier if necessary [9]. In addition to the large surface-area-to-volume ratio, polymer nanofibers have other additional advantages for controlled drug delivery. For example, unlike common encapsulation involving some complicated preparation process, therapeutic compounds can be conveniently incorporated into the carrier polymers by using electrospinning [9]. The drug release can be easily modulated by changing the morphology, porosity, composition and structure of the nanofibrous membrane. The resulting nanofibrous membrane containing drugs can be applied topically for skin and wound healing, or post-processed for other kinds of drug release.

Xie and Wang [39] prepared a formulation consisting of nonwoven electrospun PLGA mats loaded with the chemotherapeutic agent Paclitaxel for treatment of gliomas (brain cancer). Implanted nanofiber mats have the advantage that they can be fabricated or modified to almost any size and therefore represent an attractive form for local delivery to different target geometries as well as allowing modulation of drug release rate by controlling fiber diameter. In this study, the main objectives were to obtain a controllable diameter of PLGA fibers, to encapsulate paclitaxel in electrospun fibers and to examine the stability of the encapsulated drug as well as the release kinetics. The prescribed time window in this study correlated well with the period for polymer degradation, suggesting the possibility of tuned drug release kinetics. Paclitaxel was encapsulated in fibers with an encapsulation efficiency of more than 90%, and the sustained release could last for more than 2 months *in vitro*. *In vitro* cell viability test results indicated that tumor cell density was much lower after administration of different concentrations of Paclitaxel-loaded PLGA nanofibers, as compared to control and blank PLGA nanofibers after 72 h. Based on the results of this study, electrospun micro- and nanofibers may be a good option for achieving the sustained release of Paclitaxel for treatment of brain tumors. However, one potentially negative aspect of the formulation used in this study and many other drug delivery studies, including those discussed above, was the observed initial burst release of drug. Although the system was able to provide sustained release of about 80% of the encapsulated drug over 60 days, approximately 15%–20% of the encapsulated drug was released over the first 24 h. This could be especially problematic in the use of a powerful chemotherapeutic agent, for example, wherein excessive brain concentrations could cause tissue damage.

Huang *et al*. [40] demonstrated effective electrospinning of double-layered composite nanofibers using a high molecular weight polymer (PCL) as the shell and two different pure drugs (Resveratrol, a kind of antioxidant and Gentamycin Sulfate, an antibiotic) of low molecular weight as cores. As shown in Fig. 7.11, drug release was smooth in both the drug-loaded nanofibers with no burst release, indicating that these core–shell structure drug-loaded PCL nanofibers have potential applications in functional dressings for wound healing.

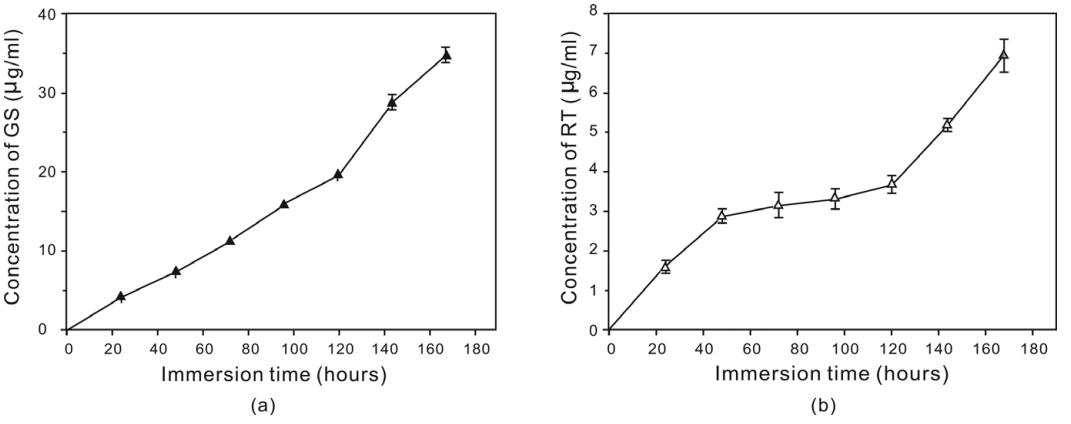

Fig. 7.11 *In vitro* release of drugs from electrospun fibrous membranes that are incubated in the PBS containing lipase. (a) GS/PCL with 40% GS in the core and (b) RT/PCL with 10% RT in the core [40].

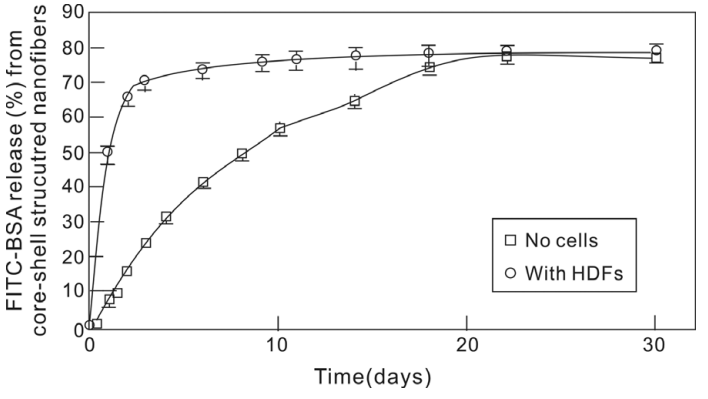

Fig. 7.12 A 10% release of FITC-BSA from PCL core–shell structured nanofibers against time. Faster release was observed for nanofibers cultured with HDFs [41].

Ramakrishna *et al*. [41] developed core–shell structured nanofibers for drugs encapsulation and other therapeutics. A gradual release of fluorescein–isothiocyanate-conjugated bovine serum albumin (FITC-BSA) was demonstrated in the release kinetic studies of the core–shell nanofibers with core-encapsulated FITC-BSA when cultured with human dermal fibroblasts (HDFs). By contrast, when cells were cultured with human dermal fibroblasts (HDFs), there was a resulting undesirable burst release profile (Fig. 7.12). When the nanofibers are cultured with cells, a faster release of FITC-BSA is observed. One possible explanation for this is that it is a result of a higher polymer degradation rate in the presence of degradative enzymes secreted by the cells. This faster release could be desirable for applications like wound dressing, where an initially higher but sustained release of antibiotics is preferred. This release profile is crucial for regulating cell growth if nanofiber scaffolds for tissue engineering applications are to encapsulate bioactive molecules or to allow slow passive delivery in drug delivery

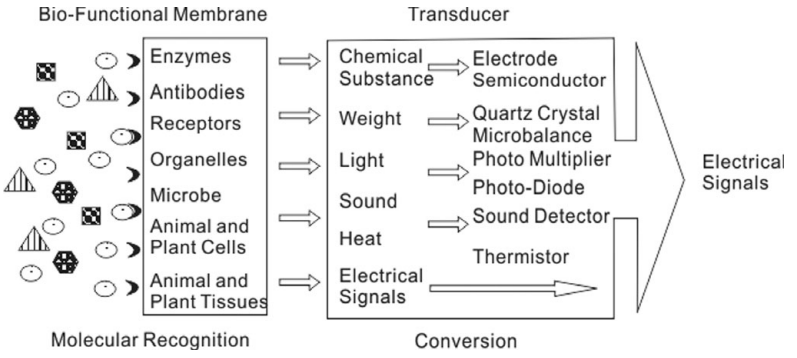

Fig. 7.13 The principle of biosensors [43].

apparatuses. Biological and chemical ligands can be conjugated onto nanofibers for cell-specific targeting or in order to produce biosensors, i.e. controlled delivery of insulin, in response to physiological chances, in diabetic patients.

Nanofiber composites, composed of biocompatible and biodegradable polymers and magnetite nanoparticles, are of potential interest for various applications in medicine, especially drug delivery to precise target areas. Tan *et al*. [42] reported the fabrication of super-paramagnetic polymer nanofibers intended for drug delivery and therapy. The electrospinning technique was employed for preparing polymer nanofibers containing magnetite nanoparticles from commercially available poly-hydroxyethyl methacrylate (PHEMA) and poly-L-lactide (PLLA).

7.2.3 Nanofibers for biosensors

7.2.3.1 Biosensors

The ability to detect pathogenic and physiologically relevant molecules in the body with high sensitivity and specificity offers a powerful opportunity in early diagnosis and treatment of diseases. Early detection and diagnosis can be used to greatly reduce the cost of patient care associated with advanced stages of many diseases. These costs have been estimated to be ~$75 billion [1] and ~$90 billion for cancer and diabetes, respectively. Currently, cancer can be detected by monitoring the concentration of certain antigens present in the bloodstream or other bodily fluids, or through tissue examinations. Correspondingly, diabetes is monitored by determining the glucose concentrations in the blood over time [38].

A biosensor is commonly defined as an analytical device that uses a biological recognition system to target molecules or macromolecules, which is generally coupled to a physiochemical transducer that converts the recognition to a detectable output signal [43], as shown in Fig. 7.13. A typical biosensor consists of three components [38]: (1) the detector, which identifies the stimulus; (2) the transducer, which converts the stimulus to a useful output; and (3) the output system, which amplifies and displays the output in an appropriate format.

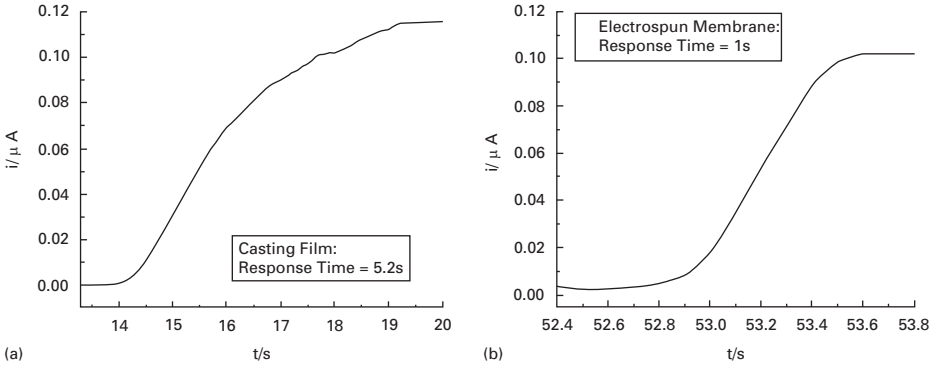

Fig. 7.14 Response time of the immobilized enzyme electrode modified by casting film (a) and electrospun membrane (b), respectively, with the glucose concentration of 0.5 мм [47].

7.2.3.2 Nanofiber biosensors

Sensitivity, selectivity and fast response and recovery times are crucial to a sensor. Nanosensors have the advantage of increasing the number of available sensing sites without increasing the amount of overall sample required through their increased surface area of the detector substrates [44, 45]. Nanofiber-based sensors give the advantage of fast response times and high sensitivity due to the higher surface-area-to-volume ratio compared to common sensors.

The successful incorporation of biotin in PLA nanofibers through electrospinning for biosensors based on biotin–streptavidin specific binding was reported by Lu *et al*. [46]. A biotinylated DNA probe was captured by immobilized streptavidin in a preliminary biosensor assay by using this PLA nanofiber membrane substrate. Biosensor assay experiments confirmed that the PLA nanofiber membranes could successfully transport analyte solutions via wicking.

A glucose biosensor can be fabricated with electrospun glucose oxidase (GOD) with PVA nanofibers membrane [47]. The glucose biosensors have a rapid response time (1 s) and a higher output current (microampere level) to glucose than in both normal and diabetic conditions. The linear response ranging from 1 mmol/l to 10 mmol/l and the lower detection limit (0.05 mmol/l) of the sensor can meet the demands for detection of glucose in medical diagnosis. Figure 7.14 shows the response time of the immobilized enzyme electrode modified by casting film and electrospun nanofiber membrane.

A novel gas sensor composed of electrospun nanofibrous membranes and a quartz crystal microbalance (QCM) has been demonstrated [48]. The electrospun fibers with diameters of 100–400 nm were deposited on the surface of QCM by electrospinning homogenous blend solutions of cross-linkable PAA and PVA. The sensitivity of the nanofibrous membrane-coated QCM sensor was much higher than that of a continuous film-coated QCM sensor.

Microsensors fabricated from four different cross-selective electrospun polymer composite fiber arrays for detection and identification of volatile organic compounds have also been reported [49]. The four organic compounds could be discriminated based

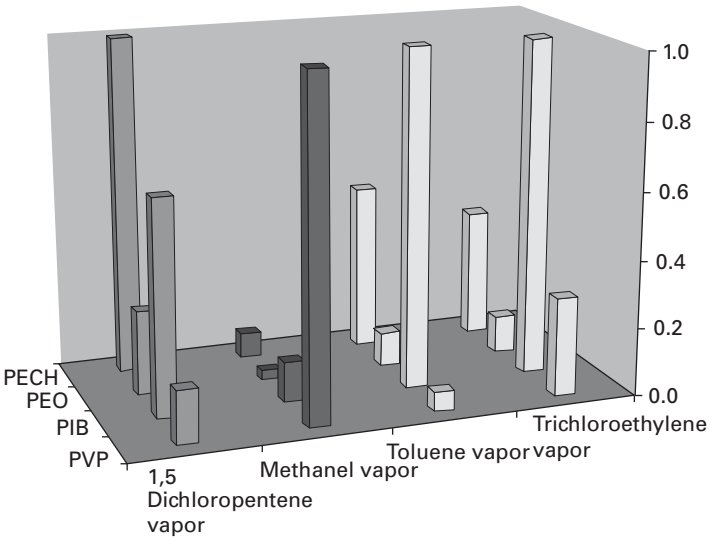

Fig. 7.15 Three-dimensional graph of sensor array response pattern to four different analyte vapors [49]: 1,5-dichloropentane; methanol; toluene; and trichloroethylene.

on the unique response pattern from the sensor array. Figure 7.15 compares the sensor array response pattern to four different analyte vapors.

Single-molecule detection could be achieved by using the nanochannels that can provide zeptoliter detection volume. Wang *et al*. [50] fabricated silica nanochannels with inner diameter as small as 20nm using scanned coaxial electrospinning. A fluorescent dye was injected by capillary force into the individual nanochannels and single-molecule detection was performed by monitoring the photon signals from 5-iodoacetamidofluorescein (5-IAF). Figure 7.16 shows (a) a fluorescent micrograph of aligned nanochannels filled with IAF, (b) a schematic diagram of single molecule detection, (c) photon counts of a blank nanochannel, and (d) photon counts of a nanochannel filled with 4.9 μM/l of IAF solution.

Nanofibers offer a higher sensitivity than thin films as chemiresistors. Flueckiger *et al*. [51] fabricated a polymer blend PANi/PEO nanofiber-based sensor as well as a metal oxide TiO_2 nanofiber-based sensor using electrospinning. The conductivity of those fibers is highly sensitive to the chemical environment and is modified through the absorption of different species.

7.3 Assessment of nanofiber bioactivity

Bioactivity is the key of biomaterials. To evaluate the bioactivity of a biomaterial, biocompatibility and biodegradation are usually tested and assessed. In general, the evaluations are conducted first under *in vitro* conditions prior to animal tests or *in vivo* tests.

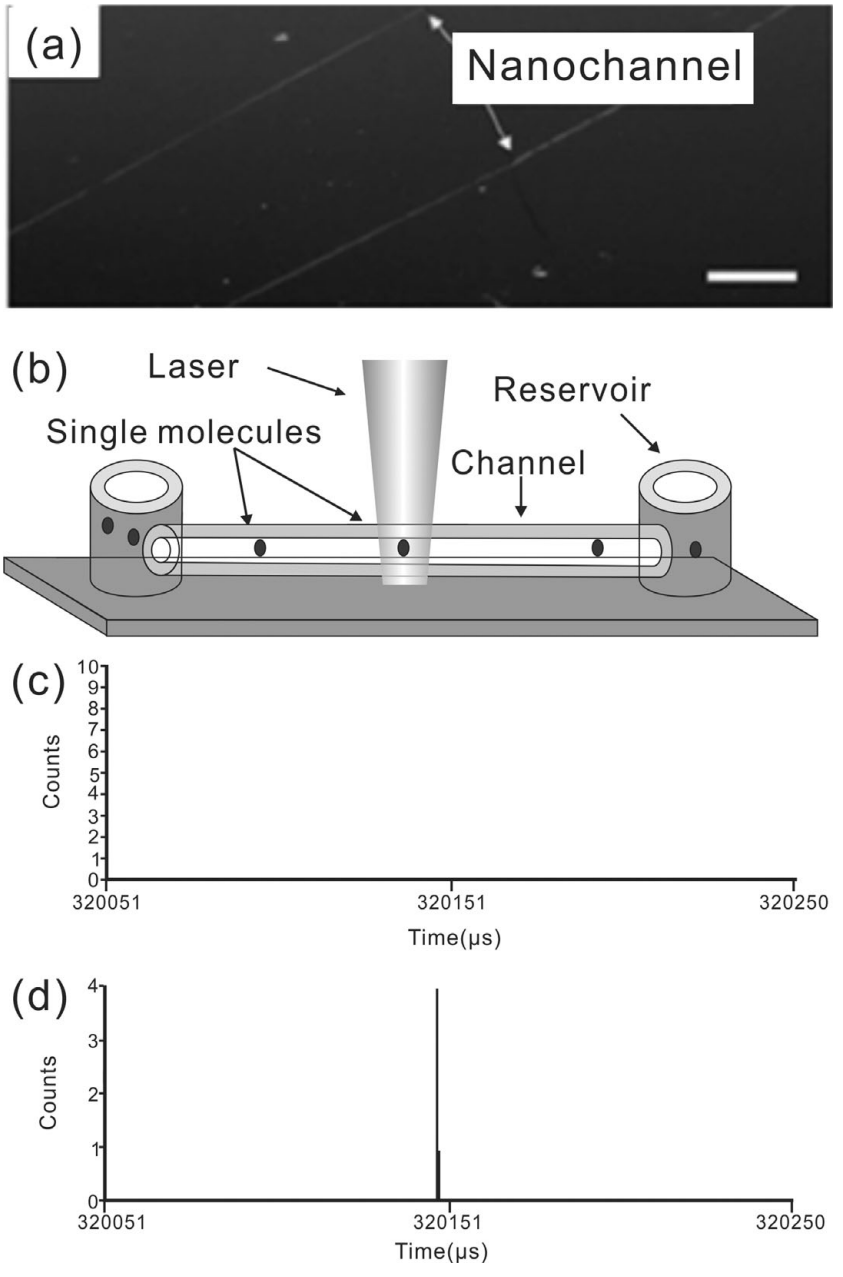

Fig. 7.16 (a) Fluorescent micrograph of aligned nanochannels filled with IAF. The scale bar is 10 μm. (b) Schematic diagram of single molecule detection. (c) Photon counts of a blank nanochannel. (d) Photon counts of a nanochannel filled with a 4.9 μM/l of IAF solution [50].

7.3.1 Assessment of tissue compatibility

A toxic material is defined as a material that releases a chemical in sufficient quantities to kill cells either directly or indirectly through inhibition of key metabolic pathways. The number of cells that are affected is an indication of the dose and potency of the chemical. Biocompatibility is generally evaluated by using three primary cell culture assays: direct contact, agar diffusion and elution (also known as extract dilution). The outcomes are measured by observations of changes in the morphology of the cells.

Assessment of tissue compatibility is the same for nanofiber biomaterials as for the common biomaterials. The choice of method varies with the characteristics of the test material, the rationale for doing the test and the application of the data for evaluating biocompatibility. Detailed precedures of the compatibility tests can be found in the literature.

7.3.2 Assessment of degradation

Assessment of the degradation behavior of porous scaffolds plays an important role in the engineering process of a new tissue. The degradation rate of porous scaffolds affects cell vitality, cell growth and even host response. Upon implantation, a scaffold should maintain mechanical properties and structural integrity until the loaded cells adapt to the environment and excrete a sufficient amount of extracellular matrix; after the mission is accomplished, completely degradation and absorption of the scaffold are desired. It is believed that the ideal *in vivo* degradation rate may be similar or slightly less than the rate of tissue formation. The details for assessment of scaffold degradation can be found in Refs. [52, 53].

It should be noted that synergistic pathways should be considered to understand the biological degradation of implant materials[54]. For example, swelling and water uptake can similarly increase the number of site for reaction. Degradation products can alter the local pH, stimulating further reaction. Hydrolysis of polymers can generate more hydrophilic species, leading to polymer swelling and the entry of degrading species into the bulk of the polymer. Cracks might also serve as sites initiating calcification.

References

1. J. Park, and J. Bronzino, *Biomaterials: Principles and Applications*. Boca Raton, FL: CRC Press, 2003.
2. H. Ernest, and R. Shetty, "Impact of nanotechnology on biomedical sciences: review of current concepts on convergence of nanotechnology with biology," *Tissue Engineering*, vol. 18, p. 19, 2005.
3. L. L. Hench, and J. M. Polak, "Third-generation biomedical materials," *Science*, vol. 295 (5557), pp. 1014–1017, 2002.
4. R. Flemming, *et al*., "Effects of synthetic micro- and nano-structured surfaces on cell behavior," *Biomaterials*, vol. 20(6), pp. 573–588, 1999.

5. T. Desai, "Micro- and nanoscale structures for tissue engineering constructs," *Medical Engineering and Physics*, vol. 22(9), pp. 595–606, 2000.
6. A. Curtis, and C. Wilkinson, "Nanotechniques and approaches in biotechnology," *Materials Today*, vol. 4(3), pp. 22–28, 2001.
7. Y. Zhang, *et al*., "Recent development of polymer nanofibers for biomedical and biotechnological applications," *Journal of Materials Science: Materials in Medicine*, vol. 16(10), pp. 933–946, 2005.
8. J. Gerardo-Nava, *et al*., "Human neural cell interactions with orientated electrospun nanofibers in vitro," *Nanomedicine*, vol. 4(1), pp. 11–30, 2009.
9. Y. Zhang, *et al*., "Recent development of polymer nanofibers for biomedical and biotechnological applications," *Journal of Materials Science: Materials in Medicine*, vol. 16(10), pp. 933–946, 2005.
10. R. Skalak, C. F. Fox, and Y. C. Fung. "Preface," in *Tissue Engineering*, in *NSF Workshop on Tissue Engineering*. Lake Tahoe, California: Granlibakken, 1988.
11. R. Langer, and J. P. Vacanti, "Tissue engineering," *Science*, vol. 260(5110), pp. 920–926, 1993.
12. T. Dvir, *et al*., "Nanotechnological strategies for engineering complex tissues," *Nat Nano*, vol. 6(1), pp. 13–22, 2011.
13. W. J. Li, *et al*., "Electrospun nanofibrous structure: a novel scaffold for bioengineering," *Journal of Biomedical Materials Research*, vol. 58, pp. 613–621, 2002.
14. F. K. Ko, and M. Gandhi, *Producing Nanofiber Structures by Electrospinning for Tissue Engineering*, P. J. Brown and K. Stevens, Ed. Woodhead Publishing, 2007.
15. C. Laurencin, *et al*., "Tissue engineering: orthopedic applications," *Annual Review of Biomedical Engineering*, vol. 1(1), pp. 19–46, 1999.
16. R. Zhang, and P. Ma, "Synthetic nano-fibrillar extracellular matrices with predesigned macroporous architectures," *Journal of Biomedical Materials Research*, vol. 52(2), pp. 430–438, 2000.
17. P. X. Ma, "Biomimetic materials for tissue engineering," *Advanced Drug Delivery Reviews*, vol. 60(2), pp. 184–198, 2008.
18. M.-S. Khil, *et al*., "Novel fabricated matrix via electrospinning for tissue engineering," *Journal of Biomedical Materials Research*, vol. 72B(1), pp. 117–124, 2005.
19. J. Venugopal, Y. Zhang, and S. Ramakrishna, "In vitro culture of human dermal fibroblasts on electrospun polycaprolactone collagen nanofibrous membrane," *Artificial Organs*, vol. 30 (6), pp. 440–446, 2006.
20. V. Leung, and F. Ko, "Biomedical applications of nanofibers," *Polymers for Advanced Technologies*, vol. 22(3), pp. 350–365, 2011.
21. A. Greiner, *et al*., "Biohybrid nanosystems with polymer nanofibers and nanotubes," *Applied Microbiology and Biotechnology*, vol. 71(4), pp. 387–393, 2006.
22. M. Li, *et al*., "Electrospun protein fibers as matrices for tissue engineering," *Biomaterials*, vol. 26, pp. 5999–6008, 2005.
23. J. Li, *et al*., "Preparation and biodegradation of electrospun PLLA/keratin nonwoven fibrous membrane," *Polymer Degradation and Stability*, vol. 94(10), pp. 1800–1807, 2009.
24. J. Yuan, J. Shen, and I. Kang, "Fabrication of protein-doped PLA composite nanofibrous scaffolds for tissue engineering," *Polymer International*, 57(10), pp. 1188–1193, 2008.
25. M. V. Jose, *et al*., "Aligned PLGA/HA nanofibrous nanocomposite scaffolds for bone tissue engineering," *Acta Biomaterialia*, vol. 5, pp. 305–315, 2009.
26. H. Nie, *et al*., "BMP-2 plasmid loaded PLGA/HAp composite scaffolds for treatment of bone defects in nude mice," *Biomaterials*, vol. 30(5), pp. 892–901, 2009.

27. R. L. Price, *et al*., "Selective bone cell adhesion on formulations containing carbon nanofibers," *Biomaterials*, vol. 24(11), pp. 1877–1887, 2003.
28. T. W. Chung, *et al*., "Preparation of alginate/galactosylated chitosan scaffold for hepatocyte attachment," *Biomaterials*, vol. 23(14), pp. 2827–2834, 2002.
29. X. H. Chu, *et al*., Chitosan nanofiber scaffold enhances hepatocyte adhesion and function," *Biotechnology Letters*, vol. 31, pp. 347–352, 2009.
30. K. N. Chua, *et al*., "Stable immobilization of rat hepatocyte spheroids on glactosylated nanofiber scaffold," *Biomaterials*, vol. 26, pp. 2537–2547, 2005.
31. J. Xie, *et al*., "The differentiation of embryonic stem cells seeded on electrospun nanofibers into neural lineages," *Biomaterials*, vol. 30, pp. 354–362, 2009.
32. F. Yang, *et al*., "Electrospinning of nano/micro scale poly (L-lactic acid) aligned fibers and their potential in neural tissue engineering," *Biomaterials*, vol. 26, pp. 2603–2610, 2005.
33. C. Xu, *et al*., "Aligned biodegradable nanofibrous structure: a potential scaffold for blood vessel engineering," *Biomaterials*, vol. 25(5), pp. 877–886, 2004.
34. C. Vaz, *et al*., "Design of scaffolds for blood vessel tissue engineering using a multi-layering electrospinning technique," *Acta Biomaterialia*, vol. 1(5), pp. 575–582, 2005.
35. F. K. Ko, "Fabrics," in *Encyclopedia of Biomaterials and Biomedical Engineering*, G. E. Wnek and G. L. Bowlin, Ed. Marcel Dekker, 2005.
36. F. K. Ko, "Preform architecture for ceramic matrix composites," *American Ceramic Society Bulletin*, vol. 68(2), pp. 401–414, 1989.
37. F. K. Ko, "Medical applications for textile structures," in *Textile Asia*, 1997.
38. K. E. Gonsalves, *et al*., Ed. *Biomedical Nanostructures*. John Wiley & Sons, 2008.
39. J. Xie, and C. Wang, "Electrospun micro- and nanofibers for sustained delivery of paclitaxel to treat C6 glioma *in vitro*," *Pharmaceutical Research*, vol. 23(8), pp. 1817–1826, 2006.
40. Z.-M. Huang, *et al*., "Encapsulating drugs in biodegradable ultrafine fibers through co-axial electrospinning," *Journal of Biomedical Materials Research Part A*, vol. 77A(1), pp. 169–179, 2006.
41. S. Ramakrishna, *et al*., "Electrospun nanofibers: solving global issues," *Materials Today*, vol. 9(3), pp. 40–50, 2006.
42. S. Tan, *et al*., "Biocompatible and biodegradable polymer nanofibers displaying superparamagnetic properties," *ChemPhysChem*, vol. 6(8), pp. 1461–1465, 2005.
43. H. Nakamura, and I. Karube, "Current research activity in biosensors," *Analytical and Bioanalytical Chemistry*, vol. 377(3), pp. 446–468, 2003.
44. S. Kossek, C. Padeste, and L. Tiefenauer, "Immobilization of streptavidin for immunosensors on nanostructured surfaces," *Journal of Molecular Recognition*, vol. 9(5–6), pp. 485–487, 1996.
45. R. Méallet-Renault, P. Denjean, and R. Pansu, "Polymer beads as nano-sensors," *Sensors and Actuators B: Chemical*, vol. 59(2–3), pp. 108–112, 1999.
46. Y. Lu, L. Weng, and X. Cao, "Morphological, thermal and mechanical properties of ramie crystallites–reinforced plasticized starch biocomposites," *Carbohydrate Polymers*, vol. 63(2), pp. 198–204, 2006.
47. G. Ren, *et al*., "Electrospun poly (vinyl alcohol)/glucose oxidase biocomposite membranes for biosensor applications," *Reactive and Functional Polymers*, vol. 66(12), pp. 1559–1564, 2006.
48. B. Ding, *et al*., "Electrospun nanofibrous membranes coated quartz crystal microbalance as gas sensor for NH_3 detection," *Sensors and Actuators B: Chemical*, vol. 101(3), pp. 373–380, 2004.

49. R. Kessick, and G. Tepper, "Electrospun polymer composite fiber arrays for the detection and identification of volatile organic compounds," *Sensors and Actuators B: Chemical*, vol. 117 (1), pp. 205–210, 2006.
50. M. Wang, *et al*., "Electrospinning of silica nanochannels for single molecule detection," *Applied Physics Letters*, vol. 88, p. 033106, 2006.
51. J. Flueckiger, F. K. Ko, and K. C. Cheung, "Electrospun electroactive polymer and metal oxide nanofibers for chemical sensor applications," in *Proceedings of the ASME 2010 International Mechanical Engineering Congress & Exposition*, 2010.
52. L. Wu, and J. Ding, "In vitro degradation of three-dimensional porous poly(,-lactide-co-glycolide) scaffolds for tissue engineering," *Biomaterials*, vol. 25(27), pp. 5821–5830, 2004.
53. K. Kim, *et al*., "Control of degradation rate and hydrophilicity in electrospun non-woven poly (D, L-lactide) nanofiber scaffolds for biomedical applications," *Biomaterials*, vol. 24(27), pp. 4977–4985, 2003.
54. B. Ratner, *et al*., *Biomaterials Science: an Introduction to Materials in Medicine*. Elsevier Academic Press, 2004.

8 Electroactive nanofibers

8.1 Introduction

With the rapid advances of materials used in science and technology, various intelligent materials that can sense variations in the environment, process the information, and respond accordingly are being developed at a fast pace. Shape-memory alloys, piezoelectric materials, etc., fall into this category of intelligent materials. Polymers have attractive properties compared to inorganic materials. They are lightweight, inexpensive, fracture tolerant, pliable and easily processed and manufactured [1]. An organic polymer that possesses the electrical, electronic, magnetic and optical properties of a metal while retaining the mechanical properties and processability, etc., commonly associated with a conventional polymer, is termed an "intrinsically conducting polymer" (ICP), or more commonly, a "synthetic metal" [2]. The unique properties of these materials are highly attractive for a wide range of applications such as actuators, supercapacitors, batteries, etc. With the development of nanotechnology, these materials can be engineered to develop a variety of multifunctional active materials for intelligent applications that were previously imaginable only in science fiction. Figure 8.1 shows an artistic interpretation of the Grand Challenge for EAP actuated robotics.

8.2 Conductive nanofibers

8.2.1 Conductive polymers and fibers

Conductive polymers pave the way for smart applications due to their flexibility, light weight and favorable metallic and electrical properties. The polymers listed in Table 8.1 are some of the ICP polymers. Among them, polyaniline is the most commercially available and the one that has been studied in a wide range of applications from actuators to rechargeable batteries[4–6]. To facilitate manipulation and application, conductive polymer products are mainly formed as fibers or cables.

Most commercially available conductive fibers are composed of a blend of nonconductive polymer and conductive particles, such as carbon black, carbon nanotubes, metallic particles, metal clad aramid fibers, etc. Conductive fibers containing metallic components are prone to damage due to excessive exposure to moisture and continuous fatigue. Furthermore, the high stiffness of metallic wires reduces the flexibility of

Table 8.1 Conductivities of conducting polymers

Polymer	Conductivity (Siemens/cm)	Polymer	Conductivity (Siemens/cm)
Polyacetylene	10 000[a]	Polythienylenevinylene	2700[a]
Polypyrrole	500–7500	polyphenylene	1000
Polythiophene	1000	Polyisothianapthene	50
Poly(3alkylthiophene)	1000–10 000[a]	Polyazulene	1
Polyphenylene Sulfide	500	Polyfuran	100
Polyphenylene-vinylene	10 000[a]	Polyaniline	200[a]

[a]Advanced Polymer Courses, VIII[th] International Seminar on the Technology of Inherently Conductive Polymers, June 18–20, 2001.

Fig. 8.1 An artistic interpretation of the Grand Challenge for EAP actuated robotics [3].

conductive fiber assemblies, causing decreased mobility, maintenance and durability. Conductive fibers can be integrated into a base fabric device by means of embroidering, weaving or knitting. This technique has recently been studied in wearable electronics and wearable computers [7]. Table 8.2 lists some of the commercially available conductive fibers, provides a brief description, and shows their conductivity values. Disadvantages of these conductive fibers include corrosion and fatigue, because the fibers contain metallic components. Metallics are known to have low flexibility and poor fatigue properties. Continuous bending and rubbing of wires during use might result in wire failure due to fatigue, hence disabling the function of the device. However, the disadvantages will be overcome; the electroactivity and mechanical properties of the conductive particles, metallic fibers and polymers will be thoroughly changed when the materials are made in nanosize, because matter at the nanoscle no longer follows Newtonian physics but rather quantum mechanics.

Table 8.2 Commercially available conductive fibers[7]

Type	Conductivity (Ohms/cm)
BK 50/2 – Bekaert Fiber Technologies (Steel/polyester spun yarn)	50
Bekintex – Bekaert Fiber (Continuous cold drawn stainless steel fibers)	1
Bekintex 15/2 – Bekaert Fiber (Stainless spun fibers)	1
VN 140 nyl/35 x 3 (Nylon core wrapped with continuous stainless steel wires)	10
Aracon – DuPont (Metal clad aramid fiber, Core: Kevlar; Cladding metals: Ag, Ni, Cu, Au, Sn)	0.001

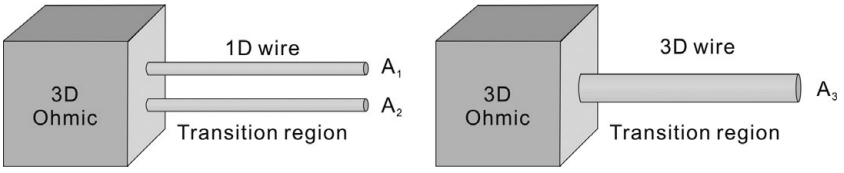

Fig. 8.2 Metals form ohmic contacts [8].

8.2.2 Fundamental principle for superior electrical conductivity

Unusual current conduction properties arise when the size of (nanometer in diameter) wires are reduced below a certain critical thickness [8]. Furthermore, the rectifying contact to a wire will work better if the wire size is reduced below such a critical thickness. Hence, it is expected that new wires and contacts (the diodes that form the building blocks of electronics) will behave more favorably when forced to operate under reduced dimensional regimes.

It is also well know that electronics, by definition, is the study of electron conduction. This conduction, or transport, is affected by the properties of the medium of conduction and its physical dimensions. Unusual properties arise when electrons become spatially confined, that is, when they are transported in a nanoscale media. The following paragraphs will identify the expected properties arising from confinement and contact between nanoscale wires and macro (3-D) systems.

Three types of contact to a nanowire exist [8]: ohmic, rectifying and tunneling. Ohmic contact is an ideal contact in which the electron wave is not reflected from the wire. Current conduction is then the property of the wire, not the contact, and is by definition the product of cross-sectional area A, charge q, carrier concentration n, and carrier velocity v ($I = A\ q\ n\ v$). However, below a critical thickness of A, carrier concentration changes due to the change in density of states and, more importantly, the velocity of carriers is altered due to differences in scattering. This is because the electrons in a 1-D system can scatter only by completely reversing their direction, whereas in 2-D and 3-D systems they can scatter by changing the angle of motion [9].

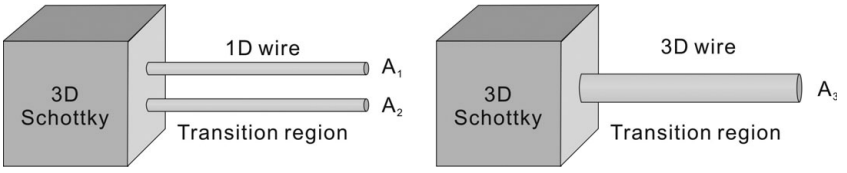

Fig. 8.3 Metals form rectifying Schottky contacts [8].

Hence, it is concluded that current conduction should increase below a critical diameter. This is schematically shown in Fig. 8.2, where it is proposed that $I(A_1) + I(A_2) > I(A_3)$ even though $A_3 = A_1 + A_2$.

Rectifying (or Schottky) contacts are produced in systems that have different electron affinities [8]. Current transport in these systems is based on kinetic energy requirements for motion from one system to another. Thermionic emission of carriers is the typical source of conduction in these systems. In a 3D–1D contact, calculation of themionic emission arises from carriers that have enough kinetic energy to overcome the barrier between the two systems. However, both carrier concentration and velocity change, due to carrier confinement in a wire as a result of (a) the changing density of electronic states and (b) the fact that electron energy is quantized. As a result, electrons that are emitted from a metal to a nanowire have to occupy higher states, causing a barrier height increase. A step-by-step mathematical derivation [10] reports that a metal has a much higher barrier and a different thermal signature than bulk material. Hence, below critical thickness the system rectifies better. This is schematically shown in Fig. 8.3, where it is proposed that $I(A_1) + I(A_2) > I(A_3)$ even though $A_3 = A_1 + A_2$.

In a 1-D system the electrons are collectively excited, producing what is known as a Luttinger (as opposed to Fermi) liquid [11]. This property then alters the tunneling probabilities compared to 3-D systems. On the basis of the previous discussion, it is proposed that by reducing the size of a wire beyond a certain dimension, it can be expected simultaneously to achieve both better rectification properties and superior transport in a nanowire.

8.2.3 Electroactive nanofibers

Using these conductive polymers in the form of nanofibrous assemblies offers us two major advantages. First, the fibrous form gives the opportunity of having electronic textiles and of obtaining tactile properties for different applications. Second, nanoscale fibers provide the fundamental building blocks for construction of devices and structures.

Electroactive nanofibers are fibers of less than 100 nm diameter that are electrically conductive (in terms of electrical, ionic and photoelectric conductivity). Polymer classes that are suitable for fabricating electroactive nanofibers include, but are not limited to, polyimides, polyamides, vinyl polymers, polyurethanes, polyureas, polythioureas, polyacrylates, polyesters and biopolymers [12]. Polyacetylene, polypyrrole, polythiophene and polyaniline are the most widely studied intrinsically conducting polymers [13]. Electroactive polymer can be doped with inclusions, such as piezoceramic powders, nanotubes and nanofibers, for dielectric enhancement. Fibers and fibrous nonwoven mat

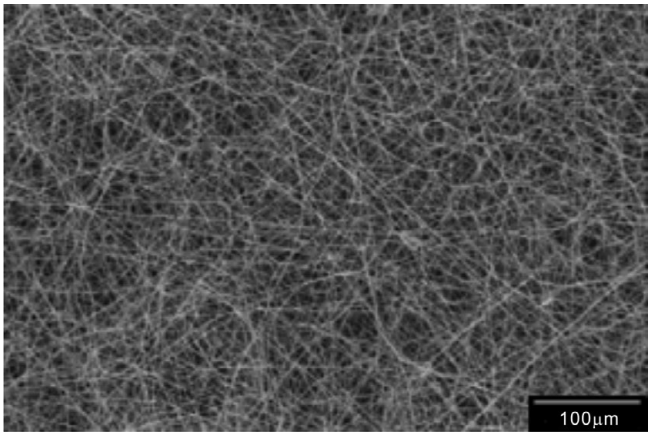

Fig. 8.4 A 50 wt% nanofiber blend of PAn.HCSA fabricated from 2 wt% PAn.HCSA and 2 wt% PEO from chloroform solution at 25 000 V (anode/cathode separation 25 cm) [19].

can be fabricated through electrospinning. It is anticipated that electroactive nanofibers will be used in the fabrication of tiny electronic devices such as sensors, actuators and Schottky junctions. Electroactive nanofibrous membranes are appropriate for use as porous electrodes in high-performance batteries because of the well-established fact that the rate of electrochemical reactions is directly proportional to the surface area of the electrode [14, 15]. The high specific surface area makes nanofibers an ideal candidate for making high-performance electronic devices. Electroactive fibrous membranes are potentially useful for applications including electrostatic dissipation, corrosion protection, electromagnetic interference shielding and photovoltaic devices[16, 17].

Electrospinning of nanofibers from pure electronic polymers (in their semiconducting and metallic regimes) or their blends in conventional organic polymers for the purpose of ascertaining their applicability in the fabrication of nano-electronic devices has already been widely explored. Norris *et al*. [14] fabricated the first conducting polymer fibers (diameter ~950 nm to 2100 nm) of polyaniline doped with *d,l*-camphorsulfonic acid (PAn.HCSA) as a blend in polyethylene oxide (PEO) (see Fig. 8.4). The chemical and physical structure of polyaniline was found preserved. The obtained fiber has a diameter ranging from 500 nm to 1600 nm. With an appropriate substrate – glass slide, silicon wafer or loop of copper wire, etc. – held between the anode and cathode at a position close to the cathode, individual fibers could be collected for certain electrical studies [18]. For a single 419 nm fiber of a blend of 50 wt% PAn.HCSA and polyethylene oxide, the conductivity was measured with two probes to be ~ 10^{-1} S/cm, as given in Fig. 8.5. Nonlinear I/V curves may be obtained from some polyaniline samples, possibly caused by the presence of defect sites induced by imperfections or impurities in the polyaniline. Such imperfections are expected to be more apparent in thin fibers since there are fewer molecular pathways by which charge carriers can bypass the defect sites[19].

By using the same method for producing polyaniline fibers [14], highly conducting sulfuric acid-doped polyaniline fibers (average, 139 nm; maximum, 275 nm; minimum, 96 nm) were obtained by placing a ~20 wt% solution of polyaniline (Versicon™, Allied Signal) in 98% sulfuric acid in a glass pipette with the tip ~3 cm above the surface

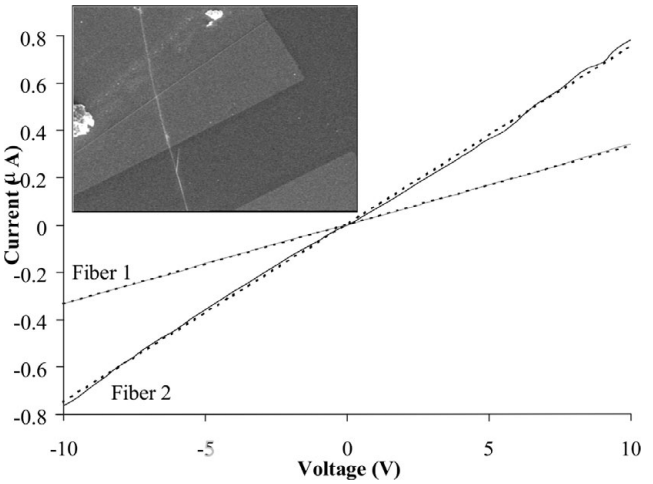

Fig. 8.5 Current/voltage curves of 50 wt% PAn.HCSA/PEO blend nanofiber [18].

of a copper cathode immersed in pure water at a potential difference of 5000 V [19]. As expected, the conductivity of the obtained fiber was ~ 0.1 S/cm (since partial fiber de-doping occurred in the water cathode). The diameter and length of the fibers appear to be sensitive to the nature of the polyaniline used [19]. No great difficulty was foreseen in producing fibers with a diameter less than 100 nm diameter.

The (reversible) conductivity/temperature relationship between 295 K and 77 K for a single 1320 nm fiber (72 wt% PAn.HCSA in PEO) spun from chloroform solution is shown in Fig. 8.6. To minimize heating effects the applied voltage was held constant at 10 mV, at which value the current is very small. The conductivity (~33 S/cm at 295 K) was unexpectedly large for a blend since the conductivity of a spun film of the pure polymer cast from chloroform solution is only ~10^{-1} S/cm [20]. The results reveals that the significance of the high surface-to-volume ratio provided by the electrospun fibers was evident from the greater than first-order magnitude increase in the rate of the vapor phase de-doping and at least two orders of magnitude increase in the rate of spontaneous re-doping, compared to the cast film. Figure 8.7 illustrates the electrical conductivity of the PAn.HCSA/PEO blend electrospun fibers and cast films prepared from the same solution [19] This suggests there may be significant alignment of polymer chains in the fiber [21, 22].

Fabrication of poly(3,4-ethylenedioxythiophene)(PEDOT)/poly(styrenesulfonate) (PSS) blend fibers were also proved to be feasible by electrospinning as shown in Fig. 8.8a. Good alignment was observed due to the phenomenon of yarn self assembly during electrospinning. It is evident as seen in Fig. 8.8b that the addition of PEDOT to the PAN system affects the diameter value of the fibers. The fibers became finer by increasing the amount of the PEDOT, but one should be cautious, as increasing the PEDOT amount to higher concentration can cause the appearance of beads, which is not required.

A 4-probe device has been used to indirectly measure the conductivity of electrospun fibers [18]. This was done by electrospinning the PEDT/PAN polymer directly to the

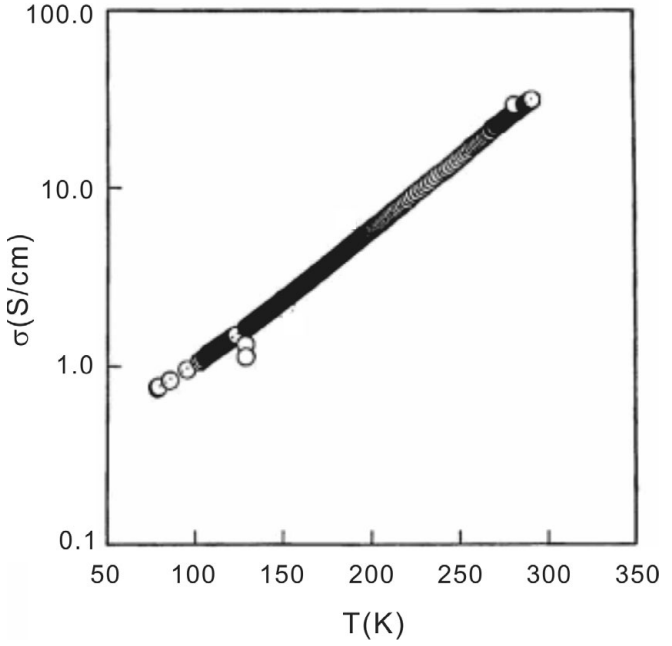

Fig. 8.6 Conductivity/temperature relationship for a 72 wt% blend fiber of PAn.HCSA in PEO [18].

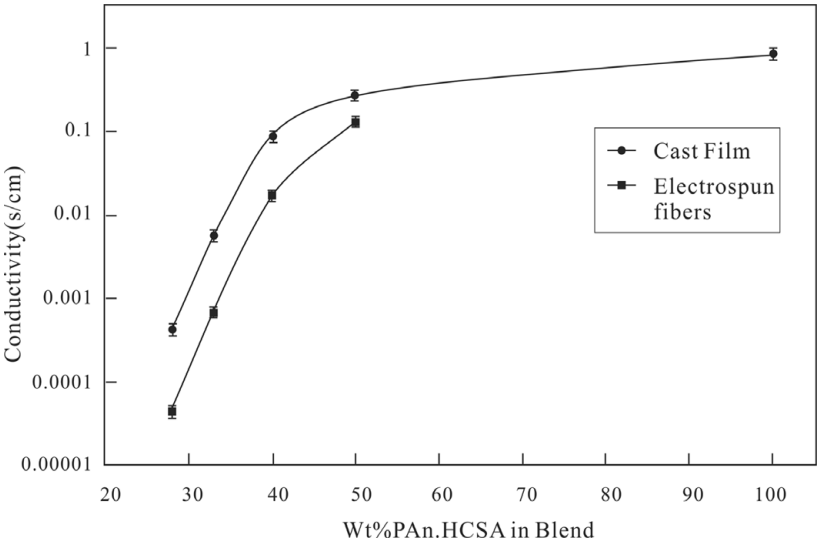

Fig. 8.7 Electrical conductivity of the PAn.HCSA/PEO blend electrospun fibers and cast films prepared from the same solution [14, 18].

Si wafer. The *I*/*V* curves of the Si wafer with and without the fibers were drawn to get the resistance of the wafer and wafer with fibers. By considering the Si wafer and the fiber mat as resistors in parallel connection, the resistance of the electrospun fibers can be calculated by applying the relationship of

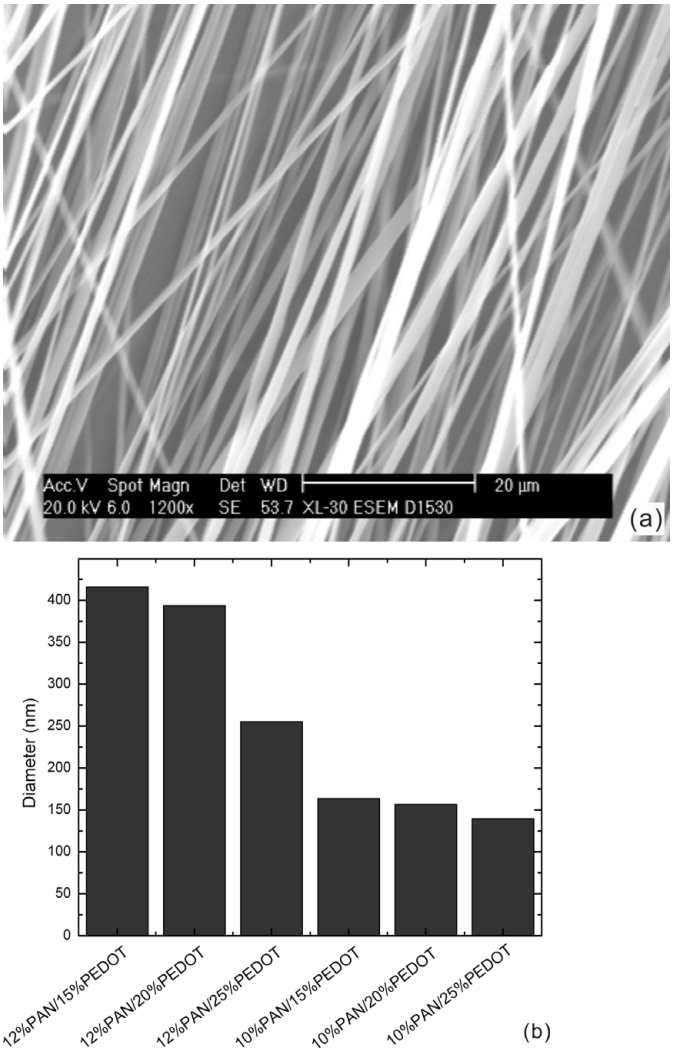

Fig. 8.8 (a) SEM of PEDOT/PSS fibers. (b) Fiber diameter vs PEDOT/PAN concentrations.

$$V = IR, \tag{8.1}$$

$$\rho = RA/L, \tag{8.2}$$

where V is the applied electrical potential, I is the current, R is the resistance of the material, A is the cross-sectional area perpendicular to the direction of the current, L is the distance between the two points at which the voltage is measured and ρ is the resistivity of the material. The conductivity of the material can be calculated from the reciprocal of resistivity. Figure 8.9 shows an I/V curve of a tested material.

It can be seen that as the fiber diameter decreases, the electrical conductivity increases, which supports the hypothesis that elimination of small-angle scattering due to size confinement can increase conductivity, as introduced in Chapter 1.

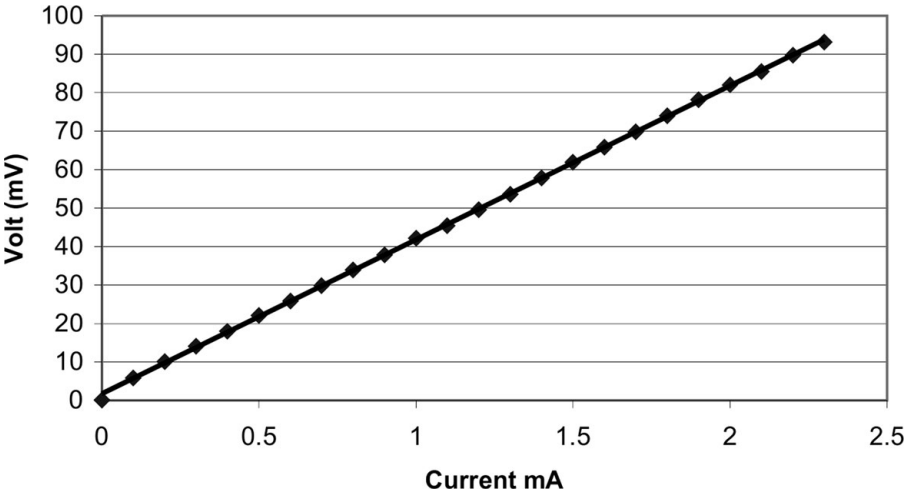

Fig. 8.9 An *I*/*V* curve of a tested nanofiber material [18].

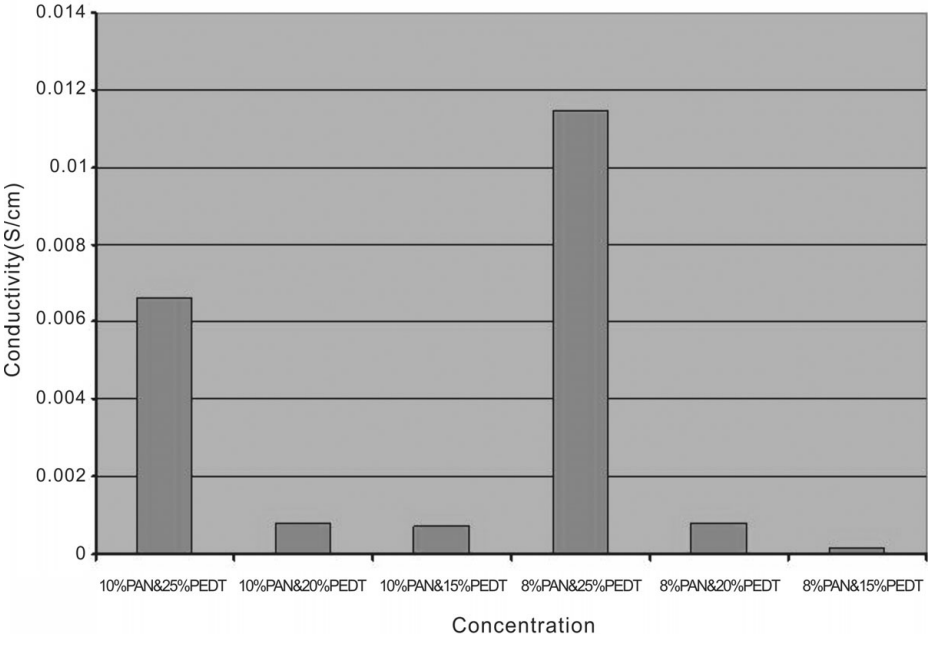

Fig. 8.10 The effect of increasing the concentration of PEDOT on the fibers' conductivity [18].

The increase of PEDOT concentration in the fibril matrix increases the electrical conductivity of the yarn [18], as shown in Fig. 8.10. The electrical conductivity of the PEDOT/PAN yarn was 0.001–0.012 S/cm.

To accomplish the goal of obtaining conductive nanofibers with a diameter <100 nm, an 8 wt% solution of polystyrene (Mw 212 400; Aldrich Co.) in THF (glass pipette orifice: 1.2 mm) was electrospun [19]. The diameters of the polystyrene nanofibers were

consistently <100 nm. It should be noted that a 16 nm fiber is ~30 polystyrene molecules wide, therefore dimensions of this size were expected to greatly affect the kinetics, as well as possibly the thermodynamics, of the polymer. It is also of interest to note that a 16 nm fiber such as the one mentioned above lies well within the ~4–30 nm diameter range of multi-walled carbon nanotubes [19, 23].

Waters *et al*. [24] reported the use of nanofibers in the development of a liquid crystal device (LCD) optical shutter, which is switchable under an electric field between substantially transparent and opaque states. This LCD mainly consisted of a layer of nanofibers permeated with a liquid crystal material, having a thickness of only a few tens of microns. The nanofibers were located between two electrodes, by means of which an electric field could be applied across the layer to vary the transmissivity of the liquid crystal/nanofiber composite. It is the fiber size used that determines the sensitivities of refractive index differences between liquid crystal material and the fibers, and consequently governs the transmissivity of the device. Evidently nanoscale polymer fibers are necessary in this kind of devices.

Li *et al*. [13] reported that the doping of gelatin with a few percent of PANi leads to an alteration of the physicochemical properties of gelatin. The electroactive PANi–gelatin fibers were used as a fibrous matrix for supporting cell growth, where H9c2 rat cardiac myoblast cells were cultured on glass cover slips coated with the electrospun fibers. The results indicated that all PANi–gelatin blend fibers supported H9c2 cell attachment and proliferation to a similar degree as the control tissue culture-treated plastic (TCP) and smooth glass substrates.

Pawlowski *et al*. [25] used electrospinning to fabricate nanofibers from a piezoelectric copolymer of PVDF and trifluoroethylene (TrFE) solution to create lightweight, electrically responsive wing skins for micro-air vehicle (MAV) wing frame designs. In preliminary attempts at fiber actuation, the fiber-coated wing frames exhibited a perceptible vibration upon excitation with a 2 kV (peak-to-peak) sine wave at 6.7 Hz. These results confirmed the feasibility of utilizing electrospinning to process novel electroactives for fabrication of lightweight, responsive MAV wings. Figure 8.11 illustrates the TrF1 fibers electrospun onto MAV wing frames.

PAN and PAN-based graphite nanofibers were obtained by electrospinning and subsequent pyrolysis [26]. The graphitization of the PAN nanofiber leads to a sharp increase in conductivity to around 490 S/m. Figure 8.12 illustrates the *I*/*V* curves of PAN-based graphite fiber under small (a) and large (b) signals.

The incorporation of carbon nanotubes into nanofibers was shown to improve the electroactivity of the nanofibers [27–31]. Single-walled carbon nanotubes (SWCNTs) and conductive poly-3,4-ethylene dioxythiophene/poly-styrene sulfonate (PEDT/PSS) with polyacrylonitrile, polyacrylonitrile, *Bombyx mori* silk, etc., have been co-elctrospun to form conducting nanofibers. The inclusion of SWCNTs showed a further increase in the electrical conductivity of nanofibrous yarn, as well as in the tensile strength.

Hwang reported the successful electrospinning of a composite fiber containing carbon black (CB) and polyurethane (PU) [32]. The effects of introducing CB into the PU-matrix in the form of fiber web were investigated with respect to mechanical,

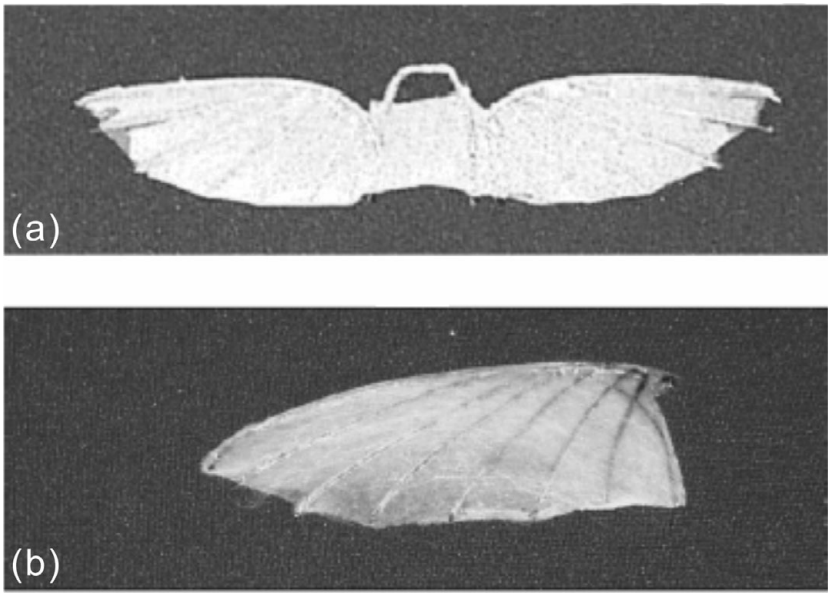

Fig. 8.11 TrF1 fibers electrospun onto MAV wing frames. (a) Double wing configuration, approximate dimensions are 15.2 cm × 5.1 cm; (b) single wing configuration, approximate dimensions are 10.2 cm × 6.4 cm [25].

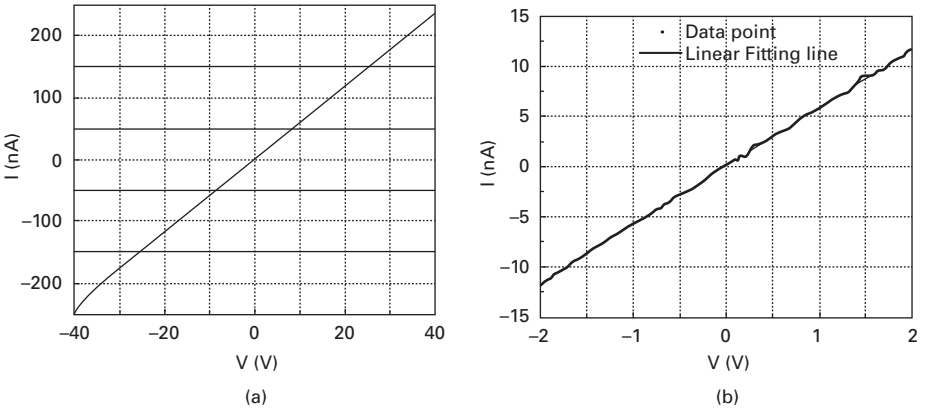

Fig. 8.12 *I*/*V* curves of PAN-based graphite fiber under small (a) and large (b) signals [26].

electrical and thermal properties. The highest conductivity of the fiber web was experimentally determined to be approximately 10^{-2} S/cm for 8.03 vol% of CB filler content, which is deemed useful for several applications including electrodes in polymer actuators.

Lee *et al*. [34] synthesized copolymer poly(acrylonitrile-co-acrylamide) (P(AN-AM)) and electrospun it into nanofibers for conversion into conductive carbon fibers. To improve the electrochemical properties of CNT fibers, Ppy was deposited on CNT fibers, and the CNT/Ppy fibers are compared with glassy carbon(GC)/Ppy. The CV

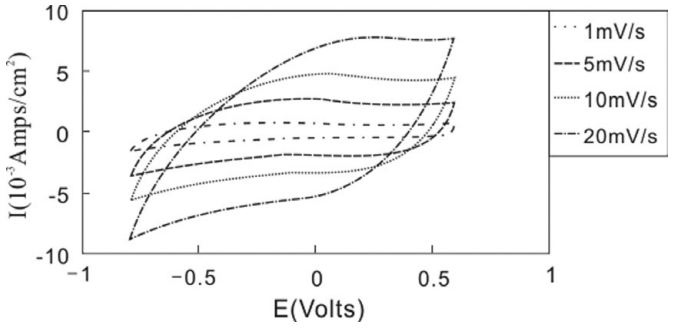

Fig. 8.13 CV of CNF/Ppy [33].

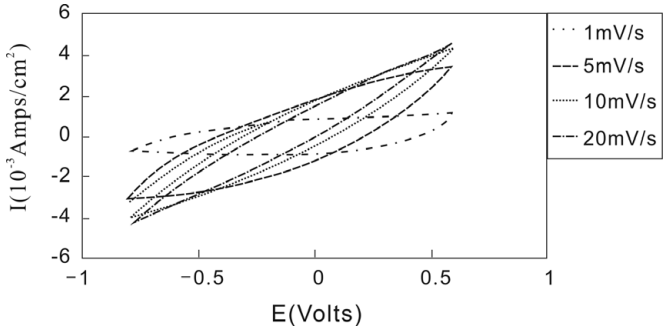

Fig. 8.14 CV of GC/Ppy [33].

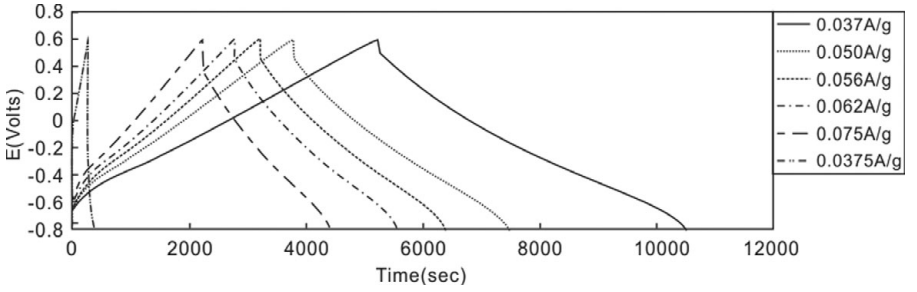

Fig. 8.15 CP of GC/Ppy [33].

curves in Fig. 8.13 and Fig. 8.14 showed that both CNF/Ppy and GC/Ppy composites were able to maintain a better capacitive behavior at lower scan rates, represented by more rectangular shaped curves. When the scan rate increased, the CV curve became oval shaped, indicating higher resistance from both electrodes. As shown in Fig. 6.43 and Fig. 8.15, at the same discharge rate of 0.05 A/g, the specific capacitance is 117 F/g for CNF/Ppy and 132 F/g for GC/Ppy. These capacitances are relatively high compared with previous studies incorporating Ppy with single (or multi)-walled carbon nanotubes in aqueous electrolyte. The result also demonstrated that Ppy is able to retain its intrinsic

Table 8.3 Critical particle diameter for supermagnetism of various metals

Metal	Critical particle diameter (nm)	Metal	Critical particle diameter (nm)
Co	70	Ni	55
Fe	14	Fe_3O_4	128

capacitance in the fibrous form. At higher scan rates, the specific capacitance of CNF/Ppy was in general ~15F/g lower than that of GC/Ppy. One contrasting result is shown in the discharge curve of Fig. 6.44. When the scan rate increased to 0.37 F/g, the discharge capacitance of GC/Ppy decreased to 29 F/g, lower than that of CNF/Ppy at a higher scan rate of 0.5 A/g. However, the capacitance of CNF/Ppy, sharing a similar trend with GC/Ppy, dropped 20% and 58% when the current density increased to 0.1 A/g and 0.5 A/g, respectively. Improving the conductivity of CNF is essential to improve the capacitance of the composite electrode at higher scan rates. The specific capacitance of polypyrrole deposited on the nanofibers was measured to be 117 F/g at 0.05 A/g in propylene carbonate. This number was fairly close to the specific capacitance of pure polypyrrole film (132 F/g at 0.05 A/g), implying that the capacitance of polypyrrole was retained in the fibrous form.

8.3 Magnetic nanofibers

8.3.1 Supermagnetism

The term *magnetism* describes how materials respond at the microscopic level to an applied magnetic field. Two well-known forms of magnetism are ferromagnetism, by which materials such as iron form permanent magnets or are attracted to magnets, and paramagnetism, whereby the paramagnetic materials are attracted only when an externally magnetic field is applied. Paramagnetic materials are attracted to magnetic field and hence have a relative magnetic permeability ≥ 1. Unlike ferromagnets, paramagnets do not retain any magnetization in the absence of an externally applied magnetic field. Thus the total magnetization will drop to zero when the applied field is removed.

Superparamagnetism is a form of magnetism that occurs in small ferromagnetic or ferrimagnetic nanoparticles. In small enough nanoparticles, magnetization can randomly flip direction. The typical time between two flips is called the Néel relaxation time. In the absence of an external magnetic field, when the time used to measure the magnetization of the nanoparticles is much longer than the Néel relaxation time, the magnetization appears to be on average zero and the particles are said to be in the superparamagnetic state. In this state, an external magnetic field can magnetize the nanoparticles, similarly to a paramagnet. However, their magnetic susceptibility is much larger than the one of paramagnets. Table 8.3 shows the critical particle diameter of various metals.

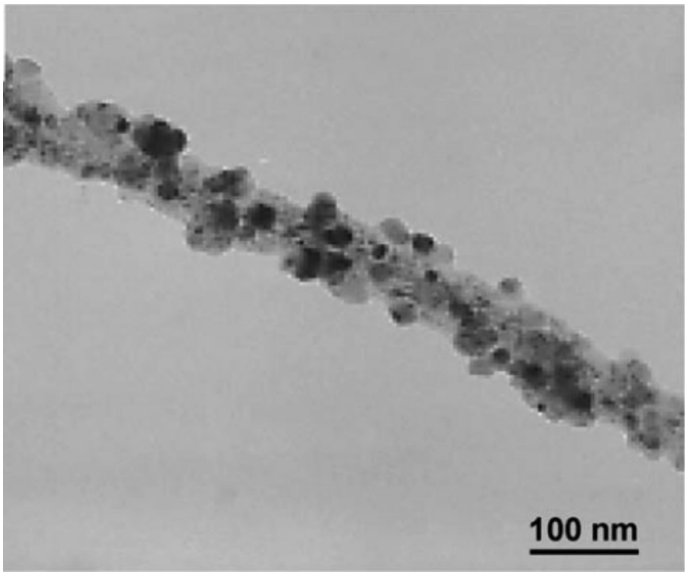

Fig. 8.16 TEM image of Fe_3O_4-filled CNFs with 40 wt% $FeAc_2$ [34].

8.3.2 Supermagnetic nanofibers

Magnetic composite fibers, in which magnetic nanoparticles are embedded in a polymeric fiber, are anticipated to possess interesting properties such as supermagnetic and magnetostrictive characteristics. These distinctive properties allow them to be applied in many areas including EMI shielding materials, medical diagnosis and electromagnetic devices, etc.

The ability to incorporate nanoparticles to fabricate electrospun nanofibers by electrospinning has inspired many studies relating to electrospun supermagnetic composites nanofibers. Zhu *et al*. [34] successfully prepared conductive and magnetic Fe_3O_4-filled CNFs with super-hydrophobic properties by electrospinning and low-temperature carbonization, as shown in Fig. 8.16. Magnetic properties of the Fe_3O_4-filled CNFs were investigated via a superconducting interference device (SQUID) magnetometer at 300 K. As shown in Fig. 8.17, the Fe_3O_4-filled CNFs with 40 wt% Fe_3Ac_2 are ferromagnetic, displaying a distinct hysteresis loop with a saturation magnetization (M_S) and coercivity (H_C) of 55.62 emu/g[1] and 150.72 Oe, respectively. shows the elationship between the $FeAc_2$ content of carbonized nanofibers and the saturation magnetization (M_s) of Fe_3O_4-filled CNFs.

Song *et al*. [35] reported that composite nanofibers of poly-caprolactone (PCL) with iron–platinum (FePt) nanoparticles were successfully fabricated via coaxial electrospinning. Figure 8.18 shows a typical TEM image of the core–shell structured composite nanofibers of FePt/PCL composite nanofiber. The magnetic behaviour of FePt/PCL composite nanofibers was investigated by alternating gradient magnetometer at room temperature. Figure 8.19 illustrates the hysteresis loop of the FePt/PCL composite nanofibers. The hysteresis loop shows superparamagnetic behavior of the FePt/PCL

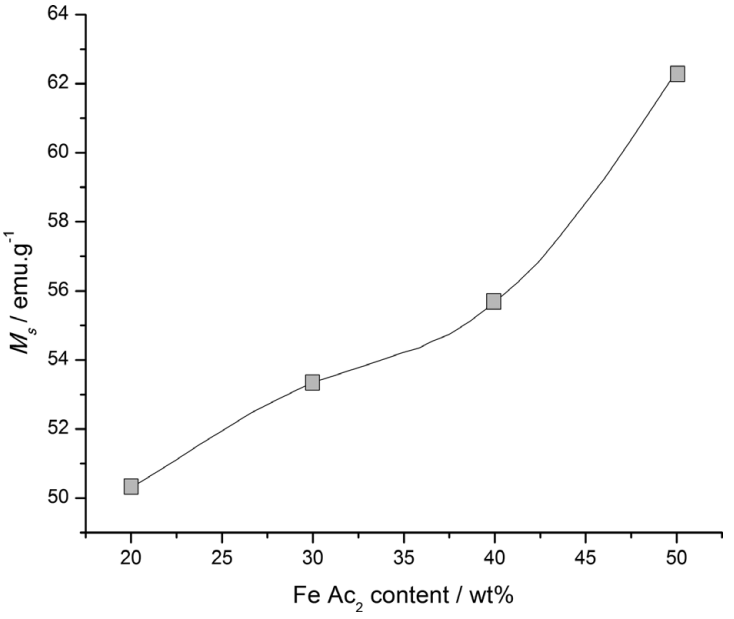

Fig. 8.17 Relationship between the content of carbonized nanofibers and the saturation magnetization (M_s) of $FeAc_2$-filled CNFs [34].

nanofibers which is ascribed that the as-synthesized FePt nanoparticles in the PCL nanofibers have a face-center cubic (fcc) phase structure and are superparamagnetic.

Chen *et al*. [36] fabricated cobalt ferrite ($CoFe_2O_4$)-embedded polyacrylonitrile (PAN) nanofibers by electrospinning. The magnetic properties of the $CoFe_2O_4$, $CoFe_2O_4$/PAN and $CoFe_2O_4$/carbon nanofibers were determined by using a vibrating sample magnetometry (VSM) with applied fields from −11 000 to 11000 Oe at 300 K, showing that the saturation magnetization of the $CoFe_2O_4$/PAN nanofibers was 45 emu/g and that the fibers demonstrated superparamagnetic behavior.

Bayat *et al*. [37, 38] produced multifunctional magnetite (Fe_3O_4) nanoparticle reinforced composite nanofibres using polyacrylonitrile (PAN) as the matrix followed by heat treatment. Various amounts of magnetite (Fe_3O_4) nanoparticles ranging from 1 wt% to 10 wt% were incorporated in the fibers. The Fe_3O_4 nanoparticles were successfully transferred into the as-spun Fe_3O_4/PAN composite nanofibrous structure, as shown in Fig. 8.20a. Electrically conductive and magnetically permeable composite carbon nanofibres were obtained by thermally treating the pristine composite nanofibres; see Fig. 8.20b,c. The electrical conductivity of carbonized samples increases with increasing the carbonization temperature ss shown in Fig. 8.21. The electrical conductivity increases from 0.055±0.004 S/cm to 2.6±0.9 S/cm with increasing the carbonization temperature from 700 °C to 900 °C. This increase was attributed to increasing the degree of graphitization resulted from the higher pyrolysis temperature, as revealed by the XRD and Raman spectra. The magnetism hysteresis loops of as-spun nanofibers are almost at the same level of Fe_3O_4 nanoparticles. Carbonized composite nanofibers show larger M_s as shown in Fig. 6.47. The sample has M_s of 5.2 emu/g, which has been

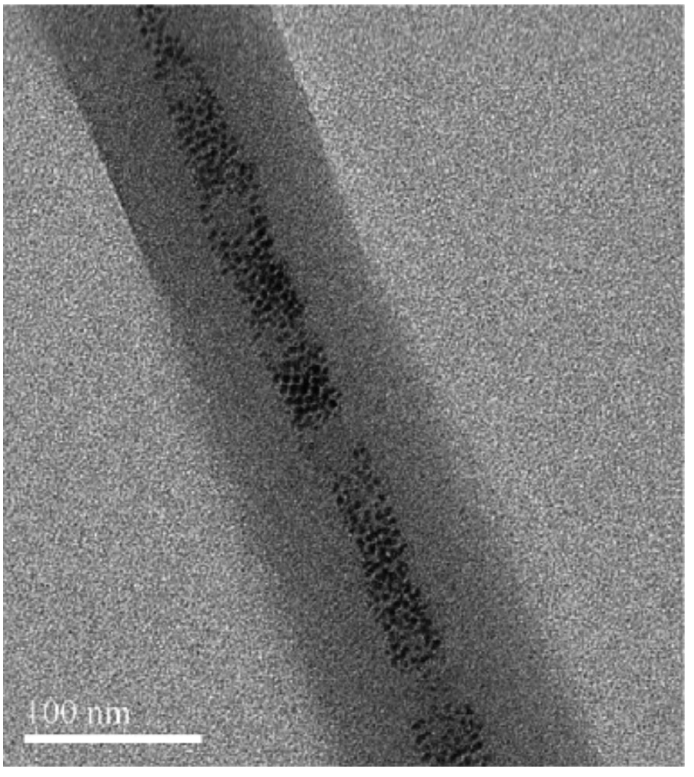

Fig. 8.18 The coaxial electrospun FePt/PCL composite nanofibers observed under transmission electron microscope [36].

increased to 12 emu/g and 16 emu/g after carbonization at 700 °C and 900 °C respectively. Simultaneously, the H_c value increased from 105 Oe to 500 Oe and 600 Oe the same coercivity value as bulk magnetite respectively. The magnetic properties and electrical conductivity of the composite materials were able to be tuned by adjusting the amount of Fe_3O_4 nanoparticles in the matrix and carbonization process.

8.4 Photonic nanofibers

8.4.1 Polymer photonics

Owing to structural flexibility, easy processing and fabrication capabilities, polymers are becoming increasingly attractive for a variety of photonic applications including telecommunications, optical interconnects, high-density data storage, optical processing, electro-optic (EO) modulation, switching and displays. The advantages of polymers over the other materials for the fabrication of optical devices include the following [39]. (1) Polymers can provide a wider bandwidth of amplification if an appropriate gain mechanism is identified. (2) The microstructure can be easily engineered at low cost to provide desired optical parameters such as bandwidth of transparency, high EO

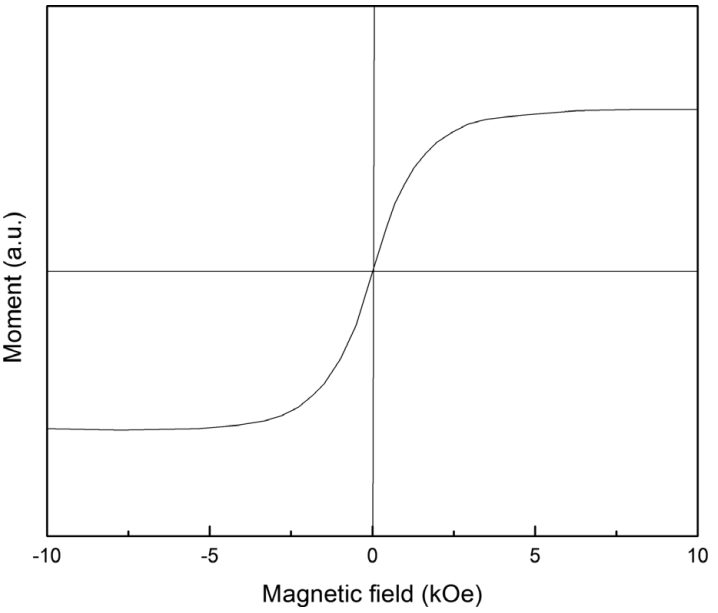

Fig. 8.19 The hysteresis loop of the FePt/PCL composite nanofibers [35].

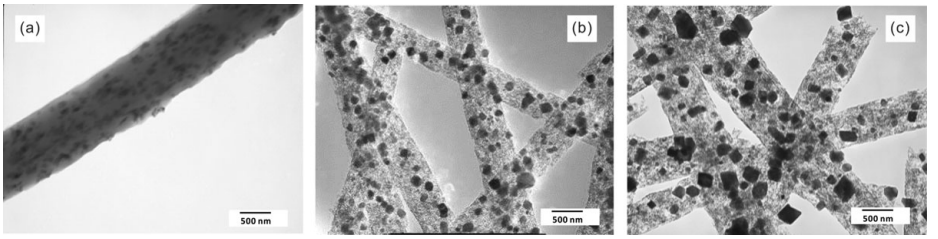

Fig. 8.20 TEM micrographs of (a) as spun Fe_3O_4/PAN nanofiber, (b) Fe_3O_4/PAN nanofiber calcinated at 700 °C and (c) Fe_3O_4/PAN nanofiber calcinated at 900 °C [37].

coefficient values, and temperature stability for specific applications. (3) The thermo-optic (TO) coefficient (*Dn*/*DT*) of polymeric material is one order of magnitude, more than that of SiO_2; as a result a polymer-based thermal optical switch can potentially perform both switching and variable attenuation functions simultaneously. (4) Unlike any of the inorganic materials that cannot be transferred to other substrates, the polymeric passive and active devices proposed herein can be easily integrated on any surface of interest.

Polymer photonic fiber technology has advanced rapidly in recent years, with the expectation that a polymer fiber will remain mechanically flexible, which, in combination with easy and inexpensive connectivity of the fibers during manipulation, is in contrast to an inorganic photonic material. Owing to the capability of producing photonic nanofibers in a simple way, electrospinning has attracted much attention in recent years.

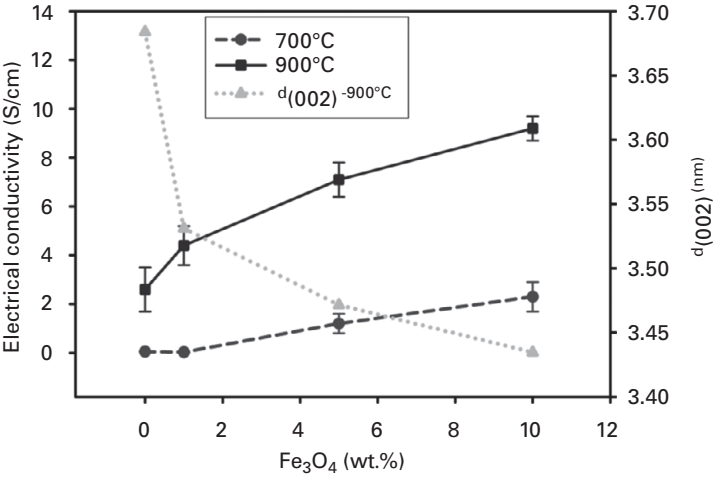

Fig. 8.21 Effect of Fe_3O_4 content on electrical conductivity and planar spacing of (002) plane ($d_{(002)}$) of carbonized samples [37].

8.4.2 Fluorescent nanofibers

Fluorescent nanofibers have potential applicability for nano-optoelectronic devices such as photoluminescent (PL), electroluminescent (EL) and non-linear optical devices, flat panel displays and photocathodes for solar cells.

Sui *et al*. [40] successfully prepared polyethylene oxide/ZnO (PEO/ZnO) composite fibers via the electrospinning technique. It was shown that PEO passivated the interface defects and quenched the visible emission of ZnO quantum dots by forming O–Zn bonds with ZnO nanoparticles and that the passivation effect of PEO could be enhanced by increasing the electrospinning voltage. Furthermore, the fibers prepared at higher voltages exhibited more intense ultra-violet emission. Figure 8.22 shows that the fibers electrospun at higher voltage exhibit more intense ultra-violet emission with small FWHM and large I_U/I_D.

Wang *et al*. reported that 1-D TiO_2 nanoparticles within polyvinylpyrrolidone (PVP) fiber matrices were prepared via coupling sol–gel method and electrospinning [41]. TEM analysis indicated that a TiO_2 nanoparticle chain was in the middle of the PVP fiber and was dispersed linearly along the fiber direction, which originated from the effect of polarization and orientation caused by a high electric field. With the increase of the concentration of sol–gel precursor in the electrospinning solution, the diameter of nanoparticles in resulting fibers decreased from 60 nm to 13 nm. Figure 8.23 shows the TEM images of PVP/TiO_2 composite fibers with different TBT concentrations at 10.5 wt% (left) and 14.0 wt% (right). Figure 8.24 shows ultra-violet–visible spectra of various PVP/TiO_2 composite fibers with different TBT concentrations. This composite nanofiber is anticipated to be applied in PL, electroluminescent (EL) and nonlinear optical devices, and photocathodes for solar.

Yang [42] co-electrospun cadmium sulphide (CdS) quantum dots with polyethylene oxide for the production of a fluorescent nanofiber composite. The results suggested

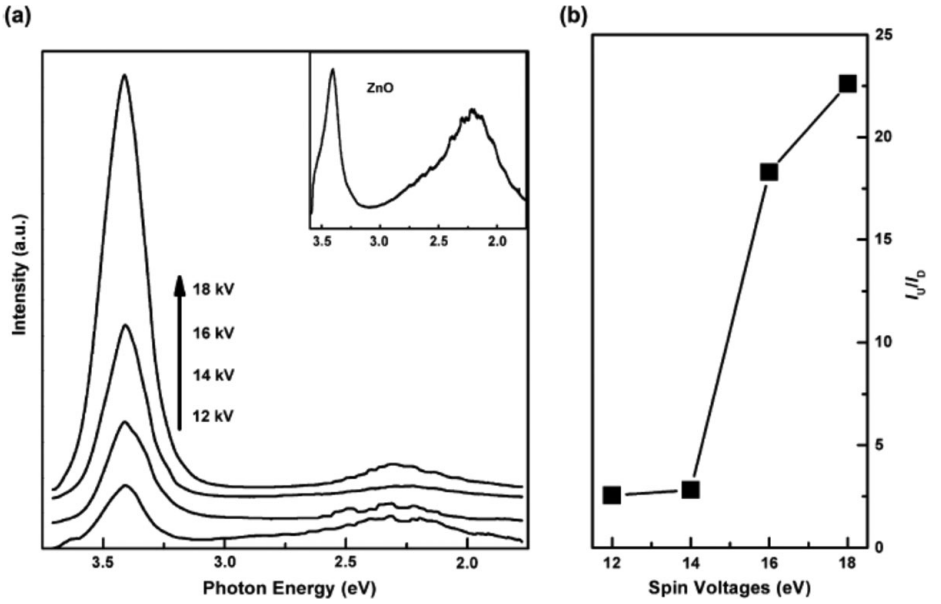

Fig. 8.22 (a) PL spectra of ZnO/PEO electrospun fibers under voltages of 12, 14, 16 and 18 kV at room temperature. (b) Inset is the PL spectrum of ZnO composite fibers. The ultra-violet emission peak I_U/I_D of ZnO/PEO electrospun fibers is shown as a function of the electrospinning voltages [40].

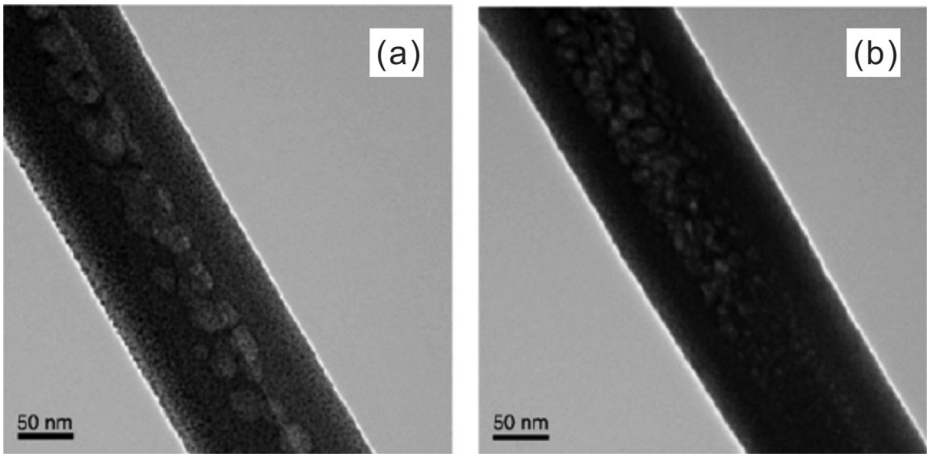

Fig. 8.23 TEM images of PVP/TiO_2 composite fibers with different TBT concentrations at 10.5 wt% (a) and 14.0 wt% (b) [41].

successful transfer of optical properties from CdS quantum dots to polyethylene oxide nanofibers, which demonstrated stable fluorescence properties and characterized the photoluminescence. Figure 8.25 shows the photoluminescence of CdS–PEO electrospun composite fibers.

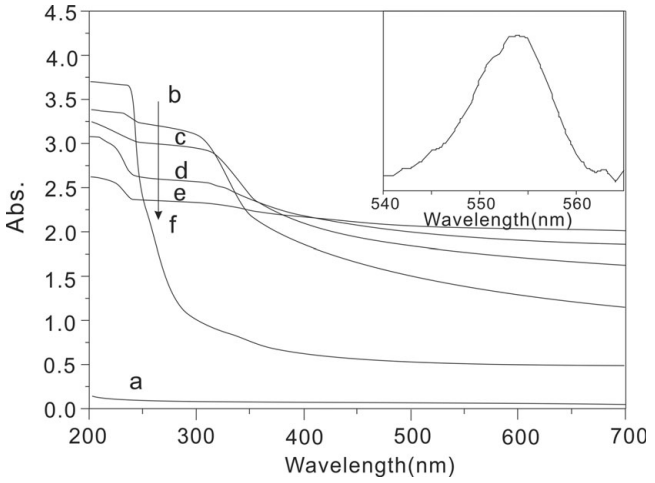

Fig. 8.24 Ultra-violet–visible spectra of various PVP/TiO2 composite fibers with different TBT concentrations: (a) PVP fibers, (b) 0.0, (c) 1.4, (d) 5.6, (e) 10.5 and (f) 14.0. Inset is PL spectrum of TiO_2 in PVP fibers [41].

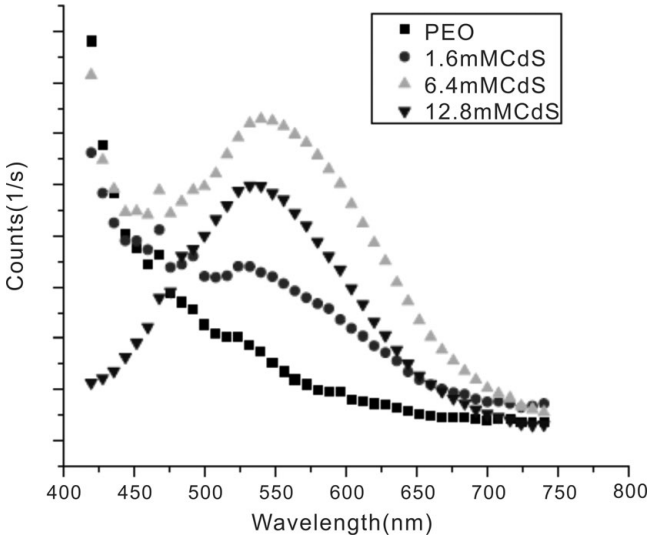

Fig. 8.25 Photoluminescence of CdS–PEO electrospun composite fibers [43].

8.4.3 Photo-catalytic nanofibers

Photo-catalytic nanofibers have potential applications in highly oriented, wire-like assemblies of metal nanoparticles for chemical or biological sensing, as antimicrobials and as solar energy collectors, etc. TiO_2 is one of the well-known oxide semiconductors for photocatalysis. With the irradiation of ultra-violet light (>3.2 eV), the absorption of photons by TiO_2 promotes electrons from the valence band into the empty conduction band, thus generating electron–hole pairs. The photogenerated holes can oxidize water

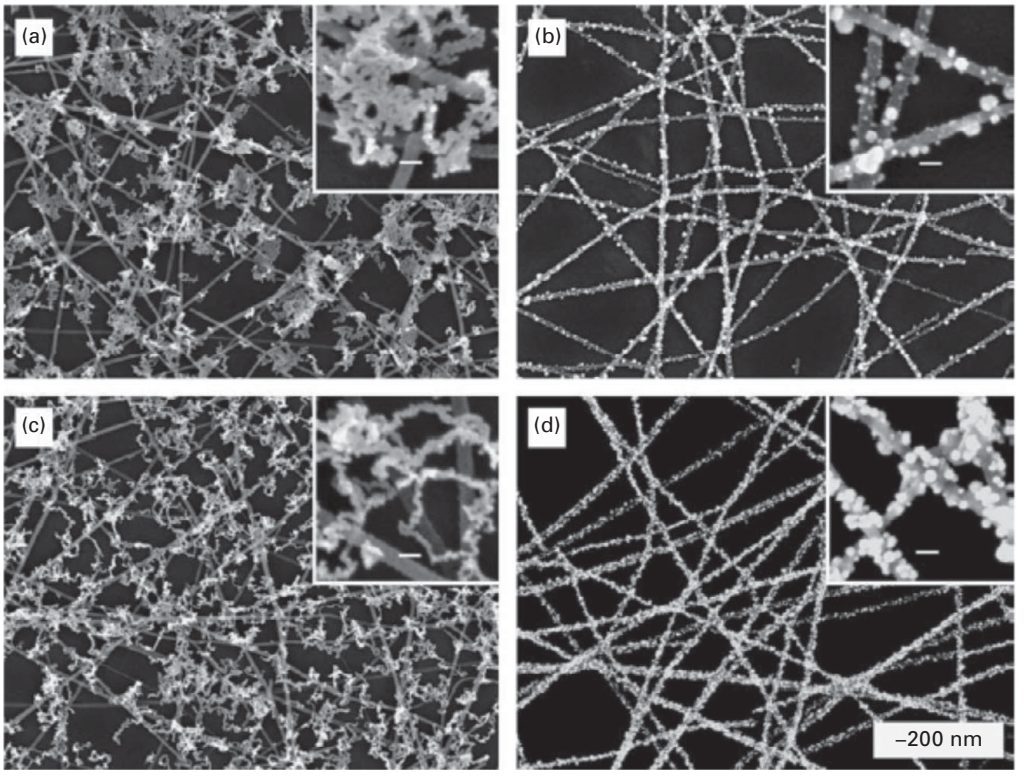

Fig. 8.26 SEM images of TiO_2 nanofibers that have been irradiated by ultra-violet light in a solution containing 1.0×10^{-4} M of $HAuCl_4$ and different capping reagents at various concentrations for 1 h: (a) poly-vinyl pyrrolidone (PVP), 5.0×10^{-6} M; (b) PVP, 0.1 M; (c) poly-vinyl alcohol (PVA), 5.0×10^{-6} M; and (d) PVA, 0.1 M. The scale bar in the insets is 50 nm [43].

to produce hydroxyl radicals, which can further oxidize organic contaminants. The excited electrons have the ability to reduce some metal ions. Therefore TiO_2 has been intensively involved in research on photo-catalytic nanofibers.

Li *et al*. [43] demonstrated that gold nanostructures could be selectively deposited on electrospun titania nanofibers through the photocatalytic reduction of $HAuCl_4$ in the presence of an organic capping reagent. Depending on the type and concentration of capping reagent used, gold nanoparticles, fractal nanosheets or nanowires could be obtained. The experiment results showed that thephotocatalytic reduction is well-suited for decorating TiO_2 nanofibers with gold nanoparticles. Figure. 8.26 shows the SEM images of TiO_2 nanofibers that have been irradiated by ultra-violet light in a solution that contained 1.0×10^{-4} M of $HAuCl_4$ and different capping reagents at various concentrations for 1 h. The selective deposition scheme is expected to provide a new route to the fabrication of highly oriented, wire-like assemblies of metal nanoparticles for chemical or biological sensing.

Zhan *et al*. [44] reported fabricated mesoporous TiO_2/SiO_2 composite nanofibers with a diameter of 100–200 nm and silica shell thickness of 5–50 nm by a sol–gel

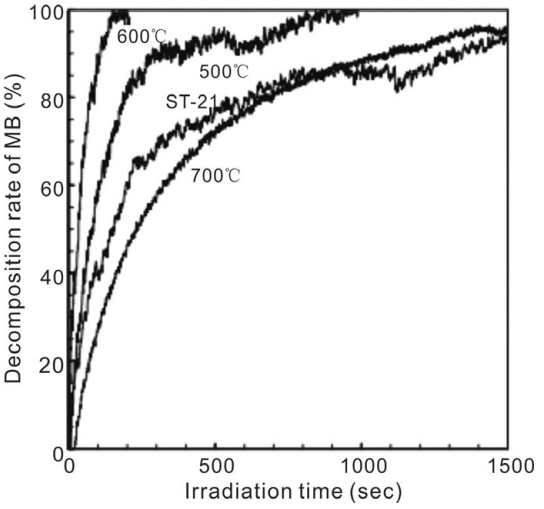

Fig. 8.27 Effect of irradiation time of white light upon the decomposition rate of methylene blue by the photocatalysis of TiO_2 nanotubes calcined at various temperatures and commercially available TiO_2 nanoparticles (ST-21) [45].

combined two-capillary co-electrospinning method. The selective photocatalytic activities of the composite nanofibers were investigated by photo-oxidation of methylene blue (MB) and disperse red S-3GFL (DR) dyes. The absorptions at 664 nm and 228 nm are proportional to the concentrations of MB and DR, respectively, and the concentrations of these two dyes are measured as a function of irradiation time. Using the nanofibrous cores after dissolution of SiO_2 as a photocatalyst, the absorptions of both MB and DR almost completely disappear after irradiation for 50 min. However, using the composite nanofibers as the photocatalyst, only the absorption peaks of MB disappear and the DR absorption at 228 nm hardly changes. The selective photocatalytic activity of this nanofiber might open new potential fields of applications such as separation processes.

Nakane *et al*. [45] demonstrated that photocatalysis of the TiO_2 nanotubes was superior to that of commercially available anatase type TiO_2 nanoparticles (ST-21). TiO_2 hollow nanofibers (nanotubes) were fabricated by using electrospun poly-vinyl alcohol (PVA) nanofibers as precursor nanofibers. The precursor nanofibers of the PVA–Ti alkoxide hybrid were formed by the impregnation of Ti alkoxide into PVA nanofibers obtained by electrospinning. The photocatalytic reaction using the TiO_2 nanotubes formed was investigated. The nanotubes obtained had a high specific surface area and the existence of mesopores on the nanotube wall was indicated by the nitrogen adsorption isotherms. Figure 8.27 shows the relationship between the decomposition rate of methylene blue and the irradiation time of white light for each TiO_2. The photocatalysis of the anatase type TiO_2 nanotube (calcination at 500 °C and 600 °C) is higher than that of ST-21, and the nanotube (calcination at 600 °C) shows the highest photocatalysis in this experiment. The specific surface area of ST-21 is higher than that of TiO_2 nanotubes, but the TiO_2 nanotubes perform better

in terms of photocatalysis, which could be due to the mesoporous walls of the nanotubes that lead to the efficient photocatalysis of TiO_2 nanotubes.

References

1. Y. Bar-Cohen, *Electroactive polymer (EAP) actuators as artificial muscles: reality, potential, and challenges*. Society of Photo Optical, 2004.
2. A. MacDiarmid, "Nobel Lecture:"Synthetic metals": A novel role for organic polymers," *Reviews of Modern Physics*, vol. 73(3), pp. 701–712, 2001.
3. Y. Bar-Cohen, "Biologically inspired intelligent robots using artificial muscles," *Strain*,. vol. 41(1), pp. 19–24, 2005.
4. A. MacDiarmid, *et al*., "Polyaniline: electrochemistry and application to rechargeable batteries," *Synthetic Metals*, vol. 18(1–3), pp. 393–398, 1987.
5. W. Huang, B. Humphrey, and A. MacDiarmid, "Polyaniline, a novel conducting polymer. Morphology and chemistry of its oxidation and reduction in aqueous electrolytes," *Journal of the Chemical Society, Faraday Transactions 1*, vol. 82(8), pp. 2385–2400, 1986.
6. A. MacDiarmid, and W. Zheng, "Electrochemistry of conjugated polymers and electrochemical applications," *MRS Bulletin*, vol. 22(6), pp. 24–30, 1997.
7. E. Post, *et al*., "E-broidery: design and fabrication of textile-based computing," *IBM Systems Journal*, vol. 39(3&4), pp. 840, 2000.
8. B. Nabet, *When is Small Good? On Unusual Electronic Properties of Nanowires*, PA-19104, Philadelphia.
9. Z. Yao, *et al*., "Carbon nanotube intramolecular junctions," *Nature*, vol. 402(6759), pp. 273–276, 1999.
10. B. Nabet, *et al*., "Heterodimensional contacts and optical detectors," *International Journal of High Speed Electronics and Systems*, vol. 10(1), pp. 375–386, 2000.
11. H. Dai, *et al*., "Controlled chemical routes to nanotube architectures, physics, and devices," *Journal of Physics and Chemistry B*, vol. 103(51), pp. 11 246–11 255, 1999.
12. J. S. Harrison, *et al*., *Electrospun electroactive polymers*, U.S.A.as represented by the Administrator of the National Aeronautics and Space Administration (Washington, DC, USA) United States, 2006.
13. M. Li, *et al*., "Electrospinning polyaniline-contained gelatin nanofibers for tissue engineering applications," *Biomaterials*, vol. 27(13), pp. 2705–2715, 2006.
14. I. Norris, *et al*., "Electrostatic fabrication of ultrafine conducting fibers: polyaniline/polyethylene oxide blends," *Synthetic Metals*, vol. 114(2), pp. 109–114, 2000.
15. K. Yun, *et al*., Korea, 2001. **DETAILS PLEASE**.
16. K. Senecal, *et al*., *Conductive (electrical, ionic and photoelectric) membrane articlers, and method for producing same*, The United States of America as represented by the Secretary of the Army: United States, 2001.
17. K. Senecal, *et al*. Photoelectric response from nanofibrous membranes, in *2001 Materials Research Society Fall Meeting*. Boston, 2001.
18. F. Ko, A. El-Aufy, and H. Lam, "Electrostatically generated nanofibres for wearable electronics, in *Wearable Electronics and Photonics*, X. M. Tao, Ed. Cambridge, UK: Woodhead Publishing Ltd., 2005, pp. 13–40.
19. A. MacDiarmid, *et al*., "Electrostatically-generated nanofibers of electronic polymers," *Synthetic Metals*, vol. 119(1–3), pp. 27–30, 2001.

20. Y. Xia, A. MacDiarmid, and A. Epstein, "Camphorsulfonic acid fully doped polyaniline emeraldine salt: in situ observation of electronic and conformational changes induced by organic vapors by an ultraviolet/visible/near-infrared spectroscopic method," *Macromolecules*, vol. 27(24), pp. 7212–7214, 1994.
21. A. G. MacDiarmid, *et al*., "Towards optimization of electrical and mechanical properties of polyaniline: is crosslinking between chains the key?" *Synthetic Metals*, vol. 55(2–3), pp. 753–760, 1993.
22. S. Pomfret, *et al*., "Electrical and mechanical properties of polyaniline fibres produced by a one-step wet spinning process 1," *Polymer*, vol. 41(6), pp. 2265–2269, 2000.
23. S. Iijima, "Helical microtubules of graphitic carbon," *Nature*, vol. 354(6348), pp. 56–58, 1991.
24. C. M. Waters, *et al*., *Liquid Crystal Devices*. United States: Imperial Chemical Industries PLC, 1992.
25. K. Pawlowski, *et al*., "Electrospinning of a micro-air vehicle wing skin," *Polymer*, vol. 44(4), pp. 1309–1314, 2003.
26. Y. Wang, S. Serrano, and J. Santiago-Aviles, "Conductivity measurement of electrospun PAN-based carbon nanofiber," *Journal of Materials Science Letters*, vol. 21(13), pp. 1055–1057, 2002.
27. A. El-Aufy, B. Nabet, and F. Ko, "Carbon nanotube reinforced (PEDT/PAN) nanocomposite for wearable electronics," *Polymer Preprints*, vol. 44(2), pp. 134–135, 2003.
28. F. Ko, *et al*., "Electrospinning of continuous carbon nanotube-filled nanofiber yarns," *Advanced Materials*, vol. 15(14), pp. 1161–1165, 2003.
29. F. K. Ko, *et al*., "Coelectrospinning of carbon nanotube reinforced nanocomposite fibrils," *A. C. S. Symposium Series*, vol. 918, pp. 231–245, 2006.
30. F. K. Ko, and H. J. Yang, "Functional nanofibre: enabling materials for the next generation SMART textiles," *Textile Bioengineering and Informatics Symposium Proceedings*, vols. 1 and 2, pp. 1–12 1217, 2008.
31. J. Ayutsede, *et al*., "Carbon nanotube reinforced *Bombyx mori* silk nanofibers by the electrospinning process, *Biomacromolecules*, vol. 7(1), pp. 208–214, 2006.
32. J. Hwang, *Carbon Black Filled Electrospun Fiberweb: Electrical and Mechanical Properties*, North Carolina State University, 2006.
33. N. Lee, *et al*., *Polypyrrole Coated Carbon Nanofibers for Supercapacitor Electrodes, in SAMPE* 2010: Seattle.
34. Y. Zhu, *et al*., "Multifunctional carbon nanofibers with conductive, magnetic and superhydrophobic properties," *ChemPhysChem*, vol. 7(2), pp. 336–341, 2006.
35. T. Song, *et al*., "Encapsulation of self-assembled FePt magnetic nanoparticles in PCL nanofibers by coaxial electrospinning," *Chemical Physics Letters*, vol. 415(4–6), pp. 317–322, 2005.
36. I. H. Chen, C.-C. Wang, and C.-Y. Chen, "Fabrication and characterization of magnetic cobalt ferrite/polyacrylonitrile and cobalt ferrite/carbon nanofibers by electrospinning," *Carbon*, vol. 48(3), pp. 604–611, 2010.
37. M. Bayat, H. Yang, and F. Ko, *Electrical and Magnetic Properties of Fe_3O_4/Carbon Composite Nanofibres, in SAMPE* 2010: Seattle.
38. M. Bayat, H. Yang, and F. Ko, "Electromagnetic properties of electrospun Fe_3O_4/carbon composite nanofibers," *Polymer*, vol. 52(7), pp. 1645–1653, 2011.
39. M. Uddin, and H. Chan, "The challenges in the fabrication of reliable polymer photonic devices," *Journal of Materials Science: Materials in Electronics*, vol. 20(1), pp. 277–281, 2009.

40. X. Sui, C. Shao, and Y. Liu, "Photoluminescence of polyethylene oxide–ZnO composite electrospun fibers," *Polymer*, vol. 48(6), pp. 1459–1463, 2007.
41. C. Wang, *et al*., "Preparation of one-dimensional TiO2 nanoparticles within polymer fiber matrices by electrospinning," *Materials Letters*, vol. 61(29), pp. 5125–5128, 2007.
42. H. Yang, *Fabrication and Characterization of Multifunctional Nanofiber Nanocomposite Structures through Co-electrospinning Process*. Drexel University, 2007.
43. D. Li, *et al*., "Photocatalytic deposition of gold nanoparticles on electrospun nanofibers of titania," *Chemical Physics Letters*, vol. 394(4–6), pp. 387–391, 2004.
44. S. Zhan, *et al*., "Mesoporous TiO_2/SiO_2 composite nanofibers with selective photocatalytic properties," *Chemical Communications*, vol. 2007(20), pp. 2043–2045, 2007.
45. K. Nakane, *et al*., "Formation of TiO_2 nanotubes by thermal decomposition of poly(vinyl alcohol)–titanium alkoxide hybrid nanofibers," *Journal of Materials Science*, vol. 42(11), pp. 4031–4035, 2007.

9 Nanocomposite fibers

A nanocomposite is a materials of which the matrix contains reinforcement materials having at least one dimension in the nanoscale (<100 nm), wherein the small size offers some level of controllable performance that is expected to be better than in conventional composites. In another words, these nanocomposites should show great promise either in terms of superior mechanical properties, or in terms of superior thermal, electrical, optical and other properties, and in general, at relatively low-reinforcement volume fractions [1, 2]. The principle properties for such reinforcement effects are that (1) the properties of nano-reinfrocements are considerabley higher than the reinforcing materials in use and (2) the ratio of their surface area to volume is very high, which provides a greater interfacial interaction with the matrix [1]. Table 9.1 shows the geometries, types and surface-to-volume relations of reinforcements and their arrangement modes in fiber composites.

Table 9.2 lists the typical functional nanoparticles and matrices that have been used for the composites. Among all the nano-reinforcements, carbon nanotubes (CNTs), nanoclay, graphene and nanofibers are the most usually involved materials for the structural nanocomposites that are introduced in this chapter.

9.1 Carbon nanotubes

Single-wall carbon nanotubes (SWCNT) and multi-wall carbon nanotubes (MWCNT) are the two major types of nanotubes popular as reinforcement materials. The SWCNT is made of a single graphene sheet rolled seamlessly into a cylinder with a diameter on the order of 1 nm and a length that varies in the range of around 100 nm to the centimeter scale [3–6]. The MWCNTs range from 2 nm to 100 nm in diameter and can be tens of centimeters in length [7, 8]. The most common synthesis methods for CNTs include laser ablation [9], chemical vapour deposition [10], arc discharge [11] and gas catalytic decomposition [12, 13].

9.1.1 Structure and properties

9.1.1.1 Structure

Carbon nanotubes, composed of honeycomb lattices, are built from sp^2 carbon units and are structurally seamless. The SWCNT consists of a single seamlessly rolled graphene sheet with a typical diameter on the order of 1 nm, while the MWCNT is an array of

Table 9.1 Reinforcement geometries and their arrangement mode in fiber composites

Dimension	Type	Surface/Volume relation	Arrangement mode
0-D (3 Nano Axis)	Nanoparticle Nanosphere	$\frac{3}{r}$	
1-D (2 Nano Axis)	Nanotube Nanowire Nanowhisker Nanofiber	$\frac{2}{r}+\frac{2}{l}$	
2-D (1 Nano Axis)	Nanoplatelet	$\frac{2}{t}+\frac{4}{l}$	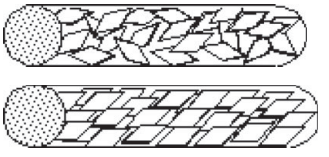

Table 9.2 Typical functional nanoparticles and matrices

Function	Nanoparticles	Polymer
Mechanical	CNT, Graphene	PAN, PVDF, Cellulose
Thermal	Clay	PAN
Electrical	CNT	PEDT, SBS
Magnetic	Fe_3O_4	PVDF, PCL PAN PEO
Optical	CdS	PEO PMMA
Biological/ antimicrobial	Ag, TiO_2	PCL, PLGA
Hydrophillicity	SiO_2	PAN, PA66
Photocatalytic	TiO_2	PU

concentric SWCNT cylinders with a 0.35 nm separation between each two walls, which is identical to the basal plane separation in graphite [5]. Also, MWCNTs tend to form in bundles which are parallel in contact and consist of tens to hundreds of nanotubes [14]. Figure 9.1 illustrates a TEM image of SWCNTs, and Fig. 9.2 shows a TEM image of an MWCNT.

The manner in which the graphene walls of the nanotube are rolled together can lead to the formation of an armchair, a zigzag or a chiral structure [17] Figure 9.3 illustrates the atomic structure of (a) an armchair and (b) a zigzag nanotube.

These groups are distinguished by their unit cells, which are determined by the chiral vector given by the equation: $C_h = n\hat{a}_1 + m\hat{a}_2$, where $\hat{a}_1$ and $\hat{a}_2$ are unit vectors in the 2-D hexagonal lattice, and n and m are integers. Another important parameter is the chiral angle, which is the angle between C_h and $\hat{a}_1$ [17]. Figure 9.4 shows a schematic diagram of the way a hexagonal sheet of graphite is "rolled" to form a CNT.

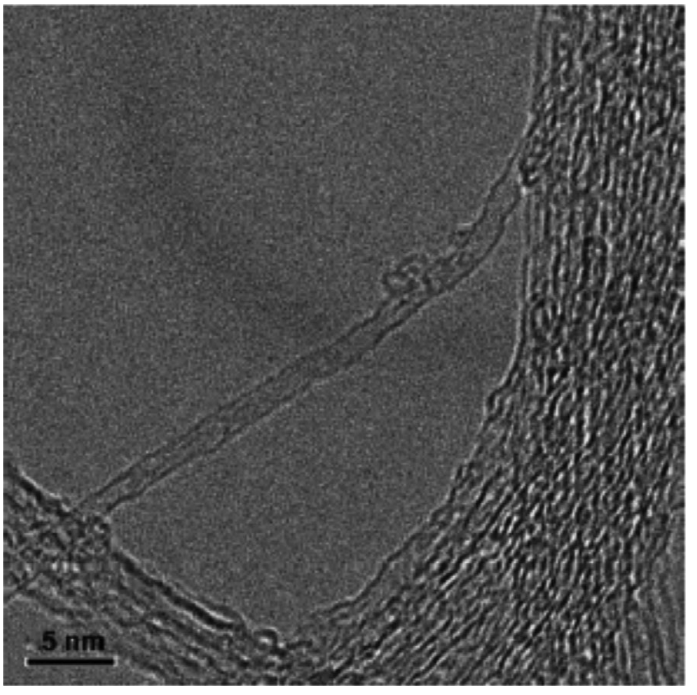

Fig. 9.1 TEM image of SWCNTs [15].

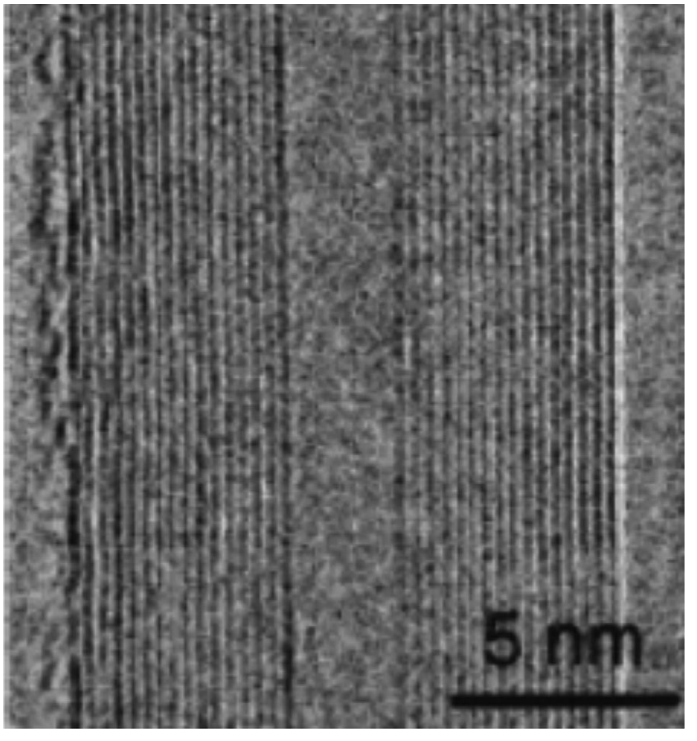

Fig. 9.2 TEM image of an MWCNT [16].

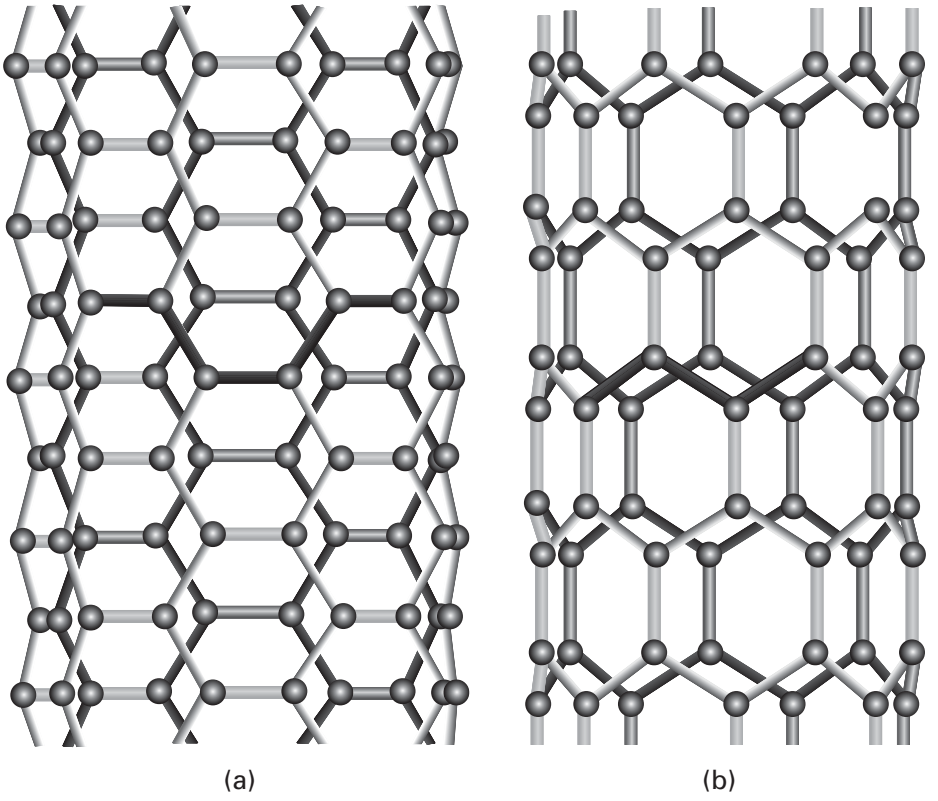

Fig. 9.3 Illustrations of the atomic structure of (a) an armchair and (b) a zigzag nanotube [17].

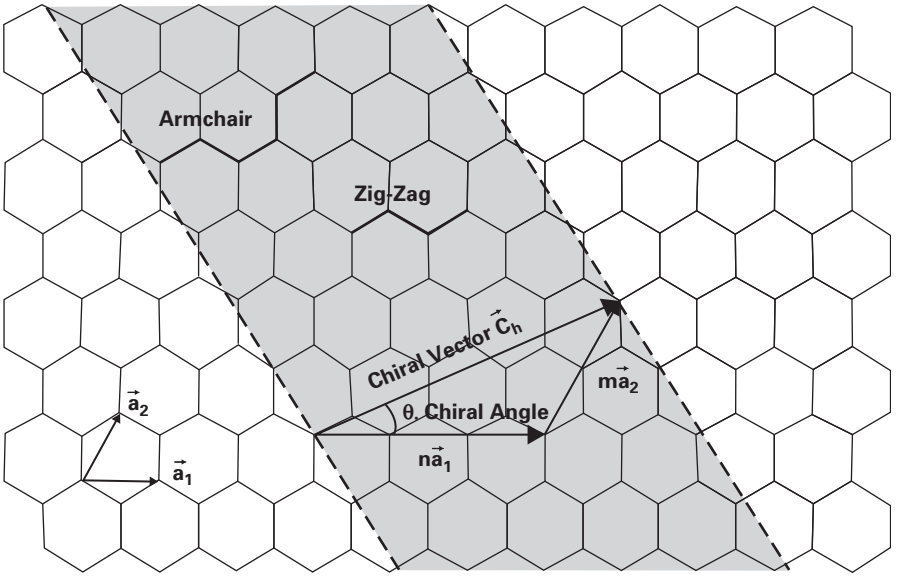

Fig. 9.4 Schematic diagram showing how a hexagonal sheet of graphite is "rolled" to form a CNT [17].

The nanotube is of the armchair type when $n = m$ and the chiral angle is 30°. When m or n is zero and the chiral angle is equal to zero, the nanotube is known as a zigzag nanotube. When the chiral angles are between 0° and 30°, chiral nanotubes are formed. The chiral angles and tube diameter determine the properties of the nanotube. The CNTs can be semiconducting or metallic. The metallic behavior occurs when $n - m{=}3L$ and $L = 0$, resulting in the highest occupied molecular orbital and lowest unoccupied molecular orbital (HOMO–LUMO), the fundamental gap being 0 eV. The electronic properties are a result of the electrons being normal to the nanotube axis. While acting as a semiconductor, the fundamental gap was found to be 0.5 eV, and a function of the diameter which causes them to exist as ropes in their native state [18]. The energy gap is determined by the equation $E_{gap} = 2y_0a_{cc}/d$, where y_0 is the C–C tight bonding overlap energy (2.7 ± 0.1 eV), a_{cc} is the nearest neighbour C–C distance (0.142 nm), and d is the diameter. It was shown that a small gap would exist because of π/σ bonding orbital and π^*/σ^* anti-bonding orbital at the Fermi level. The Fermi energy is the highest occupied orbital, and has neighboring finite density carbon atoms in the flat sheet. The phase difference is known to be at the 2π levels for a metallic tube and zero for a semiconductor. The density state occurs at sharp peaks as the energy level is increased.[19]

9.1.1.2 Mechanical properties

The interatomic bonding strength determines the mechanical properties of solid matter. Based on the C–C sp^2 bonding energy, CNTs are predicted to have high stiffness and axial strength [20]. CNTs were reported have an elastic modulus greater than 1 TPa, and a tensile strength of up to 150 GPa according to both experimental and theoretical results [17, 21, 22]. Unlike carbon fibers, which easily fracture, nanotubes are found very flexible. They can be elongated, twisted, flattened, or bent into circles before fracturing, and regain their original shape up to a very large bending angle [23–25]. The "kink-like" ridges allow the structure to relax elastically while under compression [26]. Nanotubes were also found to have an extremely large breaking strain, which decreased with temperature [27]. The elastic modulus, Poisson's ratio and the bulk modulus were all found to be directly affected by the tube's radius.

9.1.1.3 Electrical properties

It was shown that metallic conduction in CNTs can occur in the absence of the doping effects. The I-tight-binding model within the zone folding scheme elucidated that one third of CNTs were found to be metallic while two thirds were semiconducting, depending on their chirality [20]. Semiconducting nanotubes have chirality-dependent band gaps that are inversely proportional to the diameter, ranging from approximately 1.8 eV for very small diameter tubes, to 0.18 eV for the widest possible stable SWCNT [28]. High-purity CNTs are extremely conductive. Owing to their 1-D nature and ensuing quantum confinement effects, charge carriers can travel through nanotubes without scattering, resulting in ballistic transport. The absence of scattering means that Joule heating is minimized such that nanotubes can carry very large current densities, of up to 100 MA/cm^2 [29]. In addition, carrier mobilities as high as 10^5 cm^2/Vs have been reported in semiconducting nanotubes [30]. Superconductivity has also been observed in

SWCNTs, albeit with transition temperatures of 5 K [31]. Theoretical and experimental results showed superior electrical properties of CNTs. They can produce electric current carrying capacity 1000 times higher than copper wires [32]. The electronic capabilities possessed by CNTs are seen to arise predominately from interlayer interactions, rather than from interactions between multilayers within a single CNT or between different CNTs [33]. These optical properties have proved to be especially unique, and confer either metallic or semiconducting capabilities, depending on tubule diameter and chiral angle.

9.1.1.4 Thermal properties

Phonons determine the thermal properties (specific heat capacity and thermal conductivity) of CNTs [20]. A phonon is a quantum of acoustic energy identical to that of a photon. Phonons are a result of lattice vibrations observed in the Raman spectra [33]. The phonon contribution to these quantities dominates and is due in particular to acoustic phonons at low temperatures. Nanotubes have been found to be very conductive for phonons. Theory predicts that CNTs can have a room-temperature thermal conductivity of up to 6000 W/m K [34]. While this has not yet been attained in practice, values around 200 W/m K have been measured [35].

9.1.2 Dispersion of carbaon nanotubes

Owing to the nanoscale diameter, strong attractions present among CNTs make agglomeration the main challenge to uniform distribution of CNTs in CNT nanocomposites. Therefore a great deal of effort has been focused on CNT dispersion when it comes to CNT nanocompsites. Approaches for dispersion of CNTs have been proposed, including mechanical or chemical methods or a combination of these.

9.1.2.1 Purification

As-grown CNTs assemble as ropes or bundles with the presence of some catalyst residuals, amorphous carbon, polyhedron graphite nanoparticles and other forms of impurities. Thus, purification is necessary prior to any processes having CNTs involved in applications.

Purification of CNTs usually involves the following methods: gas- or vapor-phase oxidation [36], wet chemical oxidation [37], filtration [38, 39] or centrifugation [40]. Gas- or vapor-phase oxidation purification is typically conducted by annealing raw CNTs at a high temperature ranging from 225 °C to 760 °C under an oxidizing atmosphere such as air, a mixture of Cl_2, H_2O and HCl, a mixture of Ar, O_2 and H_2O [41], a mixture of O_2, SF6 and $C_2H_2F_4$, H_2S and O_2, etc. [42].

Figure 9.5 compares the raw CNTs with oxidized CNTs at 750 °C for 30 min, which evidently shows the success of the oxidation method in removing impurities. However, gas- and vapor-phase oxidation purifications are usually found to result in very low yields. It should also be noted that metal particles present in raw material catalyze CNTs in the presence of oxygen and other oxidizing gases. Therefore it is necessary to remove the metal particles before running an oxidation removal of carbonaceous impurities [43].

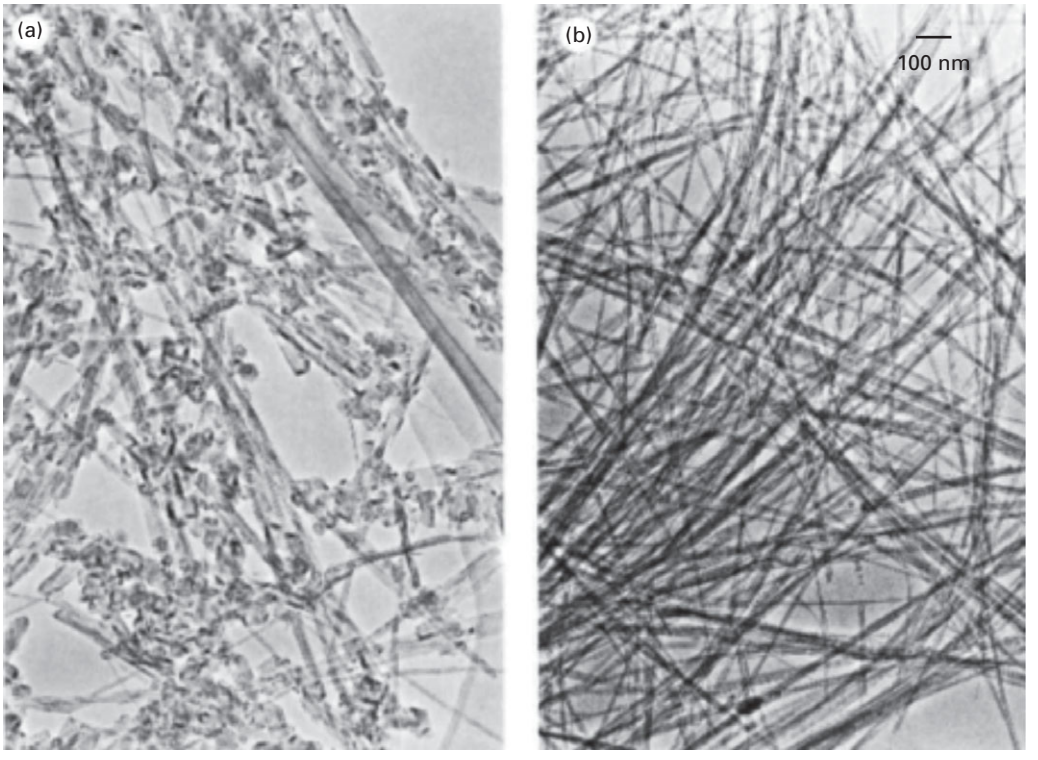

Fig. 9.5 TEM images of CNTs: (a) raw CNTs produced by arc-charge and (b) CNTs oxidized at 750 °C for 30 min [36].

Unlike gas- or vapor-oxidation, wet chemical oxidation using oxidative ions and acid ions can simultaneously remove both amorphous carbon and the metal catalyst. Therefore selection of oxidant type and precise control of treatment condition can produce high-purity CNTs in a high yield. The commonly used oxidants for wet chemical oxidation include HNO_3, H_2O_2 or a mixture of H_2O_2 and HCl, a mixture of H_2SO_4, HNO_3, $KMnO_4$ and NaOH, and $KMnO_4$ [42]. Nitric acid is the most commonly used reagent for wet chemical oxidation purification for its mild oxidation ability, inexpensive and nontoxic nature [36].

Ultimately, the purification method consists of refluxing CNTs in 2.6 M nitric acid and resuspending the nanotubes in pH 10 water with the aid of surfactant. The purified CNTs are then filtrated with a cross-flow filtration system [44]. A further purification process involving cutting the CNTs could be followed. [44]: 10 mg of the CNTs are suspended in 40 ml of a 3:1 mixture of concentrated H_2SO_4/HNO_3 in a 100 ml test tube and sonicated in a water bath (55 kHz) for 24 h at 35 °C to 40 °C. The resultant suspension is then diluted with 200 ml of water, collected on a 100 nm pore filter membrane and washed with 10 mM NaOH solution. The tubes are then further polished by suspension in a 4:1 mixture of concentrated H_2SO_4: 30% aqueous H_2O_2 with stirring at 70 °C for 30 min, followed by filtration and washing. However, strong oxidation and

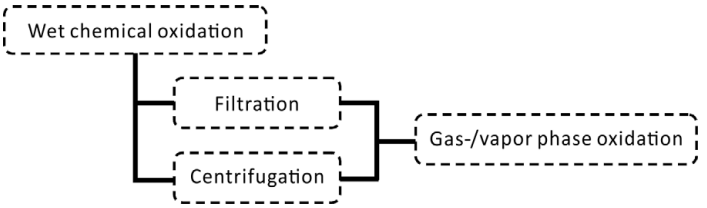

Fig. 9.6 A combination process for purification of CNTs.

acid refluxing affect the structure of CNTs. These CNTs can be opened, shortened and thinned. Wet chemical oxidation gives rise to functional groups on the nanotube surface as well [43], which bring considerably property alterations for CNT.

Unlike oxidation, filtration works based on the differences of physical size, aspect ratio and solubility between CNTs and impurities. Small size and low aspect ratio particles and soluble matter will be filtered out along with the solution while CNTs will remain. The filtration process is quite straightforward. The raw CNTs are dispersed in a solution with or without surfactant, followed with repeated filtration or microfiltration until a desired result is achieved. The advantage of filtration is that it avoids strong chemical reactions, and thus leaves CNT undamaged. The disadvantage is that this procedure is time consuming and ineffective in removing impurities that are stuck on CNTs. Moreover, the purification result relies on the dispersion quality to a large extent.

Similar to filtration, centrifugation has been used to physically separate carbon nanoparticles (CNPs) from CNTs at suitable concentrations based on the observation that well-dispersed CNTs remains stable in the solution while CNPs precipitate as sediment and therefore can be decanted, due to the difference of net surface charge [40]. Basically centrifugation is considered a supplementary mean to the other methods since it can only separate graphenes from CNTs on the condition of a well dispersion.

Except filtration and centrifugation, another mean worthy of note is electrophoresis [45–47] which is also a mild process for CNT purification by applying an electric field to surfactant-stabilized single-walled CNT (SWCNT) suspensions and induces separation of metallic particles from CNTs relying on their different electric field-induced polarizabilities. As a matter of fact, purification of CNTs is a combination of these above methods in most cases, following the sequence with possible repetition of some of the methods, as shown in Fig. 9.6. In some cases, gas- or vapor-phase oxidation may be conducted before wet chemical oxidation.

9.1.2.2 Mechanical dispersion

CNTs can be mechanically dispersed in a solution or melt by means of ultrasonication, high-shear-stress separation methods and ball milling.

Ultrasonication is an extremely common tool used to break up nanotube aggregates in solution processing of CNTs because it is convenience and practical. Ultrasonication dispersion is primarily done through a cavitation mechanism: bubbles nucleate at the CNT surface and expand rapidly, pushing CNTs apart; CNTs remain separated after implosion of the bubbles, hence the CNTs are dispersed [48, 49]. There are two major

methods for delivering ultrasonic energy into liquids and hence into CNT bundles: the ultrasonic bath and the ultrasonic horn. The frequency of the ultrasound determines the maximum bubble size in the fluid. Low frequencies (about 20 kHz) produce large bubbles and generate high energy forces as bubbles collapse. Increasing frequency reduces bubble size and nucleation, as well as cavitation. An ultrasonication bath does not produce a defined cavitation zone as does a horn, and the energy seems to be more uniformly dispersed through the liquid phase [50] However, CNTs are usually found damaged and shortened as a side effect of the involvement of high energy [51]. Buckling and compression defects, as well as stripping and fracture of CNT walls, were observed. In practice, ultrasonication dispersion is an essential approach widely involved with almost all the other mechanical methods and all the chemical methods.

The principle of high-shear-stress dispersion is the shear stress exerted on CNTs during mixing that overcomes electrostatic and van der Waals' interactions between CNTs and results in the breakup of agglomerates [52]. High-shear-stress dispersion of CNTs can be conducted with different apparatus including a high-shear homogenizer [53, 54], single [55] or twin-screw extruder [56], injection-molding machine [57] and microfluidic channels [58].

Ball milling is usually used for the opening [59] and shortening [60, 61] of CNTs, or producing nanoparticles [62] from material sources including CNTs. As strong mechanical stresses shorten the length of CNTs, the entanglements of CNTs are subsequently broken, which makes ball milling one of the solutions for the dispersion of CNTs in solution or matrix.

Experimental results from Wang *et al*. [63] showed that most of the mechanical methods cannot completely separate CNTs from entanglements but can decrease the size of the CNT agglomerates for one or two orders when applied, respectively. With the aid of a surfactant and a combination of ultrasonication, high-shear stress generated from a homogenizer and a microfluidic system, SWCNT dispersion in water was found to be significantly improved, as well as the stability [58].

9.1.2.3 Chemical dispersion

In order to achieve a uniform dispersion of CNTs, chemical methods are employed in most cases. The CNTs are to be chemically functionalized either by cutting the entangled CNTs into short pieces, or by modifying the surfaces to improve the solubility of CNTs. These chemical approaches are generally classified as covalent and noncovalent functionalization, according to their structural effects on CNTs.

9.1.2.3.1 Noncovalent functionalization

Noncovalent functionalization is a very straightforward strategy for solubilizing CNTs simply by noncovalent interactions, such as enclosing, π-stacking, wrapping and electron donor–acceptor complexation without causing structural damage to CNTs. Generally noncovalent functionalization of CNTs is fulfilled by mechanically dispersing CNTs and chemical agents in a certain solvent to have CNTs uniformly coated with the chemicals.

One type of the most common chemicals used for coating CNTs is a surfactant. Surfactants are attracted to the surface of CNTs by hydrophobic interactions and induce electrostatic or steric repulsions that can counterbalance van der Waals attractions between CNTs. Some commonly used surfactants are sodium dodecyl sulfate (SDS), Triton X-100 (TX-100), lithium dodecyl sulfate (LDS), cetyltrimethyl ammonium chloride (CTAC) and dodecyltrimethyl ammonium bromide (DTAB). Polymers are another type of chemical for coating CNTs. Amphiphilic polymers such as poly(styrene)-*block*-poly(acrylic acid) copolymers (PS_{49}-*b*-PAA_{54}, PS_{159}-*b*-PAA_{58}, or PS_{106}-*b*-PAA_{16}) [64], polystyrene-block-poly(4-vinylpyridine) copolymers (PS-b-P4VP20, PS-b-P4VP40, PS-b-P4VP70) [65], pyrene-containing copolymers ((1-pyrene)methyl 2-methyl-2-propenoate (PyMMP)-co-poly(MMA) and poly(ethylene-co-butylene)-b-poly(MMA-co-PyMMP)) [66] were found to be capable of enclosing CNTs and forming soluble CNT micelles. Proteins [67–71] and peptides [72] were also found to be excellent intermedia for separation of CNTs in solution.

Some chemicals can keep CNTs separated in solvents by wrapping them up. Linear short-chain polymers such as polyvinyl pyrrolidone (PVP), polystyrene sulfonate (PSS), poly((5-alkoxy-m-phenylenevinylene)-co-((2,5-dioctyloxy-p-phenylene)vinylene)) (PAmPV) derivatives [73], pentaoxoethylenedodecyl ether (C12E5), polyoxyethylene lauryl($C_{12}EO_8$) [74], amylase [75], porphyrin [76], polysaccharide (dextrin) and gum arabic (GA) [77] were found gaining dispersion of CNTs with this mechanism, as shown in Fig. 9.7 [78].

We may distinguish π-stacking from the wrapping approach by solubilizing CNTs via short, rigid conjugated polymers. The rigid backbone of such polymers cannot wrap around CNTs and thus the major interaction between polymer backbone and nanotube is most likely to be π-stacking, which allows control over the distance between functional groups and the CNT surface, through variation of the polymer backbone and side chains [79]. Most polymers having π-stacking with CNTs are amphiphilic, therefore the hydrophobic interaction is another major mechanism. Polymers that have been explored are mostly polyelectrolytes, including poly(aryleneethynylene)s (PPE) [79], fluorescein−polyethylene glycol (Fluor-PEG) [80], 1-pyrenebutanoic acid [81], sodium lignosulfonate (SLS) [82], oligothiophene-terminated poly(ethylene glycol) (TN-PEG) [83] and humic acid (HA) [84].

CNTs are reported to behave amphoterically (in a Lewis acid/base sense), i.e. they interact strongly with both electron donors and electron acceptors [85]. Alkali metals, small molecules such as NH_3 and H_2, and larger molecules such as aromatic amines [86] have been studied as electron donors. Halogens, small molecules like NO_2 and O_2, and organic amine have been investigated as electron acceptors [85]. The solubility of SWCNTs in anilines is up to 8 mg/ml, which is believed to be among the highest standard [86].

9.1.2.3.2 *Covalent functionalization*

Covalent functionalization is distinguished from the noncovalent approach by breaking some carbon–carbon bonds of CNTs and making new bonds through chemical reactions. Covalently functionalized CNTs are expected to have a better solubility and can be more easily integrated into inorganic, organic and biological systems.

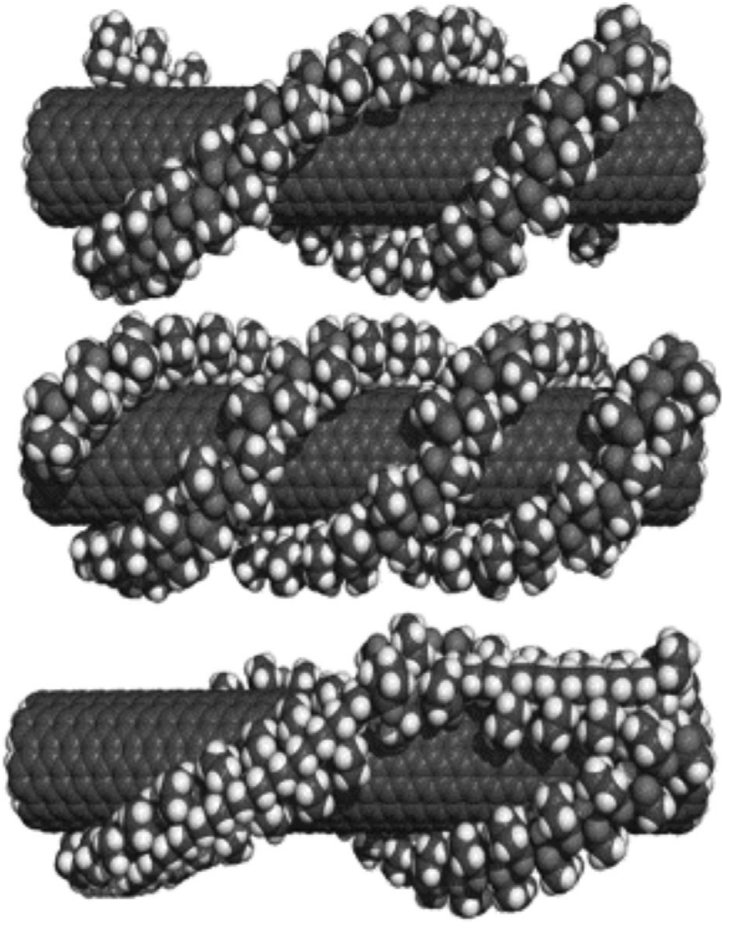

Fig. 9.7 Some possible wrapping arrangements of PVP on an SWCNT [78].

As we have mentioned in the previous section, oxidation will cut CNTs into small pieces and leave their ends open. In effect, these oxidative processes are capable of generating a variety of oxygenated functional groups, such as aldehydic, ketonic, esteric, alcoholic and carboxylic moieties [87–89], at the nanotube ends or along the tube walls [90–92]. In particular, the predominance of carboxylic acid groups on CNTs has been the basis for many of the subsequent functionalizations, thus far. Oxidized SWCNTs have been solubilized by reaction with long-chain amines, by mixing with polymers, through coordinate complexation using metal complexes, and even by attaching titanium oxide nanocrystals and quantum dots using carbodiimide chemistry.

Fluorination is one of the popular approaches for CNT functionalization. CNTs can be fluorinated by elemental fluorine at between room temperature and 600 °C [93–97]. But the best results were achieved at temperatures between 150 °C and 400 °C [98]. Fluorinated SWCNTs are found to be appreciably soluble in alcoholic solvents with evidence showing CNTs are separted from exfoliation of CNT ropes and bundles.

However, fluorination was found to cut the CNTs to an average length of less than 50 nm when applied to small diameter HipCO-SWCNT [99], and dramatically to impair the electrical conductivity of SWCNTs. A sample of untreated SWCNTs was reported to have a resistance of 10–15 Ω, while a fluorinated SWCNT sample had a resistance of >20 MΩ [100]. The fluorine substituents on SWCNTs can be displaced by treatment with strong nucleophiles such as Grignard and alkyllithium reagents [101–103] and metal alkoxides [100]. Alkylated CNTs can disperse in common organic solvents like THF and can be completely dealkylated upon heating at 500 °C in an inert atmosphere, to recover pristine CNT. Diamines [104, 105] and OH group-terminated moieties [106] can also react with fluoronanotubes via nucleophilic substitution reactions by refluxing fluoro-nanotubes in the corresponding diamine for 3 h in the presence of a catalytic amount of pyridine. Aminoalkylated CNTs are soluble in dilute acids and water, while hydroxyl CNTs form stable suspension solutions in polar solvents such as water, ethanol and dimethylformamide. Organic peroxide functionalizations for phenyl and undecyl sidewall attached CNTs from fluoro-nanotubes were also reported [107, 108].

Cycloaddition is another important type of chemical modification method of CNTs. Cycloaddition of CNTs with dichlorocarbene was first reported by Haddon's group [90, 109–111]. The cycloadditions were generated with potassium hydroxide from chloroform [90], and later from phenyl(bromodichloromethyl)mercury [110, 111], as shown in Fig. 9.8. However, the functionalization degree in these cases was low. Sidewall functionalization of CNTs via nitrene cycloadditions [90, 109–114] allows for covalent binding of a variety of different groups such as alkyl chains, aromatic groups, dendrimers, crown ethers and oligoethylene glycol units, and leads to a considerable increase

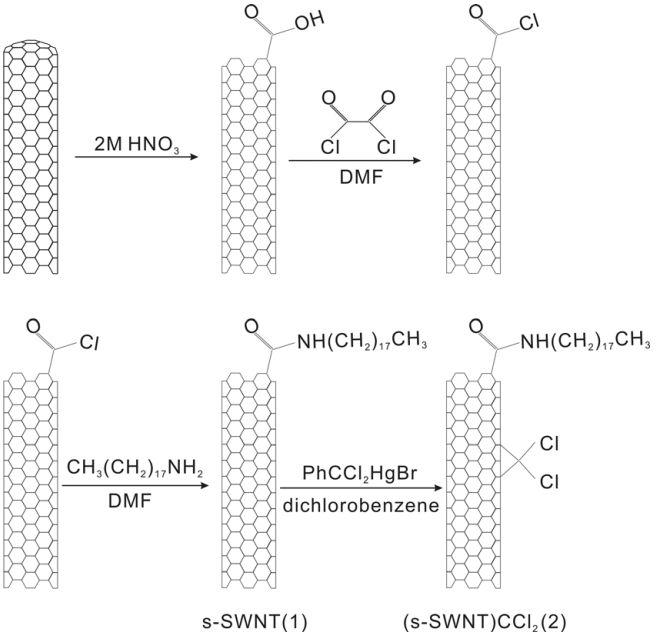

Fig. 9.8 Dissolution and dichlorocarbene reaction of SWCNTs [111].

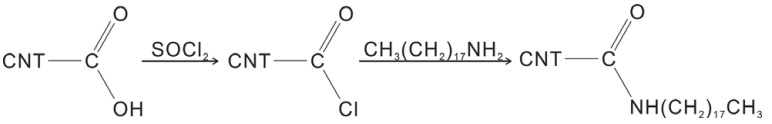

Fig. 9.9 Schematic depiction of oxidated SWCNTs followed by treatment with thionyl chloride, and subsequent amidation.

in the CNT solubility in organic solvents such as 1,1,2,2-tetrachloroethane (TCE), dimethyl sulfoxide (DMSO) and 1,2-dichlorobenzene (ODCB). The highest solubilities of 1.2 mg/ml were found for SWCNT adducts with nitrenes containing crown ether of oligoethylene glycol moieties in DMSO and TCE, respectively [114].

Grafting polymers with CNTs is a method that plays an important role in producing CNT nanocomposites. Through "grafting to" or "grafting from" methods, oligomers and polymers are covalently linked to the defect sites of CNTs formed during purification and oxidization, resulting in pastes containing well distributed CNTs, which then go through a series of composite manufacturing process and are formed into CNT composites.

The "grafting to" method means the readymade polymers react with the functional groups on the surface of CNTs. Most reported "grafting to" procedures involve with initial treatment of the oxidized CNTs with thionyl chloride for acryl chloride activation. A typical example is as follows (Fig. 9.9). (1) Mix CNTs in $SOCl_2$/dimethylformamide (DMF) (volume ratio is 20:1), stir the solution at 70 °C for 24 h, followed by centrifugation and washing the CNTs with anhydrous tetrahydrofuran (THF). (2) Heat the mixture of the resulting CNTs and long-chain molecule octadecylamine (ODA) at 90 °C to 100 °C for 96 h, followed by removal of the excess ODA by washing in ethanol. (3) Dissolve the remaining solid in dichloromethane, filter and dry. The yield of the grafted SWCNTs is usually >60% (based on shortened SWCNTs) [109]. The obtained SWCNTs are substantial soluble in chloroform, dichloromethane, aromatic solvents (benzene, toluene, chlorobenzene, 1,2-dichlorobenzene) and carbon disulfide (CS_2). Polymers terminated with amino or hydroxyl moieties are commonly involved in amidation and esterification grafting reactions with the functionalized CNTs [115, 116]. So far poly(styrene-cohydroxymethylstyrene) (PSA) [109], poly(styrene-co-p-(4-(4′-vinylphenyl)-3-oxabutanol)) (PSV) [117], poly(vinyl alcohol) (PVA) [118], poly(vinyl acetate-co-vinyl alcohol) (PVA-VA) [119] and poly[3-(2-hydroxyethyl)-2,5-thienylene] (PHET) [120], functionalized porphyrin(5-p-hydroxyphenyl-10,15,20-tritolylporphyrin, por-OH) [121], oligomeric species containing derivatized pyrenes(3-decyloxy-5-pyrenyloxyphenylmethan-1-ol, I_{Py}) [122] and lipophilic and hydrophilic dendra which are terminated with long alkyl chains and oligomeric poly(ethylene glycol) moieties [123] have been grafted to CNTs via ester linkages; poly(propionylethylenimine-co-ethylenimine) (PPEI-EI) [124], poly(styrene-co-aminomethylstyrene) (PSN) [125], poly(amic acid) containing bithiazole ring [126], poly(propionylethylenimine-co-ethylenimine) (PPEI-EI) [127–129], poly(m-aminobenzene sulfonic acid) (PABS) [130], monoamine-terminated poly(ethylene oxide) (PEO) [131] and glucosamine [132] have been successfully grafted to acryl chloride activated CNTs via amidation reaction.

The "grafting from" method, also known as *in situ* synthesis, means the monomers were covalently attached to CNTs and then polymerized for CNT containing polymers. Polymers such as polystyrene (PS) [133], poly(sodium 4-styrenesulfonate) (PSS) [134], poly(4-vinylpyridine) [135], polyamide (PA), and poly(methylmethacrylate)-*block*-polystyrene (PMMA-*b*-PS) [136] have been radically grafted onto CNTs. Xu *et al.* [137] constructed amphiphilic polymer brushes with a hard core of multi-walled CNTs (MWCNTs) and a relatively soft shell of polystyrene-*block*-poly (*N*-isopropylacrylamide) (PS-*b*-PNIPAM) by *in situ* surface reversible addition–fragmentation chain transfer (RAFT) polymerization of styrene and *N*-isopropylacrylamide on the modified convex surfaces of MWCNTs (MWCNT-PS). *In situ* atom transfer radical polymerization (ATRP) is a novel approach for functionalization of CNTs for its capability of controlling the thickness of functional layers by control the molecular weight of graft polymer chains. Kong *et al.* [138] summarized the general four-step strategy for grafting polymers from the CNTs via ATRP: (1) functionalization of CNT (CNT-COCl) with carbonyl chloride groups, (2) introduction of hydroxyl groups onto the surface of CNT by reaction of CNT-COCl with glycol, generating CNT-OH, (3) initiation sites (CNT-Br) for ATRP by reacting CNT-OH with 2-bromo-2-methylpropionyl bromide, and (4) grafting polymerization of methyl methacrylate (MMA) from MWCNT-Br by means of *in situ* ATRP. The resulted MWCNT-PMMA following this procedure showed a relatively good solubility in non- or weakly polar solvents such as THF and $CHCl_3$, but a poor solubility in strong polar solvents such as DMF and DMSO [138]. *In situ* nitroxide mediated polymerization (NMP) is a very attractive method for CNT/polymer composites with controllable polymer architecture. This method does not involve any indispensable CNT pre-treatment and can be used for polymerization of hydrophilic polymers, such as acrylic acid. Using NMP methods, Datsyuk *et al.* [139] successfully polymerized amphiphilic block copolymers (a hydrophilic block (polyacrylic acid PAA) and a hydrophobic block (polystyrene PS)) with double-walled CNTs(DWCNTs).

9.1.3 Alignment of carbon nanotubes

To take full advantage of the anisotropic nature of nanotubes, it is important to have CNTs aligned in a polymer matrix. The aligment of CNTs in a matrix can be fulfilled before, during or after process the composite fabrication process. Before or during the process, an external force field, such as a magnetic or electric field, or a shear force, is usually applied to the fluid containing CNTs to align CNTs. After the process, shear stress mechanically applied through slicing, rubbing or stretching becomes a effective method for CNT alignment.

9.1.3.1 Alignment of carbon nanotubes in solution

A high magnetic field has been shown to be an efficient and direct means to align CNTs. Fujiwara *et al.* [140] sussessfully aligned arc-grown MWCNTs by applying a high magnetic field of 7 T to an MWCNT dispersion in methanol. The MWCNTs were found aligned parallel to the field. The result was explained by the difference between the diamagnetic susceptibilities parallel and perpendicular to the tube axis. If the parallel

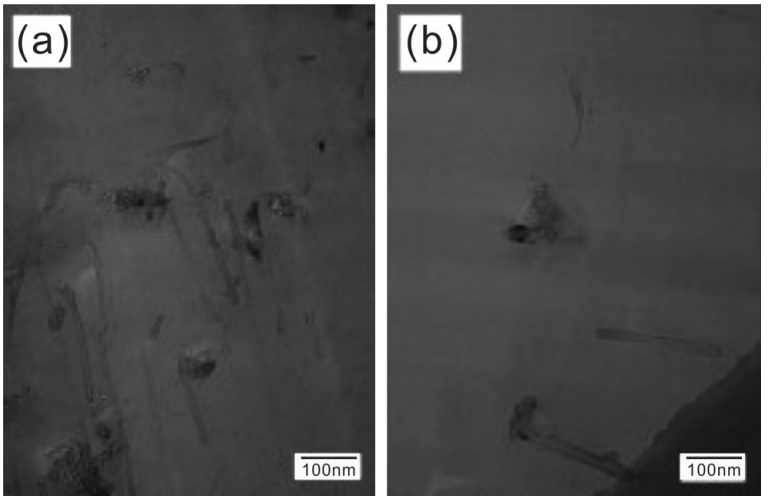

Fig. 9.10 TEM of a 100 nm thin film of 1 wt% MWCNT–polyester composite [141]. The composite was sliced (a) parallel and (b) perpendicular to the applied magnetic field.

diamagnetic susceptibility is larger than the perpendicular diamagnetic susceptibility, MWCNTs tend to align parallel to the magnetic field by overcoming the thermal energy. Based on the work done by Fujiwara *et al*., Kimura *et al*. [141] demonstrated that this technique is helpful for fabricating aligned nanotube reinforced polymer composites possessing anisotropic electrical and mechanical properties. It can be seen from Fig. 9.10 that MWCNTs parallel to the direction of the magnetic field are relatively longer than those in a perpendicular direction.

9.1.3.1.1 *Electric field*

Application of an electric field during nanocomposite curing can induce the formation of aligned conductive nanotube networks between the electrodes. Through this method, Martin *et al*. [142] achieved well-aligned CVD-grown MWCNTs as electrically conductive fillers in an epoxy system based on a bisphenol-A resin and an amine hardener. Figure 9.11 shows a transmission optical micrograph of the MWCNT containing epoxy composites.

9.1.3.1.2 *Liquid crystalline phase*

Liquid crystal phase can force CNTs aligned to a great extent. The cooperative reorientation of liquid crystals and the overall direction of the nanotube alignment can be further controlled both statically and dynamically by the application of external electric, magnetic, mechanic, or even optic in nature fields [143]. When dispersed in superacids at low concentrations, SWCNTs were found to dissolve as individual tubes behaving as Brownian rods. At higher concentrations, SWCNTs formed an unusual nematic phase consisting of spaghetti-like self-assembled supermolecular strands of mobile, solvated tubes in equilibrium with a dilute isotropic phase. At even higher concentrations, the spaghetti strands self-assemble into a polydomain nematic liquid crystal. The liquid

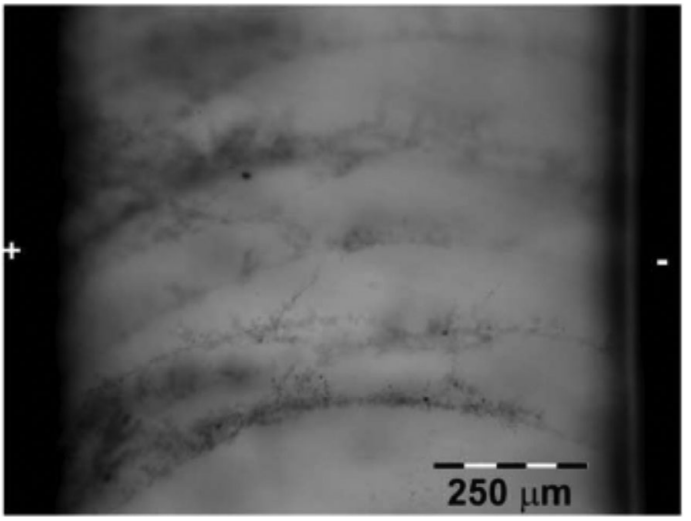

Fig. 9.11 Transmission optical micrographs of epoxy composites containing well-aligned 0.01 wt% multi-wall carbon nanotubes during curing at 80 °C in a D.C. field of 100 V/cm [142].

crystal phase separated into needle-shaped strands (~20 μm long) of highly aligned SWCNTs, termed alewives, upon the introduction of small amounts of water [144].

9.1.3.2 Alignment of carbon nanotubes in matrix

9.1.3.2.1 Composite slicing

Ajayan *et al.* reported a CNT alignment method in a polymer matrix by cutting thin slices (50–200 nm) of a CNT–polymer composite [145]. The nanotube-reinforced composite demonstrated a parallel and well-separated arrangement of nanotubes. Nanotube alignment by composite slicing showed the nature of rheology on nanometer scales in composites and flow-induced anisotropy, produced by the cutting process.

9.1.3.2.2 Film rubbing

DeHeer *et al.* [148] reported that aligned nanotube-reinforced composites could be obtained by rubbing the surface of a randomly aligned nanotube film with a thin Teflon sheet or aluminum foil. The nanotube film was first prepared by drawing a nanotube suspension through a 0.2 μm pore ceramic filter, which left a uniform black deposit on the filter. The deposited material was then transferred onto a plastic surface (Delrin or Teflon) by pressing the tube-coated side of the filter onto the polymer. The surface facing the filter was exposed by lifting it from the filter. A remarkable transformation was observed when this surface was lightly rubbed with a thin Teflon sheet or aluminum foil [146]. The surface became silvery in appearance and was found to be densely covered with nanotubes.

9.1.3.2.3 Mechanical stretching

Jin *et al.* demonstrated nanotube alignment in a polymer matrix by mechanical stretching [147]. The composites were fabricated by casting a suspension of CNTs in a solution of a thermoplastic polymer and chloroform. These composites were uniaxially stretched at 100 °C and were found to remain elongated after removal of the load at room temperature. The orientation and the degree of alignment were determined by

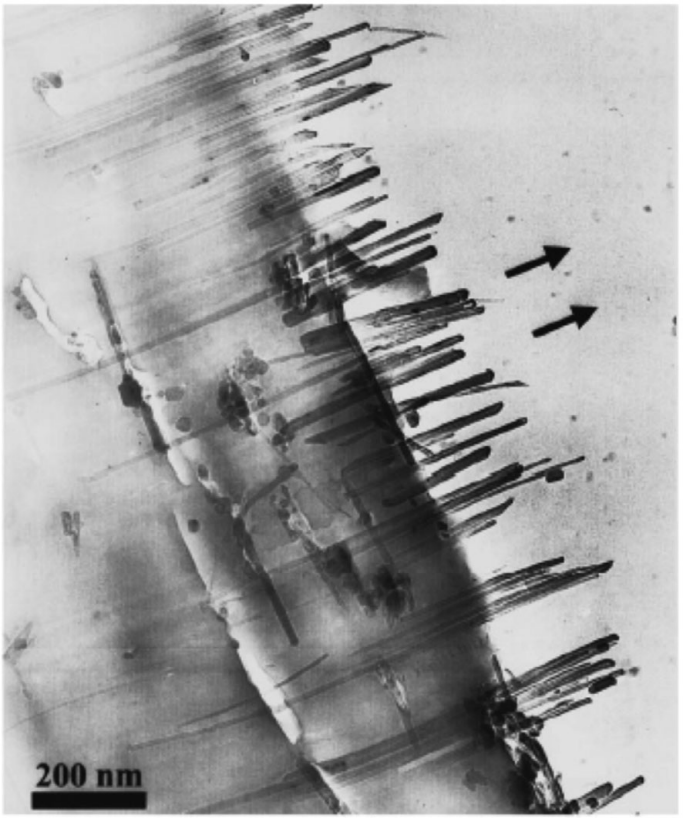

Fig. 9.12 TEM image of an internal fracture surface of a composite after being sliced parallel to the stretching direction by a microtome [147].

X-ray diffraction. Figure 9.12 shows a TEM of an internal fracture surface of a composite after being sliced parallel to the stretching direction by a microtome. The sample thickness is about 90 nm. It shows fiber pull-out. The nanotubes are aligned parallel to the stretching direction. In some areas, nanotubes bridge the microvoids (or microcracks) in the matrix and presumably enhance the strength of the composite.

Haggenmueller *et al*. [148] applied a high draw ratios ($\lambda = 20$–3600) stretching to melting spun SWCNT/PMMA fibers. Raman spectra of the fibers at the indicated fiber angles with respect to the incident laser polarization axis showed the mosaic distribution width at half maximum (FWHM) was as small as 4°, which indicates the good alignment of SWCNTs along the fiber axis. Owing to the alignment of the SWCNTs, these PMMA/SWCNT nanocomposite fibers show improved mechanical properties and the nanocomposite films show increased electrical conductivity.

9.1.3.2.4 *Electrospinning*

Alignment of nanotubes in a polymer matrix can also be achieved through electrospinning. It was shown that electrospinning is an effective and efficient technique to induce nanotube alignment in a polymer composite [149–152]. During co-electrospinning of

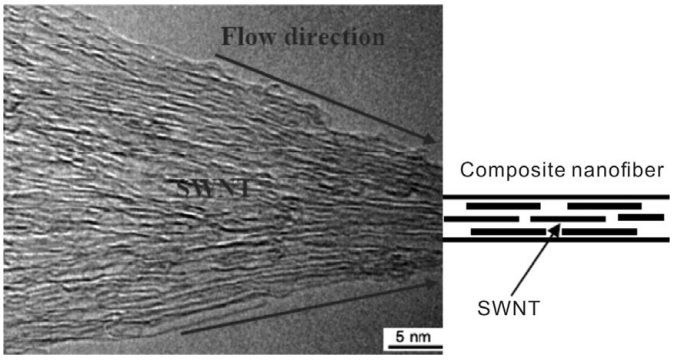

Fig. 9.13 "Logs in a river" analogy (LIRA).

CNT and polymer, alignment of the CNT is induced by the flow of the polymer solution, the presence of electrostatic charge, and nanometer diameter confinement. Flow induced alignment is analogous to "logs in a river," as shown in Fig. 9.13, where the SWCNT tends to orient parallel to the fiber axis. The presence of electrostatic charge further orients the CNT along the fiber due to the stretching of the polymer jet. Stretching of the polymer jet also induces molecular orientation. Lastly, diameter confinement is due to the fact that the produced fibers have diameters on the nanoscale and the SWCNTs are ~1–2 μm in length. Normally, the SWCNTs appear in bundles of relatively longer length. Therefore, orientation of the SWCNT ropes along the fiber direction is confined by the diameter of the nanofiber.

9.1.4 Carbon nanotube nanocomposite fibers

The desire to translate the outstanding mechanical, thermal and electrical properties of individual CNTs into bulk structures has motivated the search for continuous fabrication methods for nanotube assemblies. In order to exploit the remarkable mechanical properties of an individual nanotube, continuous CNT fibers (collection of CNT) and yarns (collection or linear assembly of CNT fibres) purely or largely comprising CNTs have been fabricated by several methods. In this section the key methods for producing continuous CNT composite fibers and yarns are reviewed. To demonstrate the feasibility of manufacturing nanotube-reinforced multifunctional continuous yarns, the structure and properties of SWCNT-filled continuous PAN yarns produced by electrospinning and MWCNT-reinforced continuous cellulosic yarns by liquid crystal electropinning are presented.

A number of processes are dedicated to the production of CNT based fiber and fibrous assemblies. Each of these processes has its own unique features and thus potential applications. Table 9.3 provides a summary of the structural features of various CNT fiber/yarn produced by different processes and their corresponding strength and modulus. One obvious observation is that none of these CNT based structures comes close to reaching the property potential of the CNT. Similar to staple textile yarn structures, the mechanical properties of CNT assemblies are governed by the cohesive/interaction forces between CNTs. Therefore the critical factor for making a

Table 9.3 Properties of CNT fibers and yarns [154]

Fiber	Method	Volume fraction	Alignment fraction	Content (%)	Diameter (μm)	Modulus (GPa)	Strength (GPa)
Neat SWCNT fibers	CVD [155]	< 0.48	0.85	95	7∼20	360	4(9)
	Dry spinnning [156, 157]	∼ 0.53	twist angel 21°		2∼10	330	3.3
	Liquid crystal spinning (Smalley) [158, 159]	∼ 0.70	0.9 mosaic angle 31°	100	/	120	0.1
Composite CNT fibers	Liquid crystal spinning (10% SWCNT/PBO) [160]	10 wt%	/	10	25	167	4.2
	Wet spinning [161–163]	/	Alignment angle 9°	60	50	80	3.2
	Electrospinning [152]	0.028 (4 wt%)	/	4	/	207	/
	Gel spinning (5% MWCNT/ UHMWPE)	/	/	5	/	136.8	4.2

strong CNT assembly is related to the perfection of the structural features or fiber architecture, which depends on the packing density and orientation of the CNTs in the fiber and yarn structures. Therefore a hybrid process combining an ability to orient CNTs and a defect-free matrix to transfer the load would provide the pathway to connect the outstanding properties of CNTs to the fiber and yarn structures. Owing to the alignment ability and nanosize, electrospinning is expected to achieve nanotube nanocomposites with a high load transfer ratio [153, 154].

9.1.4.1 Methods for producing carbon nanotube fibers

In the decade since the discovery of CNTs, several methods have been developed to manufacture fibres and yarns from CNT of discrete length. These methods include: chemical vapor deposition (CVD) process [164–169], solid-state processes [156, 157, 170, 171], electrophoretic proceses [172], liquid crystal spinning [158, 173], wet spinning [163, 174–182], electrospinning [183–189] and traditional spinning, which includes traditional wet spinning and melt spinning. The first three processes produce pure CNT fibers, whereas the latter three produce CNT composite fibers. The liquid crystal spinning process can produce pure CNT fibers as well as composite fibers. Each method has its advantages and disadvantages. Invariably, these methods are still in the laboratory development stage. There is a strong desire to transition these methods to robust manufacturing processes.

9.1.4.2 Chemical vapor deposition

Strands of CNTs have been produced by variations of the chemical vapor deposition (CVD) process [164–167]. Alan Windle's group showed the possibility of obtaining continuous fibers without an apparent limit to the length by mechanically drawing the

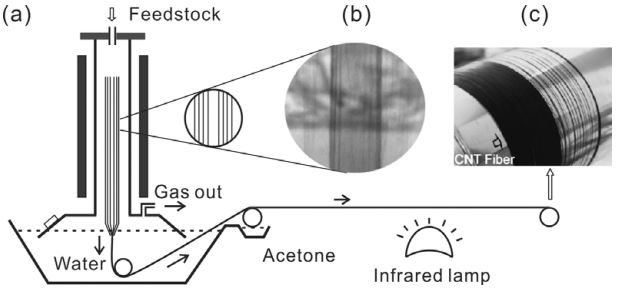

Fig. 9.14 CVD synthesis and spinning set-up for the fabrication of continuous CNT yarns. (a) Schematic diagram of the synthesis and spinning set-up. (b) A photograph showing a layered CNT sock formed in the gas flow, and spinning of the finished fiber on the final spool (c) [192].

CNTs from the chemical vapor deposition (CVD) synthesis zone of a furnace [168, 169]. In the MWCNT fibers, the nanotube diameters were 30 nm, with an aspect ratio of 1000. They contained 5 wt%–10 wt% iron but no extraneous carbon particles. The quality of alignment of the nanotubes measured from transforms of scanning electron microscope images showed the full width (at half maximum) of the inter-nanotube interference peak measured around the azimuthal circle was 11°. There are indications that the degree of alignment can be improved if greater tension is applied to the fiber during processing. The SWCNT fibers contained more impurities than the MWCNT fibers, with the proportion of SWCNTs estimated from transmission electron microscope observations as being 50 vol%. The SWCNTs had diameters between 1.6 nm and 3.5 nm and they were organized in bundles with lateral dimensions of 30 nm. The highest strength reported for direct spun CNT fiber was 2.2 *N*/tex, and the stiffness was 160 *N*/tex (equivalent to 4.4 GPa and 320 GPa respectively, assuming a density of 2.0 g/cc) These values are within the range of properties of typical carbon fibers [190]. The electrical conductivity measured along a fiber was $8.3 \times 10^5\ \Omega^{-1}\mathrm{m}^{-1}$, which is slightly higher than the typical value for carbon fibers [191]. Li's group [192] further developed a water-densification and spinning process for this technique, which allows fabrication of continuous CNT yarns with a length of over several kilometers, as shown in Fig. 9.14. The yarn consists of multiple monolayers of CNTs concentrically assembled in seamless tubules along the yarn axis. The yarn quality close to conventional textile yarns. This direct spinning process allows one-step production of nanotube fibers, ribbons and coatings with potentially excellent properties and wide-range applications [191].

The CVD process has currently been scaled up in 2004 by Nanocomp Technologies, as shown in Fig. 9.15. It has been reported that Nanocomp Technologies has produced and delivered 10 km of CTex™ CNT yarn to aerospace customers, and it was claimed that they are capable of delivering 4 × 8 square foot CNT mats [193]. Taking advantage of the outstanding properties of the CNT products, value added components such as conductive cables, thermal straps, EMI shielding "skins," and high strength sheets or yarns for incorporation into final end-user products are also being developed.

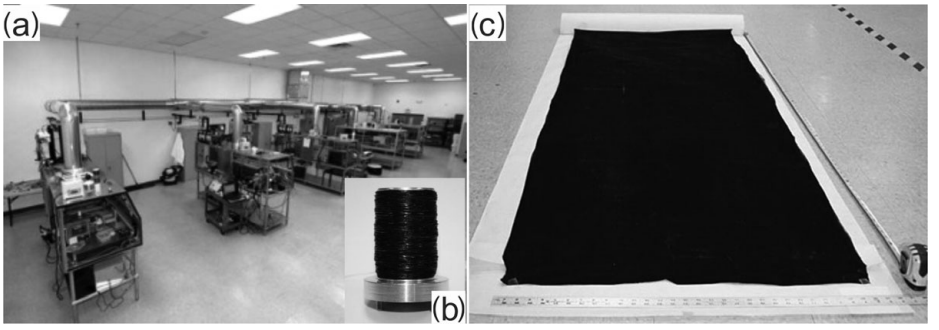

Fig. 9.15 Scale-up CVD process [193]. Equipment in Nanocomp Technologies Inc: (a) CVD setup; (b) CTex™ CNT yarn; (c) CNT mats.

9.1.4.3 Dry spinning

Dry spinning is a method by which the carbon nanotube yarns are drawn from an as-grown nanotube forest [170]. This process is quite similar to that used in the conversion of card webs to slivers and subsequently twisted yarns in textile manufacturing. As shown in Fig. 9.16, during spinning a collection of carbon naotubes from a CNT forest are being drawn-twisted to form a linear twisted CNT yarn assembly. The strength development of the CNT forest derives from the cohesion of the CNT assembly and the entanglement of CNTs as in the staple yarn. As the CNTs at the edge of the forest are pulled away from the forest, the CNTs cling together and form a continuous strand. Because of high inter-fiber contact area per yarn volume as a result of the very high surface-to-volume ratio of the MWCNTs, the yarns can be twisted, knitted and knotted to form higher-order structures [171]. The highest tensile strength of CNT fibers attained is 3.3 GPa [156], spun from a 1 mm array, which is much higher than that of CNT fibers from the 0.65 mm array (1.91 GPa) [157]. The highest reported Young's modulus is up to 330 GPa [157].

9.1.4.4 Liquid crystal spinning

Analogous to the formation of conventional rod-like polymers such as poly(p-phenylene benzobisoxazole) (PBO) and poly(p-phenylene benzobisthiazole) (PBZT), Smalley's group developed a liquid crystal spinning process for pure CNT yarns [158, 194]. A dispersion of purified SWCNTs (5 wt%–10 wt%) in 102% sulfuric acid (2 wt% excess SO_3) were prepared in a nitrogen-purged dry box. The mixture was manually mixed and then transferred to the mixing apparatus via a stainless steel syringe. The material was subsequently extruded through a small capillary tube into a coagulation bath. Continuous lengths of macroscopic neat SWCNT fibers were obtained. The neat SWCNT fibers possess a Young's modulus of 120 ± 10 GPa, at a tensile strength of 116 ± 10 MPa. The relatively low strength is attributed to the presence of localized defects and voids [158].

To take advantage of the extraordinary mechanical, electrical and thermal properties of CNTs, studies have been done to reinforce polymers and other matrix systems with CNTs. Kumar *et al.* [160] synthesized PBO in poly(phosphoric acid) (PPA) in the

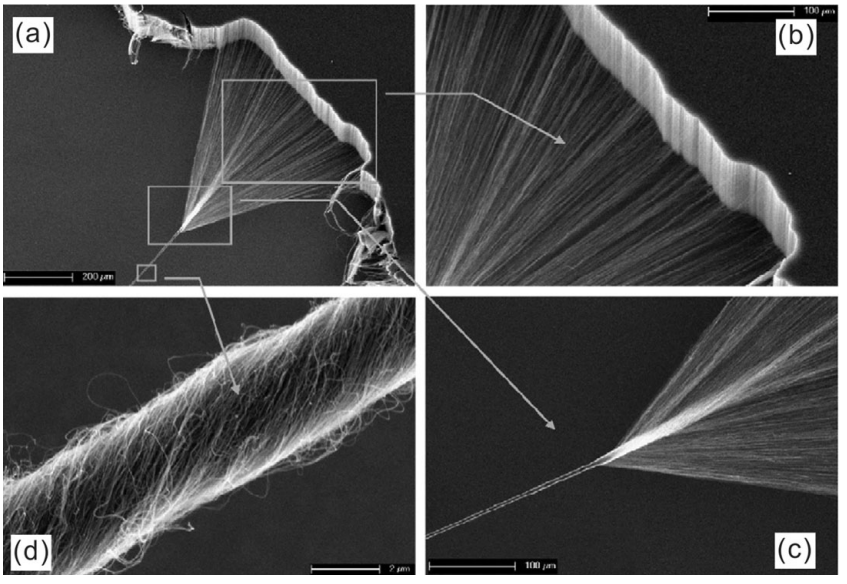

Fig. 9.16 Dry spinning of CNT yarns from CNT array: (a) overview; (b) close-up of self-assembly of CNTs; (c) detail of twist insertion; and (d) detail of yarn structure. [171].

presence of purified HiPco SWCNTs with 5 wt% and 10 wt% concentration. The solution was dry-jet wet spun into water coagulant with an air gap of 10 cm. For 10 wt% SWCNT solutions, the modulus, tensile strength and elongation at break of obtained fibers were improved by 20%, 60% and 40% respectively for (90/10) PBO fiber.

9.1.4.5 Wet spinning

Vigolo's group has successfully coagulated SWCNT-reinforced poly(vinyl acetate) (PVA) fibers [163, 174–179] by using the wet spinning process by injecting SWCNTs aqueous solution into a rotating bath of PVA solution to obtain gel-like composite fibers [174, 180]. Although strong nanotube composite fibers were obtained after wash and post-processes, the condensed gel-like fibers are difficult to handle thus limiting chance to scale up the process.

To improve the mechanical properties and solve the handling problem, Baughman's group modified the Vigolo process and enabled it to produce continuous SWCNT/PVA composite fibers [181, 182] as shown in Fig. 9.17. The gel fibers were assembled by manual pulling from the coagulation bath and mechanically drawn using a range of draw ratios. The composite fibres were subsequently dried in air (with or without further washing) [182]. For the treated fibers, the density-normalized modulus and strength values were measured to be 56 GPa cm^3/g and 1.30 GPa cm^3/g^1 respectively. From the dried fiber density of 1.4 g/cm^3 (measured by flotation), these density-normalized parameters translate to modulus and strengths of 78 GPa and 1.8 GPa, respectively. While these fibers contain about 60% SWCNTs by weight (from thermogravimetric analysis), the measured properties fall far short of the theoretical value of individual SWCNTs. The fibers reported here have comparable properties to PVA-SWCNT fibers

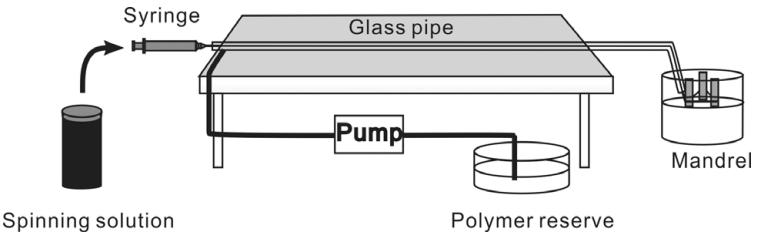

Fig. 9.17 Schematic diagram of the Baughman continuous spinning system [182].

prepared by a similar spinning method that are post-processed by hot drawing. Moreover, the properties achieved are comparable to other high-performance natural such as spider silk and synthetic fibers such as Kevlar.

9.1.4.6 Traditional spinning

CNT-reinforced polymer composite fibers have also been obtained through traditional spinning. SWCNT-reinforced polyacrylonitrile (PAN) and PVA fibers, and MWCNT cellulose composite fibers were produced by traditional wet spinning process [195–198]. The highest reported Young's modulus is 80 GPa at a tensile strength of 3.2 GPa [162, 163]. The first melt spun composite SWCNT fibers were produced by Andrews *et al*. using carbon pitch as the main component [199]. The results highlight the potential that exists for developing a spectrum of material properties through the control of the matrix, nanotube dispersion, alignment and interfacial bonding [199].

SWCNT functionalization and surfactant stabilization improved the nanotube dispersion in solvents, but only functionalization was shown to be capable of improving the dispersion in composites. However, functionalization induced nanotube length decrease and larger nanotube separation resulted from functional groups limited mechanical and electrical properties of the composites containing these nanotubes [200]. Gao *et al*. reported a chemical processing method that allows the continuous spinning of single-walled CNTs (SWCNTs)–nylon 6 (PA6) fibers by the *in situ* polymerization of caprolactam in the presence of 0.1 wt%–1.5 wt% SWCNTs. This process simultaneously optimizes the morphology of the composite [201].

9.1.4.7 Electrospinning

CNTs have been co-electrospun with a wide range of polymers including polyethylene oxide (PEO) [183, 184], polyacrylonitrile (PAN) [184, 188, 202], polyvinyl alcohol (PVA) [184], polymethyl methacrylate (PMMA) [187], and *Bombyx mori* silk [189, 203–205]. By encapsulation of CNT in a polymeric nanofiber matrix the CNTs are protected from direct contact and facilitaes stress transfer from the CNT to the linear composite assembly. CNT composite nanofibers have been shown not only to enhance the mechanical properties but also improve the electrical conductivities and thermal conductivities of the matrix.

Through continuously electrospun SWCNTs into PAN nanofibers, Ko *et al*. [152] demonstrated the feasibility of incorporation of CNTs in nanofibers through

electrospinning and proved the alignment effects on CNTs of this technique. SWCNTs were shown to maintain their straight shape and were parallel to the axis direction of the PAN fibres indicating that a good alignment of SWCNTs has been achieved. The improved orientation also resulted in a better distribution – nearly every investigated section of the polymer fibers contained at least some SWCNTs. The elastic modulus of the fiber was calculated to be around 207 GPa using the linear portion of the load–deformation curve at small deformation and under low forces (<100 nN).

9.2 Nanoclay

9.2.1 Structure and properties

Nanoclays, from the smectite family, have a unique morphology. They form platelets of about 1 nm thick and 100 nm in diameter. The essential nanoclay raw material is montmorillonite (MMT), a two-to-one layered smectite clay mineral with a platey structure. Individual platelet thickness of the MMT is just 1 nm, but the lateral dimensions of these layers may range from 200 nm to 2000 nm, resulting in an unusually high aspect ratio. The crystal structure of each layer contains two outer tetrahedral sheets, filled mainly with Si, and a central octahedral sheet of alumina or magnesia (Fig. 9.18). The layers are separated by a very small gap, called the interlayer or the gallery. The negative charge, generated by isomorphic substitution of Al^{3+} with Mg^{2+} or Mg^{2+} with Li^{+} within the layers, is counterbalanced by the presence of hydrated alkaline cations, such as Na or Ca, in the interlayer. Since the forces that hold the layers together are relatively weak, it is possible to intercalate small organic molecules between the layers. The surface area of each nanoclay particle is around 750 m^2/g and the aspect ratio is larger than 50 [1, 206].

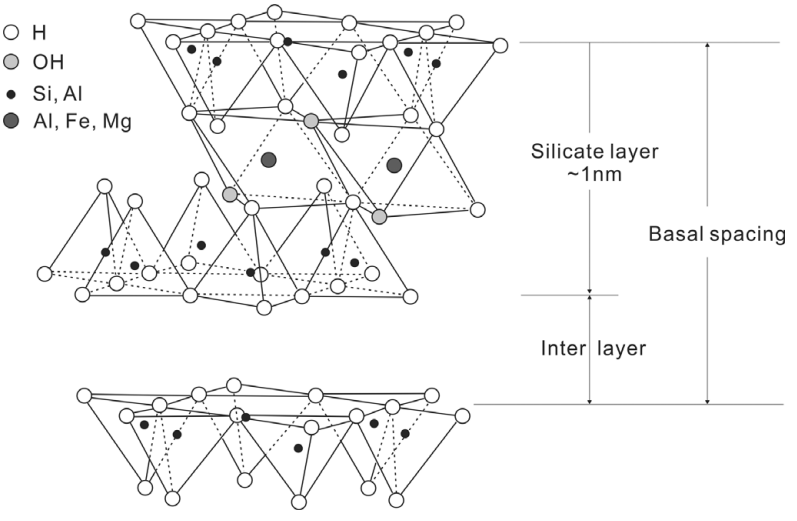

Fig. 9.18 Crystal structure of smectite clay [206].

9.2.2 Clay nanocomposites

Clay can be incorporated with polymers by dispersing with polymeric species or with the monomers, which will be subsequently be polymerised *in situ* to give the corresponding polymer–clay nanocomposite. The second method is the more successful approach to date. Both thermosets and thermoplastics have been used for clay nanocomposites, including nylons, polyolefins (e.g. polypropylene), polystyrene, ethylene-vinyl acetate (EVA) copolymer, epoxy resins, polyurethanes, polyimides and poly (ethylene terephthalate) (PET).

One important consequence of the charged nature of the clays is that they are generally highly hydrophilic species and thus naturally incompatible with a wide range of polymer types. A necessary pre-requisite for successful formation of polymer–clay nanocomposites is therefore alteration of the clay polarity to make the clay "organophilic." An organophilic clay can be produced from a normally hydrophilic clay by ion exchange with an organic cation such as an alkylammonium ion.

Depending on the nature of the components used (layered silicate, organic cation and polymer matrix) and the method of preparation, three main types of composites may be obtained when layered clay is associated with a polymer [1, 207], as shown in Fig. 9.19. (1) The phase-separated dispersion, in which the polymer is unable to intercalate the silicate sheets and the silicate particles are dispersed as phase-separated domains, called tactoids. (2) The intercalated dispersion, in which one or more polymer molecules are intercalated between the silicate layers. The resulting material has a well-ordered multilayered morphology of alternating polymer and silicate layers. The spacing between the silicate layers is between 2 and 3 nm. (3) The exfoliated dispersion, in which the silicate layers are completely delaminated and are uniformly dispersed in the polymer matrix. The spacing between the silicate layers is between 8 nm and 10 nm. This is the most desirable dispersion for improved properties.

The intercalation of the polymer chains usually increases the interlayer spacing, in comparison with the spacing of the organoclay used, leading to a shift of the diffraction peak towards lower angle values in XRD pattern [207]. Figure 9.20 shows the typical XRD patterns for different intercalated structures of polymer/silicate hybrids.

Transmission electronic spectroscopy (TEM) can be used to characterize the nanocomposite morphology [208]. Figure 9.21 shows the TEM micrographs obtained for the three types of dispersions. Besides intercalation and exfoliation, other intermediate arrangements can exist presenting both intercalation and exfoliation. In this case, a broadening of the diffraction peak is often observed by XRD and one must rely on TEM observation to define the overall structure [207].

Incorporation of nanoclay in polymer composites can significantly improve a variety of properties of the composites, including mechanical properties, gas barrier properties and fire retardant properties. The mechanical analysis conducted by Fischer's group indicates an increase in elastic modulus and the stiffness of monomorillonite–polyamide nanocomposites compared to the pure polymer matrix by 100%–150%; the yield at break has been increased by 20% [209]. Similar mechanical property improvements were presented for polymethyl methacrylate–clay hybrids [210]. The gaseous barrier

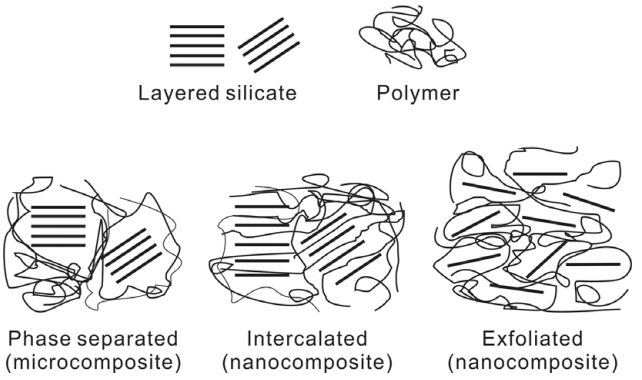

Fig. 9.19 Three main types of clay dispersion in composites [207].

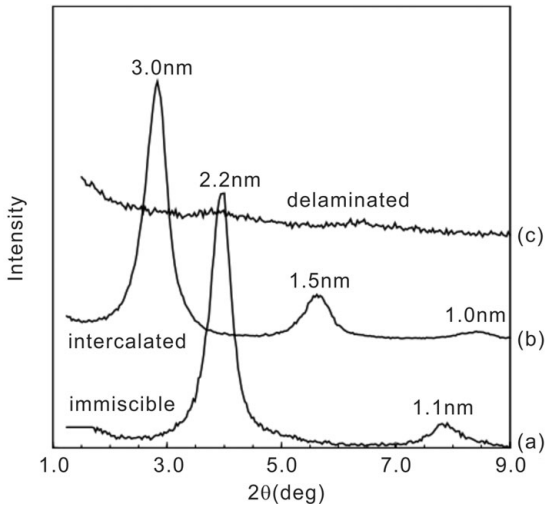

Fig. 9.20 Typical XRD patterns from polymer/silicate hybrids. (a) XRD obtained from an "immiscible" system (here polyethylene/C18FH), and is identical with the XRD of the neat or gano-silicate (C18FH). For intercalated hybrids the *d*-spacing shifts to a higher value (b) as the gallery expands to accommodate the intercalating polymer (here polystyrene/ C18FH); second and third order reflections – as shown here – are very common and sometimes intercalated hybrids can have up to 13 order reflections, manifesting a remarkable long-range registry. (c) Typical XRD of an exfoliated/delaminated structure or a disordered system (here a siloxane/C18FH delaminated hybrid) [207].

property improvement can result from incorporation of relatively small quantities of nanoclay materials. The oxygen and carbon dioxide barrier properties of the PP/EPDM blend demonstrated about two-fold improvement with the addition of only 1.5 vol% organoclay. Both the amount of clay incorporated in the polymer and the aspect ratio of the filler contribute to the overall barrier performance. In particular, the aspect ratio is shown to have a major effect: the higher the ratio, the more dramatic the enhancement of gaseous barrier properties. Such excellent barrier characteristics have resulted in

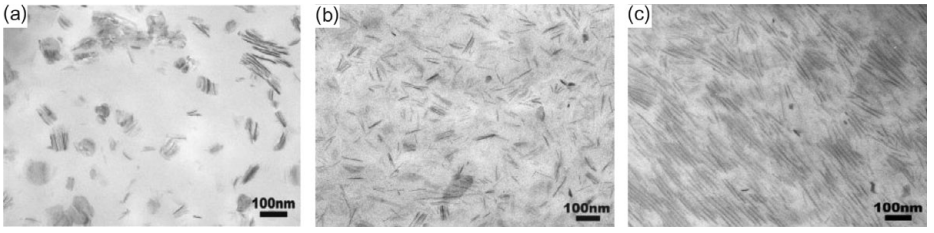

Fig. 9.21 TEM micrographs of nanoplatelet in epoxy matrices. (a) Phase-separated dispersion; (b) intercalated dispersion; and (c) exfoliated dispersion [208].

considerable interest in nanoclay composites in food packaging applications, both flexible and rigid [211]. Nazaré *et al*. studied the effects of nanoclay on the flammability properties of unsaturated polyester resin by using cone calorimetry. The results suggested that incorporation of nanoclays (5% w/w) reduces peak heat release rate (PHRR) by 23%–27% and total heat release (THR) values by 4%–11%. The fire growth rate index (FIGRA) is also reduced by 23%–30% following nanoclay inclusion [212].

9.2.3 Nanoclay nanocomposite fibers

Since the mechanical properties of fibers in general improve substantially with decreasing fiber diameter, there is considerable interest in nanoclay-reinforced electrospun nanofibers.

The crystalline strucuture of electrospun nanofibers was shown to be significant improved by addition of nanoclay. Lincoln *et al*. [213] reported that the degree of crystallinity of nylon-6 annealed at 205 °C increased substantially with the addition of MMT, implying that the silicate layers could act as nucleating agents and/or growth accelerators. Fong *et al*. showed a very similar overall degree increase of the crystallinity for electrospun nylon-6 and nylon-6/cloisite-30B nanocomposite fibers containing 7.5 wt% of O-MMT layers [214]. Fornes and Paul [215] found that O-MMT layers could serve as nucleating agents at the low concentration of 3% in a nylon-6/O-MMT nanocomposite, but retarded the crystallization of nylon-6 at high concentration of around 7%. Li *et al*. [216] demonstrated the increase of both crystallinity and the crystallite size of nylon-6 nanofibers reinforced by organically modified montmorillonite (O-MMT), cloisite-30B.

Crystal polymorphism was found in electrospun nanoclay-reinforced poly(vinylidene fluoride) (PVDF) fibers [217]. Both of the nanoclays, Lucentite™ STN and SWN, induced more extended PVDF chain conformers in the beta and gamma phases but reduced the alpha phase conformers in electrospun PVDF/nanoclay composite nanofibers. With the attached organic modifier, even a small amount of STN can totally eliminate the non-polar alpha crystal conformers while SWN cannot. The ionic organic modifier makes STN much more effective than SWN in causing crystallization of the polar beta and gamma phases of PVDF. The behavior was explained by an ion–dipole interaction mechanism, as suggested by Ramasundaram *et al*. [218]: the partially

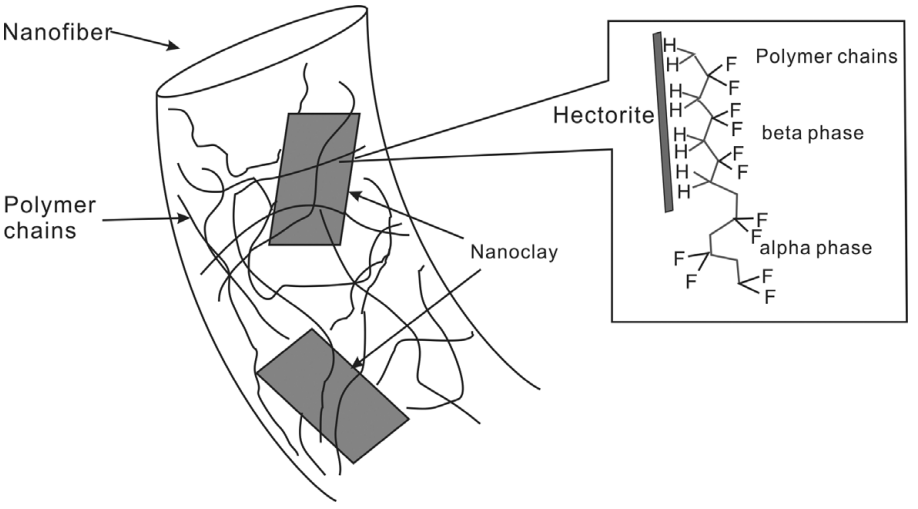

Fig. 9.22 The possible interaction between hectorite and PVDF chain in the electrospun composite nanofiber: partially positive C–H bond is attracted by the negatively charged silicate layer in STN and SWN due to the static electric force [217].

positive CH_2 dipoles on the PVDF chains could have an ion–dipole interaction with the negatively charged nanoclay platelets and make the polymer chains align on the surface of hectorite, which will enhance the extended TTTT conformers and result in formation of the beta crystallographic phase. The tiny amount of TTTGTTTG' conformers existing in the nanofiber is likely to be due to the gauche effects formed from local internal chain rotation. Figure 9.22 shows the possible interaction between hectorite and PVDF chain in the electrospun composite nanofiber: the partially positive C–H bond is attracted by the negatively charged silicate layer in STN and SWN due to the static electric force. Similar behaviour was shown by Liu *et al.* [219], who worked on electrospun organically modified montmorillonite reinforced PVDF nanofibers.

The thermal behavior of electrospun nanofibers was found to be enhanced by nanoclays. Adanur reported that when the Laponite® nanoclay was added in PVA, both the glass transition and the melting point temperatures increased [220]. Park *et al.* [221] found that higher thermal stability of PVA nanofibers with embedded high content rate of MMT was achieved, and this was attributed to the higher chain compactness resulting from the interaction between the PVA and the clay. However, the thermal behavior differs with nanoclay-reinforced PA6 nanofibers [222]. Under pyrolytic conditions, PA6 nanofibers and PA6/ Fe–OMT composite nanofibers degraded in one step. The onset thermal stability of the PA6/Fe–OMT composite nanofibers was not enhanced relative to that of pure PA6 nanofiber. The onset temperature of the degradation (5 wt% weight loss) for the PA6/Fe–OMT composite nanofibers was reduced from 390.3 °C for the pure PA6 nanfiber to 373.6 °C and 327.6 °C, respectively. The reasons were attributed to (1) the degradation of instable alkylammonium cations; (2) the decomposition of alkyl ammonium cations in Fe–OMT following the Hofmann elimination reaction and the reaction product catalyzed the degradation of PA6 materials; and

(3) the possibility that the clay itself could also catalyze the degradation of polymer materials. However, the yield of charred residue at 700 °C for the PA6/Fe–OMT composite nanofibers increased from 4.94% for the pure PA6 nanofiber to 8.23% and 9.78%, respectively. The reasons might be that the cations of some transition metals (e.g., Fe^{3+}) promoted the molecular cross-linking and so increased the charred residue. It may also attributed to the nanosized silicate clay layers, which could presumably facilitate the reassembly of lamellas to form 3-D char that might occur on the surface of the composite nanofibers and create a physical protective barrier. Meanwhile, the silicate clay layers could act as a superior insulator and mass-transport barrier and subsequently mitigate the escape of volatile products generated during the thermal decomposition. The increased amount of charred residue contributed to the improved thermal stability of the PA6 composite nanofibers [222].

Flammability tests were also conducted on Laponite® filled PVA nanofiber webs [223]. When the pure PVA web burned, it cringed and turned into a greenish blue solid gel in some parts where the PVA was exposed to heat more than flame. The PVA/Laponite® web cringed and turned into a gold-brown brittle substance, while the parts highly exposed to the flame were turned into black ash. The burning rate of pure PVA was 0.01 g/s while 5 wt% Laponite® in PVA decreased it to 0.005 14 g/s indicating 48.63% reduction of burning rate. Good flame retardation was achieved by adding Laponite® nanoclay in electrospun PVA webs. The Laponite® in the polymer may not delay the ignition but it probably acts as a char promoter, delaying the chain scission and forming a protective layer, thereby slowing down the decompositionso that burning rate decreases.

By measuring the tensile properties of the fiber mat, Li *et al.* [216] found the Young's modulus and ultimate strength of the nanocomposite mats electrospun from 15% NC5 (Nylon-6/O-MMT composite with 5 wt% of O-MMT) solution were increased by 70% and 30%, respectively. Park *et al.* [221] noticed that MMT has a reinforcement effect on MMT-reinforced PVA nanofibers. But the tensile strength reaches a maximum value at a clay concentration of 5 wt%. Further increase in the clay concentration results in a decrease in the tensile strength due to the aggregation of a large amount of MMT particles in the polymer matrix at high concentration conditions.

Contact angles and the time required for water penetration were also found to be increased for most of the PA/nanoclay composites relative to the uncoated substrate [224].

9.3 Graphite graphenes

9.3.1 Structure and properties

Natural flake graphite (NFG) is composed of layered nanosheets, where carbon atoms positioned on the NFG layer are held tightly by covalent bonds, while those positioned in adjacent planes are bound by much weaker van der Waals forces. The weak interplanar forces allow for certain atoms, molecules and ions to intercalate into the interplanar spaces of the graphite. The interplanar spacing is thus increased. As it does not bear any net charge, intercalation of graphite cannot be carried out by ion exchange

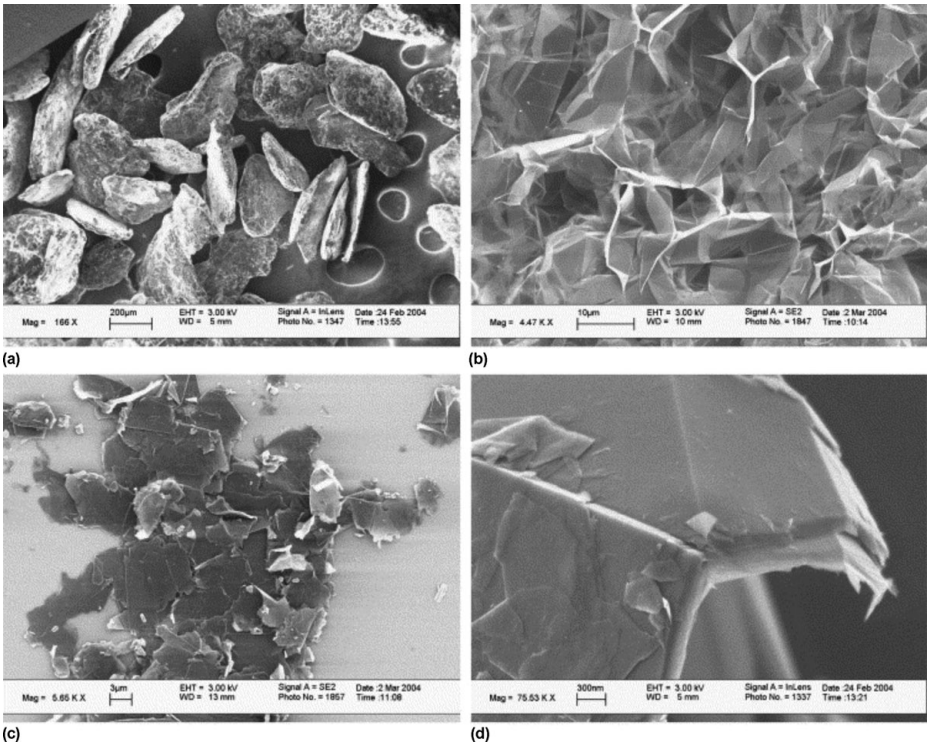

Fig. 9.23 SEM images of (a) intercalated, (b) expanded, (c) sonicated (exfoliated) and (d) graphite nanosheet [229].

reactions into galleries like layered silicates. Expanded graphite (EG) can be easily prepared by rapid heating of an intercalation compound (GIC), which is initially prepared from an NFG [225]. The original graphite flakes with a thickness of 0.4–60 mm may expand up to 2–20 000 mm in length [226]. These sheets/layers get separated down to 1 nm thickness, forming a high aspect ratio (200–1500) and high modulus (~1 TPa) graphene. When dispersed in the matrix, graphene exposes an enormous interface surface area (2630 m^2/g) and plays a key role in the improvement of both the physical and mechanical properties of the resultant nanocomposite [227]. Basically, EG is a loose and porous vermicular product. Its structure is essentially parallel boards, which collapse and deform desultorily. This collapse and deformation forms many pores of different sizes ranging from 10 nm to 10 μm. Because of the high expansion ratio (generally 200–300) of EG in the *c*-axis, the interplanar spacing is larger than that of the nontreated graphite. Thus galleries of EG can be easily intercalated by suitable monomer molecules and/or catalysts through physical adsorption because of the porous native of EG and the polar interaction between monomer and the –OH and –COOH groups on EG sheets. These polar groups result from chemical oxidation of the double bonds of graphite sheets during the preparation of GIC [225]. Figure 9.23 shows the SEM images of graphite before and after being expended. Graphite is also a good electrical conductor with an electrical conductivity of 10^{-4} S/cm at room temperature [228].

9.3.2 Graphene nanocomposites

Graphene–polymer composites possess outstanding physical, chemical, mechanical and membrane-like properties, which perfectly meet the essential requirement for the construction of advanced magnetic, electronic, optical and electro-optical devices and sensors.

Improvement in a polymer's electrical conductivity can be achieved by adding graphenes to a polymer. Addition of graphenes immediately transforms the polymer from an electrical insulator to an electrical semiconductor. The percolation threshold value of the conducting composite (with 1.8 wt% of expanded graphite) was much lower than that of conventional composites [226].

Yasmin and Daniel [230] fabricated graphite/epoxy and clay/epoxy nanocomposites respectively to investigate the reinforcement performance of the two types of particles. They found that graphite/epoxy has a higher (16% for 2 wt% particle content) elastic modulus compared to that of clay/epoxy with the same particle content.

Incorporation of the graphene shows an pronounced improvement in composite thermal stability. The incorporation of 2.5 wt% and 5 wt% graphene in pure epoxy matrix increased the 5% decomposition temperature of pure epoxy by 13 °C and 25 °C, respectively. The composites also showed higher char content and reduced weight loss at 800 °C as the graphene content increased. The homogeneous distribution of graphite particles and the tortuous path in the composites hinders the diffusion of volatile decomposition products in composites compared to that in pure epoxy [230]. A low thermal expansion coefficient (CTE) is often desirable for a composite to achieve dimensional stability. The CTE of epoxy was reduced from 60×10^{-6}/°C to $36–41 \times 10^{-6}$/°C as well by the addition of 2.5 wt% graphene as the fine dispersion and rigidity of graphite platelets in the epoxy matrix inhibits the expansion of polymer chains with increasing temperature [230].

9.3.3 Graphene nanocomposite nanofibers

To develop linear, planar and 3-D assemblies of graphite nanocomposite fibrils for macroscopic composites, electrospinning has been employed to produce graphene reinforced nanofibers [231].

Graphite was synthesized by using known graphite-intercalation chemistry [232] and then exfoliated for graphenes. Figure 9.24 shows the simplified schematic of the intercalation and exfoliation process. The first-stage is intercalation: the intercalation compound, KC_8, is readily formed by heating graphite powder with potassium metal under vacuum at 200 °C. Addition of an aqueous solvent, in this case ethanol, caused exfoliation of graphite. Ethanol solvates the potassium, producing potassium ethoxide, and hydrogen gas evolution aided in separating the graphitic layers into nanoplatelets, as shown below:

$$KC_8 + CH_3CH_2OH \rightarrow 8C + KOCH_2CH_3 + 1/2H_2. \quad (9.1)$$

PAN was used as the polymer matrix. The electrospun graphene/PAN nanofibers have a fairly uniform size distribution. The fiber diameters range from 5 nm to 500 nm, with an

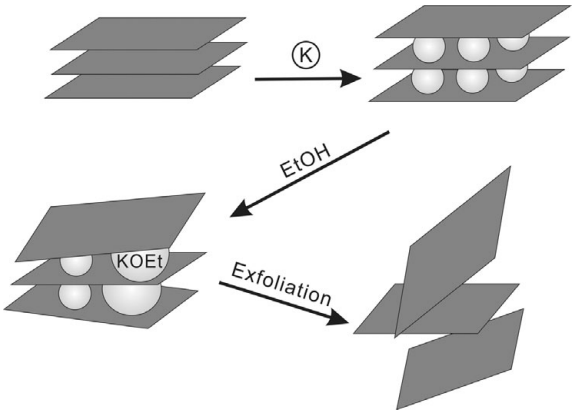

Fig. 9.24 Schematic showing intercalation of pristine graphite with potassium metal, followed by exfoliation with ethanol to form graphenes [231].

average diameter of 300 nm. TEM graphs proved the presence of graphenes within the polymer fiber. While the PAN nanofibers are amorphous, the graphenes showed some degree of crystallinity, as shown in Fig. 9.25. The hexagonal polycrystalline spot pattern was indexed to the graphene crystal structure, $a = 2.49$ Å, $c = 6.67$ Å [231].

The addition of graphenes leaded to a modest improvement in the thermal stability of the composite nanofibers. At 50% weight loss, the incorporation of 2 wt% and 4 wt% graphenes increased the thermal stability to oxidation by 10 °C and 25 °C, respectively [231].

The elastic moduli of the nanocomposite fibers were measured to be ~77, 113, 121 and 133 GPa, respectively, for nanoplatelet contents of 1, 2, 3 and 4 wt%. The trend shows an increase in Young's modulus with increasing content of graphenes. The two-fold increase in reinforcement for the 4 wt% graphene/PAN nanocomposite is noteworthy. The significant stiffening attributes to the high stiffness and high aspect ratio of the incorporated graphenes and is comparable to result seen for CNT/PAN nanofibers [231, 152].

9.4 Carbon nanofibers

Carbon nanofibers (CNF) are a unique form filling the gap in physical properties between conventional carbon fiber (5–10 μm) and CNTs. CNF are produced either in vapor-grown form or by electrospinning. They are typically 20–200 nm in diameter. The reduced diameter of the nanofiber provides a larger surface area with surface functionalities in the fiber.

9.4.1 Vapor-grown carbon nanofibers

Vapor-grown carbon nanofibers (VGCNF) are produced in the vapor phase by decomposing carbon-containing gases such as methane (CH_4), ethane (C_2H_6), acetylene (C_2H_2), carbon monoxide (CO), benzene or coal gas in the presence of floating metal

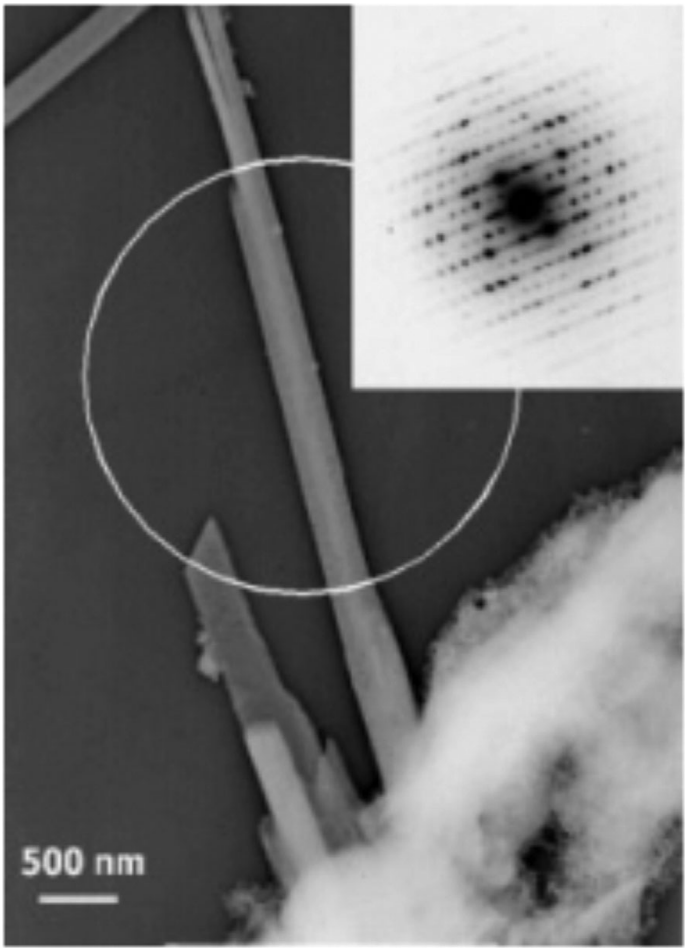

Fig. 9.25 TEM micrograph of a 1wt% graphene/PAN nanofiber (the inset is a selected-area electron-diffraction pattern taken from the circled area of the nanofiber). [231].

catalyst particles inside a high-temperature reactor [1]. The most common structure of CNFs is truncated cones, but the internal structure of carbon nanofibers varies and is composed of various configurations of modified graphene sheets (cone, stacked coins, etc). The conical structures of CNTs range from a few to hundreds of nanometers in diameter, and from less than a micron to millimetres in length [233]. The stacked cone structure is usually referred to as a herringbone (or fishbone) formation because the cross-sectional TEM images resemble a fish skeleton (Fig. 9.26a), while the stacked cups structure is mostly referred to as bamboo type, resembling the compartmentalized structure of a bamboo stem (Fig. 9.26b) [234]. Currently there is no strict classification of nanofiber structures. The main distinguishing characteristic of nanofibers from nanotubes is the stacking of graphene sheets of varying shapes.

Mechanical properties such as strength, stiffness, fracture behaviour and toughness of materials depend on the microstructure of the fiber. An important material characteristic

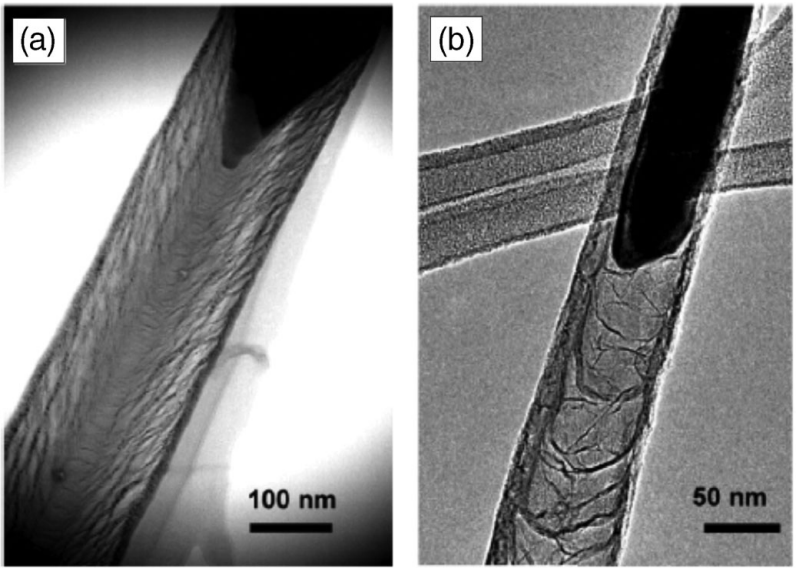

Fig. 9.26 (a) STEM image of a herringbone CNF produced by dc C-PECVD with Ni catalyst; (b) TEM image of a bamboo-type CNF grown under the same conditions with Fe catalyst [233].

of a small-diameter fiber is that it confers much higher strength than the bulk material due to its reduced probability of containing critical structure flaws with decreasing specimen volume [235]. CNFs contain polycrystalline and amorphous carbon in structure, therefore their tensile strengths are on an order of magnitude lower than CNTs, ranging from 1.5 GPa to 4.8 GPa. Their Young's modulus is between 228 GPa and 724 GPa [236]. The tensile modulus and strength of CNFs will not be affected by water, solvents, acids or bases at room temperature. Even though their mechanical properties are not as astounding as those of CNTs, CNFs are more economical and have higher manufacturability compared. Table 9.4 lists the properties of a commercial carbon nanofiber (Pyrograf III).

Lee *et al*. [237] investigated the electrical characteristics of individual CNFs by measuring the *I–V* characteristics of suspended nanofiber bridges. At low positive and negative applied voltages, the nanofibers exhibited linear *I–V* characteristics. The measured section of the nanofiber had a resistance of 622 Ω, which corresponds to 1 kΩ·μm of nanofiber length. The resistivity was estimated varying between 10^{-6} and 10^{-5} Ω·m based on an assumption that conduction was through the entire cylindrical cross-sectional area of the nanofiber. Generally, the resistivities of CNFsare comparable to those of arc-grown MWCNTs and ropes of SWCNTs whose resistivities are approximately 10^{-6} Ω·m [238, 239].

9.4.2 Electrospun carbon nanofibers

Traditional vapor-growth methods and plasma-enhanced chemical vapor depositing methods involve complicated processes and high costs. On the contrary, stabilization and carbonization of electrospun nanofiber precursors is a straightforward and low-cost

Table 9.4 Properties of a commercial vapor-grown CNF (Pyrograf III, produced by Applied Sciences, Inc.)

Properties	CNF-(pyrotically stripped)
Diameter (nm)	60–200
Density (g/cm^3)	1.8
Tensile Modulus (GPa)	600
Tensile Strength (GPa)	7
Coefficient of thermal expansion(10^{-6}/°C)	−1.0
Electrical resistivity (mV cm)	55

Table 9.5 Carbon nanofiber precursors and their properties

Polymer	Ref.	Diameter (nm)	d_{002}	I_D/I_G	Temperature (°C)	Conductivity (S/m)
Poly(acrylonitrile) (PAN)	[240]	200–600	0.36	2.73	700	6.8×10^{-3}
	/	/	/	1.39	1000	1.96
	[241]	50–400	/	2.93–1.67	873–1473	/
	[242]	200–300	/	3.81	700	/
	/	/	/	3.41	1000	2.193
	/	/	/	1.31	2000	55.41
	[243]	90–300	0.37	/	900	/
	/	/	0.34	/	1300	/
poly(amic acid) (PAA)	[244]	110±40	0.368	0.925±0.004	1100	/
	[245]	1000–2000	/	/	1000	2.5
Polyvinyl alcohol (PVA)	[246]	80–200	/	/	600	3.7×10^{-1}
Pitch	[247]	2000–6000	/	/	2200	5.3
	/				1000	6.3
					1200	8.3

approach for fabricating CNFs. The CNFs based on electrospun nanofibers also have an advantage in making multifunctional nanocomposite carbon nanofibers. Simply by adding functional nanoparticles to the electrospun precursors, multifunctional nanocomposite CNFs can be achieved. Table 9.5 lists the polymers that have been used as the precursors for CNFs and their properties.

9.4.3 Carbon nanofiber composites

Similar to graphene and CNT reinforced composites, the performance of CNF-incorporated polymer matrix can be significantly enhanced.

Finegan *et al*. [248] conducted studies on the tensile properties of CNF/PP specimens prepared by using melt processing (injection molding) with 15 vol% CNF loaded. In all cases, they observed an increase in both tensile modulus and strength compared with pure PP. The tensile modulus and strength of the composite with CNFs treated in a CO_2

atmosphere at 850 °C were 4 GPa and 70 MPa, respectively; both were three times greater than the corresponding values for pure PP. Tibbetts and McHugh's study also showed a notable improvement in the mechanical properties of VGCNF/PP. The tensile strength was doubled and the Young's modulus was more than tripled [248, 249]. Patton *et al*. [250] reported that addition of CNFs improved the mechanical properites of epoxy by nearly doubling the flexural modulus and increasing the flexural strength for about 36%.

Goravev *et al*. [251] studied the D.C. electrical resistivity of VGCNF/polypropylene (PP) composite. They found complex time- and voltage-dependent changes in composite resistivity as the fiber network adjusted to current flow. Tibbetts *et al*. conducted extensive conductivity measurements for VGCNF/PP and VGCNF/nylon composites. They found the percolation threshold is around 3 vol% (6 wt%) and a resistivity values as low as 0.15 Ω/cm can be obtained with about 20 vol% fiber loading. They also verified that long milling treatments which decreases the length of fiber strongly diminished the composite conductivity; by processing the fibers more carefully to avoid breakage, the percolation threshold can be lowered to 1/2 vol% (1 wt%) loading of VGCNF fibers [252]. Donohue and Pittman [253] demonstrated that conductivity values for VCGNF/resin composites are sufficiently high to offer significant protection from electromagnetic interference. They measured a 45 db shielding effectiveness at 200 MHz for 15 wt% high temperature heat-treated VGCNF in a vinyl ester matrix.

Lafdi and Matzek [254] demonstrated an increase of thermal conductivity from 0.2 W/(m K) to 2.8 W/(m K) for epoxy resin with 20 wt% VGCNF.

References

1. P. K. Mallick, *Polymer Nanocomposites*, in *Fiber-Reinforced Composites: Materials, Manufacturing, and Design*. London: CRC Press, 2009.
2. R. Gupta, E. Kennel, and K. Kim, *Polymer Nanocomposites Handbook*. CRC, 2009.
3. D. Bethune, *et al*., *Cobalt-catalysed growth of carbon nanotubes with single-atomic-layer walls*, 1993. **MORE DETAILS?**
4. S. Iijima, and T. Ichihashi, *Single-shell carbon nanotubes of 1-nm diameter*, 1993. **MORE DETAILS?**
5. S. Iijima, "Helical microtubules of graphitic carbon," *Nature*, vol. 354(6348), pp. 56–58, 1991.
6. Y. Qian, *et al*., "Superlong-oriented single-walled carbon nanotube arrays on substrate with low percentage of metallic structure," *The Journal of Physical Chemistry C*, vol. 113(17), pp. 6983–6988, 2009.
7. Q. Wen, *et al*., "Growing 20 cm long DWNTs/TWNTs at a rapid growth rate of 80−90 μm/s," *Chemistry of Materials*, vol. 22(4), pp. 1294–1296, 2010.
8. Q. Wen, *et al*., "100 mm long, semiconducting triple-walled carbon Nanotubes," *Advanced Materials*, vol. 22(16), pp. 1867–1871, 2010.
9. A. Puretzky, *et al*., "In situ imaging and spectroscopy of single-wall carbon nanotube synthesis by laser vaporization," *Applied Physics Letters*, vol. 76, p. 182, 2000.
10. K. Hernadi, *et al*., "Catalytic synthesis of carbon nanotubes using zeolite support," *Zeolites* vol. 17(5–6), pp. 416–23, 1996.

11. C. Journet, *et al*., "Large-scale production of single-walled carbon nanotubes by the electric-arc technique," *Nature*, vol. 388(6644), pp. 756–757, 1997.
12. J. H. Hafner, *et al*., "Catalytic growth of single-wall carbon nanotubes from metal particles," *Chemical Physics Letters*, vol. 296(1–2), pp. 195–202, 1998.
13. P. Nikolaev, *et al*., "Gas-phase catalytic growth of single-walled carbon nanotubes from carbon monoxide," *Chemical Physics Letters*, vol. 313(1–2), pp. 91–97, 1999.
14. Q. Zhao, Z. Gan, and Q. Zhuang, "Electrochemical sensors based on carbon nanotubes," *Electroanalysis*, vol. 14(23), pp. 1609–1613, 2002.
15. T. Zhao, and Y. Liu, "Large scale and high purity synthesis of single-walled carbon nanotubes by arc discharge at controlled temperatures," *Carbon*, vol. 42(12–13), pp. 2765–2768, 2004.
16. J.-P. Salvetat, *et al*., "Elastic modulus of ordered and disordered multiwalled carbon nanotubes," *Advanced Materials*, vol. 11(2), pp. 161–165, 1999.
17. E. T. Thostenson, Z. Ren, and T.-W. Chou, "Advances in the science and technology of carbon nanotubes and their composites: a review," *Composites Science and Technology*, vol. 61(13), pp. 1899–1912, 2001.
18. Y. Saito, and S. Uemura, "Field emission from carbon nanotubes and its application to electron sources," *Carbon*, vol. 38(2), pp. 169–182, 2000.
19. M. S. Dresselhaus, G. Dresselhaus, and P. C. Eklund, *Science of Fullerenes and Carbon Nanotubes*. London: Academic Press, 1996.
20. V. Popov, "Carbon nanotubes: properties and application," *Materials Science and Engineering: R: Reports*, vol. 43(3), pp. 61–102, 2004.
21. T. Yamabe, "Recent development of carbon nanotube," *Synthetic Metals*, vol. 70(1–3), pp. 1511–1518, 1995.
22. E. W. Wong, P. E. Sheehan, and C. M. Lieber, "Nanobeam mechanics: elasticity, strength, and toughness of nanorods and nanotubes," *Science*, vol. 277(5334), p. 1971, 1997.
23. B. I. Yakobson, C. J. Brabec, and J. Bernholc, "Nanomechanics of carbon tubes: instabilities beyond linear response," *Physical Review Letters*, vol. 76(14), pp. 2511–2514, 1996.
24. S. Iijima, *et al*., "Structural flexibility of carbon nanotubes," *The Journal of Chemical Physics*, vol. 104(5), pp. 2089–2092, 1996.
25. M. Buongiorno Nardelli, B. I. Yakobson, and J. Bernholc, "Mechanism of strain release in carbon nanotubes," *Physical Review B*, vol. 57(8), pp. R4277–R4280, 1998.
26. J. Bernholc, *et al*., "Mechanical and elctrical properties of nanotubes," *Annual Review of Materials Research*, vol. 32(1), pp. 347–375, 2002.
27. B. I. Yakobson, *et al*., "High strain rate fracture and C-chain unraveling in carbon nanotubes," *Computational Materials Science*, vol. 8(4), pp. 341–348, 1997.
28. R. C. Johnson, *CVD process tames carbon nanotube growth*. 2002 [cited 2010 July 19]; Available from: http://www.eetimes.com/story/OEG20020416S0014.
29. B. Wei, R. Vajtai, and P. Ajayan, "Reliability and current carrying capacity of carbon nanotubes," *Applied Physics Letters*, vol. 79, p. 1172, 2001.
30. T. Durkup, B. Kim, and M. Fuhrer, "Properties and applications of high-mobility semiconducting nanotubes," *Journal of Physics Condensed Matter*, vol. 16(18), pp. 553–580, 2004.
31. Z. K. Tang *et al*., "Superconductivity in 4 angstrom single-walled carbon nanotubes," *Science*, vol. 292(5526), pp. 2462–2465, 2001.
32. P. G. Collins, and P. Avouris, "Nanotubes for electronics," *Scientific American*, vol. 283(6), pp. 62–69, 2000.

33. M. Dresselhaus, G. Dresselhaus, and R. Saito, "Physics of carbon nanotubes," *Carbon*, vol. 33(7), pp. 883–891, 1995.
34. J. Che, T. Çagin, and W. Goddard III, "Thermal conductivity of carbon nanotubes," *Nanotechnology*, vol. 11, pp. 65–69, 2000.
35. J. Hone, *et al*., "Thermal properties of carbon nanotubes and nanotube-based materials," *Applied Physics A: Materials Science & Processing*, vol. 74(3), pp. 339–343, 2002.
36. T. W. Ebbesen, *et al*., "Purification of nanotubes," *Nature*, vol. 367(6463), p. 519, 1994.
37. E. Dujardin, *et al*., "Purification of single-shell nanotubes," *Advanced Materials*, vol. 10(8), pp. 611–613, 1998.
38. K. B. Shelimov, *et al*., "Purification of single-wall carbon nanotubes by ultrasonically assisted filtration," *Chemical Physics Letters*, vol. 282(5–6), pp. 429–434, 1998.
39. S. Bandow, *et al*., "Purification of single-wall carbon nanotubes by microfiltration," *The Journal of Physical Chemistry B*, vol. 101(44), pp. 8839–8842, 1997.
40. A. Yu, *et al*., "Application of centrifugation to the large-scale purification of electric arc-produced single-walled carbon nanotubes," *Journal of the American Chemical Society*, vol. 128(30), pp. 9902–9908, 2006.
41. I. W. Chiang, B. E. Brinson, and A. Y. Huang, "Purification and characterization of single-wall carbon nanotubes (SWNTs) obtained from the gas-phase decomposition of CO (HiPco Process)," *Journal of Physical Chemistry B*, vol. 105(35), p. 8297, 2001.
42. P.-X. Hou, C. Liu, and H.-M. Cheng, "Purification of carbon nanotubes," *Carbon*, vol. 46 (15), pp. 2003–2025, 2008.
43. I. W. Chiang, *et al*., "Purification and characterization of single-wall carbon nanotubes," *The Journal of Physical Chemistry B*, vol. 105(6), pp. 1157–1161, 2001.
44. J. Liu, *et al*., "Fullerene pipes," *Science*, vol. 280(5367), pp. 1253–1256, 1998.
45. R. Krupke, *et al*., "Surface conductance induced dielectrophoresis of semiconducting single-walled carbon nanotubes," *Nano Letters*, vol. 4(8), pp. 1395–1399, 2004.
46. Y. Kunitoshi, *et al*., "Orientation and purification of carbon nanotubes using ac electrophoresis," *Journal of Physics D: Applied Physics*, vol. 31(8), p. L34, 1998.
47. B. Suárez, *et al*., "Separation of carbon nanotubes in aqueous medium by capillary electrophoresis," *Journal of Chromatography A*, vol. 1128(1–2), pp. 282–289, 2006.
48. L. A. Crum, and J. B. Fowlkes, "Acoustic cavitation generated by microsecond pulses of ultrasound," *Nature*, vol. 319(6048), pp. 52–54, 1986.
49. C. Sauter, *et al*., "Influence of hydrostatic pressure and sound amplitude on the ultrasound induced dispersion and de-agglomeration of nanoparticles," *Ultrasonics Sonochemistry*, vol. 15(4), pp. 517–523, 2008.
50. J. Hilding, *et al*., "Dispersion of carbon nanotubes in liquids," *Journal of Dispersion Science and Technology*, vol. 24(1), pp. 1–42, 2003.
51. K. L. Lu, *et al*., "Mechanical damage of carbon nanotubes by ultrasound," *Carbon*, vol. 34(6), pp. 814–816, 1996.
52. J. W. Cho, and D. R. Paul, "Nylon 6 nanocomposites by melt compounding," *Polymer*, vol. 42(3), pp. 1083–1094, 2001.
53. J. Zhu, *et al*., "Improving the dispersion and integration of single-walled carbon nanotubes in epoxy composites through functionalization," *Nano Letters*, vol. 3(8), pp. 1107–1113, 2003.
54. Y. Y. Huang, S. V. Ahir, and E. M. Terentjev, "Dispersion rheology of carbon nanotubes in a polymer matrix," *Physical Review B*, vol. 73(12), p. 125 422, 2006.
55. A. I. Isayev, R. Kumar, and T. M. Lewis, "Ultrasound assisted twin screw extrusion of polymer-nanocomposites containing carbon nanotubes," *Polymer*, vol. 50(1), pp. 250–260, 2009.

56. Y. Li, and H. Shimizu, "High-shear processing induced homogenous dispersion of pristine multiwalled carbon nanotubes in a thermoplastic elastomer," *Polymer*, vol. 48(8), pp. 2203–2207, 2007.
57. Y. Xiao, *et al*., "Dispersion and mechanical properties of polypropylene/multiwall carbon nanotubes composites obtained via dynamic packing injection molding," *Journal of Applied Polymer Science*, vol. 104(3), pp. 1880–1886, 2007.
58. C. A. Silvera-Batista, *et al*., Long-term improvements to photoluminescence and dispersion stability by flowing SDS-SWNT suspensions through microfluidic channels," *Journal of the American Chemical Society*, vol. 131(35), pp. 12 721–12 728, 2009.
59. Y. A. Kim, *et al*., "Effect of ball milling on morphology of cup-stacked carbon nanotubes," *Chemical Physics Letters*, vol. 355(3–4), pp. 279–284, 2002.
60. Z. Jia, *et al*., "Production of short multi-walled carbon nanotubes," *Carbon*, vol. 37(6), pp. 903–906, 1999.
61. N. Pierard, *et al*., "Production of short carbon nanotubes with open tips by ball milling," *Chemical Physics Letters*, vol. 335(1–2), pp. 1–8, 2001.
62. Y. B. Li, *et al*., "Transformation of carbon nanotubes to nanoparticles by ball milling process," *Carbon*, vol. 37(3), pp. 493–497, 1999.
63. Y. Wang, J. Wu, and F. Wei, "A treatment method to give separated multi-walled carbon nanotubes with high purity, high crystallization and a large aspect ratio," *Carbon*, vol. 41(15), pp. 2939–2948, 2003.
64. Y. Kang, and T. A. Taton, "Micelle-encapsulated carbon nanotubes: a route to nanotube composites," *Journal of the American Chemical Society*, vol. 125(19), pp. 5650–5651, 2003.
65. H.-I. Shin, *et al*., "Amphiphilic block copolymer micelles: new dispersant for single wall carbon nanotubes," *Macromolecular Rapid Communications*, vol. 26(18), pp. 1451–1457, 2005.
66. X. Lou, *et al*., "Synthesis of pyrene-containing polymers and noncovalent sidewall functionalization of multiwalled carbon nanotubes," *Chemistry of Materials*, vol. 16(21), pp. 4005–4011, 2004.
67. F. Balavoine, *et al*., "Helical crystallization of proteins on carbon nanotubes: a first step towards the development of new biosensors," *Angewandte Chemie International Edition*, vol. 38(13–14), pp. 1912–1915, 1999.
68. B. R. Azamian, *et al*., "Bioelectrochemical single-walled carbon nanotubes," *Journal of the American Chemical Society*, vol. 124(43), pp. 12 664–12 665, 2002.
69. S. S. Karajanagi, *et al*., "Structure and function of enzymes adsorbed onto single-walled carbon nanotubes," *Langmuir*, vol. 20(26), pp. 11 594–11 599, 2004.
70. S. S. Karajanagi, et al., "Protein-assisted solubilization of single-walled carbon nanotubes," *Langmuir*, vol. 22(4), pp. 1392–1395, 2006.
71. Y. Lin, L. F. Allard, and Y.-P. Sun, "Protein-affinity of single-walled carbon nanotubes in water," *The Journal of Physical Chemistry B*, vol. 108(12), pp. 3760–3764, 2004.
72. G. R. Dieckmann, *et al*., "Controlled assembly of carbon nanotubes by designed amphiphilic peptide helices," *Journal of the American Chemical Society*, vol. 125(7), pp. 1770–1777, 2003.
73. A. Star, *et al*., "Preparation and properties of polymer-wrapped single-walled carbon nanotubes 13," *Angewandte Chemie International Edition*, vol. 40(9), pp. 1721–1725, 2001.
74. X. Gong, *et al*., "Surfactant-assisted processing of carbon nanotube/polymer composites," *Chemistry of Materials*, vol. 12(4), pp. 1049–1052, 2000.

75. O.-K. Kim, *et al*., "Solubilization of single-wall carbon nanotubes by supramolecular encapsulation of helical amylose," *Journal of the American Chemical Society*, vol. 125(15), pp. 4426–4427, 2003.
76. A. Satake, Y. Miyajima, and Y. Kobuke, "Porphyrin−carbon nanotube composites formed by noncovalent polymer wrapping," *Chemistry of Materials*, vol. 17(4), pp. 716–724, 2005.
77. R. Bandyopadhyaya, *et al*., "Stabilization of individual carbon nanotubes in aqueous solutions," *Nano Letters*, vol. 2(1), pp. 25–28, 2002.
78. M. J. O'Connell, *et al*., "Reversible water-solubilization of single-walled carbon nanotubes by polymer wrapping," *Chemical Physics Letters*, vol. 342(3–4), pp. 265–271, 2001.
79. J. Chen, *et al*., "Noncovalent engineering of carbon nanotube surfaces by rigid, functional conjugated polymers," *Journal of the American Chemical Society*, vol. 124(31), pp. 9034–9035, 2002.
80. N. Nakayama-Ratchford, *et al*., "Noncovalent functionalization of carbon nanotubes by fluorescein−polyethylene glycol: supramolecular conjugates with pH-dependent absorbance and fluorescence," *Journal of the American Chemical Society*, vol. 129(9), pp. 2448–2449, 2007.
81. R. J. Chen, *et al*., "Noncovalent sidewall functionalization of single-walled carbon nanotubes for protein immobilization," *Journal of the American Chemical Society*, vol. 123(16), pp. 3838–3839, 2001.
82. Y. Liu, L. Gao, and J. Sun, "Noncovalent functionalization of carbon nanotubes with sodium lignosulfonate and subsequent quantum dot decoration," *The Journal of Physical Chemistry C*, vol. 111(3), pp. 1223–1229, 2006.
83. J. U. Lee, *et al*., "Aqueous suspension of carbon nanotubes via non-covalent functionalization with oligothiophene-terminated poly(ethylene glycol)," *Carbon*, vol. 45(5), pp. 1051–1057, 2007.
84. L. Yangqiao, *et al*., "Debundling of single-walled carbon nanotubes by using natural polyelectrolytes," *Nanotechnology*, vol. 18(36), p. 365 702, 2007.
85. K. E. Wise, *et al*., "Stable dispersion of single wall carbon nanotubes in polyimide: the role of noncovalent interactions," *Chemical Physics Letters*, vol. 391(4–6), pp. 207–211, 2004.
86. Y. Sun, S. R. Wilson, and D. I. Schuster, "High dissolution and strong light emission of carbon nanotubes in aromatic amine solvents," *Journal of the American Chemical Society*, vol. 123(22), pp. 5348–5349, 2001.
87. A. M. Bond, W. Miao, and C. L. Raston, "Mercury(II) immobilized on carbon nanotubes: synthesis, characterization, and redox properties," *Langmuir*, vol. 16(14), pp. 6004–6012, 2000.
88. H. Hiura, T. W. Ebbesen, and K. Tanigaki, "Opening and purification of carbon nanotubes in high yields," *Advanced Materials*, vol. 7(3), pp. 275–276, 1995.
89. J. L. Bahr, and J. M. Tour, "Covalent chemistry of single-wall carbon nanotubes," *Journal of Materials Chemistry*, vol. 12(7), pp. 1952–1958, 2002.
90. Y. Chen, *et al*., "Chemical attachment of organic functional groups to single-walled carbon nanotube material," *Journal of Material Research*, vol. 13(9), pp. 2423–2431, 1998.
91. W. Zhou, *et al*., "Structural characterization and diameter-dependent oxidative stability of single wall carbon nanotubes synthesized by the catalytic decomposition of CO," *Chemical Physics Letters*, vol. 350(1–2), pp. 6–14, 2001.
92. A. G. Rinzler, *et al*., "Large-scale purification of single-wall carbon nanotubes: process, product, and characterization," *Applied Physics A: Materials Science & Processing*, vol. 67(1), pp. 29–37, 1998.

93. A. Hamwi, *et al*., "Fluorination of carbon nanotubes," *Carbon*, vol. 35(6), pp. 723–728, 1997.
94. S. Kawasaki, *et al*., "Fluorination of open- and closed-end single-walled carbon nanotubes," *Physical Chemistry Chemical Physics*, vol. 6(8), pp. 1769–1772, 2004.
95. H. Touhara, *et al*., "Property control of new forms of carbon materials by fluorination," *Journal of Fluorine Chemistry*, vol. 114(2), pp. 181–188, 2002.
96. N. F. Yudanov, *et al*., "Fluorination of arc-produced carbon material containing multiwall nanotubes," *Chemistry of Materials*, vol. 14(4), pp. 1472–1476, 2002.
97. H. Touhara, and F. Okino, "Property control of carbon materials by fluorination," *Carbon*, vol. 38(2), pp. 241–267, 2000.
98. E. T. Mickelson, *et al*., "Fluorination of single-wall carbon nanotubes," *Chemical Physics Letters*, vol. 296(1–2), pp. 188–194, 1998.
99. Z. Gu, *et al*., "Cutting single-wall carbon nanotubes through fluorination," *Nano Letters*, vol. 2(9), pp. 1009–1013, 2002.
100. E. T. Mickelson, *et al*., "Solvation of fluorinated single-wall carbon nanotubes in alcohol solvents," *The Journal of Physical Chemistry B*, vol. 103(21), pp. 4318–4322, 1999.
101. R. K. Saini, *et al*., "Covalent sidewall functionalization of single wall carbon nanotubes," *Journal of the American Chemical Society*, vol. 125(12), pp. 3617–3621, 2003.
102. P. J. Boul, *et al*., "Reversible sidewall functionalization of buckytubes," *Chemical Physics Letters*, vol. 310(3–4), pp. 367–372, 1999.
103. V. N. Khabashesku, W. E. Billups, and J. L. Margrave, "Fluorination of single-wall carbon nanotubes and subsequent derivatization reactions," *Accounts of Chemical Research*, vol. 35(12), pp. 1087–1095, 2002.
104. J. L. Stevens, *et al*., "Sidewall amino-functionalization of single-walled carbon nanotubes through fluorination and subsequent reactions with terminal diamines," *Nano Letters*, vol. 3(3), pp. 331–336, 2003.
105. J. Stevens, *et al*., "Sidewall functionalization of single-walled carbon nanotubes through CN bond forming substitution reactions of fluoronanotubes," *Nanotechnology*, vol. 3, pp. 169–172, 2003.
106. L. Zhang, *et al*., "Sidewall functionalization of single-walled carbon nanotubes with hydroxyl group-terminated moieties," *Chemistry of Materials*, vol. 16(11), pp. 2055–2061, 2004.
107. H. Peng, *et al*., "Sidewall functionalization of single-walled carbon nanotubes with organic peroxides," *Chemical Communications*, vol. 2003(3), pp. 362–363, 2003.
108. H. Peng, *et al*., "Oxidative properties and chemical stability of fluoronanotubes in matrixes of binary inorganic compounds," *Journal of Nanoscience and Nanotechnology*, vol. 1(2), pp. 87–92, 2003.
109. J. Chen, *et al*., "Solution properties of single-walled carbon nanotubes," *Science*, vol. 282 (5386), pp. 95–98, 1998.
110. K. Kamaras, *et al*., "Covalent bond formation to a carbon nanotube metal," *Science*, vol. 301(5639), p. 1501, 2003.
111. H. Hu, *et al*., "Sidewall functionalization of single-walled carbon nanotubes by addition of dichlorocarbene," *Journal of the American Chemical Society*, vol. 125(48), pp. 14 893–14 900, 2003.
112. M. Holzinger, *et al*., "Sidewall functionalization of carbon nanotubes," *Angewandte Chemie International Edition*, vol. 40(21), pp. 4002–4005, 2001.
113. M. Holzinger, *et al*., "[2+1] cycloaddition for cross-linking SWCNTs," *Carbon*, vol. 42 (5–6), pp. 941–947, 2004.

114. M. Holzinger, *et al*., "Functionalization of single-walled carbon nanotubes with (R-) oxycarbonyl nitrenes," *Journal of the American Chemical Society*, vol. 125(28), pp. 8566–8580, 2003.
115. K. Jiang, *et al*., "Protein immobilization on carbon nanotubes via a two-step process of diimide-activated amidation," *Journal of Materials Chemistry*, vol. 14(1), pp. 37–39 2004.
116. S. E. Baker, *et al*., "Covalently bonded adducts of deoxyribonucleic acid (DNA) oligonucleotides with single-wall carbon nanotubes: synthesis and hybridization," *Nano Letters*, vol. 2(12), pp. 1413–1417, 2002.
117. D. E. Hill, *et al*., "Functionalization of carbon nanotubes with polystyrene," *Macromolecules*, vol. 35(25), pp. 9466–9471, 2002.
118. Y. Lin, *et al*., "Polymeric carbon nanocomposites from carbon nanotubes functionalized with matrix polymer," *Macromolecules*, vol. 36(19), pp. 7199–7204, 2003.
119. S. S. Wong, *et al*., "Covalently functionalized nanotubes as nanometre- sized probes in chemistry and biology," *Nature*, vol. 394(6688), pp. 52–55, 1998.
120. B. Philip, *et al*., "A novel nanocomposite from multiwalled carbon nanotubes functionalized with a conducting polymer," *Smart Materials and Structures*, vol. 13(2), p. 295, 2004.
121. D. Baskaran, *et al*., "Carbon nanotubes with covalently linked porphyrin antennae: photoinduced electron transfer," *Journal of the American Chemical Society*, vol. 127(19), pp. 6916–6917, 2005.
122. L. Qu, *et al*., "Interactions of functionalized carbon nanotubes with tethered pyrenes in solution," *The Journal of Chemical Physics*, vol. 117, p. 8089, 2002.
123. Y.-P. Sun, *et al*., "Soluble dendron-functionalized carbon nanotubes: preparation, characterization, and properties," *Chemistry of Materials*, vol. 13(9), pp. 2864–2869, 2001.
124. J. E. Riggs, *et al*., "Strong luminescence of solubilized carbon nanotubes," *Journal of the American Chemical Society*, vol. 122(24), pp. 5879–5880, 2000.
125. E. Darron, Y. Lin, and F. Lawrence, "Solubilization of carbon nanotubes via polymer attachement," *International Journal of Nanoscience*, vol. 1(3–4), pp. 213–221, 2002.
126. B. He, *et al*., "Preparation and characterization of a series of novel complexes by single-walled carbon nanotubes (SWNTs) connected poly(amic acid) containing bithiazole ring," *Materials Chemistry and Physics*, vol. 84(1), pp. 140–145, 2004.
127. J. E. Riggs, *et al*., "Optical limiting properties of suspended and solubilized carbon nanotubess," *The Journal of Physical Chemistry B*, vol. 104(30), pp. 7071–7076, 2000.
128. W. Huang, *et al*., "Sonication-assisted functionalization and solubilization of carbon nanotubes," *Nano Letters*, vol. 2(3), pp. 231–234, 2002.
129. Y. Lin, *et al*., "Functionalizing multiple-walled carbon nanotubes with aminopolymers," *The Journal of Physical Chemistry B*, vol. 106(6), pp. 1294–1298, 2002.
130. B. Zhao, H. Hu, and R. C. Haddon, "Synthesis and properties of a water-soluble single-walled carbon nanotube-poly(m-aminobenzene sulfonic acid) graft copolymer," *Advanced Functional Materials*, vol. 14(1), pp. 71–76, 2004.
131. M. Sano, *et al*., "Self-organization of PEO-graft-single-walled carbon nanotubes in solutions and Langmuir−Blodgett films," *Langmuir*, vol. 17(17), pp. 5125–5128, 2001.
132. F. Pompeo, and D. E. Resasco, "Water solubilization of single-walled carbon nanotubes by functionalization with glucosamine," *Nano Letters*, vol. 2(4), pp. 369–373, 2002.
133. M. Shaffer, and K. Koziol, "Polystyrene grafted multi-walled carbon nanotubes," *Chemical Communications*, vol. 2002(18), pp. 2074–2075, 2002.

134. S. Qin, *et al*., "Solubilization and purification of single-wall carbon nanotubes in water by in situ radical polymerization of sodium 4-styrenesulfonate," *Macromolecules*, vol. 37(11), pp. 3965–3967, 2004.
135. S. Qin, *et al*., "Grafting of poly(4-vinylpyridine) to single-walled carbon nanotubes and assembly of multilayer films," *Macromolecules*, vol. 37(26), pp. 9963–9967, 2004.
136. G. Xu, *et al*., "Constructing polymer brushes on multiwalled carbon nanotubes by in situ reversible addition fragmentation chain transfer polymerization," *Polymer*, vol. 47(16), pp. 5909–5918, 2006.
137. G. Xu, et al., "Functionalized carbon nanotubes with polystyrene-block-poly (N-isopropylacrylamide) by in situ RAFT polymerization," *Nanotechnology*, vol. 18, p. 145606, 2007.
138. H. Kong, C. Gao, and D. Yan, "Controlled functionalization of multiwalled carbon nanotubes by in situ atom transfer radical polymerization," *Journal of the American Chemical Society*, vol. 126(2), pp. 412–413, 2004.
139. V. Datsyuk, *et al*., "Double walled carbon nanotube/polymer composites via in-situ nitroxide mediated polymerisation of amphiphilic block copolymers," *Carbon*, vol. 43(4), pp. 873–876, 2005.
140. A. Fujiwara, *et al*., *Proc. of Super Carbon (IUMRS-ICA-97)*, S. Fujiwara, ed. Tokyo, 1998.
141. T. Kimura, *et al*., "Polymer composites of carbon nanotubes aligned by a magnetic field," *Advanced Materials*, vol. 14(19), pp. 1380–1383, 2002.
142. C. Martin, *et al*., "Electric field-induced aligned multi-wall carbon nanotube networks in epoxy composites," *Polymer*, vol. 46(3), pp. 877–886, 2005.
143. I. Dierking, G. Scalia, and P. Morales, "Liquid crystal–carbon nanotube dispersions," *Journal of Applied Physics*, vol. 97, p. 044309, 2005.
144. V. A. Davis, *et al*., "Phase behavior and rheology of SWNTs in superacids," *Macromolecules*, vol. 37(1), pp. 154–160, 2004.
145. P. Ajayan, *et al*., "Aligned carbon nanotube arrays formed by cutting a polymer resin–nanotube composite," *Science*, vol. 265(5176), p. 1212, 1994.
146. W. De Heer, *et al*., "Aligned carbon nanotube films: production and optical and electronic properties," *Science*, vol. 268(5212), pp. 845–847, 1995.
147. L. Jin, C. Bower, and O. Zhou, "Alignment of carbon nanotubes in a polymer matrix by mechanical stretching," *Applied Physics Letters*, vol. 73, p. 1197, 1998.
148. R. Haggenmueller, *et al*., "Aligned single-wall carbon nanotubes in composites by melt processing methods," *Chemical Physics Letters*, vol. 330(3–4), pp. 219–225, 2000.
149. F. Ko, W. Han, and O. Zhou. *Carbon nanotube reinforced nanocomposites by electrospinning*. 2001. **MORE DETAILS?**
150. F. K. Ko, *et al. Structure and properties of carbon nanotube reinforced nanocomposites*. 2002. **MORE DETAILS?**
151. A. El-Aufy, B. Nabet, and F. Ko, "Carbon nanotube reinforced (PEDT/PAN) nanocomposite for wearable electronics," *Polymer Preprints*, vol. 44(2), pp. 134–135, 2003.
152. F. Ko, *et al*., "Electrospinning of continuous carbon nanotube-filled nanofiber yarns," *Advanced Materials*, vol. 15(14), pp. 1161–1165, 2003.
153. Y. Wan, and F. Ko, *Multifunctional Carbon Nanotube Yarns*, in *SAMPE 2009*. Wichita, Kansas USA, 2009.
154. Y. Wan, *et al*., *Multifunctional Carbon Nanotube Fibers and Yarns*, in *SAMPE 2010*. Seattle, WA, USA, 2010.

155. K. Koziol, *et al*., "High-performance carbon nanotube fiber," *Science*, vol. 318(5858), pp. 1892–1895, 2007.
156. Q. W. Li, *et al*., "Sustained growth of ultralong carbon nanotube arrays for fiber spinning," *Advanced Materials*, vol. 18(23), p. 3160, 2006.
157. X. Zhang, *et al*., "Strong carbon-nanotube fibers spun from long carbon-nanotube arrays," *Small*, vol. 3(2), pp. 244–248, 2007.
158. L. M. Ericson, *et al*., *Macroscopic, Neat, Single-Walled Carbon Nanotube Fibers*, American Association for the Advancement of Science, pp. 1447–1450, 2004.
159. W. Zhou, *et al*., "Single-walled carbon nanotubes in superacid: X-ray and calorimetric evidence for partly ordered H_2SO_4," *Physical Review B*, vol. 72(4), p. 45 440, 2005.
160. C. Drew, *et al*., "Electrospun photovoltaic cells," *Journal of Macromolecular Science, Part A*, vol. 39(10), pp. 1085–1094, 2002.
161. P. Miaudet, *et al*., "Hot-drawing of single and multiwall carbon nanotube fibers for high toughness and alignment," *Nano Letters*, vol. 5(11), pp. 2212–2215, 2005.
162. A. B. Dalton, *et al*., "Continuous carbon nanotube composite fibers: properties, potential applications, and problems," *Journal of Materials Chemistry*, vol. 14(1), pp. 1–3, 2004.
163. A. B. Dalton, *et al*., "Super-tough carbon-nanotube fibres," *Nature*, vol. 423(6941), pp. 703, 2003.
164. K. Mukhopadhyay, *et al*., "Double helical carbon microcoiled fibers synthesis by CCVD method," *Carbon*, vol. 43(11), pp. 2400–2402, 2005.
165. X. F. Zhang, *et al*., "Self-organized arrays of carbon nanotube ropes," *Chemical Physics Letters*, vol. 351, pp. 183–188, 2002.
166. C. Liu, *et al*., "Synthesis of macroscopically long ropes of well-aligned single-walled carbon nanotubes, *Applied Physics Letters*, vol. 72, p. 1835, 1998.
167. H. W. Zhu, *et al*., "Direct Synthesis of Long Single-Walled Carbon Nanotube Strands," *Science*, vol. 296 (5569), pp. 884–886, 2002.
168. C. Singh, M. S. P. Shaffer, and A. H. Windle, "Production of controlled architectures of aligned carbon nanotubes by an injection chemical vapour deposition method," *Carbon*, vol. 41(2), pp. 359–368, 2003.
169. Y. L. Li, I. A. Kinloch, and A. H. Windle, *Direct Spinning of Carbon Nanotube Fibers from Chemical Vapor Deposition Synthesis*, American Association for the Advancement of Science, pp. 276–278, 2004.
170. K. Jiang, Q. Li, and S. Fan, "Nanotechnology: spinning continuous carbon nanotube yarns", *Nature*, vol. 419(6909), pp. 801–801, 2002.
171. K. R. Atkinson, *et al*., "Multifunctional carbon nanotube yarns and transparent sheets: fabrication, properties, and applications," *Physica B: Condensed Matter*, vol. 394(2), pp. 339–343, 2007.
172. H. H. Gommans, *et al*., "Fibers of aligned single-walled carbon nanotubes: polarized Raman spectroscopy," *Journal of Applied Physics*, vol. 88, p. 2509, 2000.
173. S. Ramesh, *et al*., "Dissolution of pristine single walled carbon nanotubes in superacids by direct protonation," *J Phys Chem B*, vol. 108(26), p. 8794–8798, 2004.
174. B. Vigolo, *et al*., "Macroscopic fibers and ribbons of oriented carbon nanotubes," *Science*, vol. 290(5495), pp. 1331–1334, 2000.
175. B. Vigolo, *et al*., "Improved structure and properties of single-wall carbon nanotube spun fibers," *Applied Physics Letters*, vol. 81, p. 1210, 2002.
176. P. Poulin, B. Vigolo, and P. Launois, "Films and fibers of oriented single wall nanotubes," *Carbon*, vol. 40(10), pp. 1741–1749, 2002.

177. M. Lucas, *et al*., "Alignment of carbon nanotubes in macroscopic fibers," *AIP Conference Proceedings*, vol. 633, p. 579, 2002.
178. B. Vigolo, *et al*., "Dispersions and fibers of carbon nanotubes," *Materials Research Society Symposium Proceedings*, vol. 633, 2001.
179. R. H. Baughman, "Materials science: putting a new spin on carbon nanotubes," *Science*, vol. 290(5495), p. 1310, 2000.
180. B. Vigolo, *et al*., "Fibers of carbon nanotubes," *Making Functional Materials with Nanotubes as held at the 2001 MRS Fall Meeting*, pp. 3–15, 2001.
181. A. Lobovsky, *et al*., *Spinning, processing, and applications of carbon nanotube filaments, ribbons, and yarns*, 2007, Google Patents.
182. J. M. Razal, *et al*., "Arbitrarily shaped fiber assemblies from spun carbon nanotube gel fibers," *Advanced Functional Materials*, vol. 17(15), p. 2918, 2007.
183. Y. Dror, *et al*., "Carbon nanotubes embedded in oriented polymer nanofibers by electrospinning," *Langmuir*, vol. 19(17), pp. 7012–7020, 2003.
184. T. Wang, C. F. Zhou, and S. Kumar, "Electrospun poly (acrylonitrile)/poly(acrylonitrile-co-styrene)/carbon nanotube fiber mat for electrochemical supercapacitors," *Abstracts of Papers of the American Chemical Society*, vol. 229, pp. U1105–U1105, 2005.
185. G. M. Kim, G. H. Michler, and P. Puschke, "Deformation processes of ultrahigh porous multiwalled carbon nanotubes/polycarbonate composite fibers prepared by electrospinning," *Polymer*, vol. 46(18), pp. 7346–7351, 2005.
186. J. S. Jeong, *et al*., "Fabrication of MWNTs/nylon conductive composite nanofibers by electrospinning," *Diamond and Related Materials*, vol. 15(11–12), pp. 1839–1843, 2006.
187. B. Sundaray, *et al*., "Electrical conductivity of a single electrospun fiber of poly(methyl methacrylate) and multiwalled carbon nanotube nanocomposite," *Applied Physics Letters*, vol. 88(14), p. 143114, 2006.
188. F. Ko, *et al*., "Electrospinning of continuous carbon nanotube-filled nanofiber yarns," *Journal of the American Chemical Society*, vol. 124, p. 740, 2002.
189. J. Ayutsede, *et al*., "Carbon nanotube reinforced *Bombyx mori* silk nanofibers by the electrospinning process," *Biomacromolecules*, vol. 7(1), pp. 208–214, 2006.
190. A. M. Motta, I. A. Kinloch, and Alan H. Windle, "High performance fibres from 'dog bone' carbon nanotubes," *Advanced Materials*, vol. 19(21), pp. 3721–3726, 2007.
191. Y. L. Li, I. A. Kinloch, and A. H. Windle, "Direct spinning of carbon nanotube fibers from chemical vapor deposition synthesis," *Science*, vol. 304(5668), pp. 276–278, 2004.
192. X.-H. Zhong, *et al*., "Continuous multilayered carbon nanotube yarns," *Advanced Materials*, vol. 22(6), pp. 692–696, 2010.
193. [cited 2010 August 12]; Available from: http://www.nanocomptech.com/html/nanocomp-technology.html.
194. W. Zhou, *et al*., "Single wall carbon nanotube fibers extruded from super-acid suspensions: preferred orientation, electrical, and thermal transport," *Journal of Applied Physics*, vol. 95, p. 649, 2003.
195. T. V. Sreekumar, *et al*., "Polyacrylonitrile single-walled carbon nanotube composite fibers," *PAN*, vol. 10, p. 100, 2004.
196. H. G. Chae, *et al*., "Stabilization and carbonization of gel spun polyacrylonitrile/single wall carbon nanotube composite fibers," *Polymer*, vol. 48(13), pp. 3781–3789, 2007.
197. H. G. Chae, *et al*., "A comparison of reinforcement efficiency of various types of carbon nanotubes in polyacrylonitrile fiber," *Polymer*, vol. 46(24), pp. 10 925–10 935, 2005.

198. H. Zhang, *et al*., "Regenerated-cellulose/multiwalled-carbon-nanotube composite fibers with enhanced mechanical properties prepared with the ionic liquid 1-allyl-3-methylimidazolium chloride," *Advanced Materials*, vol. 19(5), pp. 698–698, 2007.
199. R. Andrews, *et al*., "Nanotube composite carbon fibers," *Applied Physics Letters*, vol. 75, p. 1329, 1999.
200. R. Haggenmueller, *et al*., "Interfacial in situ polymerization of single wall carbon nanotube/nylon 6, 6 nanocomposites," *Polymer*, vol. 47(7): p. 2381–2388, 2006.
201. J. B. Gao, *et al*., "Continuous spinning of a single-walled carbon nanotube-nylon composite fiber," *Journal of the American Chemical Society*, vol. 127(11), pp. 3847–3854, 2005.
202. J. J. Ge, *et al*., "Assembly of well-aligned multiwalled carbon nanotubes in confined polyacrylonitrile environments: electrospun composite nanofiber sheets," *Journal of the American Chemical Society*, vol. 126(48), pp. 15 754–15 761, 2004.
203. J. Ayutsede, *et al*., "Regeneration of *Bombyx mori* silk by electrospinning. Part 3: characterization of electrospun nonwoven mat," *Polymer*, vol. 46(5), pp. 1625–1634, 2005.
204. S. Sukigara, *et al*., "Regeneration of Bombyx mori silk by electrospinning–part 1: processing parameters and geometric properties," *Polymer*, vol. 44(19), pp. 5721–5727, 2003.
205. S. Sukigara, *et al*., "Regeneration of Bombyx mori silk by electrospinning. Part 2. Process optimization and empirical modeling using response surface methodology," *Polymer*, vol. 45(11), pp. 3701–3708, 2004.
206. A. Okada, and A. Usuki, "Twenty years of polymer-clay nanocomposites," *Macromolecular Materials and Engineering*, vol. 291(12), pp. 1449–1476, 2006.
207. M. Alexandre, and P. Dubois, "Polymer-layered silicate nanocomposites: preparation, properties and uses of a new class of materials," *Materials Science and Engineering: R: Reports*, vol. 28(1–2), pp. 1–63, 2000.
208. W. J. Boo, *et al*., "Effect of nanoplatelet dispersion on mechanical behavior of polymer nanocomposites," *Journal of Polymer Science Part B: Polymer Physics*, vol. 45(12), pp. 1459–1469, 2007.
209. H. Fischer, "Polymer nanocomposites: from fundamental research to specific applications," *Materials Science and Engineering: C*, vol. 23(6–8), pp. 763–772, 2003.
210. A. Dortmans, *et al*., "Nanocomposite materials: from lab-scale experiments to prototypes," e-Polymers, vol. 2(1), pp. 135–144, 2013.
211. J. N. Hay, and S. J. Shaw, *A Review of Nanocomposites 2000*, 2000.
212. S. Nazaré, B. K. Kandola, and A. R. Horrocks, "Flame-retardant unsaturated polyester resin incorporating nanoclays," *Polymers for Advanced Technologies*, vol. 17(4), pp. 294–303, 2006.
213. D. M. Lincoln, *et al*., "Secondary structure and elevated temperature crystallite morphology of nylon-6/layered silicate nanocomposites," *Polymer*, vol. 42(4), pp. 1621–1631, 2001.
214. H. Fong, *et al*., "Generation of electrospun fibers of nylon 6 and nylon 6–montmorillonite nanocomposite," *Polymer*, vol. 43(3), pp. 775–780, 2002.
215. T. D. Fornes, and D. R. Paul, "Crystallization behavior of nylon 6 nanocomposites," *Polymer*, vol. 44(14), pp. 3945–3961, 2003.
216. L. Li, *et al*., "Formation and properties of nylon-6 and nylon-6/montmorillonite composite nanofibers," *Polymer*, vol. 47(17), pp. 6208–6217, 2006.
217. L. Yu, and P. Cebe, "Crystal polymorphism in electrospun composite nanofibers of poly (vinylidene fluoride) with nanoclay," *Polymer*, vol. 50(9), pp. 2133–2141, 2009.
218. S. Ramasundaram, *et al*., "Preferential formation of electroactive crystalline phases in poly (vinylidene fluoride)/organically modified silicate nanocomposites," *Journal of Polymer Science Part B: Polymer Physics*, vol. 46(20), pp. 2173–2187, 2008.

219. Y.-L. Liu, *et al*., "Cooperative effect of electrospinning and nanoclay on formation of polar crystalline phases in poly(vinylidene fluoride)," *ACS Applied Materials & Interfaces*, 2010. **DETAILS?**
220. S. Adanur, and B. Ascioglu, "Nanocomposite fiber based web and membrane formation and characterization," *Journal of Industrial Textiles*, vol. 36(4), pp. 311–327, 2007.
221. J. Park, *et al*., "Electrospinning and characterization of poly(vinyl alcohol)/chitosan oligosaccharide/clay nanocomposite nanofibers in aqueous solutions," *Colloid & Polymer Science*, vol. 287(8), pp. 943–950, 2009.
222. Y. Cai, *et al*., "Structure, morphology, thermal stability and carbonization mechanism studies of electrospun PA6/Fe-OMT nanocomposite fibers," *Polymer Degradation and Stability*, vol. 93(12), pp. 2180–2185, 2008.
223. C. Yacoob, W. Liu, and S. Adanur, "Properties and flammability of electrospun PVA and PVA/Laponite (R) membranes," *Journal of Industrial Textiles*, 2010. **DETAILS?**
224. N. Ristolainen, *et al*., "Poly(vinyl alcohol) and polyamide-66 nanocomposites prepared by electrospinning," *Macromolecular Materials and Engineering*, vol. 291(2), pp. 114–122, 2006.
225. Y.-X. Pan, *et al*., "A new process of fabricating electrically conducting nylon 6/graphite nanocomposites via intercalation polymerization," *Journal of Polymer Science Part B: Polymer Physics*, vol. 38(12), pp. 1626–1633, 2000.
226. F. Hussain, *et al*., "Polymer-matrix nanocomposites, processing, manufacturing, and application: an overview," *Journal of Composite Materials*, vol. 40(17), pp. 1511–1575, 2006.
227. L. T. F. Drzal, "Graphite nanoplatelets as reinforcements for polymers," *Polymer Preprints*, vol. 42(2), pp. 42–43, 2001.
228. J. A. King, *et al*., "Electrically and thermally conductive nylon 6,6," *Polymer Composites*, vol. 20(5), pp. 643–654, 1999.
229. A. Yasmin, J.-J. Luo, and I. M. Daniel, "Processing of expanded graphite reinforced polymer nanocomposites," *Composites Science and Technology*, vol. 66(9), pp. 1182–1189, 2006.
230. A. Yasmin, and I. Daniel, "Mechanical and thermal properties of graphite platelet/epoxy composites," *Polymer*, vol. 45(24), pp. 8211–8219, 2004.
231. J. J. Mack, *et al*., "Graphite nanoplatelet reinforcement of electrospun polyacrylonitrile nanofibers," *Advanced Materials*, vol. 17(1), pp. 77–80, 2005.
232. N. Bartlett, and B. W. McQuillan, *Intercalation Chemistry*, M. S. Whittingham and A. J. Jacobson, ed., New York: Academic, 1982.
233. A. Melechko, *et al*., "Vertically aligned carbon nanofibers and related structures: controlled synthesis and directed assembly," *Journal of Applied Physics*, vol. 97, p. 041301, 2005.
234. A. Krishnan, *et al*., "Graphitic cones and the nucleation of curved carbon surfaces," *Nature*, vol. 388(6641), pp. 451–454, 1997.
235. L. Zhang, *et al*., "Four-probe charge transport measurements on individual vertically aligned carbon nanofibers," *Applied Physics Letters*, vol. 84, p. 3972, 2004.
236. W. D. Callister, *Materials Science and Engineering: an Introduction*. John Wiley & Sons, 2003.
237. S. B. Lee, *et al*., "Study of multi-walled carbon nanotube structures fabricated by PMMA suspended dispersion," *Microelectronic Engineering*, vol. 61–62, pp. 475–483, 2002.
238. C. Schönenberger, *et al*., "Interference and Interaction in multi-wall carbon nanotubes," *Applied Physics A: Materials Science & Processing*, vol. 69(3), pp. 283–295, 1999.
239. A. Thess, *et al*., "Crystalline ropes of metallic carbon nanotubes," *Science*, vol. 273(5274), p. 483, 1996.

240. C. Kim, *et al*., "Raman spectroscopic evaluation of polyacrylonitrile-based carbon nanofibers prepared by electrospinning," *Journal of Raman Spectroscopy*, vol. 35(11), pp. 928–933, 2004.
241. Y. Wang, S. Serrano, and J. J. Santiago-Avilés, "Raman characterization of carbon nanofibers prepared using electrospinning," *Synthetic Metals*, vol. 138(3), pp. 423–427, 2003.
242. C. Kim, *et al*., "Fabrication of electrospinning-derived carbon nanofiber webs for the anode material of lithium-ion secondary batteries," *Advanced Functional Materials*, vol. 16(18), pp. 2393–2397, 2006.
243. S. Park, *et al*. *Cabon Nanofibrous Materials Prepared from Electrospun Polyacrylonitrile Nanofibers for Hydrogen Storage*. Warrendale, Pa.; Materials Research Society, 1999.
244. E. Zussman, *et al*., "Mechanical and structural characterization of electrospun PAN-derived carbon nanofibers," *Carbon*, vol. 43(10), pp. 2175–2185, 2005.
245. K. Yang, *et al*., "Preparation of carbon fiber web from electrostatic spinning of PMDA-ODA poly (amic acid) solution," *Carbon*, vol. 41(11), pp. 2039–2046, 2003.
246. Y. Zhu, *et al*., "Multifunctional carbon nanofibers with conductive, magnetic and superhydrophobic properties," *ChemPhysChem*, vol. 7(2), pp. 336–341, 2006.
247. S. Park, *et al*., "Preparations of pitch-based CF/ACF webs by electrospinning," *Carbon*, vol. 41(13), pp. 2655–2657, 2003.
248. I. C. Finegan, *et al*., "Surface treatments for improving the mechanical properties of carbon nanofiber/thermoplastic composites," *Journal of Materials Science*, vol. 38(16), pp. 3485–3490, 2003.
249. G. Tibbetts, and J. McHugh, "Mechanical properties of vapor-grown carbon fiber composites with thermoplastic matrices," *Journal of Materials Research*, vol. 14(7), pp. 2871–2880, 1999.
250. R. Patton, and C. Pittman, "Vapor grown carbon fiber composites with epoxy and poly (phenylene sulfide) matrices," *Composites Part A: Applied Science and Manufacturing*, vol. 30(9), pp. 1081–1091, 1999.
251. S. A. Gordeyev, *et al*., "Transport properties of polymer-vapour grown carbon fibre composites," *Physica B: Condensed Matter*, vol. 279(1–3), pp. 33–36, 2000.
252. G. G. Tibbetts, I. C. Finegan, and C. Kwag, "Mechanical and electrical properties of vapor-grown carbon fiber thermoplastic composites," *Molecular Crystals and Liquid Crystals*, vol. 387, pp. 129–133, 2002.
253. J. Donohoe, and C. Pittman, Shielding effectiveness of vapor grown carbon nanofiber/vinyl ester composites, in *EMC Europe 2004, International Symposium on Electromagnetic Compatibility*, Eindhoven, Netherlands, 2004.
254. M. Lafdi, and K. Matzek, Carbon nanofibers as a nano-reinforcement for polymeric nanocomposites, in *48th International SAMPE symposium*. Long Beach, 2003.

10 Future opportunities and challenges of electrospinning

10.1 Past, present and future of nanotechnology

In 2000, Roco *et al*. [1] estimated that there would be two million nanotechnology workers worldwide (800 000 in the United States) and the product value would reach $1 trillion, of which $800 billion would be in the United States, by 2015, with a 25% rate growth. The initial estimation for the quasi-exponential growth in the nanotechnology workforce and the product value held up to 2008, as shown in Fig.10.1. The market is doubling every three years as a result of the successive introduction of new products, and new generations of nanotechnology products are expected to enter the market within the next few years [1]. So the estimated value of 2015 for both workforce and product value would have been realized as the 25% growth rate is expected to continue.

Nanotechnology is evolving toward new scientific and engineering challenges in areas such as assembly of nanosystems, nanobiotechnology and nanobiomedicine, development of advanced tools, environmental preservation and protection, and pursuit of societal implication studies. Key areas of emphasis in nanotechnology [1] over the next decade are as follows.

- Integration of knowledge at the nanoscale and of nanocomponents in nanosystems with deterministic and complex behavior, aiming toward creating fundamentally new products.
- Better control of molecular self-assembly, quantum behavior, creation of new molecules, and interaction of nanostructures with external fields in order to build materials, devices and systems by modeling and computational design.
- Understanding of biological processes and of nanobio interfaces with abiotic materials, and their biomedical and health/safety applications, and nanotechnology solutions for sustainable natural resources and nanomanufacturing.

Nanotechnology is already creating a strong impact in the development of many scientific and engineering areas, ranging from electronics to textiles; by 2020, it is likely to become a broad-based technology, covering multidisciplinary areas, seamlessly integrated with most technologies and applications, driven by economics and by the impetus of achieving innovative solutions in medicine, productivity, sustainable development, and human quality of life [1] Figure 10.2 shows the development timelines of nanotechnology and possible mass application areas of nanotechnology after around 2020.

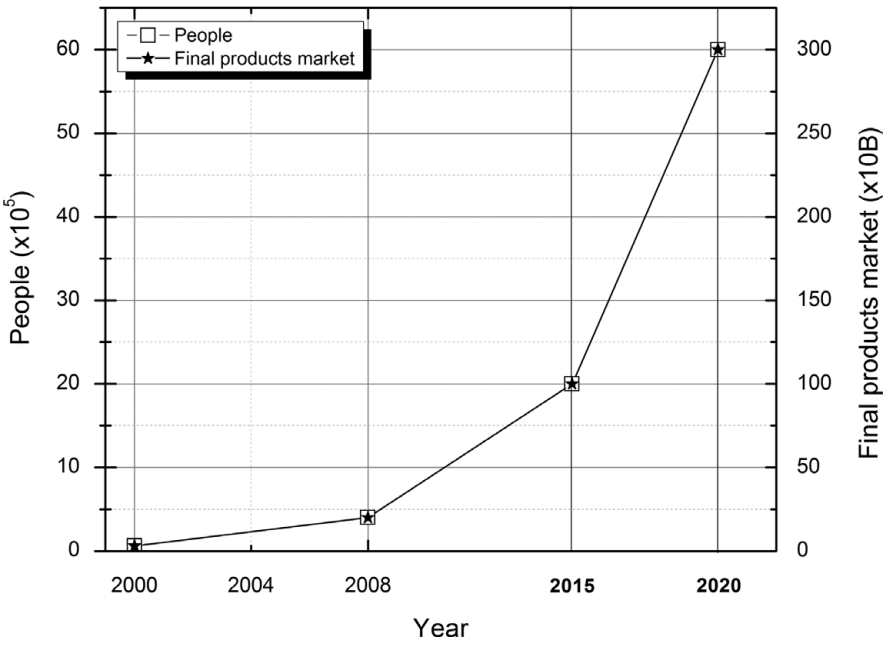

Fig. 10.1 Past and estimated worldwide number of workforce and final product value with a quasi-exponential growth (data from Ref. [1]).

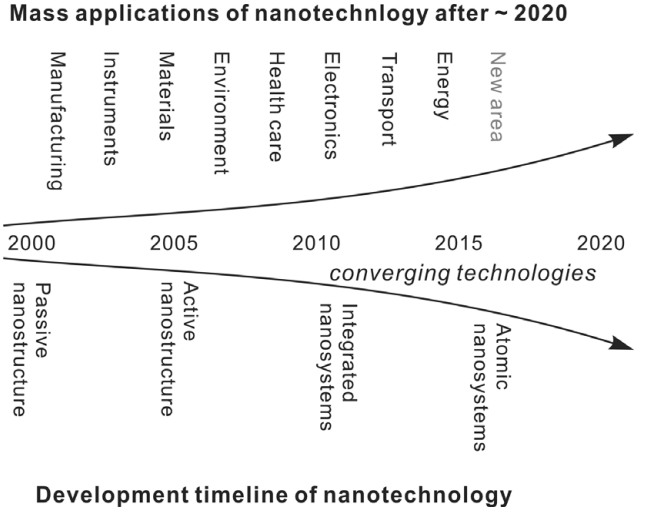

Fig. 10.2 Development timeline of nanotechnology and possible mass applications of nanotechnology after ~2020 (referred and modified from Ref. [1]).

10.2 Global challenges and nanotechnology

As referred to in his talk "Future global energy prosperity: the terawatt challenge" [2], Smalley describes energy, water, environment and disease as four out of the top ten

global challenges that need to be faced and solved as soon as possible. Still, as Smalley said, "Innovations in nanotechnology and other advances in materials science would make it possible to transform our vision of plentiful, low-cost energy into a reality."[2] Nanotechnology is also the possible solution to the challenges of "water, environment and disease."

10.2.1 Nanofibers in energy

It is estimated that, in order to give all people on the planet the level of energy prosperity those in the developed world are used to, a couple of kilowatt-hours per person, 60 terawatts around the planet need to be generated. And it is rather obvious that burning up the limited energy resources on Earth cannot solve the global energy problems; but will cause greater environmental problems by the emission of large volumes of carbon dioxide. Therefore we will require not only new sustainable energy resources but also innovations in collection, storage and transmission of energy.

10.2.1.1 Electrolytes in fuel cells or batteries

Fuel cells are devices that have been widely used for automobile propulsion and as portable electronic devices, such as personal digital assistants (PDAs), cell phones and notebook computers. With high accessible surface area and good electrical conductivity, nanofiber membranes may lower the cost of fuel cells as the anode catalyst or the anode catalyst supporting materials, and provide conducting pathways and surface interactions between nanoparticles and the electrolyte [3]. Electrospun nanofiber membranes are also good candidates for solid electrolytes in fuel cells. Experimental results indicate that the electrical performance of fuel cells is proportional to the surface area of the fibrous anodes [4]. Electrospun carbon nanofiber membrane (CFMs) supported on Pt anodes exhibit higher electrocatalytic activity, more stability, larger exchange current and smaller charge transfer resistance than that on commercial carbon papers (CPs) [5–7].

Given that nanofiber membranes having large surface area fibers for incorporation of large amounts of liquid/gel electrolyte and fully interconnected pore structures offering a good ion conduction channel, which assures the nanofiber electrolytes are capable of attaining of high ionic conductivity at room temperature [8, 9], electrospun nanofiber membranes are attractive as polymer electrolytes for lithium ion batteries and fuels cells.

10.2.1.2 Supercapacitors

The capacitance of an electrical capacitor is a function of the specific surface area, pore volume and resistivity of the sample, which indicates that electrospun nanofibers can be innovative materials for supercapacitors. Experimental studies have proved that electrospun nanofibers possess outstanding capacitance. The specific capacitance behavior of polyaniline nanofibers was characterized by using cyclic voltammetry, exhibiting the highest specific capacitance of 298 F/g [10]. The specific capacitance from the PBI precusor activated carbon nanofibers ranged from 125 F/g to 178 F/g depending on the activation temparatures [11].

10.2.1.3 Dye-sensitized solar cells

Researchers have realized that in dye-sensitized solar cells grain boundaries between nanoparticles diminish the efficiency of electron conduction in the matrix, and lead to charge–carrier recombination. One-dimensional morphology of the metal oxide fibers can contribute to better charge conduction due to their continuity compared with that of sintered nanoparticles, and also provides high specific surface area for increased adsorption of dye sensitizers. Photonic nanofibers can be easily produced [12–15] and have shown excellent photovoltaic properties – achieving an energy conversion efficiency of 6.2%[16].

10.2.1.4 Power transmission lines

New transmission line materials that are of lighter weight, are stronger and have lower loss than copper are needed to address the global demand for power. In his testimony to the Senate Committee on Energy and Natural Resources, Nobel Prize winner Professor Richard Smalley predicted massive electrical power transmission over continental distances [2]. Electrical power transmission is a superb way of moving energy from one place to another and, at least on a small scale, electrical power can be stored. He envisaged that nanotechnology in the form of single-walled carbon nanotubes, forming what he called the Armchair Quantum Wire, may play a big role in this new electrical transmission system [2]. Electrospinning, which has demonstrated its power in manufacturing multifunctional continuous fibers with nanotubes incorporated and well aligned, can be a useful tool in producing lighter weight, stronger, lower cost and more efficient power transmission lines.

10.2.2 Nanofibers in filtration

Concerning the global environmental issues such as water and air purification, membranes and filtration systems are believed to be among the most-used tools. The technical requirements for filters are a balance of the three major parameters of filter performance: filter efficiency, pressure drop and filter lifetime [17]. An improvement in one category generally means a corresponding sacrifice in another. It was shown that proper use of nanofibers provided marked improvements in both filtration efficiency and lifetime, while keeping a minimal impact on pressure drop. The large surface area of nanofiber webs allows rapid and effective adsorption of impurities and other particles such as micro-organisms or viruses from the air or water as well as hazardous molecules. Beside fineness and the resulting large specific surface area of nanofiber membranes, the high porosity and small pore size contribute further to their high adsorption and filtration efficiency [17]. Furthermore, electrospun nanofiber membranes can offer removal of impurities from the environment at lower energy and hence lower cost at high efficiency. Owing to the similar mechanism, nanofiber filtration systems for personal protection such as respiratory and clothes are also under development for efficient protection of people from biological and chemical elements [18, 19].

The application of nanofiber membranes for filtration started in the early 1980s. Since then, utilizing nanofibers as filter media has spread worldwide. More and more companies such as Donaldson, Toray and Nanoval GmBH have already used nanofibers in their commercial filter products.

Using synthetic or natural polymers bearing special functionalities or specific add-ons to the spinning solution, chemical and biological functionality can be achieved. For example the incorporation of silver nanoparticles into nanofibers offers synergies of two nanotechnologies [20].

10.2.3 Nanofibers in biomedical engineering

The power of nanotechnology in biomedical engineering lies in its ability to operate on the same small scale as all the intimate biochemical functions involved in the growth, development and aging of the human body. Nanotechnology is expected to provide a new framework for diagnosing, treating and preventing disease [21]. Characterized by nano- to microsize, a wide range of pore size distribution, high porosity, effective mechanical properties and specific biochemical properties, nanofiber membranes are morphologically and chemically similar to the extracellular matrix of natural tissue. Therefore it is hypothesized that the intrinsic properties of nanofiber membranes will facilitate the attachment and proliferation of cells, and control of their cellular functions. This has resulted in recent research on the application of polymer nanofibers in the field of biomedicine and biotechnology such as scaffolds used in tissue engineering, drug delivery, wound dressing, artificial organs and vascular grafts.

10.3 Challenges

While electrospinning has been accepted as a versatile nanofiber processing technique for a variety of applications, its true potential has yet to be realized. It is very important to gain a better fundamental understanding of electrospinning process. Therefore, better control of this process can be achieved. Effort should be made to control processing variables so as to obtain defect-free and uniform diameter nanofibers. For effective applications exploring different functionalied nanofibers by post-treatment, incorporation of functional particles or developing novel structures are generally required. Finally, to bridge the gap between scientific research and practical application, investigation on the scale-up of electrospinning and tecnniques for assembling these nanosized fibers into micro- or even higher-scaled structures are inevitable.

10.3.1 Mechanism analysis

Revealing the fundamental mechanisms of a technique is the basic way and powerful tool for one to understanding and gain control of it. It is widely accepted that the whipping/bending instability of the jet is the reason fibers we formed with a diameter in

the nanoscale. The whipping instability was explained by two possible mechanisms [22]: (1) small lateral fluctuations in the centerline of the jet result in the induction of a dipolar charge distribution and the dipoles interaction with the external electric field producing a torque that further bends the jet; and (2) mutual repulsion of surface charges carried by the jet causes the centerline to bend. Although understanding how these mechanisms work on the jet and induce the instablility is vital for controling this electrospinning, a detailed explaination is still unavailable.

As modeling plays a very important role in understanding a process, different models have been proposed for electrospinning. Some of the representative models are Spivak–Dzenis model [23, 24], Rutledge's model [25, 26] and the Wan–Guo–Pan model [27, 28]. However, applications of these models in analyzing electrospinning were conducted under very ideal and simple conditions. How to balance the complicated conditions with a more realistic analysis based on a precise model needs to be mapped out.

10.3.2 Quality control

Instead of the beauty of small size and high specific surface area, electrospun nanofibers have their own drawbacks, including non-uniform diameter distribution along a single fiber or between fibers results from the whipping instability, weak mechanical properties due to the lack of crystalline regions and defects caused by the evaporation of solvents after the fiber forming, or the spinnability of solution. Therefore efforts need to be made in investigating controling or manipulating the whipping motion of the jet, adjusting the solution properties for better spinnability and controlling of process variables for a designed fiber properties. Post-treatment of nanofiber products for high mechanical properties might also need to be conducted, considering that most of commercial fibers gain their mechanical properties during post-processes such as drawing and annealing.

10.3.3 Scale-up manufacturing

Apart from the challenges in process and property controlling, the huge challenge that hinders the commercialization of electrospun nanofibers is the productivity and scale-up of electrospinning devices. Conventional electrospinning setups are based on needle systems: the polymer solution or melt is conducted to a spinneret attached to a syringe, a Taylor cone, from which a jet is ejected if the applied electronic force surpasses the surface tension of the cone. When it forms at the tip of the spinneret, the jet then solidifies into a nanofiber when it moves towards the collector. In such a system, the throughput of a single needle is typically 0.1–1.0 g/h by fibre weight or 1.0–5.0 ml/h by flow rate, depending on the polymer solution [29, 30], which is much too low to meet the strong market requirement. Therefore many efforts have been centered on increasing output by multiplexing the electrospinning system either by stacking an array of capillaries/syringes, or by operating a multiple-jet mode.

Linear (Fig. 10.3a) [31–33], matrix (Fig. 10.3b) [31, 33, 34], hexagonal (Fig. 10.3c) [35], elliptic (Fig. 10.3e) and concentric (Fig. 10. 3d) [36] jet arrays have been proposed for scale-up electrospinning. Many companies such as Espin, MECC Co. Ltd and

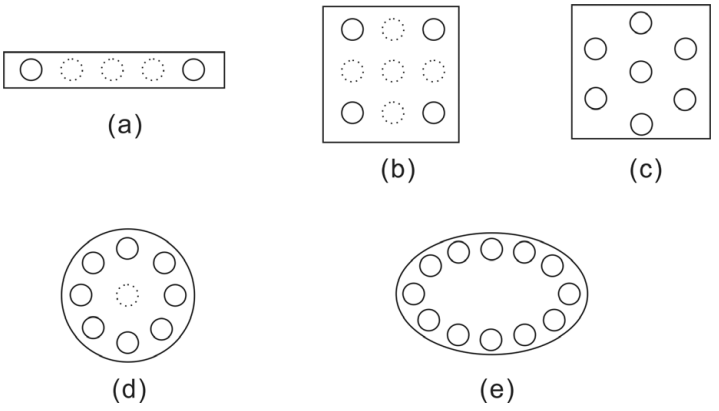

Fig. 10.3 Multiple-jet arrays: (a) linear array 2–26; (b) matrix array; (c) hexagonal array; (d) concentric array; and (e) elliptic array.

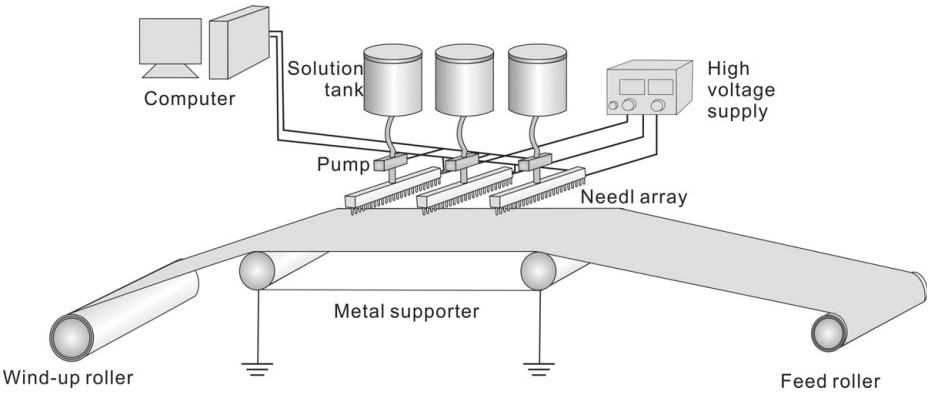

Fig. 10.4 Structure of an industrial electrospinning machine.

Electrospunra have even commercialized industrial electrospinning setups. Figure 10.4 shows the basic structure of an industrialized electrospinning machine. Although significant improvements in output can be made, there are barriers for these systems to implement robustly. One of the biggest issues is the interference among jets caused by electrostatic repulsion between each needles due to the applied electrostatic field, as shown in Fig. 10.5. As a consequence, the inference will distort jets resulting in non-uniform diameter and un-controllable deposition issues, as shown in Fig. 10.6. Needle/pore clogging is another common issue caused by the quick evaporation of solvents from the surface of Taylor tone. Moreover, fluid dripping and nozzle cleaning beset the multiple-jet electrospinning setup all the time.

To solve the electrostatic repulsion problem, Kim *et al*. [37] applied a cylindrical electrode to a five-nozzle setup, as shown in Fig. 10.7. However, obviously this could be effective only for a small nozzle array. A bottom-up multiple-jet system can avoid solution dripping problems [38], but nozzle clogging and cleaning are still challenges.

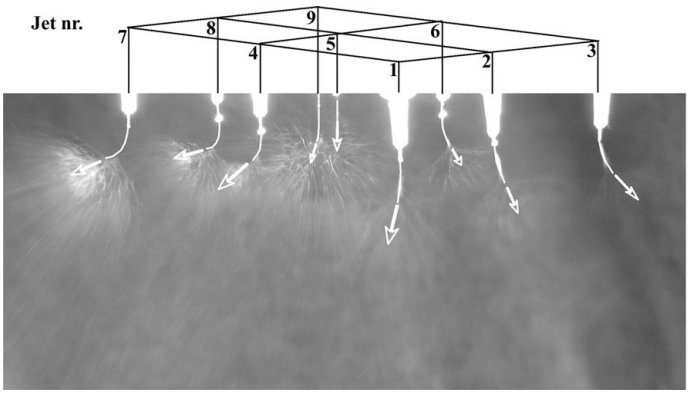

Fig. 10.5 A 3 × 3 matrix jet array [34].

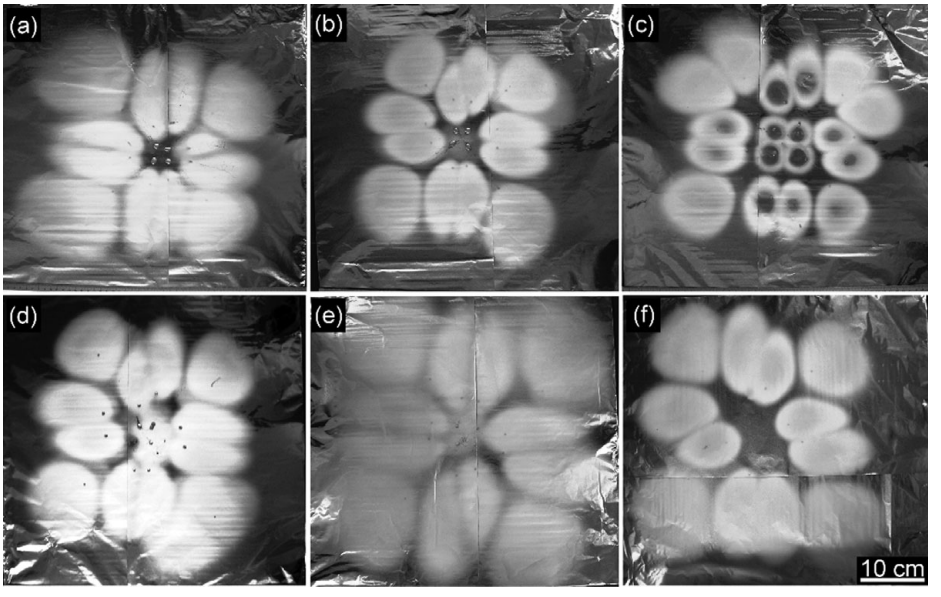

Fig. 10.6 Fibers collected from multiple-jet array at varying the solution applied voltage and the working distance [33]: (a) +20 kV, 17 cm, (b) +25 kV, 17 cm, (c) +30 kV, 17 cm, (d) +30 kV, 21 cm, (e) +30 kV, 25 cm, and setup 5: (f) +30 kV, 21 cm.

The invention of the rotary porous tube [39](Fig. 10.8a), rotary cone [40] (Fig.10. 8b), and conical wire [41] (Fig. 10.9) break the barriers of needle electrospinning, and have shown their promising in high productivity. However, for the rotary systems, the rotation aggravates the diameter distribution of nanofibers. For the conical wire spinneret, relatively high solution viscosity is required for the wire to be able to hold the solution from dripping, wherein large fiber diameter is inevitable.

To avoid the needle clogging and cleaning, and solution dripping problems, bottom-up needleless systems, including multiple-spike ([42] (Fig. 10.10a), multiple-cleft [43]

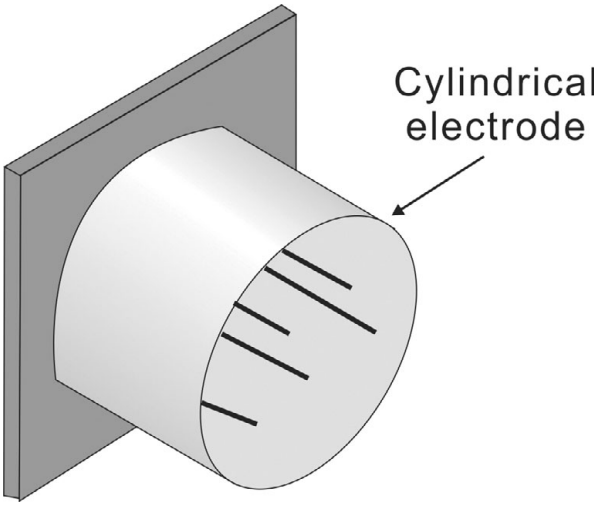

Fig. 10.7 Cylindrical electrode [37].

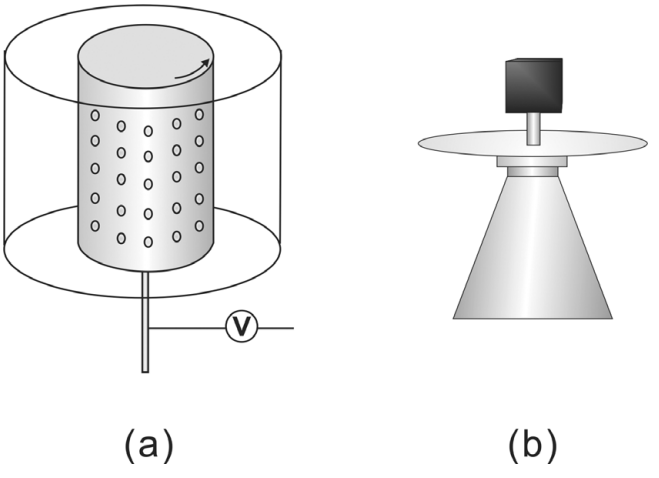

Fig. 10.8 (a) Rotary porous tube and (b) rotary cone.

(Fig. 10.10b), bubble [44](Fig. 10.10c) and rotary drum (nanospider, Fig. 10.11) [45] electrospinning systems have been proposed. In contrast to the needle-based multiple-jet electrospinning systems, there are no needle arrays in these setups. The mechanism is based on electrohydrodynamic (EHD) induced fluctuations on top of free surfaces from a thin layer of solution to create artificial liquid jets for electrospinning [43, 46]. Based on a detailed analysis of a dispersion law, Lukas *et al.* [43] made a hypothesis to explain the needleless electrospinning mechanism: above a certain critical value of applied electric field intensity/field strength the system starts to be self-organized in the mesocopic scale due to the mechanism of the "fastest forming instability," according to which there is a particular wave with a characteristic wavelength whose amplitude

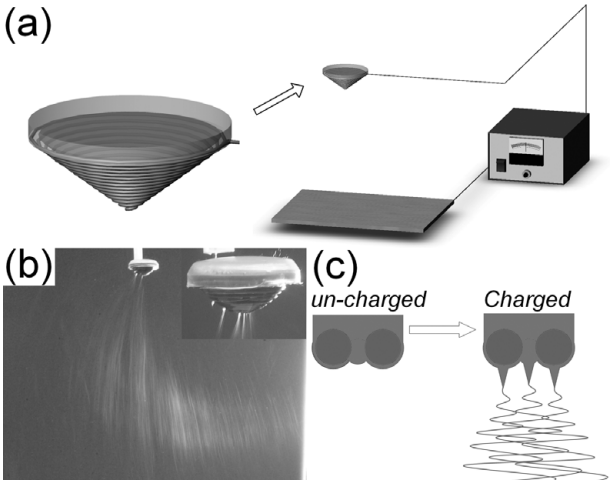

Fig. 10.9 Conical wire electrospinning [41].

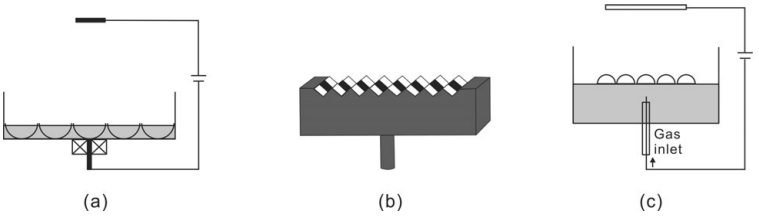

Fig. 10.10 (a) Multiple spikes; (b) mulitiple clefts; and (c) bubble spinning.

boundlessly grows faster than the others, resulting in a fastest growing stationary wave. From the free liquid surface of this wave, crests jets originate and nanofibers are obtained. In multiple-spike setup, a magnetic field and a metal-spike complex is involved to help jet origionation. A multiple-cleft setup has a setup of clefts as well. Rotary drum and bubble system are, on the contrary, trying to initiate the "wave jets" through the drum or by blowing bubbles. Compared with needle systems, needleless electrospinning does not have the issues brought by needles. However, these systems have their own problems. The involvement of free surface enlarges the diameter variation and the evaporation of solvent in the container is accelerated since all the systems are open.

Apart from the spinning setup, collecting uniform nanofiber nonwovens or aligned continuous nanofiber assemblies are challenges that have to be conquered before electrospun nanofiber products can be industrially applied. Owing to the intrinsic instability of the electrospinning process and the interference among jets, it is very hard to control the deposition of nanofibers, much less a uniform membrane or an aligned nanofiber assemblies. Two main routes have been followed for controllable fiber collection: control of the instability of jet by replacing D.C. potentials with an A.C. one [47], or using an A.C. biased D.C. potential [48] (Fig. 10.12a), applying one [37, 49, 50] or more auxiliary electric fields [51] (Fig. 10.12b) or magnetic field [52, 53] (Fig. 10.12c) to the jet; or

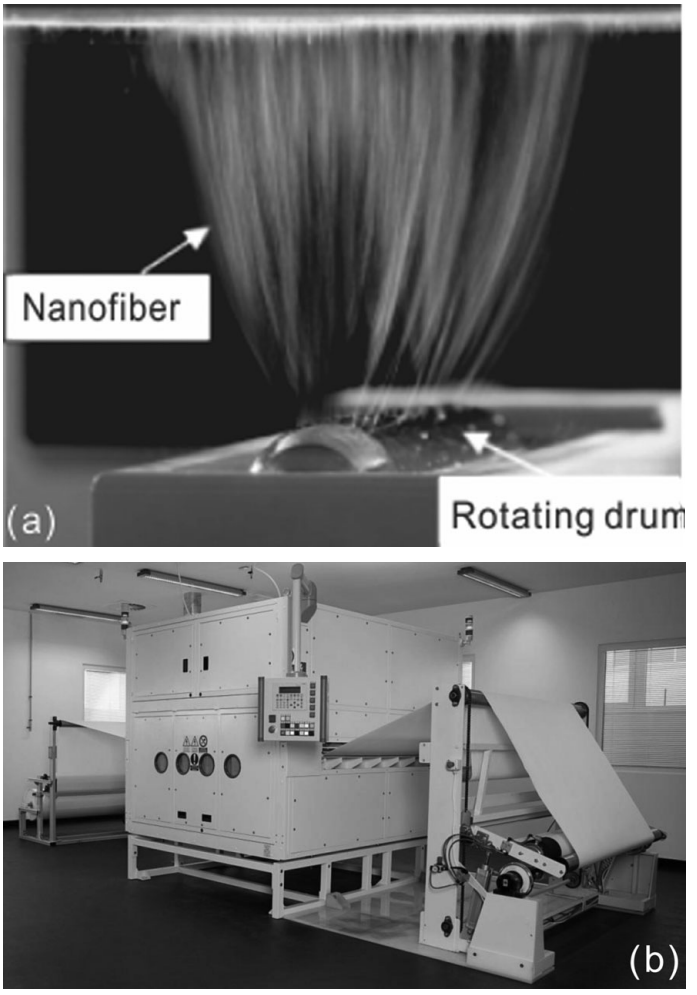

Fig. 10.11 Scale-up needleless electrospinning system – Nanospider: (a) the Nanospider™ electrospinning line and (b) a Nanospider machine [45].

shrink the jet depositing spot to a sharp edge or point with specially designed collectors. Reduced jet instability means decreased stretching on the jet and therefore increased fiber diameters, which is not favorable for nanofibers, although they do show their potential in gaining stable deposition. High-speed rotary collectors [54, 55] or multiple-electrode array [56–58] collectors, as shown in Fig. 10.13, have demonstrated their capability of collecting aligned fiber bundles. So far, the high-speed disk [59], as an extreme example of high-speed rotary collectors, is believed to be the most effective device for aligned nanofiber bundles. However, a high-speed disk can only collect a very limited amount of aligned nanofibers. As a matter of fact, most of the collection designs except the rotary collectors with large width are designated to one needle electrospinning setup, which means a scale-up of electrospinning equipment would be beyond their working scope.

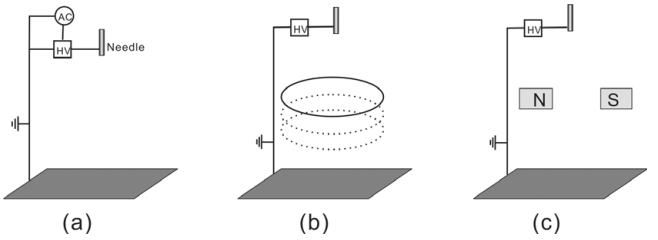

Fig. 10.12 (a) A.C. biased D.C. potentials, (b) electric field auxiliary collection, and (c) magnetic field assisted collection.

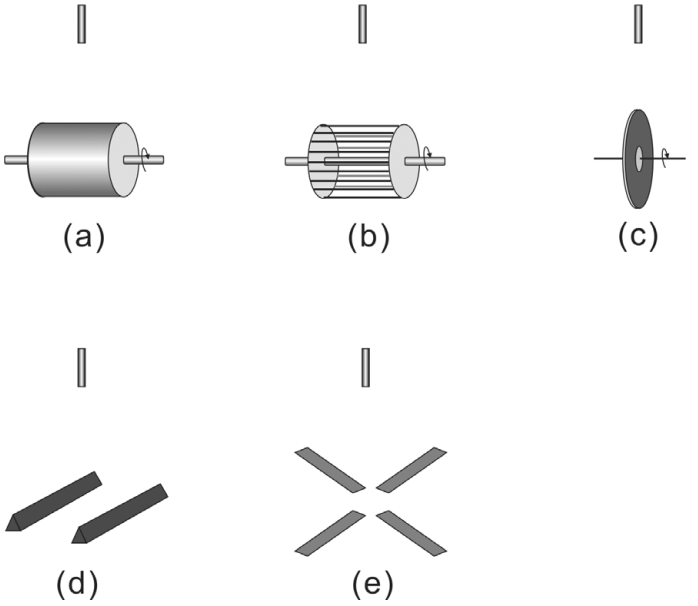

Fig. 10.13 (a) High-speed drum; (b) high-speed frame; (c) high-speed disk; (d) parallel electrodes; and (e) counter electrodes.

Thus collectors that are not only good at dealing with jet instablilty but suitable for collection of large amount of fibers need to be designed.

No matter whether they are aligned or not, fibers obtained from these collectors mentioned above are in the form of membranes unless the collection time is very short. There is strong demand for continuous aligned fiber bundles for further manufacturing. Ko's group specifically addressed the implementation of a modified drum electrospinning process for production of continuous nanofiber assemblies, as shown in Fig. 10.14 [60]. A continuous aluminium slit was wrapped around the drum as a collector. After a period of accumulation, the slit was unwrapped and fibers bundles were obtained by being peeled off the slit. Fiber bundles with length up to 2.5 m were produced using this process. These fiber bundles was shown can be twisted up to 3.48 twist per inch (tpi). After twisting, the alignment of the nanofibers in the yarn was greatly increased, as

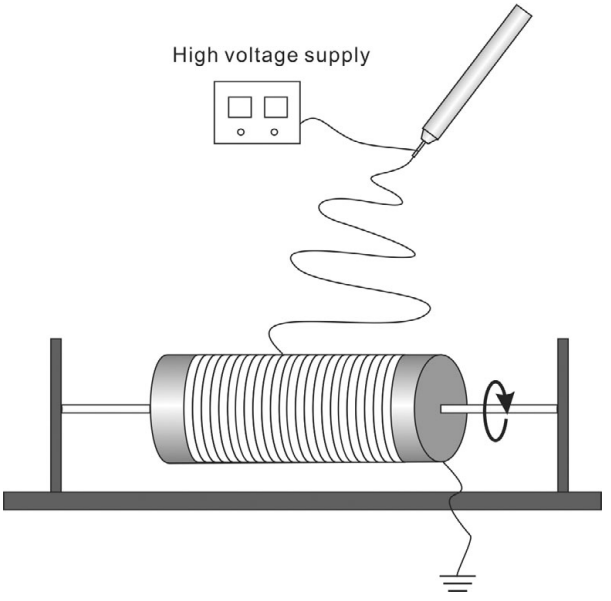

Fig. 10.14 Modified drum electrospinning process for continuous CNT yarns [60].

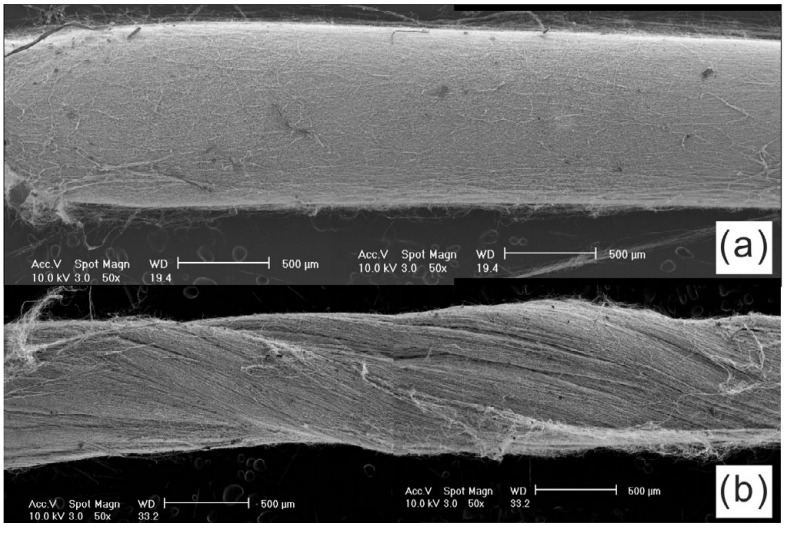

Fig. 10.15 Composite ESEM image of continuous yarn: (a) 700 untwisted yarn, and (b) 350 denier 3.48 tpi yarn [60].

shown in Fig. 10.15. The disadvantage of this method is the arbitrary separation of the fiber bundles. Fibers may be broken if they are deposited upon more than one turn of the slit.

From the point of view of the textile industry, electrospinning is two-free-end spinning. People have no control on the initiation of the jet or on the deposition. The

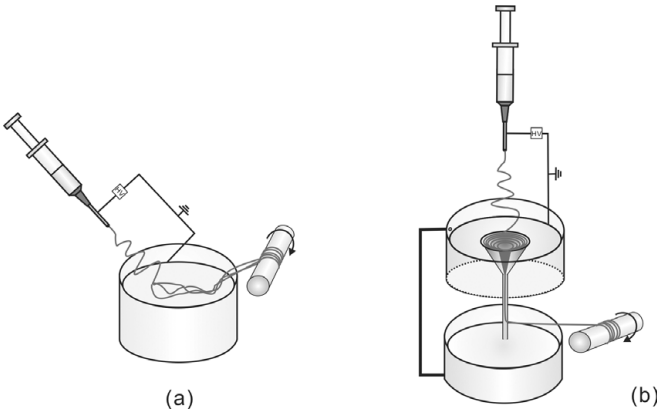

Fig. 10.16 (a) Liquid and (b) water vortex collection of continuous uniaxial electrospun nanofibers.

"invisible" size of the fiber from electrospinning makes people feel uncertain. A visible and manipulatable medium that could be of help in controlling the motion of nanofibers is desired, which stands out from a liquid support system. Smit *et al.* [61] and Khil *et al.* [62] demonstrated that by spinning nanofibers onto a water or coagulant reservoir and drawing the resulting nonwoven web of fibers across the liquid, continuous uniaxial fiber bundles of yarns can be obtained, as shown in Fig. 10.16a. In a further step, a water vortex [63] was employed for a continous twisted uniaxial fiber yarn, as shown in Fig. 10.16b. A theoretical production rate of such a collector is 180 m of yarn per hour for a single needle electrospinning setup, which is very promising. However, the yarn diameter variation is very large and fibers could adhere and coalesce if they are bundled before they are fully solidified.

10.3.4 Structural property improvement

In order to pursue novel structured nanofibers, core–shell spinning, side-by-side spinning and polymer-blend electrospinning techniques have been invented. Post-treatments, aiming at altering the nanofiber web structure, such as cross-linking, surface chemical functionalization, coating and heat treatment, have been applied. These techniques not only pave the way for brilliant multifunctional nanofibers but also diversify the types of nanofibers and broaden the applicability of elelctrospun nanofibers.

However, weakness is one of the key problems facing electrospun nanofiber products and hindering further development of electrospinning, and we are waiting for this to be solved. As previously mentioned, electrospinning cannot be applied to highly viscous solutions because it is impossibile for the weak electric force to overcome the high surface tension; the highly unstable whipping motion of the electrospinning jet is inevitable due to the uneven distribution of electrical charge in and on the surface of the jet. These two characteristics destin electrospun nanofibers to have a loose

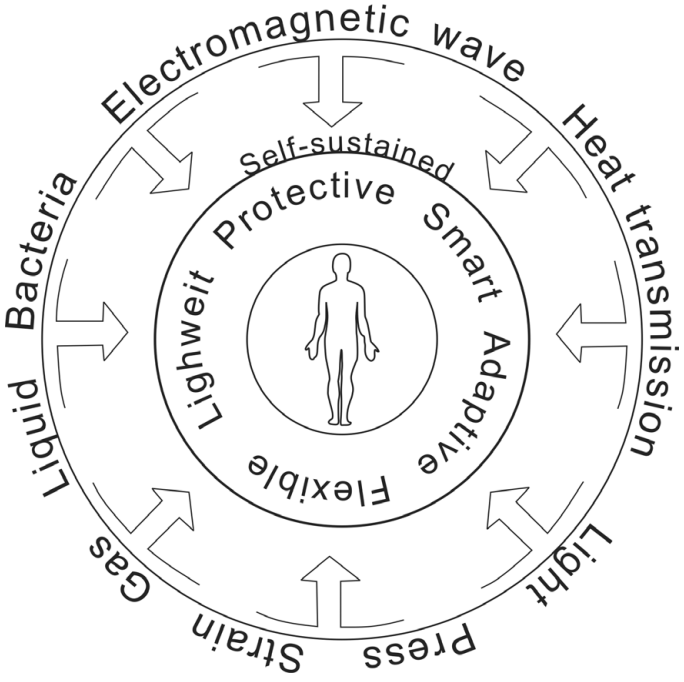

Fig. 10.17 The concept of intelligent clothes.

molecular chain arrangement in the structure, which has barely any crystallines and lack of orientation, and hence high proportion of defects and fragility of the fibers. To address the problem ultrasonic-vibration-electrospinning has been invented. Using this setup, electrospinning of high viscous polymer solutions was achieved [64] and a hint of improvement of the crystallization structure of nanofibers was also found [65]. Aside from this progress, no further report relating to significant improvement of mechincal properties of nanofibers has been published.

Therefore, to conquer the bottleneck of electrospinning and propel practical applications of electrospun nanofibers, both theoretical analysis and practical studies on structure improvement of electrospun nanofibers need to be extensively conducted and untimately solved.

10.4 New frontiers

Developments in electrospinning technology as well as all types of electrospun nanofibers provide fresh opportunities for the development of innovative nanostructured materials. Combination of nanofibers and nanotechnology has brought the novel concepts of "smart skin," or "intelligent clothes," which could perform with comprehensive functions such as being lightweight, protective, smart and adaptive. Figure 10.17 illustrates the concept of intelligent clothes.

Nanofibers and nanofiber-reinforced nanocomposites possess the advantange of being lightweight since they are composed of polymers, perform with nanoeffects and require less content of functional particles.

Nanofiber products are protective and wearable since the nanoscale dimension endow the nanofibers with high surface-to-volume aspect ratio, high porosity, high surface activity and high flexibility. High surface-to-volume aspect ratio, high porosity and surface activity provide effective and efficient protection from nuclear, biological or chemical (NBC) threats. Small diameter and abundant small pores allow the passage of water vapor. High flexibility makes the products feel comfortable and allows then to move with one's motion.

Functionalized nanofibers are intelligent and can act as gas, pressure, light, electromagnetic wave and thermal sensors. When the sensors are attached to, or emebedded in, electroconductive nanofiber networks, the environmental or one's body signal can be collected and sent away for monitoring. Clothes equipped with such intelligent components will be smart in signal capture and transmittance.

When phase-change materials are used during fabrication of nanofibers, those nanofibers can be adapted for changing conditions. For instance, when the air temperature becomes lower than the standardized one, the thermal sensor "feels" cold and sends a signal to the adaptive components; then the energy-storage phase-change material in the nanofiber will be activated, melt and hence heat one's body up. If blood-sensitive material and blood sealant are present in nanofibers, then the nanofibers will automatically seal a wound when blood immerses the nanofibers.

Furthermore, nanofibers can be designed as solar cells or motion power generators, which means clothes armed with such energy-generating components will be self-sustained, and the smart components will run with no restriction of power.

All the components involved with this "smart skin"concept have been expolored. Astonishing achievements have proved that electrospinning is a versatile and strong technique. And it is apparent that there will be many more possibilities beyond image. Therefore exploration and investigation should be continued to exploit more techniques, more products and hence wider applications.

References

1. M. C. Roco, C. A. Mirkin, and M. C. Hersam, *Nanotechnology research directions for societal needs in 2020*. Wtec, 2011.
2. R. Smalley, "Future global energy prosperity: the terawatt challenge," *MRS Bulletin*, vol. 30 (6), pp. 412–424, 2005.
3. Y. S. Kim, *et al*., "Electrospun bimetallic nanowires of PtRh and PtRu with compositional variation for methanol electrooxidation," *Electrochemistry Communications*, vol. 10(7), pp. 1016–1019, 2008.
4. P. Schechner, *et al*., "Silver-plated electrospun fibrous anode for glucose alkaline fuel cells," *Journal of The Electrochemical Society*, vol. 154(9), pp. B942–B948, 2007.

5. H. J. Kim, *et al*., "Highly improved oxygen reduction performance over Pt/C-dispersed nanowire network catalysts," *Electrochemistry Communications*, vol. 12(1), pp. 32–35, 2010.
6. M. Li, *et al*., "Electrospinning-derived carbon fibrous mats improving the performance of commercial Pt/C for methanol oxidation," *Journal of Power Sources*, vol. 191(2), pp. 351–356, 2009.
7. J.-H. Park, *et al*., "Effects of electrospun polyacrylonitrile-based carbon nanofibers as catalyst support in PEMFC," *Journal of Applied Electrochemistry*, vol. 39(8), pp. 1229–1236, 2009.
8. S. W. Choi, *et al*., "Nafion-impregnated electrospun polyvinylidene fluoride composite membranes for direct methanol fuel cells," *Journal of Power Sources*, vol. 180(1), pp. 167–171, 2008.
9. J. R. Kim, *et al*., "Electrospun PVdF-based fibrous polymer electrolytes for lithium ion polymer batteries," *Electrochimica Acta*, vol. 50(1), pp. 69–75, 2004.
10. A. Subramania, and S. L. Devi, "Polyaniline nanofibers by surfactant-assisted dilute polymerization for supercapacitor applications," *Polymers for Advanced Technologies*, vol. 19(7), pp. 725–727, 2008.
11. C. Kim, *et al*., "Characteristics of supercapaitor electrodes of PBI-based carbon nanofiber web prepared by electrospinning," *Electrochimica Acta*, vol. 50(2–3), pp. 877–881, 2004.
12. M. Y. Song, *et al*., "Electrospun TiO2 electrodes for dye-sensitized solar cells," *Nanotechnology*, vol. 15(12), pp. 1861–1865, 2004.
13. G. Hu, *et al*., "Anatase TiO 2 nanoparticles/carbon nanotubes nanofibers: preparation, characterization and photocatalytic properties," *Journal of Materials Science*, vol. 42(17), pp. 7162–7170, 2007.
14. S. Aryal, *et al*., "Multi-walled carbon nanotubes/TiO2 composite nanofiber by electrospinning," *Materials Science and Engineering: C*, vol. 28(1), pp. 75–79, 2008.
15. K. Fujihara, *et al*., "Spray deposition of electrospun TiO2 nanorods for dye-sensitized solar cell," *Nanotechnology*, vol. 18(36), p. 365709, 2007.
16. M. Y. Song, *et al*., "Enhancement of the photocurrent generation in dye-sensitized solar cell based on electrospun TiO_2 electrode by surface treatment," *Synthetic Metals*, vol. 155(3), pp. 635–638, 2005.
17. K. Schaefer, *et al*., *Nano-Fibres for Filter Materials, in Multifunctional Barriers for Flexible Structure*. Berlin, Heidelberg: Springer, p. 125–138, 2007.
18. G. Andreev, *et al*., "Nanotechnology-derived materials: potential risk in preparation and use," *Russian Journal of General Chemistry*, vol. 79(9), pp. 1974–1981, 2009.
19. H.-W. Li, *et al*., "Removal and retention of viral aerosols by a novel alumina nanofiber filter," *Journal of Aerosol Science*, vol. 40(1), pp. 65–71, 2009.
20. N. Lala, *et al*., "Fabrication of nanofibers with antimicrobial functionality used as filters: protection against bacterial contaminants," *Biotechnology and Bioengineering*, vol. 97(6), pp. 1357–1365, 2007.
21. Y. Xia, "Nanomaterials at work in biomedical research," *Nat Mater*, vol. 7(10), pp. 758–760, 2008.
22. Y. M. Shin, *et al*., "Electrospinning: a whipping fluid jet generates submicron polymer fibers," *Applied Physics Letters*, vol. 78(8), pp. 1149–1151, 2001.
23. A. F. Spivak, Y. A. Dzenis, and D. H. Reneker, "A model of steady state jet in the electrospinning process," *Mechanics Research Communications*, vol. 27(1), pp. 37–42, 2000.
24. A. F. Spivak, and Y. A. Dzenis, "Asymptotic decay of radius of a weakly conductive viscous jet in an external electric field," *Applied Physics Letters*, vol. 73(21), pp. 3067–3069, 1998.

25. Y. M. Shin, *et al*., "Experimental characterization of electrospinning: the electrically forced jet and instabilities," *Polymer*, vol. 42(25), pp. 09955–09967, 2001.
26. M. M. Hohman, *et al*., "Electrospinning and electrically forced jets. I. Stability theory," *Physics of Fluids*, vol. 13(8), pp. 2201–2220, 2001.
27. Y. Q. Wan, Q. Guo, and N. Pan, "Thermo-electro-hydrodynamic Model for Electrospinning Process," *International Journal of Nonlinear Sciences and Numerical Simulation*, vol. 5(1), pp. 5–8, 2004.
28. J. H. He, Y. Q. Wan, and J. Y. Yu, "Allometric scaling and instability in electrospinning," *International Journal of Nonlinear Sciences and Numerical Simulation*, vol. 5, pp. 243–252, 2004.
29. J. Deitzel, *et al*., *Generation of polymer nanofibers through electrospinning*, Army Research Lab Aberdeen Proving Ground Md., 1999.
30. D. R. Salem, Electrospinning of nanofibers and the charge injection methods, in *Nanofibers and Nanotechnology in Textiles*, ed. P. J. Brown and K. Stevens, ed., Cambridge, England: Woodhead Publishing Limited, 2007.
31. Y. Yamashita, *et al*., "Establishment of nanofiber preparation technique by electrospinning," *Sen'i Gakkaishi*, vol. 64(1): pp. 24–28, 2008.
32. J. S. Varabhas, G. G. Chase, and D. H. Reneker, "Electrospun nanofibers from a porous hollow tube," *Polymer*, vol. 49(19), pp. 4226–4229, 2008.
33. A. Varesano, R. A. Carletto, and G. Mazzuchetti, "Experimental investigations on the multi-jet electrospinning process," *Journal of Materials Processing Technology*, vol. 209(11), pp. 5178–5185, 2009.
34. S. A. Theron, *et al*., "Multiple jets in electrospinning: experiment and modeling." *Polymer*, vol. 46(9), pp. 2889–2899, 2005.
35. Y. Yang, *et al*. *Electrospun Uniform Fibres with a Special Regular Hexagon Distributed Multi-needles System*. IOP Publishing, 2008.
36. W. Tomaszewski, and M. Szadkowski, "Investigation of electrospinning with the use of a multi-jet electrospinning head," *Fibres & Textiles in Eastern Europe 2005*. 13(4): p. 22–26, 2005.
37. G. Kim, Y.-S. Cho, and W. D. Kim, "Stability analysis for multi-jets electrospinning process modified with a cylindrical electrode," *European Polymer Journal*, vol. 42(9), pp. 2031–2038, 2006.
38. A. Varesano, *et al*., "Multi-jet nozzle electrospinning on textile substrates: observations on process and nanofibre mat deposition," *Polymer International*, 2010. **DETAILS**?
39. O. O. Dosunmu, *et al*., "Electrospinning of polymer nanofibers from mulitple jets on a porous tubular surface," *Nanotechnology*, vol. 17, p. 1123, 2006.
40. B. Lu, *et al*., "Superhigh-throughput needleless electrospinning using a rotary cone as spinneret," *Small*, vol. 6(15), pp. 1612–1616, 2010.
41. X. Wang, *et al*., "Needleless electrospinning of nanofibers with a conical wire coil," *Polymer Engineering & Science*, vol. 49(8), pp. 1582–1586, 2009.
42. A. L. Yarin, and E. Zussman, "Upward needleless electrospinning of multiple nanofibers," *Polymer*, vol. 45, p. 2977, 2004.
43. D. Lukas, A. Sarkar, and P. Pokorny, "Self-organization of jets in electrospinning from free liquid surface: a generalized approach," *Journal of Applied Physics*, vol. 103(8), p. 084309–7, 2008.
44. Y. Liu, and J. He, "Bubble electrospinning for mass production of nanofibers," *International Journal of Nonlinear Sciences and Numerical Simulation*, vol. 8(3), p. 393, 2007.

45. S. Petrik, and M. Maly. *Production Nozzle-Less Electrospinning Nanofiber Technology. in 2009 Fall MRS Symposium*. Boston, MA, 2009.
46. D. Wu, *et al*., High throughput tip-less electrospinning via a circular cylindrical electrode," *Journal of Nanoscience and Nanotechnology*, vol. 10(7), pp. 4221–4226, 2010.
47. R. Kessick, J. Fenn, and G. Tepper, "The use of AC potentials in electrospraying and electrospinning processes," *Polymer*, vol. 45(9), pp. 2981–2984, 2004.
48. S. Sarkar, S. Deevi, and G. Tepper, "Biased AC electrospinning of aligned polymer nanofibers," *Macromolecular Rapid Communications*, vol. 28(9), pp. 1034–1039, 2007.
49. L. Buttafoco, *et al*., "Electrospinning of collagen and elastin for tissue engineering applications," *Biomaterials*, vol. 27(5), pp. 724–734, 2006.
50. J. J. Stankus, J. Guan, and W. R. Wagner, "Fabrication of biodegradable elastomeric scaffolds with sub-micron morphologies," *Journal of Biomedical Materials Research Part A*, vol. 70A(4), pp. 603–614, 2004.
51. J. M. Deitzel, *et al*., "The effect of processing variables on the morphology of electrospun nanofibers and textiles," *Polymer*, vol. 42(1), pp. 261–272, 2001.
52. Y. Wu, *et al*., "Controlling stability of the electrospun fiber by magnetic field," *Chaos, Solitons and Fractals*, vol. 32(1), pp. 5–7, 2007.
53. D. Yang, *et al*., "Fabrication of aligned fibrous arrays by magnetic electrospinning," *Advanced Materials*, vol. 19(21), pp. 3702–3706, 2007.
54. J. Matthews, *et al*., "Electrospinning of collagen nanofibers," *Biomacromolecules*, vol. 3(2), pp. 232–238, 2002.
55. P. Katta, *et al*., "Continuous electrospinning of aligned polymer nanofibers onto a wire drum collector," *Nano Letters*, vol. 4(11), pp. 2215–2218, 2004.
56. D. Li, Y. Wang, and Y. Xia, "Electrospinning of polymeric and ceramic nanofibers as uniaxially aligned arrays," *Nano Letters*, vol. 3(8), pp. 1167–1171, 2003.
57. Q. Zhang, *et al*., "Electrospun carbon nanotube composite nanofibres with uniaxially aligned arrays," *Nanotechnology*, vol. 18(115611): p. 115611, 2007.
58. W. E. Teo, and S. Ramakrishna, "Electrospun fibre bundle made of aligned nanofibres over two fixed points," *Nanotechnology*, vol. 16(9), p. 1878, 2005.
59. A. Theron, *et al*., "Electrostatic field-assisted alignment of electrospun nanofibres," *Nanotechnology*, vol. 12(3), p. 384, 2001.
60. R. Foedinger, *et al*., High strength nanomaterials fiber for lightweight composite missile cases, in *230th ACS National Meeting*. Washington, DC, USA, 2005.
61. E. Smit, U. Buttner, and R. D. Sanderson, "Continuous yarns from electrospun fibers," *Polymer*, vol. 46(8), pp. 2419–2423, 2005.
62. M.-S. Khil, *et al*., "Novel fabricated matrix via electrospinning for tissue engineering," *Journal of Biomedical Materials Research*, vol. 72B(1), pp. 117–124, 2005.
63. W.-E. Teo, *et al*., "A dynamic liquid support system for continuous electrospun yarn fabrication," *Polymer*, vol. 48(12), pp. 3400–3405, 2007.
64. Y. Q. Wan, *et al*., "Electrospinning of high molecule PEO solution," *Journal of Applied Polymer Science*, vol. 103(6), pp. 3840–3843, 2007.
65. Y. Q. Wan, J. H. He, and J. Y. Yu, "Carbon nanotube-reinforced polyacrylonitrile nanofibers by vibration-electrospinning," *Polymer International*, vol. 56(11), pp. 1367–1370, 2007.

Appendix I Terms and unit conversion

Terms for structure character

Cotton count (N_e) The number of pieces of fibers/yarns, 840 yards long needed to make up 1 lb weight. Hence 10 count cotton means that 10 × 840 yards weighs 1lb.

Denier A unit measuring the linear mass density of fibers/yarns. It is defined as the mass in grams per 9000 m. 1 denier = 1 g/9000 m.

Dtex decitex, the mass in grams per 10 000 m.

Engineering stress A measure of the average force per unit area of a surface.

Metric count (N_m) The number of pieces of fibers/yarns of 1 m long to make up 1 g weight.

Specific area (Asp) Area per unit bulk volume. For a fiber, Asp (cm^2) = Denier/(9 × 105 × ρ).

Specific stress (σ_{sp}) The force per unit linear density. It is more useful for fibres and is the usual mode in the textile community: $\sigma_{sp} = N$/tex.

Specific stress for textile The fore force per areal density divided by width.

Tenacity the length of a fiber/yarn falling under its own weight.

Tex A unit measuring the linear mass density of fibers/yarns. It is defined as the mass in grams per 1000 m.
$TPI = TM \times \sqrt{count}$, where TM is the twist multiplier, also known as K or the twist factor. This twist multiplier is an empirical parameter that has been established by experiments and practice that the maximum strength of a yarn is obtained for a definite value of K.

Twist Measures the twist degree of a yarn, the number of twists applied to a yarn in one unit length(1 inch, tpi/1 meter, m^{-1}).

Unit conversion

dTex = 10 × Tex = 1.11 × Denier
Tex = 0.11 × Denier = 0.1 × Tex = 590.5 / N_e = 1000 / N_m
Denier = 9 × Tex = 0.9 × dTex = 5315 / N_e = 9000 / N_m

Twist factor = Turns/cm × $(\text{Tex})^{1/2}$ = 9.57 × TPI / $(\text{Ne})^{1/2}$
1 N/tex = 1 GPa / ρ (g/cm^3)
1 N/tex = 1 kJ.g = $1(km/s)^2$ = 10.2 g/dtex = 11.3 g/denier
1 g/denier = 0.88 N/tex
1 N/tex = 102 km = 3.94×10^6 inch= 145000 psi/(g/cm^3)
1 GPa = 102 kg/mm^2 = 145,000 psi = 10^4 bar = 10000 kg/cm^2
1psi = g/denier × 12800 × ρ

Diameter and linear density

$$d(\text{m}) = \sqrt{\frac{4}{\pi}\left(\frac{Denier}{9 \times 10^9 \times \rho}\right)}$$

$$d(\text{cm}) = \sqrt{\frac{4}{\pi}\left(\frac{Denier}{9 \times 10^5 \times \rho}\right)}$$

$$d(\text{in}) = \sqrt{\frac{4}{\pi}\left(\frac{Denier}{58 \times 10^5 \times \rho}\right)}$$

$$d(\text{mil}) = \sqrt{\frac{4}{\pi}\left(\frac{Denier}{58 \times 10^{11} \times \rho}\right)}$$

Appendix II Abbreviation of polymers

Abbreviation	Polymer
DNA	Deoxyribonucleic acid
PA	polyamide (nylon)
PAA	poly acetic acid
PAI	polyamide-imide
PAEK	polyaryletherketone
PAK	polyester alkyd
PAL	polyanaline
PAN	polyacrylonitrile
PANI	polyaniline
PARA	polyaryl amide
PAS	polyarylsulfone
PB	polubutylene
PBAN	polybutadiene acrylonitrile
PBD	polybutadine
PBI	polybenzimidazole
PBN	polybutylene napthalate
PBS	polybutadiene styrene
PBT	polybutylene terephthalate
PC	polycarbonate
PC/ABS	polycarbonate/acrylonitrile butadiene styrene blend
PCL	polycaprolactone
PCT	polycyclohexylene terephthallate
PCT-G	glycol modified polycyclohexyl terephthallate
PCTFE	polymonochlorotrifluoroethylene
PDLA	poly(D,L-lactic acid)
PE	polyethylene
PEBA	polyether block amide or polyester block amide
PEEK	polyetheretherketone
PEI	polyetherimide
PEK	polyetherketone
PEKEKK	polyetherketone etherketone ketone
PEKK	polyetherketoneketone
PEN	polyethylene napthalene
PEO	polyethylene oxide
PES	polyethersulfone
PET	polyethylene terephthalate
PET-G	glycol modified polyethylene terephthalate

(cont.)

Abbreviation	Polymer
PFA	perfluoroalkoxy
PI	polyimide
PI	polyisoprene
PIB	polyisobutylene
PIR	polyisocyanurate
PLA	polylactic acid
PLLA	poly(L-lactic acid)
PMAN	polymethactylonitrile
PMMA	polymethylmethacrylate (acrylic)
PMP	polymethylpentene
PMS	paramethylstyrene
PO	polyolefin
POM	polyoxymethylene (acetal)
PP	polypropylene
PPA	polyphthalamide
PPC	chlorinated polypropylene
PPC	polyphthalate carbonate
PPE	polyphenylene ether
PPI	polymeric polyisocyanate
PPO	polyphenylene oxide
PPOX	polypropylene oxide
PPS	polyphenylene sulfide
PPSU	polyphenylene sulfone
PPT	polypropylene terephthalate
PS	polystyrene
PS-b-PI	polystyrene/polyisoprene block copolymer
PSO, PSU	polysulfone
PTFE	polytetrafluoroethylene
PTMT	polytetramethylene terephthalate
PU,PUR	polyurethane
PUU	polyurethaneurea
PVA	polyvinyl alcohol (sometimes polyvinyl acetate)
PVAc	polyvinyl acetate
PVB	polyvinyl butyryl
PVC	polyvinyl chloride
PVCA	polyvinyl chloride acetate
PVDA	polyvinylidene acetate
PVDC	polyvinylidene chloride
PVDF	polyvinylidene fluoride
PVF	polyvinyl fluoride
PVK	polyvinyl carbazole
PVOH	polyvinyl alcohol
PVP	polyvinyl pyrrolidone
SBSa	styrene–butadiene–styrene triblock copolymer

Appendix III Classification of fibers

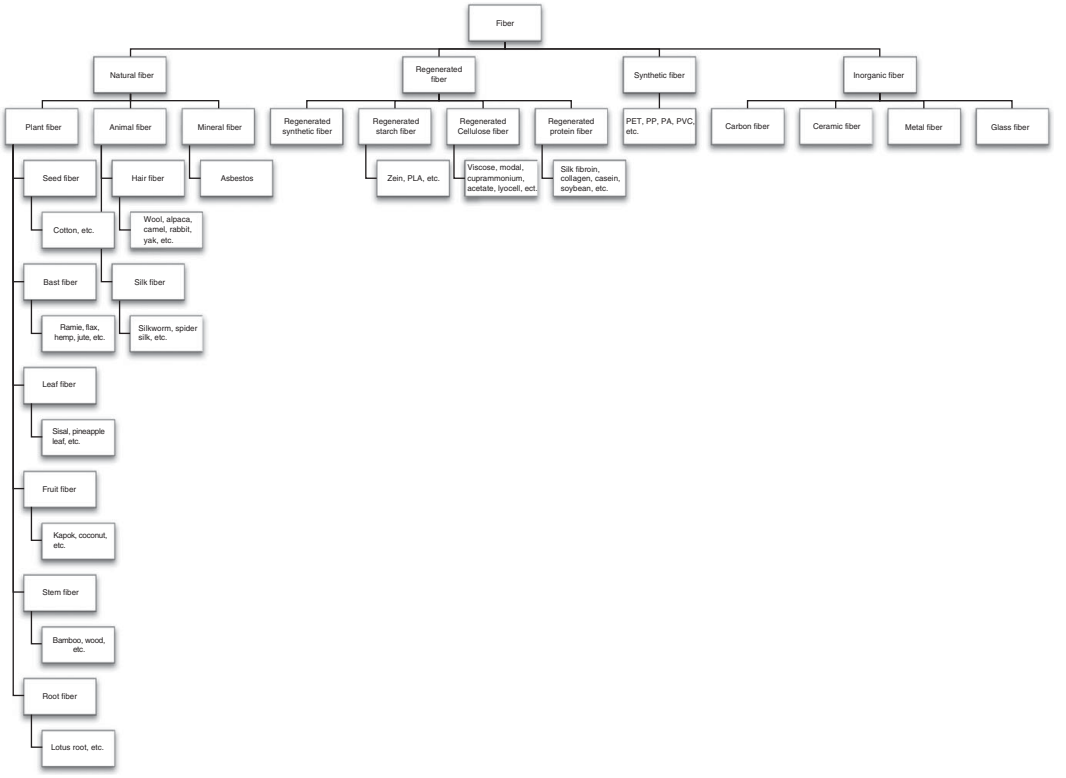

Appendix IV Polymers and solvents for electrospinning

1 Natural polymers

Cellulose	lithium chloride (LiCl, 8%)/*N*,*N*-dimethyl acetamide (DMAc)
	N-methylmorpholine oxide (NMMO)/water = 85/15
Cellulose acetate	Acetic acid/ acetone = 3/1
	Acetic acid/DMAc = 2/1,3/1,5/1,10/1
Ethyl cellulose	Tetrahydrofuran (THF)/dimethylacetamide (DMAc) = 100/0, 60/40, 50/50
Chitin	1,1,1,2,2,2-hexafluoro-2-propanol (HFIP)
Chitosan	90% acetic acid
	Trifluoroacetic acid (TFA)
	TFA /dichloromethane (MC) = 90/10, 80/20, 70/30
Collagen	1,1,1,2,2,2-hexafluoro-2-propanol (HFIP)
Dextran	water
	Dimethyl sulfoxide (DMSO)/ *N*,*N*-dimethyl formamide (DMF) = 60:40
DNA	Water:ethanol 7:3
Alpha-elastin	1,1,1,3,3,3-hexafluoro-2-propanol (HFP)
Gelatin	2,2,2-trifluorothanol
Hyaluronic acid (HA)	acidic aqueous solution (pH = 1.5)
Tropoelastin	1,1,1,3,3,3-hexafluoro-2-propanol (HFP)
Silk fibroin	98% formic acid
	hexafluoroacetone trihydrate/ HFA·3H_2O
Spider silk fibroin	formic acid
Zein	ethanol/water = 70/30, 80/20, 90/10

2 Synthetic polymers

Polymer	Solvent
Nylon 6	1,1,1,3,3,3-hexa-fluoro-2-propanol (HFIP)
	1,1,1,3,3,3-hexa-fluoro-2-propanol (HFIP)/*N*,*N*-dimethyl formamide (DMF) = 95/5
PAA	ethanol/water = 40/60
PAN	dimethylformamide (DMF)
PBI	*N*,*N*-dimethylacetamide, lithium chloride (4%)
PC	dichloromethane
	THF/DMF = 100:0, 70/30, 60/40
PCL	chloroform
	acetone
	methylene chloride (MC)/ dimethylformamide (DMF) = 40/60
	chloroform/methanol
PDLA	dimethyl formamide
PE	dichloromethane/trifluoroacetic acid = 1/1
	p-xylene
PEO	water
	water/ethanol = 60/40
PET	trifluoroacetic acid
PLA	chloroform: acetone 2:1
	N,*N*-dimethyl formamide (DMF)
PLLA	dichloromethane
P(LLA-CL)	acetone
PLGA	*N*,*N*-dimethyl formamide (DMF)
PMMA	dimethylformamide/toluene=90/10
PMMA-r-TAN	dimethylformamide/toluene=90/10
PPy	chloroform with DBSA
MEH-PPV	1,2-dichloroethane
PS	dimethylformamide
PSU	pyridine
PTT	Trifluoroacetic acid (TFA) /methylene chloride (MC) = 50/50
PU	*N*,*N*-Dimethyl formamide
	tetrahydrofuran (THF)/ethanol = 50/50
	N,*N*-dimethylformamide: tetrahydrofuran
PUU	dimethyl formamide
PVA	water
	acetone
	methylene chloride(MC)/ dimethylformamide (DMF) = 75/25, 40/60
PVK	dichloromethane
PVP	ethanol
	2-propanol
SBS	tetrahydrofuran/dimethylformamide = 3/1

Index

alignment 205
  composite slicing 207
  electric field 206
  electrospinning 208
  film rubbing 207
  liquid crystal solution 206
  magnetic field 205
  mechanical stretching 207
amorphous 27
  differential scanning calorimetry 131
applications 47
applied voltage 52
atomic force microscopy 108, 125

battery 242
bioactive nanofiber 148
boiling point 55

carbon nanofiber 223
carbon nanotube 192
carbon nanotube fiber 209–210
  chemical vapor deposition 210
  electrospinning 214
  liquid crystal spinning 212
  solid-state spinning 212
  traditional spinning 214
  wet spinning 213
challenge 244
characterization 102
  bioactivity 161
  degradation 163
  electrical conductivity 136
  magnetic properties 140
  tissue compatibility 163
concentration 50
configuration 25
conformation 25
conservation laws 67
contact angle 134
covalent functionalization 201
cross-linking 26
crystal structure 27
  differential scanning calorimetry 131

dielectric constant 57
differential scanning calorimetry 131
dispersion 197
drug delivery 61, 156–157, 244
dye-sensitized solar cell 243

electrical conductivity 53
electrical-active nanofiber 62
electroactive nanofiber 170
  conductive 167
  magnetic nanofiber 179
  PAn.HCSA 171
  photonic 182
  Poly(3,4-ethylenedioxythiophene)(PEDOT) 172
  polyaniline 171
  superior electrical conductivity 169
  supermagnetic nanofiber 180
  supermagnetism 179
electrolyte 242
electrospinning 49
electrospinning mechanism 65, 244
electrospinning process 49
EMI shielding 180
energy 242

feeding rate 57
fiber formation 39
fiber properties 40
  process 43
  structure 40
  theoretic modulus 82
fiber size 7
filtration 60, 115, 243
formation of nanofibers 45
  chemical vapour deposition 45
  conjugate spinning 45
  drawing 47
  electrospinning 49
  meltblown technology 47
  phase separation 46
  self-assembly 47
  template synthesis 47
four-element model 21

Fourier transform infra-red spectroscopy 116
fuel cell 242

graphite nanoplatelet 220

heterogeneity 14
historical development of nanotechnology 2
humidity 56
hydrogen bonding 24

intrinsic viscosity 36

linear kinetics 14

Maxwell model 17
measurement of order and disorder 29
mechanical dispersion 199
  ball milling 200
  high shear stress 200
  ultrasonication 199
mechanical testing 125
  microtensile testing 123
medical prostheses 61
melt electrospinning 58
melt spinning 39
mercury porosimetry 115
modeling
  jet 68
  one-dimensional (1-D) model 70
  parametric analysis 74
  Rutledge's model 72
  Spivak–Dzenis model 72
  Taylor cone 67
  three-dimensional (3-D) models 72
  Wan–Guo–Pan model 73
molecular bondings 23
molecular weight 29, 36, 53
molecular weight distribution 29

nanoclay 215
nanocomposite fiber 192
  carbon nanofiber 226
  graphite 222
  nanoclay 218
nanofiber 5
nanofiber technology 45
nanomaterials 5
nanosensor
  biosensor 159
nanotechnology 1 240
Newton's law 66
noncovalent functionalization 200
nonlinear behavior 15
nonlinearity 14
nonwoven
  deformation 86
  geometry 84
  mechanical properties 84
nuclear magnetic resonance 121

optical microscopy 102
optical nanofiber 62
orientation 28
orifice diameter 55

photonic nanofiber
  fluorescent nanofiber 184
  photo-catalytic nanofibers 186
porosimetry 115
power transmission line 243
protective clothing 59
purification 197
  centrifugation 197, 199
  electrophoresis 199
  filtration 197, 199
  gas-phase oxidation 197
  vapor-phase oxidation 197
  wet chemical oxidation 197–198

quality control 245

Raman spectroscopy 119
reinforcement 59

scale-up manufacturing 245
scanning electron microscopy 103
scanning tunnelling microscopy 110
sensor 62
simulation 75
size-effect 81
solubility parameter 33
solutions 33
spinning angle 55
spinning distance 54
structural characterization 102
structure of hierarchy of textile materials 81
supercapacitor 242
surface tension 52

temperature 52
thermal behavior 32 128
  differential scanning calorimetry 131
  thermogravimetric analysis 129
thermo analysis 128
tissue scaffold 61, 149, 244
transmission electron microscopy 106

van der Waals forces 24
viscoelastic 16
viscosity 36, 50
Voigt (Kelvin) model 20

wet spinning 40
wettability 134

wound dressing 61, 244
woven fabric
  geometry 97
  mechanical properties 96

X-ray diffraction 112
  small-angle X-ray scattering 114
  wide-angle X-ray diffraction 114

yarn properties
  geometry 88
  linear fiber assemblies 90
  mechanical properties 87
  staple yarns 93